Optimizing Laser-Tissue Interactions to Improve Targeting during Infrared Neural Inhibition

By

Jeremy Berlin Ford

Dissertation

Submitted to the Faculty of the

Graduate School of Vanderbilt University

in partial fulfillment of the requirements

for the degree of

DOCTOR OF PHILOSOPHY

In

Biomedical Engineering

September 30, 2020

Nashville Tennessee

Approved:

E. Duco Jansen, Ph.D.

Anita Mahadevan-Jansen, Ph.D.

Charles Caskey, Ph.D.

Hillel Chiel, Ph.D.

Peter Konrad, M.D.

Acknowledgements

This dissertation would not have been possible without the support of many people. I would like to thank my advisor and committee chair, E. Duco Jansen, for his guidance throughout this entire project. He allowed me the freedom to pursue this project and develop it as my own, always working with me to make it better. I have appreciated his insights both about science and life, and his mentorship has meant a lot to me throughout this entire process. I would also like to thank Dr. Anita Mahadevan-Jansen for her continued mentorship. She was the professor that first introduced me to the field of biophotonics, and then was the first person to spark my interest in infrared neural modulation. She has continued to mentor me academically and professionally and has provided myself and others with extensive resources and community as the director of the Vanderbilt Biophotonics Center. I want to thank Dr. Hillel Chiel who was instrumental in my training and opened his lab to me on multiple occasions. This thesis would not have been possible without the training from Dr. Hui Lu, Dr. Catherine Kehl, and Jeffrey Gill on electrophysiological techniques, surgical techniques, and keeping an *Aplysia* tank, which I learned during visits to Dr. Chiel's laboratory. I would like to thank Dr. Charles Caskey for his guidance and providing me with exposure to other neuromodulation techniques through hosting journal clubs on ultrasound neuromodulation. I also want to thank Dr. Marc Huntoon and Dr. Peter Konrad for providing their clinical expertise towards this project, especially Dr. Konrad his neurosurgical insights even before he was one of my committee members and for agreeing to serve on this committee on short notice.

Numerous others helped guide me and influenced the work in this dissertation throughout my time in graduate school. My collaborators at Case Western Reserve University were instrumental in my technical training, the experimental design process, and with understanding my data. I appreciate all of the feedback from Dr. Hillel Chiel, Dr. Michael Jenkins, Dr. Charles Horn, and their lab members on our weekly Skype meetings and visits to Case Western. Thank you Dr. Jenkins and Junqi Zhuo for your input and technical expertise. The members of the Vanderbilt Biophotonics Center (VBC) deserve more recognition than can be expressed here for all their support, feedback, and for creating a supportive community that was both conducive to learning and valued the importance of socialization and life outside of the lab. There are more current and previous members of the VBC than can be properly named here, but among them are Christine O'Brien, Isaac Pence, Oscar Ayala, and John Nguyen who all helped guide my early graduate career and pushed me to better myself as a scientist. My fellow neurophotonics researchers, Mohit Ganguly, Wilson Adam, Logan Jenkins, Manqing Wang, Graham Throckmorton, Ana Borracherro-Conejo, and Trevor Voss have all supported this work with their feedback and hours of conversation about research, graduate school, and life. I would like to thank Dr. Mohit Ganguly. His dissertation research made all of this possible. Thank

you for the years of scientific insight and feedback, being my first lab-mate, the long conversations, and the many conference rooftop drinks and Indian lunch buffets.

I would like to thank all of my friends for reminding me that there is a life outside of the lab. There are so many of you and not enough room to thank you for everything that you have done for me. I am grateful to my high school friends for putting up with my inconsistent participation as a fantasy football manager, but for never forgetting to rub it in when they beat me. I'm sorry Jeremy and Brandon for all of the rejected trades. I appreciate getting to spend every new years with all of you and thank you Jacob, Jeremy, Ethan, Josh, and Brandon for hosting the festivities and for always having a couch (crib) for me (and Tiffany) to sleep on no matter what the occasion. I would like to thank all of my undergraduate Vanderbilt friends for continuing to be like family even after we've graduated. You've all shown me what life after graduate school can be like and have constantly given me reasons to take a break with all of the bachelor parties, weddings, and Friendsgivings. To all of my graduate school friends, thank you for all of the much-needed chats and beers. Thank you for all of the March birthday parties and being such a great community. I would have never guessed that I would become a volleyball player, but after playing year-round for 6 years, you have all managed to help me become slightly competent at hitting a volleyball. Thank you to Evan, Kristina, Jake, Kristy, Wilson, Kat, and Megan, for the weekend sand volleyball games that I will greatly miss. The coffee shops around Nashville also deserve mention. Countless hours (and dollars) were spent at JJ's market (R.I.P.), Café Coco (R.I.P.), and Revelator reading papers, processing data, writing grants, making presentations, and writing manuscripts.

I want to thank my mom and dad for their support throughout graduate school. Despite each of them living far away and moving multiple times, there was always a room in their houses/apartments to come home to. For my sister, Charley Rita, for who inspired my graduate career, thank you for all of our conversations about video games and for putting up with all of my questions about your schooling. You have come a long way since you moved out to Portland the summer before I started graduate school. To my grandmother, Lillian, thank you for always being interested in the work I was doing.

Last and certainly not least, I want to thank my fiancée, Dr. Tiffany Heaster, for her unwavering support. From starting as classmates to becoming engaged while in a long distance relationship, she has continued to not only help keep me sane when times were tough, but also listen and provide feedback as a fellow scientist. Thank you for all of the work dates, all of the Skype dates, all of the late nights, and all of the coffee.

Table of Contents

Page

ACKNOWLEDGEMENTS …… iii

LIST OF TABLES…….. ix

LIST OF FIGURES……...…….. x

CHAPTER

I. Introduction 1

1.1 Motivation 1

1.2 Specific Aims 6

1.3 Dissertation Outline 8

1.4 References 9

II. Background 14

2.1 Neurophysiology 14

2.1.1 The Action Potential 14

2.1.2 Modeling Neural Conduction 15

2.1.3 Peripheral Pain Physiology 20

2.1.4 *Aplysia* as a Model System 21

2.2 Neuromodulation 22

2.2.1 Commonly Used Techniques 22

2.2.2 Infrared Neural Modulation 26

2.3 Laser-Tissue Interactions 30

2.3.1 Optical Interactions 32

2.3.2 Determining Light Distributions 33

2.3.3 Methods of optical property measurement 35

2.3.4 Thermal Interactions 38

2.3.5 Thermal Measurements 39

2.4 References 42

III. The Effect of Light Scattering on the Temperature Rise at Infrared Neural Inhibition Wavelengths .. 52

3.1 Abstract 52

3.2 Introduction 53

3.3 Methods 55

3.3.1 Published values for the Scattering Coefficient 55

3.3.2 Optical-Thermal Model 56
3.3.3 Phantom Creation 61
3.3.4 Optical Property Determination 61
3.3.5 Thermal Camera Validation Study 63
3.3.6 Thermocouple Validation Study 66
3.3.7 Optical Property Parametric Sweep 68
3.3.8 Water Bath Scattering Trend Validation 69
3.4 Results 72
3.4.1 Thermal Camera Measurements 72
3.4.2 Thermocouple Results 74
3.4.3 Parametric Sweep Results 76
3.4.4 Water Bath Results 80
3.5 Discussion 84
3.5.1 The effect of scattering on the temperature distribution 84
3.5.2 Model and Experimental Limitations 85
3.5.3 Practical Implications for Simulations of INI 89
3.6 Conclusions 90
3.7 References 91
IV. Identifying the Role of Block Length in Neural Heat Block to Reduce Temperatures during Infrared Neural Inhibition 97
4.1 Abstract 97
4.2 Introduction 98
4.3 Methods 101
4.3.1 Computational Modeling 101
4.3.2 Probe Design 102
4.3.3 *Ex Vivo* Electrophysiology Setup 103
4.3.4 Neural recordings 103
4.3.5 Thermal recordings 105
4.3.6 Data analysis 107
4.4 Results 108
4.4.1 Computational Modeling Suggests Increased Block Length Can Decrease Peak Temperatures 108
4.4.2 Using Two Fibers to Inhibit Decreases the Required Radiant Exposure per Fiber 109
4.4.3 Peak Temperatures Decrease when Using Two Fibers 112
4.4.4 Block Length is Increased when using Two Fibers 113

4.5 Discussion 116
4.5.1 Utilizing the Computational Model to Explore INI Parameter Space 116
4.5.2 Hypothesized Mechanism of Block Length 116
4.5.3 Sensitivity of INI to Probe Placement 117
4.5.4 Targeting Neural Subpopulations 118
4.5.5 Considerations for Thermal Measurements 120
4.5.6 Temperature Measurements Across Animal Models 122
4.6 Conclusions 124
4.7 References 125
V. Optimizing Thermal Block Length During Infrared Neural Inhibition to Minimize Temperature Thresholds 132
5.1 Abstract 132
5.2 Introduction 133
5.3 Methods 134
5.3.1 Electrophysiological Recordings 134
5.3.2 Infrared Neural Inhibition Protocols 135
5.3.3 Hot Media Inhibition Protocols 139
5.3.4 Data Analysis 141
5.4 Results 144
5.4.1 Two Block Length Regimes Are Observed During INI 144
5.4.2 Heat Block via Perfused Hot Media Validates the Longer Block Length Regime 146
5.5 Discussion 150
5.5.1 Inhibition Trends with Block Length 150
5.5.2 Optimizing Targeting 151
5.5.3 Mechanistic Considerations 152
5.6 Conclusions 153
5.7 References 154
VI. Conclusions and Future Directions 158
6.1 Summary and Conclusions 158
6.1.1 Summary 158
6.1.2 Major Conclusions 160
6.2 Future directions 161
6.2.1 Computational Investigations 161
6.2.2 Mechanistic investigation 163
6.2.3 Different threshold for different heating modalities 164

6.2.4 Vertebrate validation of BL 165
6.2.5 Clinical Feasibility Considerations 166
6.3 Protection of Research Subjects 167
6.4 Significance and Societal Implications 167
6.5 References 170

APPENDIX

A. Voltage-gated Potassium Channels are Critical for Infrared Inhibition of Action Potentials: An Experimental Study 172
A.1 Abstract 172
A.2 Introduction 172
A.3 Methods 173
A.3.1 Animal preparation 173
A.3.2 Experimental setup 173
A.3.3 Channel blockers and inhibitors 174
A.3.4 Experimental protocol 176
A.3.5 Data acquisition and analysis 176
A.4 Results 178
A.5 Discussion 180
A.6 References 180

List of Tables

Table		Page
3.1	Optical properties of neural tissues and various tissues in the infrared spectrum…….	57
3.2	Extrapolated μ_s' [mm^{-1}] in various tissues and the theoretical limits at INI wavelengths using equation 2.11……...	58
3.3	Agarose Phantom Recipes ……	60
3.4	Optical and thermal properties of simulated materials …….	65
4.1	Temperature rise for heat block across model systems……..	100
5.1	Irradiation Lengths tested for each nerve……...	138
5.2	T_{50} goodness of fit metrics for various fit types ……	145
5.3	Optimal fits of piecewise function parameters ……..	147

List of Figures

Figure		Page
1.1	Opioid related deaths during the opioid epidemic……..	4
1.2	Rate of spinal cord stimulator explants……..…….	5
2.1	Mechanism of neural conduction……..……..	16
2.2	Equivalent circuit of an axon's membrane……..……..	17
2.3	An example of a 360-channel high density electrode array……	23
2.4	Resting potential and action potential threshold potential as a function of temperature……	28
2.5	Axon diameter dependence of infrared neural inhibition……..	31
2.6	Integrating spheres to estimate optical properties……..……..	37
3.1	Phantom creation and characterization ……..……..	62
3.2	Liquid phantom creation and characterization …….....	70
3.3	Water bath thermal imaging setup ……..	71
3.4	Thermal camera validation study …….....	73
3.5	Thermocouple validation study ……..	75
3.6	Parametric sweep optical results ……	77
3.7	Parametric sweep absorbed photon distribution maps ……..	78
3.8	Parametric sweep absorbed photon distribution difference maps ……..	79
3.9	Parametric sweep thermal results ……..……..	81
3.10	Parametric sweep temperature distribution maps ……..	82
3.11	Water bath validation results ……..	83

3.12	Temperature distribution with fiber placement ……..	87
4.1	Experimental setups for comparing infrared neural inhibition thresholds using one vs two optical fibers…….……..	104
4.2	Computational modeling of one vs two fiber heat block shows longer heating along the axon results in lower temperature threshold……...	110
4.3	Electrophysiological results show using two optical fibers for infrared neural inhibition lowers the radiant exposure threshold per optical fiber……..	111
4.4	Thermocouple temperature measurements show infrared neural inhibition temperature thresholds are lowered using two optical fibers…….……	114
4.5	Magnetic resonance thermometry quantifies the increase in full width at half maximum of heating at inhibition neural inhibition threshold……..……...	115
5.1	Experimental setup to apply various block lengths for infrared neural inhibition……	136
5.2	Experimental setup to apply perfused hot media for heat block…….....	140
5.3	Representative signal processing to determine the 50% probability of inhibition……	142
5.4	50% probability of inhibition at different block lengths reveals two regimes……	148
5.5	Perfused hot media for heat block probes the longer block length regime…….....	149
A.1	Experimental setup simultaneously applying infrared neural inhibition and pharmacologic agents……..	175
A.2	Typical infrared neural inhibition……...	177
A.3	Blocking potassium ion channels eliminated infrared neural inhibition…….....	179

Chapter I

Introduction

1.1 Motivation

Neuromodulation, the external control of neurons and their signals, is a field that has been of interest for decades and has been advanced greatly in recent years. Greater understanding of the nervous system has uncovered a multitude of neurological diseases and has only broadened the questions that researchers attempt to answer. To probe the nervous system, whether for basic science, clinical research, or applied medical diagnostics and therapeutics, neuromodulation techniques are required that are tailored to each application. For example, in basic neuroscience research, an assortment of different electrical techniques are utilized that offer varying degrees of selectivity towards exciting different populations of neurons. Recently, light-based neuromodulation techniques have been developed which offer greater spatial specificity than other methodologies. Relatively new among these is using infrared laser irradiation to block the propagation of neural signals, called infrared neural inhibition (INI), as first described in 2013[1]. The advantages of INI are that it offers high spatial precision of inhibition of subsets of neurons within the bulk tissue and does not rely on introducing exogenous agents or genetic modification that other optical techniques rely on. Instead INI utilizes endogenous absorption of infrared light and may offer potential as the technique of choice specific research and clinical neuromodulation applications.

The importance of these neuromodulation techniques is highlighted by the effort in recent years for a precise understanding of the nervous system on both a cellular and systemic level through funding sources such as the BRAIN (Brain Research through Advancing Innovative Neurotechnologies) initiative and SPARC (Stimulating Peripheral Activity to Relieve Conditions) program, with an ultimate goal of mitigating the toll that neurological disease play on our society. One area of interest is the problem of chronic pain, defined as persistent pain for longer than 3-6 months. This is not a specific neurological dysfunction, but encompasses a broad spectrum of potential disease states resulting from a myriad of factors such as underlying disease[2], chronification of pain related to injury[3,4], medication rebound or overuse pain[5,6], and immune-related complications[7,8]. Examples of diseases associated with chronic pain include chronic back pain, rheumatoid arthritis, endometriosis, chronic headaches, irritable bowel syndrome, and

chronic fatigue syndrome[9], to name a few. It is estimated that 3-4.5% of the global population suffers from neuropathic pain with incidence rates increasing with age[10]. In the United States, an estimated 20% of adults are living with chronic pain, with 8% of adults having high-impact chronic pain that limits life or work activities[11]. A National Academies report from 2015 estimates the economic burden for treatment and lost productivity to be $560-635 billion[12].

Treatments for pain act to inhibit the propagation of pain signals to either block their transmission to the central nervous system or alter the perception of the pain sensation so that is not perceived as noxious. Modification of neural signals can be performed using chemicals, Most readily available treatments use pharmaceuticals, including opioids; however, increasing evidence emphasize the deleterious effects of prolonged opioid use, including abuse, overdose, and increased risk of fractures and myocardial infarctions[13,14]. Over prescription of opioids in the United States has led to their widespread use in what has been called the "opioid epidemic", a period of 16 years over which the rate of overdose deaths involving opioids has nearly quadrupled, where now opioids are responsible for 6 of every 10 overdose deaths[15]. This trend is demonstrated in Figure 1.1 from the Center for Disease Control and Prevention's webpage on the opioid epidemic[16]. In response, the NIH Pain Consortium put out a call for proposals for research into non-pharmaceutical pain-management[17], and a major national push has started to better understand the central and peripheral nervous systems and develop novel biological targets and clinical devices for pain management that do not rely on opioids, as outlined in the NIH HEAL (Helping to End Addiction Long-term) Initiative.

Non-pharmacologic, device-based methods of modulating activity to alleviate chronic pain can overcome many of the drawbacks of opioids. Methods such as transcutaneous electrical nerve stimulation (TENS) and spinal cord stimulation (SCS) are used to ameliorate peripheral neuropathies and utilize injection of current through skin or implanted electrodes; however, their use is accompanied by a variety of potential complications and side effects over time including lead migration, incompatibility with magnetic resonance imaging (MRI) scanners and pacemakers, and relatively poor specificity[18–23]. SCS in particular can suffer from >30% of devices being explanted over 5 years, where 20% of all devices are explanted due to inadequate pain relief[24] (Figure 1.2). Conversely, optical methods have shown to be spatially precise and do not interfere with electrical recordings[25,26], thus their compatibility with pacemakers and MRI scanners is expected. These optical methods, which include but are not limited to optogenetics[27], chemical uncaging[28], and infrared neural modulation[1,29], have been developed in the last few decades and represent modalities for highly targeted clinical neural control.

Thermal modulation of neural activity has been a subject of research for decades[30], and has made the jump to clinical implementation through RF based heating[31,32] and clinical trials for ultrasound neuromodulation[33]. Thermal modulation may be advantageous for a number of reasons, including: 1)

Temperature can be applied non-invasively, 2) thermal techniques do not necessarily require contact with tissue (e.g. laser heating), 3) while heat conducts through tissue, it propagates much slower than electrical current spread in tissue, potentially allowing for greater spatial localization, and 4) thermal modulation works through different mechanisms than electrical techniques and may not experience the same type of tolerance effects nor electrical toxicity effects. While the effect of temperature on neural conduction has been probed[30,34–37], there is a lack of understanding of how thermal modulation can best be utilized, and optimization of heating parameters is still needed for a clinical device to be viable. Thermal neuromodulation has been applied through radiofrequency (RF) heating[31], ultrasonic heating[38], and laser-induced heating[39,40]; however, complicating these thermal effects are concurrent electrical, mechanical, and optical (e.g. photochemical effects, ionizing radiation) interactions, respectively. Recent work has shown that temperature rises applied using short wave infrared (SWIR) lasers are effective in applying localized neuromodulation[1,29], and irradiation with these wavelengths almost exclusively result in tissue heating since they are highly absorbed by water[41], are too low in energy to induce photochemical effects, and operate in a pulse parameter regime that is not stress confined[42] (i.e. pressure in the tissue due to laser pulses does not build up). This methodology, called infrared neural modulation (INM), serves as an optimal technique to explore thermal effects on action potential propagation and optimize purely thermal parameters.

As previously discussed, INI is the regime of INM that results in block of neural signals by properly selecting laser pulse parameters[1]. This infrared optical technique has the potential to result in the development of a novel method of managing chronic neuropathic pain with lower costs, good analgesic efficacy, and improved targeting ability, without the risks associated with opioid analgesics. INI has already demonstrated a size dependence phenomenon where smaller diameter axons are inhibited with lower temperatures[43], which motivates that INI may be well suited to inhibit pain signals that typically are conducted to the central nervous system through small diameter axons[44]. Prior to clinical implementation, a clearer understanding is needed of the fundamental laser-tissue interactions. Primarily, investigation of these interactions will aid with targeting different neurons within bulk tissue in a therapeutic and non-damaging way which is a potential limitation when inducing a temperature rise on a small spatial scale. Towards reducing the probability of damage, temperatures induced in tissue should be minimized while still sufficient for inhibition. To date, INI has been implemented in acute studies in *Aplysia californica*[1,43,45], crayfish[46], rat[1], and musk shrew[43] demonstrating a reversible and non-damaging method of heat block, however the measured temperatures appear problematic for sustained clinical use. If INI is to succeed in longitudinal and clinical studies, methods of reducing the thermal load (temperature * time) applied to the tissue will be needed[47,48]. Ways of achieving this may take the form of reducing the temperature experienced by the tissue, reducing the time that a temperature is applied, and precisely applying the temperature such that only regions targeted for inhibition are heated, with minimal heating outside the region of interest.

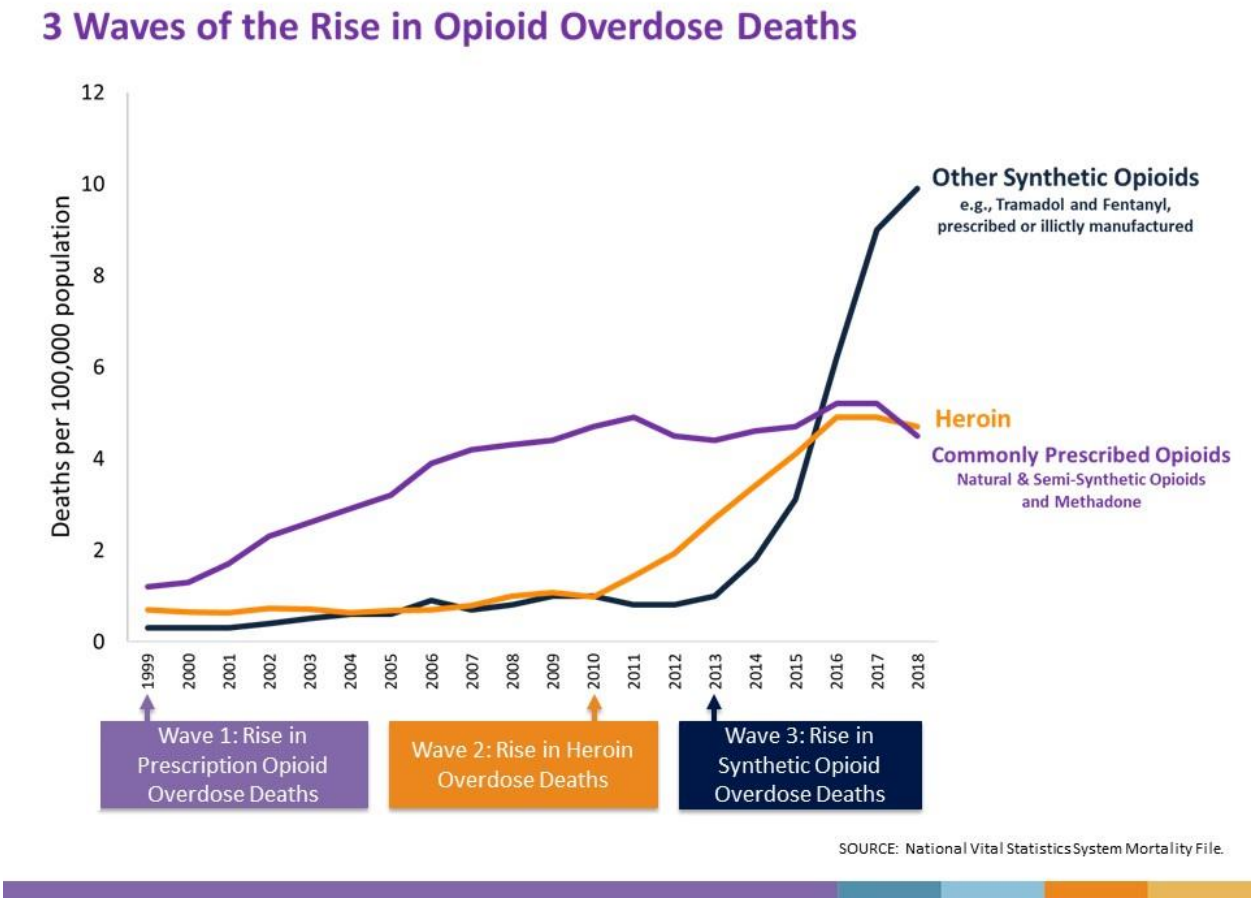

Figure 1.1. Opioid related deaths during the opioid epidemic. *Reprinted from the CDC website*[16].

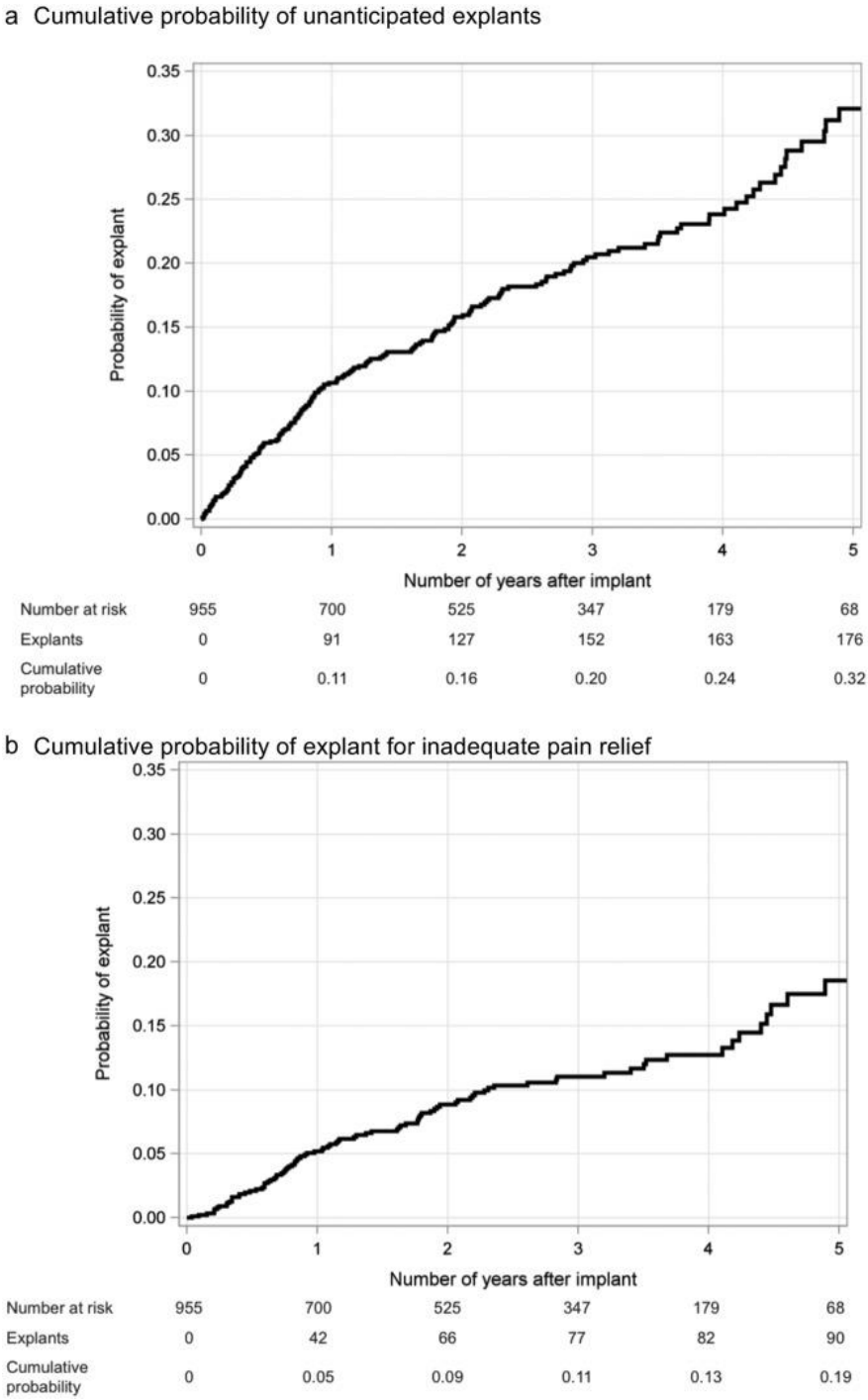

Figure 1.2. Rate of spinal cord stimulator explants. Cumulative probability of explant using the Kaplan-Meier estimator. Panel (a) shows estimated probability of unanticipated explant for any reason, while panel (b) is probability of explant for inadequate pain relief. *Reprinted from Van Buyten et al. 2017 [24]. © 2017 The Authors. Neuromodulation: Technology at the Neural Interface published by Wiley Periodicals, Inc. on behalf of International Neuromodulation Society. This is an open access article under the terms of the Creative Commons Attribution-NonCommercial License, which permits use, distribution and reproduction in any medium, provided the original work is properly cited and is not used for commercial purposes.*

1.2 Specific Aims

The work in this dissertation attempts to identify how light application can be tailored towards optimization of the heat distribution. Optimization may take many forms, but at its basic level, an understanding of where the heat goes and how hot the tissue gets during INI needs to be understood for proper targeting. Once the light and heat has been delivered to the tissue, cellular responses to this perturbation can be assessed to identify irradiation techniques that will target specific neural populations of interest. Considering an implantable research or clinical device to apply INI, neurons of interest must have therapy applied while residing within bulk tissue. Any technique towards minimizing temperature and optimizing efficacy needs to be able to be applied *in situ* with minimal physical manipulation of the neural tissue. One easily controllable parameter is the length of applied heating along an axon. Thus, the work in this dissertation assesses whether the length of heating along the axon, herein referred to as the block length (BL), may provide a method of reducing the temperature needed for INI and better targeting of neurons within bulk nerve. In addition, proper placement of any clinical device is crucial to selectively target neurons of interest, and while the temperature for inhibition can be reduced, its advantage will be lost if proper targeting is not performed. While intraoperative functional tests can be performed to aid in the placement of a device, the collateral effect of heating will be poorly quantified, and optimal placement may be hard to ensure. Therefore, an understanding of the induced heat distribution is important to guide the targeting of specific neurons in the bulk nerve. Direct measurements within a nerve may not be possible, especially clinically, but computational models offer a method of predicting how tissue will respond to laser irradiation across many different scenarios. Therefore, to optimize targeting of neurons in the bulk nerve with lower temperatures, three aims are proposed:

Specific Aim 1: Characterize the effect of optical scattering on the temperature distribution from laser irradiation

Computational modeling of biophysical phenomena provides a means of rapidly probing underlying physics, assessing biological mechanisms, and optimizing application of various techniques. Optical, thermal, and neural simulations can be paired to understand INI all the way from the light source to action potential failure. These simulations provide a method of assessing laser-induced heat distributions in tissue towards optimizing targeting of neurons in known tissue geometries. One critical barrier limiting the predictive power of these models for INI is the lack of understanding of how optical scattering contributes to the temperature distribution. The value of the scattering input parameter into Monte Carlo simulations of photon propagation is unknown for nerve at INI wavelengths, and multiple factors make direct

measurement exceedingly difficult. To probe how optical scattering ultimately affects the heat distribution from laser irradiation, a Monte Carlo was used to inform the heat source in a COMSOL Multiphysics thermal model. The results from this model were validated in two different setups, and then a parametric sweep across optical absorption and reduced scattering coefficients was performed. Subsequent validation of the trends with scattering were validated in a final set of experimental measurements.

Specific Aim 2: Identify the effect of block length during infrared neural inhibition

Temperature thresholds identified for infrared neural inhibition are non-damaging and sufficient for acute experiments; however, for long term applications, these temperatures prove problematic. It has been hypothesized that a relationship may exist between the applied BL and the temperature needed for INI. The presence of this relationship would suggest that the temperature for INI can be reduced with proper application of the BL. In this aim, the presence of this phenomenon was established by probing INI in *Aplysia*. As a first approximation, temperature thresholds for INI using one optical fiber were compared to two fibers aligned axially along nerves, doubling the irradiation length. Temperatures from laser irradiation were assessed at INI radiant exposure thresholds using a thermocouple in a water bath and magnetic resonance thermometry of an immersed nerve phantom.

Specific Aim 3: Optimize block length as a viable strategy for reducing the temperature during infrared neural inhibition

Initial investigation in Aim 2 provided the proof-of principle that there exists a relationship between the BL and the temperature needed to apply INI, and that using two adjacent optical fibers offers inhibition at a lower temperature compared to a single fiber. With this revelation, it is possible that the BL may be optimized to minimize the temperature at INI threshold. Therefore, a probe which would allow for application of many different lengths of IR irradiation, and therefore many block lengths, was constructed to explore the parameter space. A novel setup for performing simultaneous measurement of electrical activity and temperature information in *Aplysia* nerves was developed which allowed for determination of the probability of inhibition as a function of temperature for different neural populations. Performing this assessment across many nerve irradiation lengths provided a clearer picture of how BL affects the INI temperature threshold and revealed an unexpected relationship where two regimes exist. This result was then validated using non laser-induced heating, where heated saline was instead perfused over the nerve.

1.3 Dissertation Outline

The material comprising this dissertation is organized in the following manner:

Chapter I gives and introduction to the goal of this dissertation. The motivation for the work contained herein is outlined, and specific aims developed to complete this goal are discussed.

Chapter II provides background on information necessary to understand the work conducted in this dissertation. Methods of neuromodulation are introduced, the physiology of pain is discussed, and infrared neural inhibition is defined in detail. Underlying laser-tissue interactions leading to INI are described, and methodologies for computationally assessing these biophysical phenomena are presented.

Chapter III characterizes the effect of optical scattering on the temperature distribution induced by laser heating at INI wavelengths. Both a computational parametric sweep of the parameter space of absorption and scattering and a set validation studies were performed to demonstrate how the maximum temperature, full width at half maximum, and thermal penetration depth change as a function of optical scattering. This work has been written up in a manuscript that is in preparation for submission to the *Journal of Biomedical Optics* (JBO).

Chapter IV demonstrates a proof-of-principle of the presence of a block length-dependent inhibition phenomenon, performed both computationally and with an *in vitro* invertebrate nerve preparation. The work presented here was published in: Ford, J.B., Ganguly, M., Poorman, M.E., Grissom, W.A., Jenkins, M.W., Chiel, H.J. and Jansen, E.D. “Identifying the Role of Block Length in Neural Heat Block to Reduce Temperatures During Infrared Neural Inhibition”. Lasers Surg. Med., 52: 259-275. (2020)

Chapter V assesses the parameter space of BL and optimizes the length of laser-induced heat application along the nerve. This work not only identifies thermal thresholds for different block lengths but identifies two different regimes of thermal block. This work was submitted as: Ford J.B., Ganguly M., Zhuo J., McPheeters M.T., Jenkins M.W., Chiel H.J., and Jansen E.D. “Optimizing Thermal Block Length During Infrared Neural Inhibition to Minimize Temperature Thresholds” Journal of Neural Engineering. (*in review*).

Chapter VI summarizes the results of this dissertation and presents a set of conclusions about how the contained work may impact the field of infrared neural modulation, and society more broadly. Steps towards continuing this work and future studies that are possible due to the findings presented here are outlined.

Appendix A describes a study conducted in the *Aplysia* nerve to investigate the mechanism underlying INI. This work was published in: Mohit Ganguly, Jeremy B. Ford, Junqi Zhuo, Matthew T. McPheeters, Michael W. Jenkins, Hillel J. Chiel, E. Duco Jansen, "Voltage-gated potassium channels are

critical for infrared inhibition of action potentials: an experimental study," Neurophoton. 6(4) 040501 (2019).

1.4 References

1. Duke AR, Jenkins MW, Lu H, McManus JM, Chiel HJ, Jansen ED. Transient and selective suppression of neural activity with infrared light. *Sci Rep*. 2013;3:2600. doi:10.1038/srep02600

2. Sluka KA, Clauw DJ. Neurobiology of fibromyalgia and chronic widespread pain. *Neuroscience*. 2016. doi:10.1016/j.neuroscience.2016.06.006

3. Pergolizzi J V., Raffa RB, Taylor R. Treating acute pain in light of the chronification of pain. *Pain Manag Nurs*. 2014. doi:10.1016/j.pmn.2012.07.004

4. Hashmi JA, Baliki MN, Huang L, et al. Shape shifting pain: Chronification of back pain shifts brain representation from nociceptive to emotional circuits. *Brain*. 2013. doi:10.1093/brain/awt211

5. Rapoport A, Stang P, Gutterman DL, et al. Analgesic rebound headache in clinical practice: Data from a physician survey. *Headache*. 1996. doi:10.1046/j.1526-4610.1996.3601014.x

6. Newman LC, Newman EB. Rebound abdominal pain: Noncephalic pain in abdominal migraine is exacerbated by medication overuse. *Headache*. 2008. doi:10.1111/j.1526-4610.2008.01126.x

7. Grace PM, Hutchinson MR, Bishop A, Somogyi AA, Mayrhofer G, Rolan PE. Adoptive transfer of peripheral immune cells potentiates allodynia in a graded chronic constriction injury model of neuropathic pain. *Brain Behav Immun*. 2011. doi:10.1016/j.bbi.2010.11.018

8. Totsch SK, Sorge RE. Immune system involvement in specific pain conditions. *Mol Pain*. 2017. doi:10.1177/1744806917724559

9. McAllister MJ. What is Central Sensitization? Institute for Chronic Pain. https://www.instituteforchronicpain.org/understanding-chronic-pain/what-is-chronic-pain/central-sensitization. Accessed April 21, 2020.

10. Global Industry Analysts I. *Global Pain Management Market to Reach US$60 Billion by 2015, According to a New Report by Global Industry Analysts, Inc.* San Jose, CA; 2011. http://www.prweb.com/pdfdownload/8052240.pdf.

11. Dahlhamer JM, Lucas J, Zelaya C, et al. Prevalence of chronic pain and high-impact chronic pain among adults — United States, 2016. *Morb Mortal Wkly Rep*. 2018. doi:10.15585/mmwr.mm6736a2

12. A. Pizzo P, M. Clark N, Carter Pokras O. *Relieving Pain in America: A Blueprint for Transforming Prevention, Care, Education, and Research*.; 2011. doi:10.3109/15360288.2012.678473

13. Chou R, Turner JA, Devine EB, et al. The effectiveness and risks of long-term opioid therapy for chronic pain: A systematic review for a national institutes of health pathways to prevention workshop. *Ann Intern Med*. 2015;162(4):276-286. doi:10.7326/M14-2559

14. Vowles KE, McEntee ML, Julnes PS, Frohe T, Ney JP, van der Goes DN. Rates of opioid misuse, abuse, and addiction in chronic pain: a systematic review and data synthesis. *Pain*. 2015;156(4):569-576. doi:10.1097/01.j.pain.0000460357.01998.f1

15. US Department of Health and Human Services. *The Opioid Epidemic: By the Numbers*.; 2016. https://www.hhs.gov/sites/default/files/Factsheet-opioids-061516.pdf.

16. CDC. Understanding the Epidemic. https://www.cdc.gov/drugoverdose/epidemic/index.html. Published 2020. Accessed April 23, 2020.

17. NIH Pain Consortium. NIH-DoD-VA Pain Management Collaboratory Funding Opportunity Announcement. https://grants.nih.gov/grants/guide/rfa-files/RFA-AT-17-002.html. Published 2016.

18. Liebano R, Rakel B, Vance CGT, Walsh DM, Sluka K a. An Investigation of the Development of Analgesic Tolerance to Transcutaneous Electrical Nerve Stimulation (TENS) in Humans. *Pain*. 2011;152(2):335-342. doi:10.1016/j.pain.2010.10.040.An

19. Jones I, Johnson MI. Transcutaneous electrical nerve stimulation. *Contin Educ Anaesthesia, Crit Care Pain*. 2009;9(4):130-135. doi:10.1093/bjaceaccp/mkp021

20. Bergeron-Vézina K, Corriveau H, Martel M, Harvey M-P, Léonard G. High- and low-frequency transcutaneous electrical nerve stimulation does not reduce experimental pain in elderly individuals. *Pain*. 2015;156(10):2093-2099. doi:10.1097/j.pain.0000000000000276

21. Grider JS, Manchikanti L, Carayannopoulos A, et al. Effectiveness of Spinal Cord Stimulation in Chronic Spinal Pain: A Systematic Review. *Pain Physician*. 2016;19(1):E33-E54.

22. Moore DM, McCrory C. Spinal cord stimulation. *BJA Educ*. 2016:1-6. doi:10.1053/trap.2000.9683

23. Verrills P, Sinclair C, Barnard A. A review of spinal cord stimulation systems for chronic pain. *J Pain Res*. 2016;9:481-492. doi:10.2147/JPR.S108884

24. Van Buyten JP, Wille F, Smet I, et al. Therapy-Related Explants After Spinal Cord Stimulation: Results of an International Retrospective Chart Review Study. *Neuromodulation*. 2017. doi:10.1111/ner.12642

25. Wells J, Kao C, Jansen ED, Konrad P, Mahadevan-Jansen A. Application of infrared light for in vivo neural stimulation. *J Biomed Opt*. 2005;10(6):064003. doi:10.1117/1.2121772

26. Duke AR, Jenkins MW, Lu H, McManus JM, Chiel HJ, Jansen ED. Transient and selective suppression of neural activity with infrared light. *Sci Rep*. 2013;3:2600. doi:10.1038/srep02600

27. Guru A, Post RJ, Ho YY, Warden MR. Making sense of optogenetics. *Int J Neuropsychopharmacol*. 2015. doi:10.1093/ijnp/pyv079

28. Kantevari S, Matsuzaki M, Kanemoto Y, Kasai H, Ellis-Davies GCR. Two-color, two-photon uncaging of glutamate and GABA. *Nat Methods*. 2010;7(2):123-125. doi:10.1038/nmeth.1413

29. Wells J, Kao C, Jansen ED, Konrad P, Mahadevan-Jansen A. Application of infrared light for in vivo neural stimulation. *J Biomed Opt*. 2005;10(6):064003. doi:10.1117/1.2121772

30. Hodgkin AL, Katz B. the Effect of Temperature on the Electrical Activity of the Giant Axon of the Squid. *J Physiol Lucas Gasser Schoepfle Erlanger Cardot Arvanitaki*. 1949;09:240-249.

31. Slappendel R, Crul BJP, Braak GJJ, et al. The efficacy of radiofrequency lesioning of the cervical spinal dorsal root ganglion in a double blinded randomized study: No difference between 40°C and 67°C treatments. *Pain*. 1997. doi:10.1016/S0304-3959(97)00094-8

32. Byrd D, Mackey S. Pulsed radiofrequency for chronic pain. *Curr Pain Headache Rep*. 2008. doi:10.1007/s11916-008-0008-3

33. Fomenko A, Neudorfer C, Dallapiazza RF, Kalia SK, Lozano AM. Low-intensity ultrasound neuromodulation: An overview of mechanisms and emerging human applications. *Brain Stimul*. 2018. doi:10.1016/j.brs.2018.08.013

34. de la Peña E, Mälkiä A, Vara H, et al. The Influence of Cold Temperature on Cellular Excitability of Hippocampal Networks. *PLoS One*. 2012. doi:10.1371/journal.pone.0052475

35. Ganguly M, Jenkins MW, Jansen ED, Chiel HJ. Thermal block of action potentials is primarily due to voltage-dependent potassium currents: A modeling study. *J Neural Eng*. 2019. doi:10.1088/1741-2552/ab131b

36. Zhang Z, Lyon TD, Kadow BT, et al. Conduction Block of Mammalian Myelinated Nerve by Local Cooling to 15-30 ℃ after a Brief Heating. *J Neurophysiol*. 2016;115(3):1436-1445. doi:10.1152/jn.00954.2015

37. Shapiro MG, Homma K, Villarreal S, Richter C-P, Bezanilla F. Infrared light excites cells by changing their electrical capacitance. *Nat Commun*. 2012;3:736. doi:10.1038/ncomms1742

38. Blackmore J, Shrivastava S, Sallet J, Butler CR, Cleveland RO. Ultrasound Neuromodulation: A Review of Results, Mechanisms and Safety. *Ultrasound Med Biol*. 2019. doi:10.1016/j.ultrasmedbio.2018.12.015

39. Cayce JM, Friedman RM, Jansen ED, Mahavaden-Jansen A, Roe AW. Pulsed infrared light alters neural activity in rat somatosensory cortex in vivo. *Neuroimage*. 2011;57:155-166. doi:10.1016/j.neuroimage.2011.03.084

40. Fork RL. Laser stimulation of nerve cells in *Aplysia*. *Science*. 1971;171(3974):907-908. doi:10.1126/science.171.3974.907

41. Hale GM, Querry MR. Optical Constants of Water in the 200-nm to 200-microm Wavelength Region. *Appl Opt*. 1973;12(3):555-563. doi:10.1364/AO.12.000555

42. Wells J, Kao C, Konrad P, et al. Biophysical Mechanisms of Transient Optical Stimulation of Peripheral Nerve. *Biophys J*. 2007;93(7):2567-2580. doi:10.1529/biophysj.107.104786

43. Lothet EH, Shaw KM, Lu H, et al. Selective inhibition of small-diameter axons using infrared light. *Sci Rep*. 2017;7(1). doi:10.1038/s41598-017-03374-9

44. Armstrong SA, Herr MJ. Physiology, Nociception. StatPearls [Internet]. https://www.ncbi.nlm.nih.gov/books/NBK551562/#. Published 2020.

45. Ganguly M, Ford JB, Zhuo J, et al. Voltage-gated potassium channels are critical for infrared inhibition of action potentials: an experimental study. *Neurophotonics*. 2019. doi:10.1117/1.nph.6.4.040501

46. Zhu X, Lin J-W, Sander MY. Infrared inhibition and waveform modulation of action potentials in the crayfish motor axon. *Biomed Opt Express*. 2019. doi:10.1364/boe.10.006580

47. Dewhirst MW, Viglianti BL, Lora-Michiels M, Hanson M, Hoopes PJ. Basic principles of thermal dosimetry and thermal thresholds for tissue damage from hyperthermia. In: *International Journal of Hyperthermia*. Vol 19. ; 2003:267-294. doi:10.1080/0265673031000119006

48. Yarmolenko PS, Moon EJ, Landon C, et al. Thresholds for thermal damage to normal tissues: An update. *Int J Hyperth*. 2011;27(4):320-343. doi:10.3109/02656736.2010.534527

Chapter II

Background

2.1 Neurophysiology

2.1.1 The Action Potential

The action potential (AP) is the electrochemical neural signal that neurons use to communicate with other neurons and effector organs. Ultimately to understand any neuromodulation technology, the basics of neural conduction must be understood, since the end goal of neuromodulation is to either elicit APs or silence them. APs are generated by neurons, the basic unit of the nervous systems, which are composed of four separate regions: dendrites, axons, cell body, and the axon terminal[1]. The dendrites receive external information from either their environment or other neurons, and have specialized structures or ion channels to be sensitive to different stimuli, such as chemical stimuli, mechanical stimuli, or temperature[2]. Axons, the specialized long projections of the cell which can span lengths from millimeters up to a meter, are responsible for conducting action potentials across distances to reach the signal's destination. At the end of the axon is the axon terminal which turns the electrochemical signal into a chemical signal that can be sensed by other neurons or effector organs at the synapse. Neural activity is only possible because of the electrochemical gradient established across the semi-permeable cell membrane of the neuron (Figure 2.1, A). Ions are transported across the membrane using proteins (ion channels and pumps) in both passive and active transport. Separation of charge leads to both a capacitive effect and the establishment of an electrical potential across the cell membrane, and each type of charged particle, E_x, contributes to this membrane potential according to its equilibrium potential, or Nernst potential.

$$E_x = \frac{RT}{zF} \ln \frac{[Concentration\ Outside\ Cell]}{[Concentration\ Inside\ Cell]} \qquad \text{Equation 2.1}$$

where R is the ideal gas constant (R=8.314 J/mol/K), T is the temperature in Kelvin, z is the valence of the charge (ex. +1 for K^+, -1 for Cl^-), and F is Faraday's constant (F= 96,485 C/mol).

Typically, only sodium, Na^+, potassium, K^+, and chloride, Cl^-, ions are considered when calculating the resting potential, however calcium ions and negatively charged proteins may play a role as well[1]. At equilibrium, neurons have a resting potential of -60 to -80 mV (intracellular compared to extracellular). Neural signaling takes advantage of charge separation by selectively allowing ions to flow along their electrochemical gradient. An action potential is characterized by the following set of interactions (Figure 2.1, B). When a stimulus of sufficient amplitude is applied that depolarizes a region the membrane, it elicits a response in voltage-sensitive channels in the membrane. Voltage gated sodium channel (Na_V), initially in a closed state, respond to a depolarization by opening and allowing an influx of positively charge sodium ions into the negatively charged cell, resulting in further depolarization which recruits more Na_V. The membrane potential approaches the Nernst potential for Na^+ (+ 55 mV). The Na_V quickly enter an inactivated state where the pore of the channel is open, but ions may not flow through, and eventually the channels enter the closed state where the pore is closed and ions due not pass through. Depolarization of the membrane triggers voltage gated potassium channels (K_V) causing positive potassium ions to flow out of the now positively charged region of the cell towards the Nernst potential of K^+ (-90 mV) which repolarizes the cell to a state that is hyperpolarized compared its resting potential. When the membrane is hyperpolarized, the K_V channels inactivate, and the active transport of sodium and potassium through Na/K ATPase bring the potential back to the resting potential. This interaction occurs over small regions of membrane, however, depolarization in one region of membrane elicits this cascade of interactions in adjacent regions of membrane, causing a depolarization wave down the axon which is transduced at the axon terminal into a chemical signal that can be sensed by other cells. Inhibitory neuromodulation techniques can interfere with this signaling at the level of stimulus application at the dendrites, at the axonal level to block the propagation of an elicited AP, or at the axon terminal to stop chemical release the post-synaptic cell. It should be noted that this entire process relies on temperature-dependent interactions, which play a role in the mechanism of thermal neuromodulation.

2.1.2 Modeling Neural Conduction

2.1.2.1 The Hodgkin-Huxley Model

Ionic currents in neurons can be modeled to investigate ion channel kinetics, the dynamics of neural signal generation and propagation, and the mechanism of stimulation or inhibition of neuromodulation techniques. The Hodgkin-Huxley (HH) model provides a set of equations that adequately evaluates action potential propagation by considering an equivalent electric circuit of the cellular membrane (Figure 2.2). This model was introduced in a series of papers in the 1950s published by Hodgkin and Huxley[4,5]. The axon

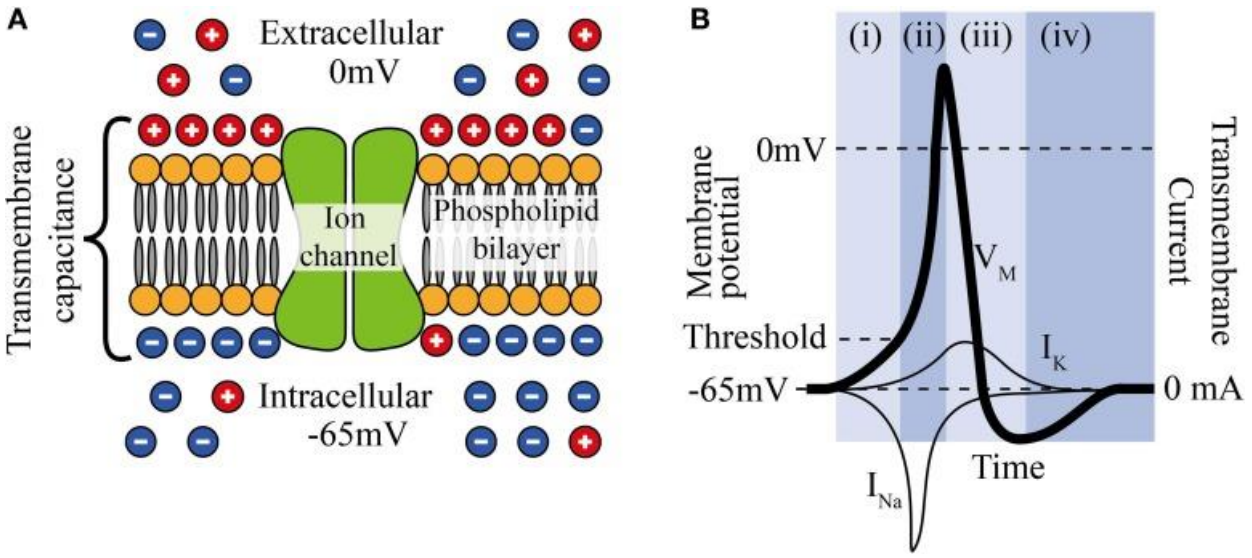

Figure 2.1 Mechanism of neural conduction. A) Axonal membrane. The phospholipid bilayer membrane separates charge, polarizing the cell and creating a capacitance. Ions can cross the membrane through ion channel proteins contained within the membrane. B) A typical action potential. Stimuli cause a depolarization of the membrane (i). Once a threshold voltage is reached, voltage gated sodium channel open providing the sodium current (I_{Na}) responsible for the rising phase of the action potential (ii). Voltage gated potassium channels are triggered which rapidly depolarize the membrane in the falling phase of the action potential (iii). The resting potential is reestablished using pump proteins (iv). *Reprinted from Luan et al.[3]. Copyright © 2014 Luan, Williams, Nikolic and Constandinou. This is an open-access article distributed under the terms of the Creative Commons Attribution License (CC BY). The use, distribution or reproduction in other forums is permitted, provided the original author(s) or licensor are credited and that the original publication in this journal is cited, in accordance with accepted academic practice. No use, distribution or reproduction is permitted which does not comply with these terms.*

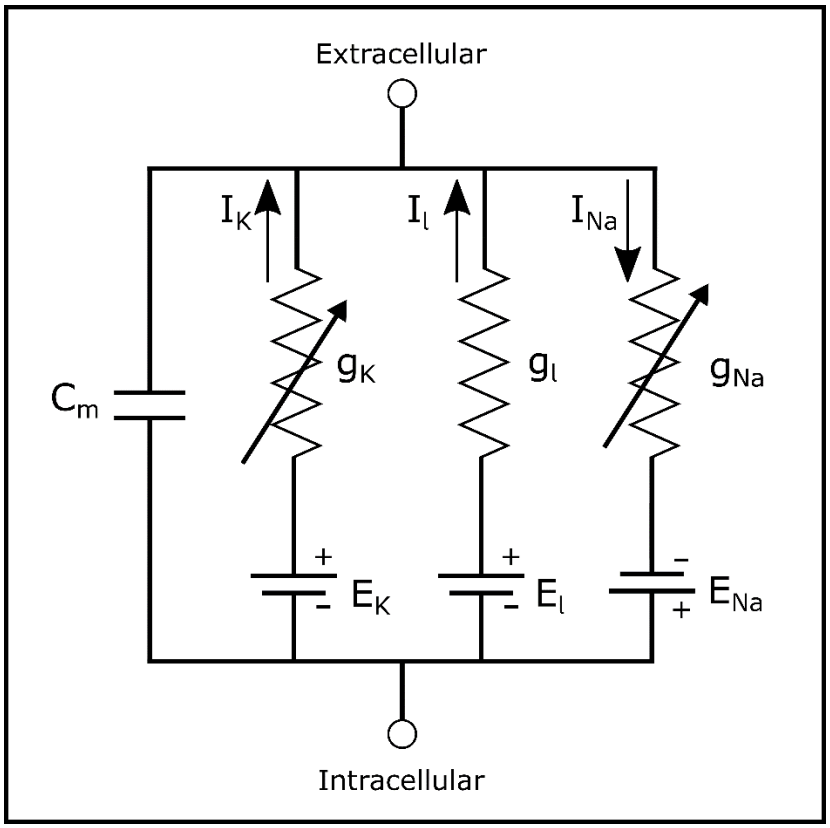

Figure 2.2. Equivalent circuit of an axon's membrane. The current across the axonal membrane is the sum of component currents from ionic components traversing the membrane (Sodium (Na), Potassium (K), and leak (l)) and from the membrane capacitive component (C_m). Ionic currents (I_{ion}) are driven by the separation of ions across the cell membrane, resulting in the Nernst potential driving force which is represented as batteries (E_{ion}). Each ion has a particular conductance (g_{ion}) across the membrane, represented as resistors, and the sodium and potassium conductances are represented as variable resistors due to their voltage-dependence. *Adapted from Hodgkin et al*[6]

is modeled as a cylinder with a radius, r_i, and negligible membrane thickness. The extracellular space is assumed to be grounded and a good conductor. Currents through the membrane are defined as either an ionic current (I_{ionic}) or a capacitive current (I_{Cm}), whereby the total current through the membrane is the sum of the capacitive current and all ionic currents. The membrane is modeled as a capacitor (the membrane capacitance) in parallel with a set of parallel resistors and voltage sources (representing ion conductances and the Nernst potentials of individual ion species, respectively)[5].

The HH model accounts for three types of ionic currents-sodium (Na^+), potassium (K^+), and leak (L) where:

$$I_{ionic} = I_{Na^+} + I_{K^+} + I_L \qquad \text{Equation 2.2}$$

In Figure 2.2, each ionic current is dictated by an Nernst potential, E_{ion}, and a conductance, g_{ion}. Variable conductance is used for Na^+ and K^+ to account for their voltage sensitivity. Each ionic current can be calculated as:

$$I_{ion} = g_{ion}(V_m - E_{ion}) \qquad \text{Equation 2.3}$$

where V_m is the membrane potential. g_{Na} and g_K are modeled as a function of gating elements which represent the probability of the channel changing into either a conducting or non-conducting state: labeled m for sodium activation, h for sodium inactivation, and n for potassium activation. Values for these gating elements were experimentally derived by monitoring sodium and potassium conductance over the course of the action potential. When fitting the change in potassium conductance, it was found that an n^4 relationship best modeled potassium activation. Similarly, sodium activation was found to have an m^3 relationship, and sodium inactivation an h relationship. Thus, conductance is modeled by the following equations:

$$g_{K^+} = \bar{g}_{K^+} n^4 \qquad \text{Equation 2.4}$$

$$g_{Na^+} = \bar{g}_{Na^+} m^3 h \qquad \text{Equation 2.5}$$

where $\bar{g}_{Na^+}$ and $\bar{g}_{K^+}$ are the maximum sodium and potassium conductance [conductance/cm^2], respectively, and n, m, and h are all dimensionless variables between 0 and 1. The gating elements n, m, and h can all be calculated from the equations:

$$\frac{dn}{dt} = \alpha_n (1 - n) - \beta_n n \quad \text{Equation 2.6}$$

$$\frac{dm}{dt} = \alpha_m (1 - m) - \beta_m m \quad \text{Equation 2.7}$$

$$\frac{dh}{dt} = \alpha_h (1 - h) - \beta_h h \quad \text{Equation 2.8}$$

where α and β are voltage dependent variables. α represents the rate of transfer for each gating variable from a non-activated state to an activated state, while β is the rate of transfer from an activated state to a non-activated state. Hodgkin and Huxley experimentally determined the values of α and β in the squid giant axon at 6.3^{O}C[5]. Both α and β values for other neural systems at other temperatures have been calculated[7,8]. A temperature dependence has been incorporated into these variables, deemed the Q_{10}. The Q_{10} is the rate by which biological processes are accelerated when their temperature increases by 10^{O}C, $Q_{10} = \frac{velocity\ at\ T_0+10}{velocity\ at\ T_0}$ [9]. Using these equation, neural activity can be adequately modeled in response to a range of conditions such as tissue heating.

2.1.2.2 The NEURON Simulation Environment

NEURON is a simulation environment which provides a platform for computational models of neurons and networks of neurons[10]. Using NEURON, the Hodgkin Huxley model, as well as other neural conduction models, may be applied. NEURON relies on the application of the cable equation:

$$\frac{\partial V}{\partial t} + I(V, t) = \frac{\partial^2 V}{\partial x^2} \quad \text{Equation 2.9}$$

which describes the current-voltage relationship in a one-dimensional cable[11,12]. Computational geometries comprised of multiple connected segments of axons can be set up over which the cable equation is solved by using applied mechanism files which define parameters such as the maximum sodium conductance, α and β for different gates, and temperature dependencies of HH parameters. NEURON has been used to simulate neural activity in many scenarios, including for heat block[13,14]. One of the parameters able to be modified is the temperature of each computational node. Ganguly *et al.* utilized the NEURON simulation environment to develop a modified HH model with a more appropriate temperature dependency at the elevated temperatures used for INI[14], and the mechanistic predictions generated from this modified model

were validated experimentally[15], which motivates that INI can be accurately computationally assessed using NEURON.

2.1.2.3 Length Constant

One important interpretation of the cable equation is the length constant of axons. Voltages in axons decay over distance when not actively propagated by Na_V, and this can be assessed by considering steady state behavior (dV/dt = 0). What emerges from this analysis is that the voltage exponentially decays as a function of distance as governed by the length constant, Λ, which is defined as the square root of the ratio of the membrane resistance, r_m, to the intracellular resistance, r_i, ($\Lambda = \sqrt{[r_m/r_i]}$).

$$V(x) = V_{max}\, e^{-x/\Lambda} \qquad \text{Equation 2.10}$$

Where V(x) is the membrane voltage over the axon, V_{max} is the maximum value of the voltage, x is the distance from where current/voltage is applied. As axon diameters increase, r_m decreases due to a larger cross-sectional circumference and r_i increases due to a larger cross-sectional area, which results in Λ increasing. Thus, voltages decay over longer distances for larger diameter axons. The practical consideration for this is that when applying a neuromodulation method, if it targets axons, both the axon diameters of the neurons and the length of axon over which the neuromodulation is applied should be considered since it may affect dosage. Indeed, for infrared neural inhibition, it was determined that larger diameter axons require greater temperatures for inhibition[16]. This was first determined analytically using the cable equation and then validated experimentally. It would also stand to reason that length dependent effects may exist for infrared neural inhibition.; however, investigation is needed into how these phenomena may interact.

2.1.3 Peripheral Pain Physiology

Pain is the unpleasant experience that is utilized to alert organisms to the occurrence, or the potential, of tissue damage. The fundamental transmission of pain signals relies on action potential propagation and utilize the architecture of the nervous system. The transmission of these signals which encode for pain is called nociception, and thus neurons that carry these signals are called nociceptors. Nociceptors, residing in the peripheral nervous system (PNS), relay information to the brain via the spinal cord which both make up the central nervous system (CNS). Once at the brain, these signals will be perceived as pain, both in terms of eliciting a physical response and affecting emotional state.

Neuromodulation for pain management can interrupt the transduction process at any of these tissues depending on the disease state and intended effect. For the purpose of this thesis, it is helpful to focus on the peripheral nervous system because it provides and advantageous morphology to investigate the effect of block length since heating can be localized to axons which are organized into bundles within nerves. This physiology allows for the approximation of each axon as an electrically excitable cable, which can then utilize the cable equation (Section 2.1.2.2) to approximate the membrane potential and inter/intracellular currents.

The axons in nerves project from different types of neurons that can encode motor or sensory information. Some of these axons are encircled by myelin which acts as an insulator to increase the speed of signal propagation, or conduction velocity, through saltatory conduction[17,18]. Neurons with myelin are referred to as A type neural fibers while those without myelin are C type neural fibers. Nociception is conducted by Aδ and C fibers[1,19,20]. Aδ fibers encode for heat, cold, and mechanothermal information from the skin, and when activated provide the fast sensation of pain typically thought of as a "pinprick" sensation. Their axons are the smallest of A type neurons, 1 to 5 μm in diameter, and conduct at speeds of 5 to 40 m/s. C fibers, on the other hand, are the smallest diameter axons, 0.02 to 1.5 μm, and conduct at 0.5 to 2 m/s. A single C fiber can encode multiple modalities of pain from either chemical, thermal, or mechanical stimulate, and therefore are sometimes referred to as polymodal nociceptors. When activated, they are associated with the slow, deep "burning" pain, and account for 70% of noxious input into the central nervous system[1]. Notably, C fibers can experience a phenomenon called "wind-up" where repetitive stimulation of these neurons results in greater intensity of pain over time[19,20]. It has been suggested that this wind-up contributes to the development of central sensitization[21–24], characterized by a decrease in the signal threshold at the spinal cord to elicit a painful response and an increase in response to suprathreshold stimuli.

2.1.4 *Aplysia* as a Model System

Aplysia californica has been a key experimental model in probing neural development, neural conduction, and memory, winning the Nobel prize for Physiology or Medicine in 2000 for Eric Kandel's work with the model in learning and memory[25]. Advantages of the *Aplysia* include their large neurons and the robustness of their neurons which can provide upwards of 8 hours of experimental manipulation of excised tissues. The *Aplysia* is an invertebrate, and thus does not have myelinated axons, nor does it have a brain. Instead, the *Aplysia*'s nervous system is made up of ganglia which act as signal integration centers for their combined 20,000 neurons. This nervous system has been mapped down to individual neurons

which reside in the same locations and demonstrate repeatable types of firing behaviors across animals[26,27]. Connective nerves run between these ganglia and, of these nerves, the longest in the animal are the pleural-abdominal nerves (also known as the Pleural Abdominal Connectives, PACs) which forms connections from the left pleural ganglion to the left abdominal ganglion and from the right pleural ganglion to the right abdominal ganglion. Axon diameters of neurons in the PAC range from 0.1 to >25 μm, with 2-3 μm being the most common diameter[28,29]. The left PAC (LPAC), and the right PAC (RPAC) are slightly different in morphology. Notably, the RPAC has two giant axons (>25 μm) while the LPAC only has one[29], and the RPAC has more axons that the LPAC (~3700 vs ~2600)[28]. The length of these nerves provide plenty of room to test length-based effects of neural conduction along axons, and their unmyelinated neurons that are only a couple microns in diameter serve as a good first approximation of vertebrate C-fibers for the purposes of INI.

Along with these advantages come some shortcomings of the *Aplysia* model. Primarily, lack of myelin presents a difficulty in truly understanding the biophysics of neural signaling in myelinated neurons. *Aplysia* are an adequate first approximation of unmyelinated neurons, but experiments in vertebrate animals and humans are necessary to probe how neuromodulation techniques interact with myelinated neurons. One other characteristic that must be monitored is that the exact complement of ion channels will be different between *Aplysia* and vertebrates, and so identified effects on neural conduction must be validated in a vertebrate to properly support its relevance for human use.

2.2 Neuromodulation

2.2.1 Commonly Used Techniques

2.2.1.1 Electrical Methods

The current gold standard for device-based modulation of neural activity is through electrical means due to its reliability, repeatability, and safety. These electrical techniques rely on injecting electric current into or applying a voltage potential to the tissue to depolarize or hyperpolarize the cell membrane. Electrical modulation offers the option to both stimulate and block neural activity[30,31] depending on the pulse parameters and stimulation hardware[32]. Large diameter axons are affected at lower currents than small diameters[30,33]. Electrodes can be as simple as bare wires or sophisticated as multielectrode arrays which can have 10s to 1000s of contact points with tissue (Figure 2.3). Their application can range in invasiveness

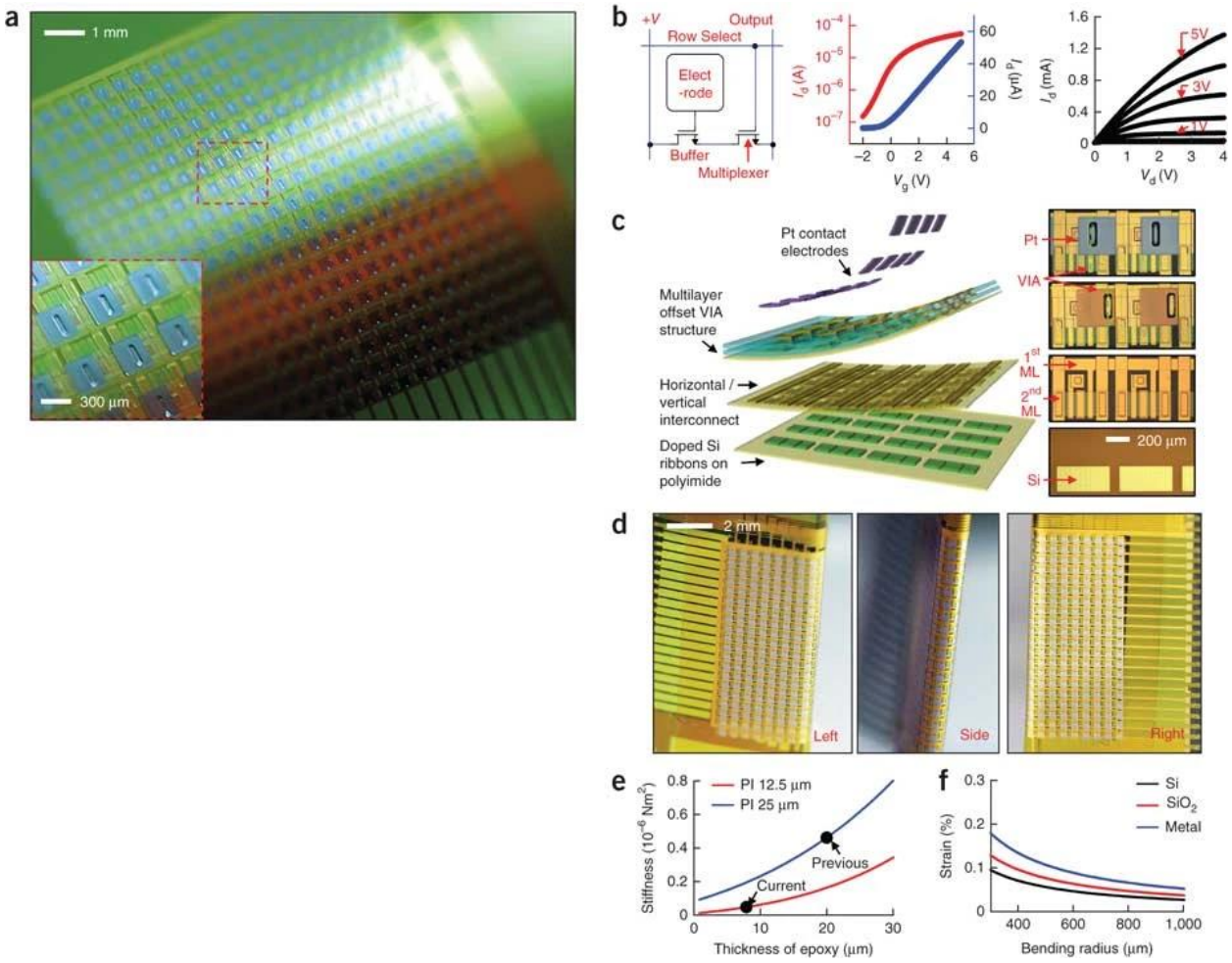

Figure 2.3. An example of a 360-channel high density electrode array. *Reprinted by permission from Springer Nature [Nature Neuroscience] Viventi et al. "Flexible, foldable, actively multiplexed, high-density electrode array for mapping brain activity in vivo" .Copyright © 2011.* [49]

from being completely non-invasive, such as placement on the skin which sacrifices spatial precision, to impaling the neural tissue for a high degree of selectivity. Many clinically implantable devices utilize electrical stimulation, and are highly effective as a therapy for a multitude of applications such as pain mitigation, prosthetics, and cardiac pacemakers. Despite these advantages, there are some drawbacks to electrical techniques. Electric current has a tendency to spread in tissue which lowers spatial selectivity and requires well optimized, expensive, and potentially invasive devices for precise stimulation. Tolerance effects have been noted for some applications of electrical stimulation[34], where more current is needed over time to elicit a response. Lastly, toxicity effects can be a problem if electrical pulse protocols and optimal hardware are not carefully considered[35].

Common pain therapies using electrical stimulation include TENS and SCS which are believed to work through Gate Control Theory in which afferent signals are gated at the spinal cord and signal from larger diameter, non-nociceptive sensory neurons will block the transmission of pain[36]. This idea is akin to rubbing a wounded area to make it feel better. Typical drawbacks for these technologies include lead migration, incompatibility with magnetic resonance imaging (MRI) scanners and pacemakers, relatively poor specificity, and paresthesia[37–42]. Particularly with SCS, there is a high cost barrier and a 30-40% incidence of complications[42]. High frequency alternating current has shown potential in providing block of both large diameter and small diameter neurons within bulk nerve[43].

2.2.1.2 Pharmacologic Methods

Neuromodulation with pharmacologic agents work by providing receptor agonists or antagonists. Some agents apply neurotransmitters or hormones, such as serotonin, dopamine, and testosterone[44]. These drugs act on receptors to either directly allow the flow of ion channels through the cell membrane or through metabotropic receptors which act through a signaling cascade in the cell. When considering alleviation of pain, pharmacologic agents (i.e. drugs) is often the first action since they offer a non-invasive and easily applied means of modulating sensory perception. Drugs can work through a multitude of mechanisms which can allow for enormous chemical specificity but can make it difficult to identify the right treatment and dosage for patients. The first response of physicians is typically nonsteroidal anti-inflammatory drugs (NSAIDs)[45,46] because of their favorable risk factors. If NSAIDs prove ineffective, treatment often turns to opioid analgesics which act on μ-opioid receptors. This presents a very high risk factor as has been identified from the emergence of the opioid epidemic[47], and guidelines for minimizing the risk of addiction and other deleterious effects have been outlined[45]. Depending on the underlying reason for pain, pharmaceuticals such as muscle relaxants, triptans, antidepressants, and anticonvulsants can be effective[46]. Pharmaceuticals which act along the axonal membrane, such as lidocaine, have been observed to require higher concentrations for larger diameter axons, demonstrating a size-selective specificity[48].

2.2.1.3 Ultrasonic Methods

Ultrasound (US) has been recently used for both neural stimulation and inhibition[50–52]. US offers extremely low invasiveness since it can be applied through the skin and even traverse the skull for modulation of brain activity[53]. In addition, focal regions are generally on the order of 1 mm[50,51,54], and it has been reported that specificity on the order of 100 μm has been achieved, but this drops to a few mm when operating transcranially[55]. This is generally a lower resolution of control compared to other methods of neuromodulation such as highly optimized electrical methods and optical modalities. A difficulty with US neuromodulation is the highly variable results[53] which could be due to the multifaceted mechanism of modulation. Particular trends in parameters have been identified to apply
stimulation or inhibition; however, the interaction of mechanical and thermal mechanisms make a true understanding of the underlying biophysics difficult[53].

2.2.1.4 Optical Methods

Optical methods have emerged in the past few decades as potential mechanisms for modulating neural activity. In the 1980s direct illumination of neural tissue with visible/near infrared light was shown to elicit an effect[56–58]. While inhibition of pain signals was shown, the issue of tissue damage was not well addressed in these papers, and inhibition was not always reversible. Low level light therapy (LLLT) has also been applied for neural modulation by looking at the easing of pain[59]. Neurotransmitter uncaging is another method of optically modulating neurons whereby signaling molecules are activated or inactivated by a photosensitive region of the molecule[60,61]. A common molecule used with this technique is glutamate due to its role in stimulating excitatory neurons. This technique has very high spatial resolution and has been used in neural circuit mapping experiments[62]. The most notable impact in recent years in the field of optical neuromodulation has been the development of optogenetics. Optogenetics uses implanted light sensitive ion channels in the membrane of target neurons[63]. By illuminating the tissue, neurons can be selectively excited or silenced. Optogenetics began with channel rhodopsin which required blue light to activate and had its response saturate at relatively low stimulation frequencies. Since then, many types of optogenetic channels have been developed which allow for stimulation over a range of wavelengths and that can respond at high pulse frequencies[63]. Despite its utility, the main drawback of optogenetics is due to the genetic modification required to implant the ion channel in neurons. This poses a problem for clinical implementation and limits the use of optogenetics to research applications. More recently, short wave infrared (SWIR) optical neuromodulation schemes have emerged[64,65]. Questions still exist about the underlying mechanisms for these techniques, but they provide a spatially precise method which may not require introducing exogenous ion channels.

2.2.2 Infrared Neural Modulation

INI is another way of applying a neural heat block but with high spatial discrimination and with a delivery scheme that enables highly customizable probes which do not require contact with tissue. While direct optical modulation of neural tissue has been studied since at least the 1980's when heat block was applied optically using light in the visible and near-infrared (NIR) wavelengths[58,66], it was shown that this irradiation resulted in a sustained disappearance of the neural signal which only recovered long after irradiation ceased and did not fully recover in many cases. It was not until 2005 that Wells *et al.* published the first account of neural excitation using mid wave infrared (MWIR) wavelengths which introduced the concept of specifically targeting water absorption in neural tissue to apply photothermal neuromodulation, and launched the field of infrared neural modulation (INM).

2.2.2.1 Thermal effects on neurons

The susceptibility of neurons to thermal effects has been noted since the beginning of the 20th century[67]. In 1949, Hodgkin and Katz systematically showed the effect of different bath media temperatures on the resting potential and action potential dynamics of *Loligo forbesi* stellar nerves[68]. One important finding from this article was that action potentials failed around 40˚C but returned when the nerves were returned to cooler temperatures. Thus, a reversible heat block was shown. Since this foundational experiment, heat block has been studied in a range of computational and animal models. Thermal requirements for heat block have been observed to be neuron type dependent[57]. Additionally, it has been shown that cooling of nerves can result in neural block[69], as well as can a mixture of both heating and cooling[70].

When neural tissue is heated there are both changes in the resting potential of neurons and in the kinetics of ion channels. The steady state resting potential of cells depolarize in response to lower temperatures and hyperpolarize in response to high temperatures[71]. Carpenter *et al*. showed that while the resting potential of neurons decreased with increasing temperature, the threshold membrane potential to elicit an action potential in *Aplysia* pacemaker cells was not temperature dependent (Figure 2.4)[71]. Both K_V and Na_V peak currents increase at elevated temperatures[72]. The duration of these currents also decreases with increasing temperature showing that ion channels inactivate more quickly. Additionally, K_V are more likely to be in a conducting state at lower voltages when temperatures are increased[72].

It has been shown that both sodium and potassium current amplitudes increase with temperature, however potassium currents have a greater temperature sensitivity[73–75] . Both sets of ion channels exhibit faster onset of currents at increased temperatures, but potassium onset times decrease in amplitude more quickly than sodium onset times[73–75]. The reason for this greater potassium channel sensitivity to

temperature is likely due to K_V channels containing a region of amino acid residues similar to those found in TRPV1 (transient receptor potential subfamily V member 1) channels, a type of cation channel which can be gated by changes in temperature alone[74]. Taken as a whole, the temperature dependency of ion channels results in altered ion currents causing action potentials that are lower amplitude, lower duration, and faster conducting when neurons are heated, and sufficient heating can create a heat block. Because of the greater temperature sensitivity of voltage gated potassium channels, it was the most likely mechanism for heat block. Recent work has determined that K_V are indeed chiefly responsible to INI[14,15], but temperature effects on other factors such as Na_V or other ion channels may play a synergistic of contradictory role. The mechanism of INI will be addressed in section 2.2.2.3.

2.2.2.2 Infrared Neural Stimulation

Wells *et al*. demonstrated the first stimulation of action potentials using MWIR light (λ= 2.1-6.1 μm)[76] in the frog sciatic nerve using a free electron laser which provided a 1-1 laser pulse to action potential resulting in a muscle twitch. This processes of optically stimulating neural tissue using IR lasers was given the name infrared neural stimulation (INS). It was shown that the mechanism for INS is likely due to a spatio-temporal thermal gradient generated in the tissue due to water's direct absorption of IR light[77]. The main advantages of INS over other neuromodulation modalities are its spatial specificity, lack of reliance on exogenous agents, and ability to be applied without contact with the tissue. In addition, these advantages are achievable using even relatively easy to implement light application methods such as optical fibers without the need for costly beam shaping components.

The underlying mechanism of INS has been investigated, and it has been shown that much of the effect is due to thermally induced capacitive changes in the cell membrane[78,79], however, the contribution of heat sensitive ion channels and the release of intracellular calcium cannot be ignored. Interestingly, INS-induced ion currents were generated in different types of cell membranes and it was shown how direct irradiation of any lipid bilayer results in these capacitive currents[80]. Since the first set of experiments in the rat sciatic nerve, INS has been tested in animal models ranging from *Aplysia* to humans and applied for motor control, stimulation of the cochlea[81,82], pacing of the heart[83,84], stimulation of non-human primate brain[85,86], stimulation of the cavernous nerve[87,88], and stimulation of human dorsal rootlets[89], to name some of the applications. Optimal wavelengths in the SWIR, 1440-1470 nm and 1860-1880 nm, were identified due to the penetration depth of the light in tissue being on the order of half the diameter of a nerve. Additionally, there is wide availability of low-cost sources at these wavelengths due to technological developments in the field of telecommunications. Since the discovery of INI was due to studies in INS, many of the same wavelengths and application methods are utilized.

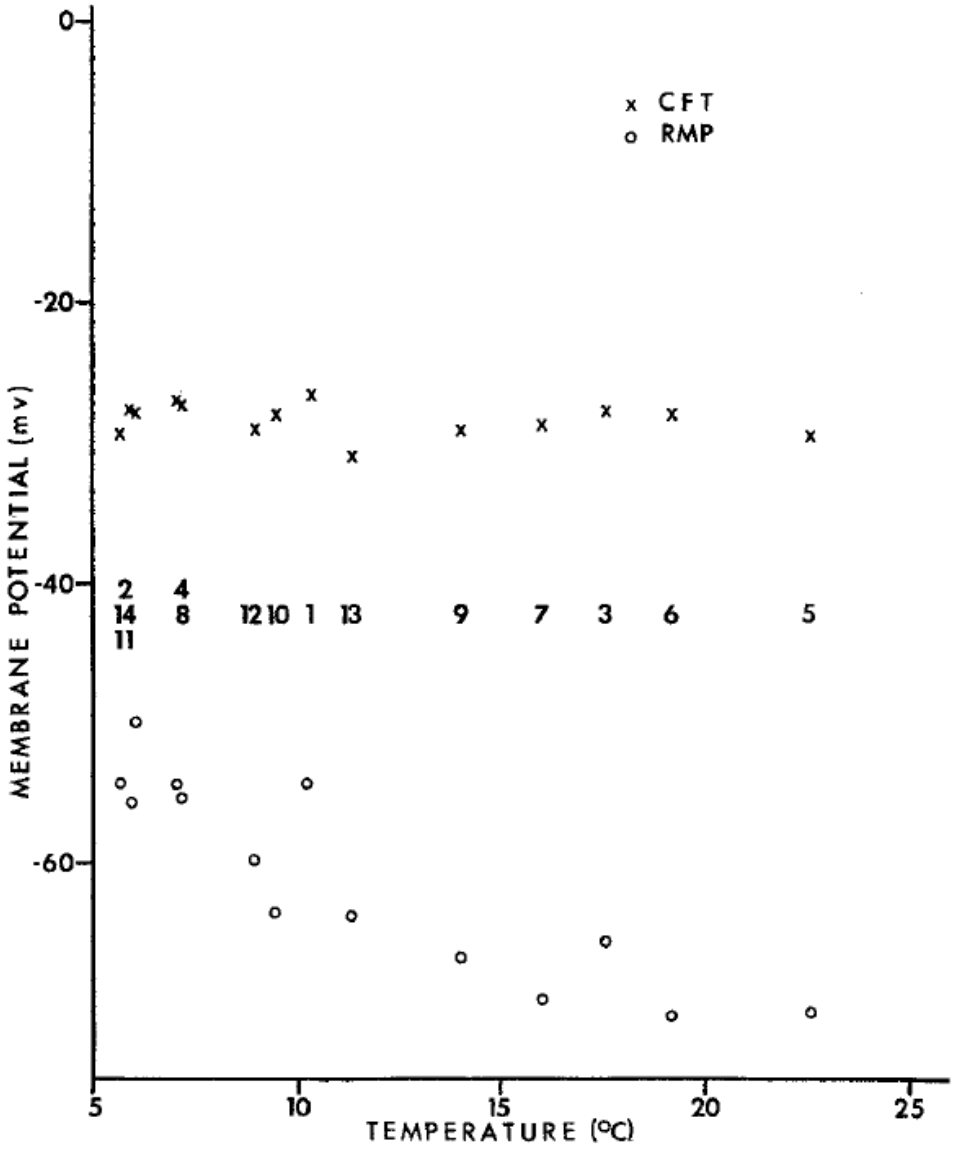

Figure 2.4. Resting potential and AP threshold potential as a function of temperature. (CFT- Critical Firing Potential) (RMP-Resting Membrane Potential). Numbers represent the order of testing. *©1967 Carpenter*[71]. *Originally published in Journal of General Physiology. https://doi.org/10.1085/jgp.50.6.1469*

Laser parameters for INS in the peripheral nervous system utilize pulse widths on the order of milliseconds and repetition rates of <5Hz due to the overlap of the temperatures of subsequent pulses resulting in a sustained elevation of tissue temperature above baseline. INS of the central nervous system applies pulse parameters more similar to INI where pulse widths are on the order of 100s of microseconds, repetition rates are in the 100s of Hz, and duration of application is 0.5 to 1.5 seconds[85]. The mechanism of stimulation of the CNS is still under investigation since a 1-1 pulse to activity is not seen, and other mechanistic factors such as heat-sensitive ion channels, intracellular calcium release, and glial activation have been implicated as having a substantial role.

Multiple methods of pairing INS with other techniques have been tested. Contrast enhanced methods using gold nanoparticles allow for the stimulating wavelength to be within the tissue optical window (800-1300 nm) which both increases the penetration depth of light and specifically tags tissue for stimulation, but requires the introduction of exogenous particles to absorb those wavelengths[90–92]. Duke *et al*. explored the advantages of combining INS with electrical stimulation and found that the optical energy required for neural stimulation could be reduced while maintaining the increased spatial specificity[93–95]. The field is continuing to expand to other cell types in the nervous system including astrocytes, microglia, and satellite glial cells, and efforts to fully elucidate the mechanisms of activation and to translate INS into a clinical modality are ongoing.

2.2.2.3 Inhibition Neural Inhibition

In 2013, Duke *et al.* used SWIR wavelengths to cause neural inhibition[96]. This initial study showed the utility of INI in both an invertebrate and a vertebrate model to inhibit AP generation, AP propagation, and muscle contraction[96]. Duke *et al.* reported an 8^{O}C rise associated with INI in the *Aplysia* buccal nerve and a 9^{O}C rise in the rat sciatic nerve. In contrast to previous optical inhibition studies, the neural signal immediately returned when irradiation ceased with no evidence of functional damage[96]. Strikingly, INI was achieved with much shorter pulses, 200 μs, and higher repetition rates, 200 Hz, than performed for INS of the peripheral nervous system. By using a pulsed approach, heat is generated during irradiation of the tissue and thermal relaxation occurs during inter-pulse periods, and an overall temperature rise results from the superposition of the heating dynamics from multiple pulses. This allows for tight control over the temperature distribution within tissue. Application of heat block using laser heating also allows for high spatial precision so that specific tissue can be targeted and small groups of plated neurons[97].

Evidence suggests that INI works through heat block mechanisms identified by Hodgkin and Kats[68], and that a temperature threshold is required. Ganguly *et al*. developed a modified Hodgkin-Huxley model that added a temperature dependence to the maximum ion conductances and axial resistivity, updated the Q_{10} temperature dependency, and added a temperature dependent sodium-potassium pump to more

adequately capture action potential conduction at elevated temperatures experienced during INI[14]. This model was used to assess the mechanism of heat block which revealed that potassium channels are critical for its occurrence. This hypothesis has been validated *in vitro* (Appendix A) by applying ion channel blockers, tetrodotoxin for Na^+ and tetraethyl-ammonium for K^+, to small sections of nerve that were blocked with INI showing that INI could not occur when the potassium channels were blocked, but was still effective when sodium channels were blocked[15]. Dynamics of inhibition were further probed in the crayfish by Zhu *et al*. to assess temperature dependent Na^+ and K^+ kinetics and membrane resistance which highlighted that the AP amplitude recovered at a different rate than the AP duration[98].

Other phenomena associated with INI have been uncovered that may help increase its selectivity and clinical adoption. A size dependence was noted whereby smaller axon diameters require lower laser radiant exposures and lower temperatures for block (Figure 2.5)[99]. This directly has implications for targeting nociceptive signals within bulk nerve since they are chiefly transmitted by small diameter axons. Another phenomenon was identified by Lothet *et al.* when testing hybrid electro-optical inhibition, using kilohertz frequency alternating current (KHFAC) in conjunction with INI[100]. KHFAC can block conduction of neural signals[30] but suffers from an onset response that can last longer than several seconds where many large amplitude, asynchronous action potentials are elicited at high frequency before block eventually sets in. This results in large muscle twitches and potentially painful sensory neuron stimulation. INI was shown to be able to block this onset response until KHFAC took effect at which point the laser was turned off, demonstrating that hybrid inhibition offered a method of lowering the thermal load associated with INI and removing the onset response of KHFAC. Methods of performing contrast enhanced INI to increase targeting specificity have been performed by using gold nanorods that highly absorb light at 785 nm which increases the penetration depth of light[101], but introduces exogenous agents, negating one of the advantages of INI.

2.3 Laser-Tissue Interactions

Laser irradiation of tissue begins a cascade of events that are dependent on the material properties of the tissue. These interactions follow well described equations so that the biophysical response can be modeled and predicted.

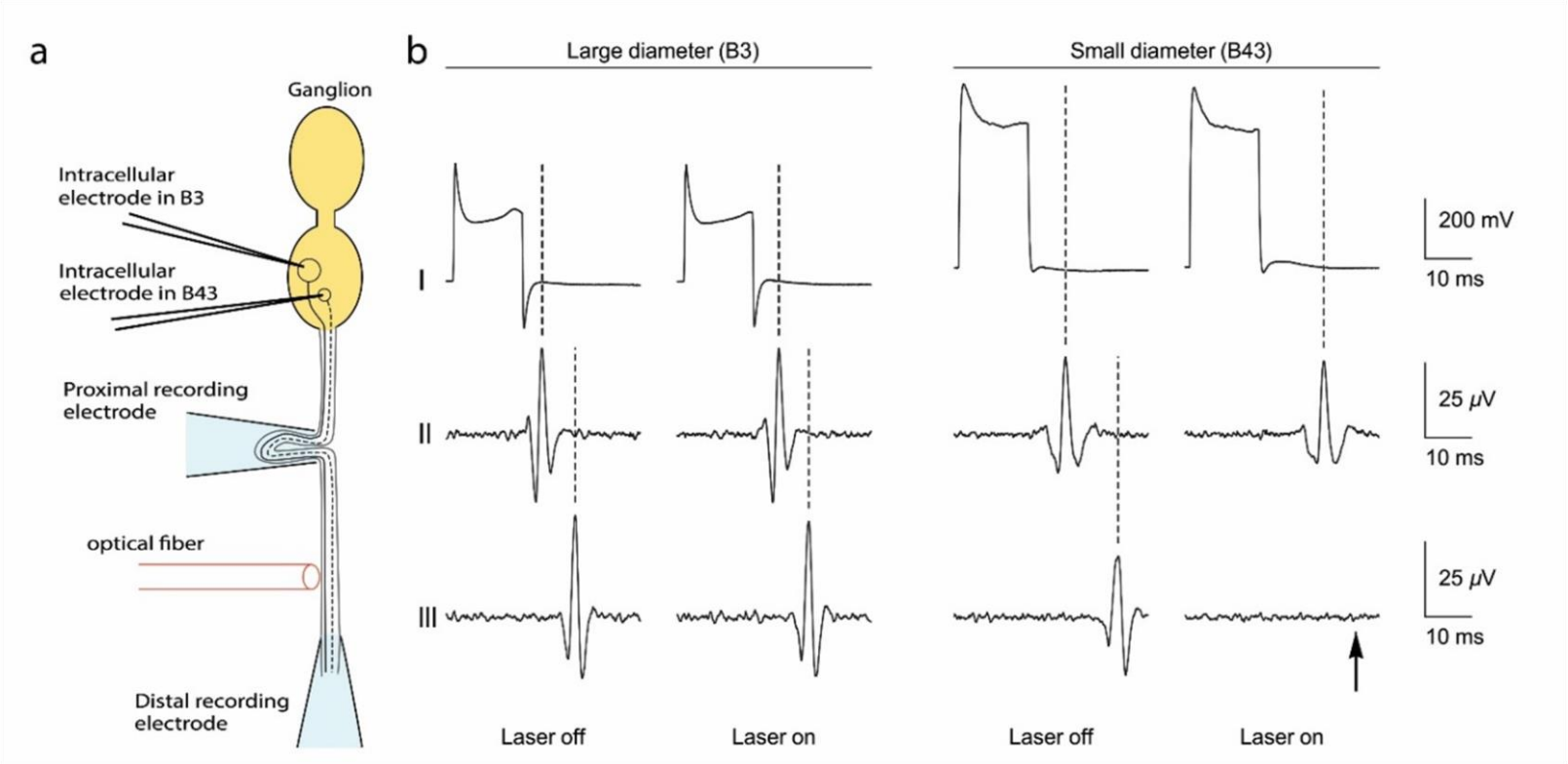

Figure 2.5. Selective block of an individual slower-conducting axon in *Aplysia californica*. (**a**) Experimental setup for selective optical inhibition. Two neurons, B3 and B43, were impaled and stimulated intracellularly. B3, a large-diameter cell, has a large-diameter axon, whereas B43, a small-diameter cell, has a small-diameter axon. Two suction recording electrodes were positioned along the length of the nerve, one proximal to the ganglion and one distal. The optical fiber (600 μm diameter) delivering the IR energy (1860 nm wavelength) was placed perpendicularly to the nerve between the recording electrodes. (**b**) Action potential recording from the large diameter soma (B3) and axon and the small-diameter soma (B43) and axon. (I) Intracellular stimulation applied to the cell body. (II) Proximal recording. (III) Distal recording beyond the IR laser application. The B43 small diameter axon was completely blocked at a radiant exposure of 0.106 J/cm2/pulse (arrow) whereas the B3 large diameter axon remained unaffected. *Reprinted from Lothet et al. 2017.* [121] *Copyright © 2017 Lothet, Shaw, Lu, et. al. This is an open-access article distributed under the terms of the Creative Commons Attribution License (CC BY). The use, distribution or reproduction in other forums is permitted, provided the original author(s) or licensor are credited and that the original publication in this journal is cited, in accordance with accepted academic practice. No use, distribution or reproduction is permitted which does not comply with these terms.*

2.3.1 Optical Interactions

When laser light is irradiant on tissue, several interactions occur. First, light interacts with the interface of the tissue due to the refractive index mismatch between the tissue and the previous medium (air if free beam irradiation and glass if an optical fiber is in contact). Photons will either be reflected back into the previous medium or transmitted into the tissue according to Fresnel Equations[102] which depends on the angle of incidence and refractive index of the medium, n, defined as the ratio of the speed of light in a vacuum to the speed of light in the medium, among other factors. Transmitted light will be refracted, whereby the angle of propagation is altered according to Snells law[102]. Once inside the tissue light-matter interactions can occur, chief among these are optical absorption and scattering. Nonlinear effects can occur at high enough optical intensities, but INI does not operate in this regime, so these effects will not be considered.

Optical absorption is characterized by energy from a photon being transferred to a molecules in the form of eliciting electronic transitions and stimulating vibrational and rotational modes in chemical bonds[102]. Once absorbed, this energy can be dissipated by the release of photons in the form of fluorescence and phosphorescence, driving photo-chemical reactions through intra- or intermolecular energy transfer, or dissipated as heat. Wavelengths used for INI are too low energy to drive electronic transitions, so fluorescence and photo-chemical reactions are ignored, and the dominant interaction is heat generation due to targeting of absorption bands of water molecules.

Optical scattering in tissue occurs from refractive index mismatches between the bulk medium and particles within the medium. Scattering can take the form of inelastic scattering, where a photon's wavelength is changed after the scattering event from either a gain or loss of energy, or elastic scattering, where the wavelength is unchanged by scattering. Inelastic scattering occurs at a much lower probability than elastic scattering[102], so for the purpose of INI, this is ignored. The amount and direction of scattering is dependent on the wavelength of light, the scattering cross-section of the scattering particle(s), and the concentration of scattering particles. Two regimes of scattering are considered: Mie and Rayleigh regimes. The Mie regime occurs when the scattering particle cross-section is comparable to or larger than the wavelength of light, λ, while Rayleigh scattering which occurs when the scattering cross-section is much smaller than the wavelength[102].

Coefficients are used to represent the relative frequency of absorption, μ_a [1/mm], and scattering, μ_s [1/mm], events in a medium, and are defined as the inverse of the mean free path length of photon propagation before an absorption or scattering event occurs. These optical properties, along with the refractive index and anisotropy factor (g), are wavelength dependent, and thus must be characterized at each wavelength of interest. In reality, μ_s cannot be directly measured because any sensed signal is

dependent on both the amount of scattering and the direction of scattered photons. The tendency towards directionality of scattering is dependent on the scattering phase function and is captured in the anisotropy factor, g, which is the average cosine of the scattering angle[103]. The value of g can be between -1 and 1, where -1 means photons are completely back scattered backward, 1 means photons are completely forward scattered, and 0 means photons are scattered isotopically. What can be calculated from measurements is the reduced scattering coefficient, μ_s', which is a function of both μ_s and g [$\mu_s' = \mu_s * (1-g)$]. Optical scattering exhibits predictable trends with wavelength. Mie theory shows that an exponential equation can be fit to the wavelength dependence of scattering in the Mie regime. Additionally, in the Rayleigh regime, the amount of scattering proportional to $(1/\lambda^4)$ [102]. By combining these relationships, an equation can be developed using measured parameters that encompasses the wavelength dependent relationship of scattering[104].

$$\mu_s'(\lambda) = a' \left(f_{Ray} \left(\frac{\lambda}{500\ (nm)} \right)^{-4} + (1 - f_{Ray}) \left(\frac{\lambda}{500\ (nm)} \right)^{-b_{Mie}} \right) \qquad \text{Equation 2.11}$$

where a' is a scaling factor equal to μ_s' at λ=500 nm, f_{Ray} is the fraction of Rayleigh scattering, λ is wavelength in nm, and b_{Mie} is the exponential fit parameter for Mie scattering.

2.3.2 Determining Light Distributions

The distribution of light within tissue can be approximated a few different ways depending on the assumptions that can be made about the tissue and the optical properties. The simplest approximation uses Beer's law, where the falloff of the intensity of light, I, at depth, z, is an exponential decay from the intensity at the surface of tissue, I_0.

$$I = I_0 e^{(-\mu_t(\lambda) \cdot z)} \qquad \text{Equation 2.12}$$

Here, μ_t [1/mm], the total attenuation coefficient, is equal to the addition of the absorption coefficient and the scattering coefficient, $(\mu_a + \mu_s)$. When scattering is negligible, this equation provides the distribution of light in the tissue for a collimated beam since absorption only affects the amount of light penetrating through the tissue and not the direction of photons. For a non-collimated beam, equation 2.12

can be coupled with information about the divergence to determine the distribution. If scattering is not negligible, this equation gives the expected measured intensity at depth, z, but does not provide information about the distribution of photons because directionality of scattering is not captured.

To more accurately approximate photon propagation analytically, one can use the radiative transport equation[102].

$$\frac{dL(r,\hat{s})}{ds} = \mu_a L(r,\hat{s}) - \mu_s L(r,\hat{s}) + \int_{4\pi} p(\hat{s},\hat{s}')L(r,\hat{s})d\omega' + S(r,\hat{s}) \qquad \text{Equation 2.13}$$

where $L(r,\hat{s})$ is the radiance [W/m^2 sr] at position r in direction $\hat{s}$, p is the scattering phase function [1/sr], and S is the optical source term.

In practice, it is difficult to solve this equation to determine propagation paths of photons and the distribution of absorption in tissue. Two commonly used methods to approximate photon flux and absorption distributions are Monte Carlo simulations of photon propagation and diffusion theory approximations. Diffusion theory treats photons as diffusing particles in a medium based on Fick's Law[102], and is less computationally intensive that a Monte Carlo, but relies on the assumption that scattering is dominant over absorption. This assumption is violated at INI wavelengths where absorption is dominant. Thus, simulating light distributions in tissue during INI relies on the Monte Carlo method.

A Monte Carlo simulation is a probabilistic model that launches discrete packets of photons into a computational geometry. Each voxel in the geometry is assigned a value of n, μ_a, μ_s, and g. Once launched, a photon (packet) propagates through the geometry until it traverses a scattering length. This scattering length is randomly determined from an exponential distribution based on μ_s. The weight of the photon is reduced according to how far it propagated during the scattering length and the absorption coefficient of the voxels it traversed. A scattering event is then considered, and a new direction of propagation is determined based on the phase function using a random number generator. The above process of propagation is then repeated. The photon is terminated if its weight drops below a threshold level or if it exits the geometry. Interpretable and reliable information about optical fluxes and absorption maps can be generated by performing these steps for millions of photons which can take up to hours to days. Recently, a graphical processing unit (GPU) accelerated Monte Carlo was developed that has provided a massive speedup so that simulations now take minutes[105].

Monte Carlo simulations are ideal for determining the distribution of absorbed photons in a wide variety of tissue geometries, and for probing absorption trends in neural tissue. For INI, these absorption distributions provide crucial insight into the distribution of heat generated. Absorption maps provide the

distribution of absorbed energy that can be used as the heat source term in Penne's bioheat equation to inform the laser-induced temperature distribution. For a single pulse the temperature can be calculated:

$$T = \frac{\mu_a H}{\rho c_p} \qquad \text{Equation 2.14}$$

where H [J/cm^2] is the radiant exposure, ρ [kg/m^3] is the density of the tissue and c_p [J/kg/K] is the specific heat[102]. This equation assumes that the duration of the laser pulse is sufficiently short compared to the thermal diffusion time constant of the tissue so that conduction does not play a role. Once a photon is absorbed and heat is generated, optics no longer dictates any further interactions.

2.3.3 Methods of optical property measurement

As discussed in the previous section, assessment of light distributions in tissue is possible through computational models, however values of the optical properties are needed as input parameters. Optical properties can be estimated through measurements of reflection and transmission through a sample. Properties are highly dependent on the components and organization of tissue, and so for accurate assessment how light truly behaves, the manipulation of tissue should be minimized. *In situ*, characterization is difficult, and some techniques require removal of tissue. Available tissue size will also affect the technique and grinding tissue into a paste has been performed to pool tissue samples, but this will alter the measured properties[106]. Dehydration, freezing, and fixation of tissue will also alter the measured parameters[107]. For the purpose of this dissertation, this overview will focus on commonly used methods to estimate μ_a and μ_s'.

Calculating the optical properties requires probing sample with known irradiation parameters, either directly or indirectly, measuring photon distributions. A vast majority of techniques rely on reflection, R, or Transmission, T, measurements (an example of a technique that does not measure R and T is using a thermal camera to measure the light-induced temperature rise which can be related to the μ_a). When measuring excised samples, both R and T can be measured since there is access to both sides of the sample. When this is the case, integrating spheres are one of the technique of choices since they allow for sensing of (ideally) all photons either reflected or transmitted. Integrating spheres are hollow spheres that are coated with a material that is highly reflective across a broad range of wavelengths. A sphere will have several ports, or openings, to accommodate the placement of a sample, a detector, and irradiation from a source. Samples can be placed over these ports to make total reflection and total transmission measurements that

are independent of the angle of photon leaving the sample (whether reflected or transmitted), hence they are said to integrate over all angles. For measurements of R, a sample is placed over the sample port and light enters from the entrance port directly opposite the sample (Figure 2.6). Light reflected off the sample will be incident on the wall of the sphere and reflected until it reaches the detection port located on the side of the sphere. Measurements of T can be made in a similar configuration where irradiation of the sample now occurs on the surface opposite the sphere such that transmitted photons are detected. Any port across from the sample is covered with the reflective material so that photons are reflected around the sphere until sensed at the detection port. Setups can be utilized with one sphere where R and T are measured separately or with two spheres where R and T are measured simultaneously. It is assumed that all light incident on the sample is either measured in the reflection sphere, measured in the transmission sphere, or absorbed by the sample. Erroneous calculations can result from lost photons due to ports that are not completely covered and from samples that are too small which leads to photons being scattered out from the sides of the sample. Consideration of photons lost due to specular reflections off the sample is needed. Processing of this information is performed using the inverse adding doubling method[108].

Other common methods of optical property estimation largely rely on only measuring reflectance distributions. The trouble with these methods for INI wavelengths is that diffuse reflections dramatically decrease when absorption is greater than scattering which limits the signal to noise ratio (SNR) of these techniques, making them not well suited for the task. One method applies fiber-based light application and sensing[109,110]. A probe is placed in contact with the tissue to deliver light, and a second probe is placed at a known offset to measure reflected light. Spatial frequency domain imaging (SFDI) is another method of approximating optical properties by projecting light on a sample with different spatial frequencies and imaging the reflected light[111,112]. The diffusion approximation of the radiative transport equation is then applied to determine the μ_a and μ_s' of the tissue. Tissue acts as a low-pass filter, meaning that lower spatial frequencies will propagate deeper and higher spatial frequencies will be attenuated more quickly. This allows for depth resolved information using SFDI. Only a camera, a light source, and a spatial modulator is needed, and the simplicity, non-contact nature, and spatial information gathered lends itself well to potential clinical implementation. Since this technique relies on the diffusion approximation which requires scattering events to be much more prevalent than absorption events, SFDI cannot be applied well to INI wavelengths. Current attempts at performing this in the SWIR have utilized extrapolated information from shorter wavelengths[113].

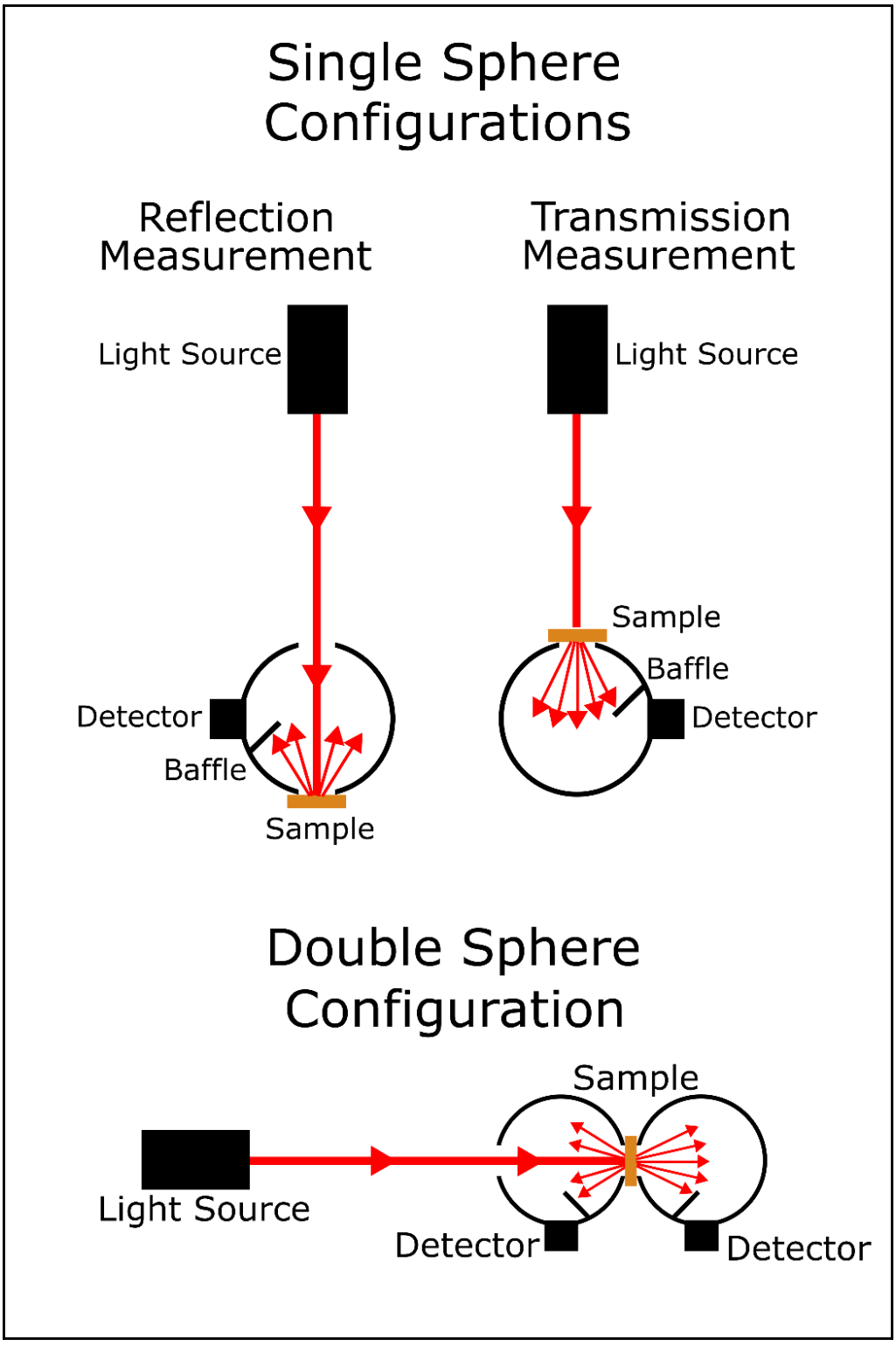

Figure 2.6 Integrating spheres to estimate optical properties. Single or double sphere configurations can be used to measure the reflectance off and transmission through a slab of tissue. Samples are placed between slides for an optically smooth surface or liquid samples are placed in a cuvette. Monochromatic sources can be used with photodetectors for single wavelengths, or polychromatic sources can be used with spectrometer detectors.

2.3.4 Thermal Interactions

Once heat is generated, it can be dissipated through three possible means: conduction, convection, and radiation. Cooling of the tissue due to irradiation is typically negligible, therefore only conduction and convection will be considered here. Thermal conduction is the movement of heat down a thermal gradient. The Fourier equation models the temperature time dependence of due to conduction[102].

$$\rho c_p \frac{dT}{dt} = k\nabla^2 T \qquad \text{Equation 2.15}$$

where T is temperature and k is the thermal conductivity [W/m/K]. Rearranging the equation, we can see another common form which utilizes the thermal diffusivity, α [m^2/s], where $\alpha = k/(\rho c_p)$.

$$\frac{dT}{dt} = \alpha\nabla^2 T \qquad \text{Equation 2.16}$$

Convection is due to the relative motion between a fluid and substrate which are in contact and typically occurs in tissue due to blood perfusion. *In vitro* setups may have convection occur due to the movement of bath media over tissues. The heat flow between the tissue and the media at the surface (Q_s [W]) due to convection is defined as:

$$\dot{Q}_s = hA(T_s - T_\infty) \qquad \text{Equation 2.17}$$

where h is the convective heat transfer coefficient [$W/m^2/K$], A is the surface area at the interface [m^2], T_s is the surface temperature [K], and T_∞ is the bulk fluid temperature [K][102]. These aspects of heat transfer, along with the heat generated due to tissue metabolism (Q_{met}), are modeled in Penne's bioheat equation[102].

$$\rho c \frac{\partial T}{\partial t} = k\nabla^2 T + \omega_b \rho_b c_b (T_a - T) + \dot{Q}_{met} \qquad \text{Equation 2.18}$$

In this version, convection due to blood perfusion (subscript b) has been accounted for with ω as the volume fraction of blood to tissue [ml/ml] and T_a as the temperature of the arterial blood. With a slight modification of the equation, a heat source (such as a laser) can be added, Q_{source} [W/m^3] .

$$\rho c_p \frac{\partial T}{\partial t} = k\nabla^2 T + \omega_b \rho_b c_b (T_a - T) + \dot{Q}_{met} + \dot{Q}_{source} \qquad \text{Equation 2.19}$$

Techniques such as finite element analysis (FEA) can be used to apply this model to understand temperature distributions and heating dynamics in bulk tissue. FEA is a method of piecewise approximation by taking a physical structure and breaking it up into a finite number of discrete elements. Equations are solved at nodes generated at the vertices of elements, which can be assigned thermal different properties based on the material. When setting up an FEA, there are there are 7 steps to follow as defined by Cook *et al.*[114] These are:

- Define the geometry by dividing the structure(s) into a finite number of elements
- Define the properties for each element
- Assemble the elements to form the model
- Apply the known loads. This will be nodal heat fluxes for heat transfer analysis
- Apply the known values. For heat transfer, this will take the form of known temperatures, initial conditions, and thermal boundary conditions.
- Solve the equations to determine nodal values: temperatures for heat transfer analysis
- Calculate the element heat fluxes from temperature values and the temperature field

After these steps, post-processing can occur. Software has been created which allow for easy setup and optimization of the geometry and meshing of the elements, as well as most the other required FEA steps. COMSOL Multiphysics Modeling Software is one of the potential softwares which can perform FEA for thermal analysis and has been used in this dissertation for its ease of implementation.

2.3.5 Thermal Measurements

Various methods exist for sensing temperature. Among these are using thermocouples (TCs)[102], thermistors and thermopiles[102], infrared imaging[102], magnetic resonance (MR) thermometry[115], fluorescence[116], ultrasound thermography[117], and temperature spatially offset Raman spectroscopy (T-SORS)[118], however this is by no means an exhaustive list. The work conducted in this dissertation utilized three techniques- TCs, infrared imaging, and MR thermometry- thus those will be highlighted.

2.3.5.1 Thermocouples

Thermocouples are the junction of two metals which utilize the Seebeck effect to measure a change in temperature. The Seebeck effect states that when a junction occurs between two metals, a potential difference will be created[102]. Practically, two different junctions are created such that one serves as a reference potential. Voltage difference will be linear with temperature over set intervals depending on the types of metals used. By varying the two types of metals used, different temperature sensitivities and different applicable temperature ranges can be achieved[102]. Thermocouples can provide very high temporal (~ millisecond) and thermal resolution (~0.01 ^{o}C). Temporal resolution is limited by the size of the metal junction and the media the medium being measured[119]. Drawbacks of this technique include being limited to point measurements, requiring multiple thermocouples for any kind of spatial measurements, and the need to be in physical contact with a sample which can affect the heating dynamics[119]. Therefore, careful attention must be paid to how they are applied. Ultimately, TCs are ideal for applications that do not require spatial information and can be implemented into a range of *ex vivo*, *in vitro*, and *in vivo* setups.

2.3.5.2 Thermal Imaging

Thermal imaging measures radiant energy from the surface of the sample to predict the sample's temperature. All matter above absolute zero irradiates energy, and blackbodies are objects that are perfect absorbers and emitters of radiant energy. The magnitude of the irradiated power emitted by a blackbody, W_b [W/m^2/μm], is related to its temperature by

$$W_b(\lambda,T) = \frac{2\pi hc^2\lambda^{-5}}{\left(e^{\frac{hc}{\lambda k_b T}} - 1\right)} \qquad \text{Equation 2.20}$$

where h is Planck's constant (6.626 x 10^{-34} [m^2 kg/s]), c is the speed of light (~3.0 x 10^8 [m/s]), λ is the wavelength of the radiation, k_b is Bolzmann's constant (1.38 x 10^{-23} [J/K]), and T is temperature in Kelvin[102]. Integrating over all wavelengths gives the total emissive power of the surface:

$$E_b(T) = \sigma T^4 \qquad \text{Equation 2.21}$$

where σ is the Stefan-Boltzmann constant (5.67 x 10^{-8} [W/m^2/K^{-4}]. Tissue, however, is not a blackbody, and to account for this an efficiency factor called the emissivity, ε, is used:

$$E_b(T) = \varepsilon \sigma T^4 \qquad \text{Equation 2.22}$$

Using thermal imaging can provide temperature information with high spatial and temporal resolution. Additionally, since it is non-contact, the sample does not need to be disturbed to take measurements. The drawback in biology is that most tissues contain high water content and must be hydrated. Thermal imaging typically senses wavelengths between either 3-5 μm or 8-12 μm, and due to the absorption coefficient of water at these wavelengths, the sensing depth is limited to 80 - 100 μm[120]. This becomes a problem in situations where the tissue must be immersed in fluid, such as in electrophysiological recordings of excised nerves. Additionally, crowded experimental setups do not lend themselves well to thermal imaging since components may physically block the field of view of the camera.

2.3.5.3 Magnetic Resonance Thermometry

MR data can be utilized in a few different ways to measure thermal changes. These include using proton density, T_1 and T_2 relaxation times, the diffusion coefficient, magnetization transfer, and proton resonance frequency (PRF) information. An overview of these can be found in Rieke *et al.*[115] In this dissertation, the PRF method was performed using the phase mapping technique where shifts in the phase of the MR images are quantified and related to temperature changes.

The resonance frequency of the (water) nucleus is determined by the local magnetic field which it experiences. This local field, B_{loc} [T], is related to the external magnetic field, B_0 (the strength of the magnet), by the equation:

$$B_{loc} = (1 - s) \cdot B_0 \qquad \text{Equation 2.23}$$

where s is the shielding constant. Water hydrogen protons are shielded from the magnetic B_0 field by their electrons, however adjacent hydrogen bonds disrupt this shielding. As the temperature increases, more vibrational states (stretching, bending) are present in the hydrogen bonds and H_2O spends less time in a hydrogen-bound state. This increases the shielding felt by the hydrogen protons, and decreases B_{loc}, thus decreasing the PRF.

Using gradient-recalled echo imaging sequences, the phase shift between images can be related to temperature change. The change in temperature is proportional to the phase shift as follows:

$$\Delta T = \frac{\varphi(T) - \varphi(T_0)}{\gamma \alpha_s B_0 TE} \qquad \text{Equation 2.24}$$

where $\varphi(T)$ is the phase of the current image while $\varphi(T_0)$ is the phase of the reference image, γ is the gyromagnetic ratio (42.58 [MHz/T]), α is the PRF change coefficient, and TE is the echo time. Therefore, when measuring the temperature rise during INI, an image can be taken before the laser turns on, and an

image can be taken once heating has occurred. The subtracted phase between these images is proportional to the temperature rise.

2.4 References

1. Kandel ER, Schwartz JH, Jessell TM. *Principles of Neural Science*. Vol 4.; 2013. doi:10.1036/0838577016

2. Patestas M, Gartner LP. A Textbook of Neuroanatomy. *A Textb Neuroanat*. 2006;(1):454. doi:10.4067/S0717-95022004000200008

3. Luan S, Williams I, Nikolic K, Constandinou TG. Neuromodulation: Present and emerging methods. *Front Neuroeng*. 2014. doi:10.3389/fneng.2014.00027

4. Hodgkin AL, Huxley AF, Katz B. Measurement of current-voltage relations in the membrane of the giant axon of *Loligo*. *J Physiol*. 1952;116(4):424-448. doi:10.1113/jphysiol.1952.sp004716

5. Hodgkin AL, Huxley AF. A Quantitative Description of Membrane Current and its Application to Conduction and Excitation in Nerves. *J Physiol*. 1952;117(4):500-544. doi:10.1016/S0092-8240(05)80004-7

6. Hodgkin AL, Huxley AF. A Quantitative Description of Membrane Current and its Application to Conduction and Excitation in Nerves. *J Physiol*. 1952;117:500-544. doi:10.1016/S0092-8240(05)80004-7

7. Lu H, Chestek CA, Shaw KM, Chiel HJ. Selective extracellular stimulation of individual neurons in ganglia. *J Neural Eng*. 2008;5(3):287-309. doi:10.1088/1741-2560/5/3/003

8. Hovey MM, Bak AF, Carpenter DO. Low internal conductivity of Aplysia neuron somata. *Science*. 1972;176(41):1329-1331. doi:10.1126/science.176.4041.1329

9. Lucas K. The temperature-coefficient of the rate of conduction in nerve. *J Physiol*. 1908;37(2):112-121. http://www.ncbi.nlm.nih.gov/pmc/articles/PMC1533545/.

10. Hines ML, Carnevale NT. The NEURON Simulation Environment. *Neural Comput*. 1997;9(6):1179-1209. doi:10.1162/neco.1997.9.6.1179

11. Rall W. Cable theory for dendritic neurons. In: *Methods in Neuronal Modeling*. ; 1989.

12. Chiel HJ. NeuroWiki: Cable Properties I: Passive Properties. https://neurowiki.case.edu/wiki/Cable_Properties_I:_Passive_Properties. Published 2016.

13. Mou Z, Triantis IF, Woods VM, Toumazou C, Nikolic K. A simulation study of the combined thermoelectric extracellular stimulation of the sciatic nerve of the xenopus laevis: The localized transient heat block. *IEEE Trans Biomed Eng*. 2012;59(6):1758-1769. doi:10.1109/TBME.2012.2194146

14. Ganguly M, Jenkins MW, Jansen ED, Chiel HJ. Thermal block of action potentials is primarily due to voltage-dependent potassium currents: A modeling study. *J Neural Eng*. 2019. http://iopscience.iop.org/10.1088/1741-2552/ab131b.

15. Ganguly M, Ford JB, Zhuo J, et al. Voltage-gated potassium channels are critical for infrared inhibition of action potentials: an experimental study. *Neurophotonics*. 2019. doi:10.1117/1.nph.6.4.040501

16. Lothet EH, Shaw KM, Lu H, et al. (In Submission) Selective inhibition of small-diameter axons using infrared light. *Sci Rep*. 2017.

17. Huxley AF, Stämpeli R. Evidence for saltatory conduction in peripheral myelinated nerve fibres. *J Physiol*. 1949. doi:10.1113/jphysiol.1949.sp004335

18. Kandel ER, Schwartz JH, Jessell TM, Siegelbaum SA, Hudspeth AJ. *Principles of Neural Science*. Fifth Edit. The McGraw-Hill Companies, Inc.; 2013.

19. Armstrong SA, Herr MJ. Physiology, Nociception. StatPearls [Internet]. https://www.ncbi.nlm.nih.gov/books/NBK551562/#. Published 2020.

20. Woller SA, Eddinger KA, Corr M, Yaksh TL. An overview of pathways encoding nociception. *Clin Exp Rheumatol*. 2017.

21. Li J, Simone DA, Larson AA. Windup leads to characteristics of central sensitization. *Pain*. 1999. doi:10.1016/S0304-3959(98)00154-7

22. Price DD, Staud R, Robinson ME, Mauderli AP, Cannon R, Vierck CJ. Enhanced temporal summation of second pain and its central modulation in fibromyalgia patients. *Pain*. 2002. doi:10.1016/S0304-3959(02)00053-2

23. Latremoliere A, Woolf CJ. Central Sensitization: A Generator of Pain Hypersensitivity by Central Neural Plasticity. *J Pain.* 2009. doi:10.1016/j.jpain.2009.06.012

24. Woolf CJ, Thompson SWN. The induction and maintenance of central sensitization is dependent on N-methyl-d-aspartic acid receptor activation; implications for the treatment of post-injury pain hypersensitivity states. *Pain*. 1991. doi:10.1016/0304-3959(91)90100-C

25. Moroz LL. Aplysia. *Curr Biol.* 2011. doi:10.1016/j.cub.2010.11.028

26. Winlow W, Kandel ER. The morphology of identified neurons in the abdominal ganglion of aplysia californica. *Brain Res.* 1976;112(2):221-249. doi:10.1016/0006-8993(76)90282-1

27. Byrne JH. Neural circuit for inking behavior in Aplysia californica. *J Neurophysiol.* 1980;43(4):896 LP - 911. http://jn.physiology.org/content/43/4/896.abstract.

28. Coggeshall RE. A Light and Electron Microscope Study of the Abdominal Ganglion of Aplysia Californica. *J Neurophysiol.* 1967;30(6):1263-1287.

29. Bedini C, Geppetti L. A morphological study on the amount and origin of axons in the pleuroabdominal connectives of Aplysia fasciata. *Ital J Zool*. 2000;67(1):9-18. doi:10.1080/11250000009356288

30. Kilgore KL, Bhadra N. Reversible nerve conduction block using kilohertz frequency alternating current. *Neuromodulation.* 2014;17(3):242-254. doi:10.1111/ner.12100

31. Bhadra N, Kilgore KL. Direct current electrical conduction block of peripheral nerve. *IEEE Trans Neural Syst Rehabil Eng.* 2004. doi:10.1109/TNSRE.2004.834205

32. Ranck JB. Which elements are excited in electrical stimulation of mammalian central nervous system: A review. *Brain Res*. 1975. doi:10.1016/0006-8993(75)90364-9

33. BeMent SL, Ranck JB. A quantitative study of electrical stimulation of central myelinated fibers. *Exp Neurol.* 1969. doi:10.1016/0014-4886(69)90012-0

34. Alon G, Smith G V. Tolerance and conditioning to neuro-muscular electrical stimulation within and between sessions and gender. *J Sport Sci Med*. 2005.

35. Günter C, Delbeke J, Ortiz-Catalan M. Safety of long-term electrical peripheral nerve stimulation: Review of the state of the art. *J Neuroeng Rehabil.* 2019. doi:10.1186/s12984-018-0474-8

36. Melzack R. Gate control theory. *Pain Forum.* 1996;5(2):128-138. doi:http://dx.doi.org/10.1016/S1082-3174(96)80050-X

37. Liebano R, Rakel B, Vance CGT, Walsh DM, Sluka K a. An Investigation of the Development of Analgesic Tolerance to Transcutaneous Electrical Nerve Stimulation (TENS) in Humans. *Pain*. 2011;152(2):335-342. doi:10.1016/j.pain.2010.10.040.An

38. Jones I, Johnson MI. Transcutaneous electrical nerve stimulation. *Contin Educ Anaesthesia, Crit Care Pain*. 2009;9(4):130-135. doi:10.1093/bjaceaccp/mkp021

39. Bergeron-Vézina K, Corriveau H, Martel M, Harvey M-P, Léonard G. High- and low-frequency transcutaneous electrical nerve stimulation does not reduce experimental pain in elderly individuals. *Pain*. 2015;156(10):2093-2099. doi:10.1097/j.pain.0000000000000276

40. Grider JS, Manchikanti L, Carayannopoulos A, et al. Effectiveness of Spinal Cord Stimulation in Chronic Spinal Pain: A Systematic Review. *Pain Physician*. 2016;19(1):E33-E54.

41. Moore DM, McCrory C. Spinal cord stimulation. *BJA Educ*. 2016:1-6. doi:10.1053/trap.2000.9683

42. Verrills P, Sinclair C, Barnard A. A review of spinal cord stimulation systems for chronic pain. *J Pain Res*. 2016;9:481-492. doi:10.2147/JPR.S108884

43. Joseph L, Butera RJ. High Frequency Stimulation Selectively Blocks Different Types of Fibers in Frog Sciatic Nerve. *Ieee Trans Neural Syst Rehabil Eng*. 2011;19(5):550-557. doi:10.1109/TNSRE.2011.2163082

44. Crockett MJ, Fehr E. Social brains on drugs: Tools for neuromodulation in social neuroscience. *Soc Cogn Affect Neurosci*. 2014. doi:10.1093/scan/nst113

45. Park HJ, Moon DE. Pharmacologic management of chronic pain. *Korean J Pain*. 2010;23(2):99-108. doi:10.3344/kjp.2010.23.2.99

46. Mathew E, Kim E, Zempsky W. Pharmacologic Treatment of Pain. *Semin Pediatr Neurol*. 2016. doi:10.1016/j.spen.2016.10.004

47. US Department of Health and Human Services. *The Opioid Epidemic: By the Numbers*.; 2016. https://www.hhs.gov/sites/default/files/Factsheet-opioids-061516.pdf.

48. Staiman A, Seeman P. Conduction-blocking concentrations of anesthetics increase with nerve axon diameter: studies with alcohol, lidocaine and tetrodotoxin on single myelinated fibers. *J Pharmacol Exp Ther*. 1977.

49. Viventi J, Kim DH, Vigeland L, et al. Flexible, foldable, actively multiplexed, high-density electrode array for mapping brain activity in vivo. *Nat Neurosci*. 2011. doi:10.1038/nn.2973

50. Tyler WJ, Tufail Y, Finsterwald M, Tauchmann ML, Olson EJ, Majestic C. Remote Excitation of Neuronal Circuits Using Low- Intensity, Low-Frequency Ultrasound. *PLoS One*. 2008;3(10). doi:10.1371/journal.pone.0003511

51. Legon W, Sato TF, Opitz A, et al. Transcranial focused ultrasound modulates the activity of primary somatosensory cortex in humans. *Nat Neurosci*. 2014;17(2):322-329. doi:10.1038/nn.3620

52. Chaplin V, Phipps MA, Caskey CF. A random phased-array for MR-guided transcranial ultrasound neuromodulation in non-human primates. *Phys Med Biol*. 2018. doi:10.1088/1361-6560/aabeff

53. Blackmore J, Shrivastava S, Sallet J, Butler CR, Cleveland RO. Ultrasound Neuromodulation: A Review of Results, Mechanisms and Safety. *Ultrasound Med Biol*. 2019. doi:10.1016/j.ultrasmedbio.2018.12.015

54. Naor O, Krupa S, Shoham S. Ultrasonic neuromodulation. *J Neural Eng*. 2016;13(3):031003. doi:10.1088/1741-2560/13/3/031003

55. Kubanek J. Neuromodulation with transcranial focused ultrasound. *Neurosurg Focus*. 2018. doi:10.3171/2017.11.FOCUS17621

56. Gysbrechts B, Wang L, Trong NN, et al. Light distribution and thermal effects in the rat brain under optogenetic stimulation. *J Biophotonics*. 2016;9(6):576-585. doi:10.1002/jbio.201500106

57. Klumpp D, Zimmermann M. Irreverisble differential block of A- and C-fibres following local nerve heating in the cat. *J Physiol*. 1980;298(1):471-482. doi:10.1113/jphysiol.1980.sp013095

58. Walker J. Relief from chronic pain by low power laser irradiation. *Neurosci Lett*. 1983;43(2-3):339-344. doi:10.1016/0304-3940(83)90211-2

59. Sushko BS, Lymans'kyi IP, Huliar SO. [Action of the red and infrared electromagnetic waves of light-emitting diodes on the behavioral manifestation of somatic pain]. *Fiziol Zh*. 2007;53(3):51-60.

60. Pettit DL, Wang SSH, Gee KR, Augustine GJ. Chemical two-photon uncaging: A novel approach to mapping glutamate receptors. *Neuron*. 1997;19(3):465-471. doi:10.1016/S0896-6273(00)80361-X

61. Kantevari S, Matsuzaki M, Kanemoto Y, Kasai H, Ellis-Davies GCR. Two-color, two-photon uncaging of glutamate and GABA. *Nat Methods*. 2010;7(2):123-125. doi:10.1038/nmeth.1413

62. Shepherd GMG. Circuit mapping by ultraviolet uncaging of glutamate. *Cold Spring Harb Protoc*. 2012;7(9):998-1004. doi:10.1101/pdb.prot070664

63. Deisseroth K. Optogenetics: 10 years of microbial opsins in neuroscience. *Nat Neurosci*. 2015;18(9):1213-1225. doi:10.1038/nn.4091

64. Wells J, Wells J, Kao C, et al. Application of infrared light for in vivo neural stimulation. *J Biomed Opt*. 2005;10:64002-64003. doi:10.1117/1.2121772

65. Duke AR, Jenkins MW, Lu H, McManus JM, Chiel HJ, Jansen ED. Transient and selective suppression of neural activity with infrared light. *Sci Rep*. 2013;3:2600. doi:10.1038/srep02600

66. Rochkind S, Nissan M, Lubart R, Avram J, Bartal A. The in-vivo-nerve response to direct low-energy-laser irradiation. *Acta Neurochir (Wien)*. 1988;94(1-2):74-77. doi:10.1007/BF01406620

67. Bernstein J. Untersuchungen zur Thermodynamik der bioelektrischen Ströme. *Pflugers Arch Eur J Physiol*. 1902;92(10-12):521-562. doi:10.1007/BF01790181

68. Hodgkin AL, Katz B. the Effect of Temperature on the Electrical Activity of the Giant Axon of the Squid. *J Physiol Lucas Gasser Schoepfle Erlanger Cardot Arvanitaki*. 1949;09:240-249.

69. Douglas WW, Malcolm JL. The effect of localized cooling on conduction in cat nerves. *J Physiol*. 1955;130(1):53-71. https://www.ncbi.nlm.nih.gov/pmc/articles/PMC1363452/.

70. Zhang Z, Lyon TD, Kadow BT, et al. Conduction Block of Mammalian Myelinated Nerve by Local Cooling to 15-30 ℃ after a Brief Heating. *J Neurophysiol*. 2016;115(3):1436-1445. doi:10.1152/jn.00954.2015

71. Carpenter DO. Temperature effects on pacemaker generation, membrane potential, and critical firing threshold in Aplysia neurons. *J Gen Physiol*. 1967;50(6):1469-1484. doi:10.1085/jgp.50.6.1469

72. Rodríguez BM, Sigg D, Bezanilla F. Voltage gating of Shaker K+ channels. The effect of temperature on ionic and gating currents. *J Gen Physiol*. 1998;112(2):223-242. doi:10.1085/jgp.112.2.223

73. Vandenberg JI, Varghese A, Lu Y, Bursill JA, Mahaut-Smith MP, Huang CL-H. Temperature dependence of human ether-a-go-go-related gene K+ currents. *Am J Physiol Cell Physiol*. 2006;291(1):C165-75. doi:10.1152/ajpcell.00596.2005

74. Yang F, Zheng J. High temperature sensitivity is intrinsic to voltage-gated potassium channels. *Elife*. 2014;3:e03255. doi:10.7554/eLife.03255

75. Collins CA, Rojas E. TEMPERATURE DEPENDENCE OF THE SODIUM CHANNEL GATING KINETICS IN THE NODE OF RANVIER. *Q J Exp Physiol*. 1982;67(1):41-55. doi:10.1113/expphysiol.1982.sp002623

76. Wells J, Kao C, Jansen ED, Konrad P, Mahadevan-Jansen A. Application of infrared light for in vivo neural stimulation. *J Biomed Opt*. 2005;10(6):064003. doi:10.1117/1.2121772

77. Wells J, Kao C, Konrad P, et al. Biophysical mechanisms of transient optical stimulation of peripheral nerve. *Biophys J*. 2007;93(7):2567-2580. doi:10.1529/biophysj.107.104786

78. Shapiro MG, Homma K, Villarreal S, Richter C-P, Bezanilla F. Infrared light excites cells by changing their electrical capacitance. *Nat Commun*. 2012;3:736. doi:10.1038/ncomms1742

79. Plaksin M, Kimmel E, Shoham S. Correspondence: Revisiting the theoretical cell membrane thermal capacitance response. *Nat Commun*. 2017;8(1). doi:10.1038/s41467-017-00435-5

80. Shapiro MG, Homma K, Villarreal S, Richter CP, Bezanilla F. Infrared light excites cells by changing their electrical capacitance. *Nat Commun*. 2012;3:736. doi:10.1038/ncomms1742

81. Matic AI, Walsh JT, Richter C-P. Spatial extent of cochlear infrared neural stimulation determined by tone-on-light masking. *J Biomed Opt*. 2011;16:118002. doi:10.1117/1.3655590

82. Tan X, Rajguru S, Young H, et al. Radiant energy required for infrared neural stimulation. *Sci Rep*. 2015;5. doi:10.1038/srep13273

83. Jenkins MW, Duke AR, Gu S, et al. Optical pacing of the embryonic heart. *Nat Photonics*. 2010. doi:10.1038/nphoton.2010.166

84. Jenkins MW, Wang YT, Doughman YQ, Watanabe M, Cheng Y, Rollins AM. Optical pacing of the adult rabbit heart. *Biomed Opt Express*. 2013;4(9):1626-1635. doi:10.1364/BOE.4.001626

85. Cayce JM, Friedman RM, Chen G, Jansen ED, Mahadevan-Jansen A, Roe AW. Infrared neural stimulation of the primary visual cortex in non-human primates. *Neuroimage*. 2013;84:181-190. doi:10.1016/j.neuroimage.2013.08.040

86. Roe AW, Chernov MM, Friedman RM, Chen G. In vivo mapping of cortical columnar networks in the monkey with focal electrical and optical stimulation. *Front Neuroanat*. 2015. doi:10.3389/fnana.2015.00135

87. Fried NM, Lagoda G a, Scott NJ, Su L-M, Burnett AL. Noncontact stimulation of the cavernous nerves in the rat prostate using a tunable-wavelength thulium fiber laser. *J Endourol*. 2008;22(3):409-413. doi:10.1089/end.2008.9996

88. Tozburun S, Hutchens TC, McClain M a, Lagoda G a, Burnett AL, Fried NM. Temperature-controlled optical stimulation of the rat prostate cavernous nerves. *J Biomed Opt*. 2013;18:067001. doi:10.1117/1.JBO.18.6.067001

89. Cayce JM, Wells JD, Malphrus JD, et al. Infrared neural stimulation of human spinal nerve roots in vivo. *Neurophotonics*. 2015;2(1):015007. doi:10.1117/1.NPh.2.1.015007

90. Sordillo LA, Pu Y, Pratavieira S, Budansky Y, Alfano RR. Deep optical imaging of tissue using the second and third near-infrared spectral windows. *J Biomed Opt*. 2014;19(5):056004. doi:10.1117/1.JBO.19.5.056004

91. Eom K, Kim J, Choi JM, et al. Enhanced infrared neural stimulation using localized surface plasmon resonance of gold nanorods. *Small*. 2014;10(19):3853-3857. doi:10.1002/smll.201400599

92. Paviolo C, Thompson AC, Yong J, Brown WGA, Stoddart PR. Nanoparticle-enhanced infrared neural stimulation. *J Neural Eng*. 2014;11(6):065002. doi:10.1088/1741-2560/11/6/065002

93. Duke AR, Cayce JM, Malphrus JD, Konrad P, Mahadevan-Jansen A, Jansen ED. Combined optical and electrical stimulation of neural tissue in vivo. *J Biomed Opt*. 2009;14(6):60501. doi:10.1117/1.3257230

94. Duke AR, Peterson E, Mackanos MA, Atkinson J, Tyler D, Jansen ED. Hybrid electro-optical stimulation of the rat sciatic nerve induces force generation in the plantarflexor muscles. *J Neural Eng*. 2012;9(6):66006. doi:10.1088/1741-2560/9/6/066006

95. Duke AR, Lu H, Jenkins MW, Chiel HJ, Jansen ED. Spatial and temporal variability in response to hybrid electro-optical stimulation. *J Neural Eng*. 2012;9(3):36003. doi:10.1088/1741-2560/9/3/036003

96. Duke AR, Jenkins MW, Lu H, McManus JM, Chiel HJ, Jansen ED. Transient and selective suppression of neural activity with infrared light. *Sci Rep*. 2013;3:2600. doi:10.1038/srep02600

97. Walsh AJ, Tolstykh GP, Martens S, Ibey BL, Beier HT. Action potential block in neurons by infrared light. *Neurophotonics*. 2016. doi:10.1117/1.nph.3.4.040501

98. Zhu X, Lin J-W, Sander MY. Infrared inhibition and waveform modulation of action potentials in the crayfish motor axon. *Biomed Opt Express*. 2019. doi:10.1364/boe.10.006580

99. Lothet E, Shaw KM, Horn CC, et al. Selective control of small versus large diameter axons using infrared laser light. In: *Proc. SPIE 9690, Clinical and Translational Neurophotonics; Neural Imaging and Sensing; and Optogenetics and Optical Manipulation*. Vol 96901N. doi:10.1117/12.221294

100. Lothet EH, Kilgore KL, Bhadra N, et al. Alternating current and infrared produce an onset-free reversible nerve block. *Neurophotonics*. 2014;1:011010. doi:10.1117/1.NPh.1.1.011010

101. Yoo S, Hong S, Choi Y, Park JH, Nam Y. Photothermal inhibition of neural activity with near-infrared-sensitive nanotransducers. *ACS Nano*. 2014;8(8):8040-8049. doi:10.1021/nn5020775

102. Welch AJ, Van Gemert MJC. *Optical-Thermal Response of Laser-Irradiated Tissue.*; 2011. doi:10.1007/978-90-481-8831-4

103. Lister T, Wright PA, Chappell PH. Optical properties of human skin. *J Biomed Opt*. 2012. doi:10.1117/1.jbo.17.9.090901

104. Jacques SL. Optical properties of biological tissues: a review. *Phys Med Biol*. 2013;58(11):R37-61. doi:10.1088/0031-9155/58/11/R37

105. Fang Q, Boas DA. Monte Carlo Simulation of Photon Migration in 3D Turbid Media Accelerated by Graphics Processing Units. *Opt Express*. 2009. doi:10.1364/oe.17.020178

106. Chan E, Menovsky T, Welch AJ. Effects of cryogenic grinding on soft-tissue optical properties. *Appl Opt*. 1996;35(22). doi:10.1364/ao.35.004526

107. Pitzschke A, Lovisa B, Seydoux O, et al. Optical properties of rabbit brain in the red and near-infrared: changes observed under in vivo , postmortem, frozen, and formalin-fixated conditions . *J Biomed Opt*. 2015. doi:10.1117/1.jbo.20.2.025006

108. Prahl SA. Everything I think you should know about inverse adding-doubling. *Oregon Med Laser Center, St Vincent Hosp*. 2011.

109. Bargo PR, Prahl SA, Jacques SL. Optical properties effects upon the collection efficiency of optical fibers in different probe configurations. *IEEE J Sel Top Quantum Electron*. 2003. doi:10.1109/JSTQE.2003.811287

110. Bargo PR, Prahl SA, Goodell TT, et al. In vivo determination of optical properties of normal and tumor tissue with white light reflectance and an empirical light transport model during endoscopy. *J Biomed Opt*. 2005. doi:10.1117/1.1921907

111. Zaccanti G, Del Bianco S, Martelli F. Measurements of optical properties of high-density media. *Appl Opt*. 2003. doi:10.1364/ao.42.004023

112. Gioux S, Mazhar A, Cuccia DJ. Spatial frequency domain imaging in 2019: principles, applications, and perspectives. *J Biomed Opt*. 2019. doi:10.1117/1.jbo.24.7.071613

113. Wilson RH, Nadeau KP, Jaworski FB, et al. Quantitative short-wave infrared multispectral imaging of in vivo tissue optical properties . *J Biomed Opt*. 2014. doi:10.1117/1.jbo.19.8.086011

114. Cook R., Malkus D., Plesha M., Witt R. *Concepts and Applications of Finite Element Analysis*.; 2002.

115. Rieke V, Pauly KB. MR thermometry. *J Magn Reson Imaging*. 2008;27(2):376-390. doi:10.1002/jmri.21265

116. Wade SA, Collins SF, Baxter GW. Fluorescence intensity ratio technique for optical fiber point temperature sensing. *J Appl Phys*. 2003;94(8):4743-4756. doi:10.1063/1.1606526

117. Liu D, Ebbini ES. Real-time 2-D temperature imaging using ultrasound. *IEEE Trans Biomed Eng*. 2010;57(1):12-16. doi:10.1109/TBME.2009.2035103

118. Gardner B, Matousek P, Stone N. Temperature Spatially Offset Raman Spectroscopy (T-SORS): Subsurface Chemically Specific Measurement of Temperature in Turbid Media Using Anti-Stokes Spatially Offset Raman Spectroscopy. *Anal Chem*. 2016;88(1):832-837. doi:10.1021/acs.analchem.5b03360

119. Incropera FP, DeWitt DP, Bergman TL, Lavine AS. Fundamentals of Heat and Mass Transfer. *Water*. 2007;6th:997. doi:10.1016/j.applthermaleng.2011.03.022

120. Hale GM, Querry MR. Optical Constants of Water in the 200-nm to 200-microm Wavelength Region. *Appl Opt*. 1973;12(3):555-563. doi:10.1364/AO.12.000555

121. Lothet EH, Shaw KM, Lu H, et al. Selective inhibition of small-diameter axons using infrared light. *Sci Rep*. 2017;7(1). doi:10.1038/s41598-017-03374-9

Chapter III

The Effect of Light Scattering on the Temperature Rise at Infrared Neural Inhibition Wavelengths

3.1 Abstract

Computational modeling of light-tissue interactions at absorption dominated wavelengths typically ignores optical scattering; however, this assumption may not be accurate. This work aims to assess how optical scattering effects the temperature distribution during laser heating to determine if scattering can be ignored and how errors in the amount of assumed scattering can alter computational predictions. A Monte Carlo simulation of photon propagation was integrated with a thermal simulation in COMSOL Multiphysics. Validation of this model was performed using a set of thermal camera and thermocouple measurements in agarose phantoms. Subsequently, the model was used to perform a parametric sweep over absorption and reduced scattering coefficients theoretically achievable in neural tissue to better understand the expected effect on the temperature distribution from scattering. A final validation of these trends was performed by thermal imaging the temperature distribution in water phantoms with and added polystyrene scattering agent. The parametric sweep showed a 7% change in the maximum temperature rise, >20% change in thermal penetration depth, and no dependency of the surface full width at half-maximum of heating over reduced scattering coefficients theoretically possible in the tissue. These trends were confirmed using the water bath validation measurements. While the effect of scattering on the heat distribution is small, it has a non-negligible effect and in most cases cannot be ignored, and therefore a Monte Carlo simulation is needed. Best estimates of scattering coefficients may be sufficient to result in small errors when simulating heat distributions if values are not available in literature.

3.2 Introduction

Optical therapeutics require precise knowledge of the dose and distribution of light to guide the therapy of interest. For infrared neural modulation (INM), infrared light is applied to neural tissue to either stimulate signal conduction[1] or block propagation of action potentials[2]. Both effects rely strongly on absorption of optical energy by tissue to create a transient temperature rise. Infrared neural inhibition (INI) requires a sustained temperature rise to create a neural heat block[3,4]. Computational models that simulate light transport[5], heat transport[6], and neural conduction[7] can be coupled to optimize light application during INI for specific therapeutic effects. A Monte Carlo model of photon transport is appropriate for simulating the distribution of absorbed photons during INI[8,9]. This probabilistic simulation launches photons packets into a simulation geometry and tracks the path of the photon packet and its relative weight as it is absorbed and scattered in the medium[10]. Each voxel in the geometry must have 4 optical properties defined: the refractive index (n), absorption coefficient (μ_a [mm^{-1}]), scattering coefficient (μ_s [mm^{-1}]), and optical anisotropy (g). Ultimately, a distribution of absorbed photons can be generated. This distribution is proportional to the heat source distribution, and can be used in a thermal model to guide the location and amplitude of the heat source term to ultimately predict laser heating as a function of the material's density (ρ), thermal conductivity (k), specific heat (c_p) using Penne's bioheat equation[10]. The output of this coupled optical-thermal model may then inform on the likelihood of therapy[11] and damage[12], or may be used as the input to a neural conduction model to predict neural response[13–15].

Utilizing these computational models to provide useful predictive information presupposes that the correct, or at least sufficiently accurate, tissue input parameters to these models are known. There is a distinct lack of information about the correct optical scattering parameters for neural tissue in both vertebrates and invertebrates in the wavelength range at which INI is applied, chiefly 1440 - 1470 nm and 1860 - 1880 nm. The main chromophore at these wavelengths can be approximated as water due to its high absorption[16], however, little information is available in literature about the scattering properties of the neural substructures. While absorption events are assumed to be dominant over scattering events at these wavelengths, scattering still occurs, and therefore a Beer's Law approximation[17] may be insufficient to estimate photon distributions. The reduced scattering coefficient, μ_s' ($\mu_s' = \mu_s * (1-g)$), can be experimentally determined, however, this is particularly difficult at these wavelengths due to absorption dominating over scattering and the reduced sensitivity of silicon detectors at longer short-wave infrared (SWIR) wavelengths. Add to this the constraints in nerve of 1) their small size which limits both the mass/volume of tissue available for probing and the beam diameters which can be used, and 2) their cylindrical geometry which creates a curved surface. These characteristics, while not impossible to

overcome, pose a daunting barrier to obtaining accurate and precise optical property measurements at these wavelengths. Operating in an absorption dominated wavelength regime further complicates measurement as it violates the assumptions of many analysis techniques (especially diffuse reflection) that utilize diffusion theory which assumes scattering as the dominant interaction in the sample. Common measurement techniques include using integrating spheres[18], probe-based techniques[19], and spatial frequency domain imaging (SFDI)[20]. Integrating spheres require a large sample of tissue compared to the beam diameter, and the entire entrance port to the sphere must be covered which is difficult when measuring nerve. Multiple samples may be laid on top of each other, or ground up and combined[21], however, this will alter the measured optical properties compared to their *in vivo* values, and any properties due to the organization of the tissue will be lost. Additionally, sample thicknesses for integrating spheres (and any other transmission measurement) require thicknesses on the order of 100s of microns to obtain enough signal in the short-wave infrared (SWIR) spectrum. For probe-based techniques, the tissue must be large enough to apply multiple adjacent optical fibers, although single fiber techniques are possible, and this technique shows reduced collection efficiency in high absorption and low scattering tissues[19,22]. SFDI can potentially be used, however detectors with high enough efficiency in the SWIR are expensive. Additionally, at INI wavelengths, diffuse reflectance will be low due to the high absorption, which also adds to the problem of signal to noise ratio. Wilson *et al.*[23] (2014) pushed SFDI into the SWIR while characterizing optical property changes due to burn, but used information from 850- 1050 nm to extrapolate out to 1800 nm, highlighting that direct measurement in the regime of INI is difficult.

Extrapolating equations out to the SWIR that are fit in the visible and near-infrared which approximate the reduced scattering coefficient may prove to be an adequate approximation since optical scattering is well characterized for particle distributions of known size and concentrations[24]. It is generally accepted that scattering can be approximated in two regimes: Mie scattering regime where the wavelength of light is on the order of the scattering particle size, and Rayleigh scattering regime where the wavelength is larger than the scattering particle. The Mie regime can be modeled as scattering decreasing exponentially with wavelength, and this exponential can be fit to experimental data to achieve the exponential term, b_{Mie}. Scattering in the Rayleigh regime is proportional to λ^{-4} (Equation 2.11). Visible wavelengths in tissue are considered to fall within the Mie regime, but moving into the SWIR shift this closer to the Rayleigh regime. Prior studies have experimentally measured the reduced scattering coefficient in tissue at different wavelengths, and these studies have been aggregated by Jacques 2013 to develop analytical approximations of reduced scattering coefficient spectra for different tissues[25]. The reduced scattering coefficient can be approximated as a function of wavelength by utilizing empirically measured coefficients which estimate Mie and Rayleigh scattering[25] as discussed in section 2.3.1:

$$\mu_s'(\lambda) = a'\left(f_{Ray}\left(\frac{\lambda}{500\ (nm)}\right)^{-4} + (1 - f_{Ray})\left(\frac{\lambda}{500\ (nm)}\right)^{-b_{Mie}}\right) \qquad \text{Equation 2.11}$$

where a' is a scaling factor equal to μ_s' at λ=500 nm, f_{Ray} is the fraction of Rayleigh scattering, λ is wavelength in nm, and b_{Mie} is the exponential fit parameter for Mie scattering. Fitted parameters for many tissues have been reported[25]. While this collection of data contains various neural tissues, information is limited at 1460 nm and does not exist for 1875 nm, thus utilizing these equations at INI wavelengths would be an extrapolation, which may be sufficient to approximate μ_s' for the purpose of predicting temperature distributions in tissue during INI. Equation 1 lays out a way to theoretically assess the expected μ_s' at various wavelengths and a means of predicting the limits of μ_s' by assuming exclusively Mie or Rayleigh regime of scattering with the actual value of μ_s' laying somewhere in between these extremes.

It would be informative to know how uncertainty in μ_s', whether from measurement error or extrapolation error, affects the expected light and heat distribution. A joint optical-thermal model was created by merging Monte Carlo Extreme (MCX) and COMSOL Multiphysics. To validate this model, two independent validation studies were developed. The first of these probed the surface temperature distribution in an agarose gel slab using thermal imaging while the second probed the temperature distribution with depth in a block of agarose using a thermocouple (TC). In each of these setups, the optical scattering coefficient was varied using the addition of polystyrene microspheres in various concentrations. After validation of the model, a parametric sweep investigation was performed to test the effect of μ_s' on expected thermal outputs by varying the amount of absorption and scattering in a Monte Carlo model of light propagation. The simulated distribution of absorbed photons was then used as the heat source distribution in a finite element analysis of thermal conduction, run in COMSOL Multiphysics. A third set of experiments was performed purely to validate the trends predicted in the parametric sweep investigation.

3.3 Methods

3.3.1 Published values for the Scattering Coefficient

A literature search for optical properties of nerve and other tissues was performed. A wealth of literature is available on optical scattering of tissue in the visible and near infrared regions[25–32] , however

few articles tested scattering in nerve[21,33] or at wavelengths in the regime of INI[27,33–35]. The only article that reported μ_s' at INI wavelengths in peripheral nerve was Jiang *et al*. 2014[33]. Filatova *et al*. 2017 reported an extinction coefficient spectrum for pig spinal cord[35], but an approximation of the contribution from scattering could not be performed. Some sources reported equations that could be used to approximate $\mu_s'(\lambda)$[25,36]. Estimates of μ_s' near INI wavelengths or in neural tissue have been aggregated in Table 3.1.

Jacques 2013 reports fitted parameters for various tissues (Optic Nerve, Muscle, Average Brain, Average Fibrous Tissue, Average Soft Tissue) for estimating the reduced scattering coefficient across wavelengths based on Equation 2.11 where the contribution of Mie and Rayleigh scattering could be varied[25], but the data used for fitting do not extend to INI wavelengths. This equation does, however, present a theoretical framework for assessing the expected bounds of μ_s' since f_{Ray} can be set to 0 or 1 to estimate μ_s' purely in the Mie or Rayleigh regime, respectively, providing the upper and lower bounds of the scattering parameter. Using this equation and the reported coefficients, the extrapolated μ_s' value and the upper and lower μ_s' limits for the above tissue types at 1460 nm and 1875 nm were calculated (Table 3.2). For optic nerve which we hypothesize will be the most similar to peripheral nerve out of the tissues reported, this methodology estimates that $\mu_s'(1460\text{ nm}) = 0.75\text{ mm}^{-1}$ and that $\mu_s'(1875\text{ nm}) = 0.56\text{ mm}^{-1}$. The approximate physiological range of μ_s' was determined to be $\mu_s' \sim 0 – 1.5\text{ mm}^{-1}$. For all tissue types tested. These estimates guided the μ_s' values used in the study.

3.3.2 Optical-Thermal Model

An HP Z6 G4 Workstation with an Intel Xeon processor was used for all computational modeling. This workstation utilized an NVIDIA GeForce RTX 2080 graphical processing unit (GPU) exclusively for computation while a second GPU provided video output. The hardware allowed for rapidly running Monte Carlo and COMSOL Multiphysics simulations (30 – 60 seconds and 3 – 20 minute simulation times for this study, respectively) and the greatest slow down came from reading and writing of data to text files. General parameters are discussed below for the joint optical-thermal model, however, simulation-specific parameters are described for each set of simulations in their respective sections.

3.3.2.1 Monte Carlo Simulations

Photon absorption maps were generated using a GPU parallelized Monte Carlo model called through MATLAB (MCXLAB[5]). These simulations utilized cubic voxels to generate computational geometries. Each geometry assumed that the optical properties of each medium were homogeneous. Simulations utilized in this study used a photon source of either a uniform diverging disk to mimic the

Table 3.1. Optical properties of neural tissues and various tissues in the infrared spectrum

Tissue	Wavelength [nm]	μ_s' [mm^{-1}]	Reference
Rat Optical Nerve	1863	0.55	Jiang 2014[33]
Rat Sciatica Nerve	1863	0.36	Jiang 2014[33]
Rat Muscle	1863	0.11	Jiang 2014[33]
Rat Heart	1863	0.67	Jiang 2014[33]
Rat Skin	1800	0.85	Wilson 2014[23]
Human Skin	1600	0.6 – 1.1	Troy 2001[37]
Rat Liver	1875	~0.6	Parsa 1989[38]
Human Skin	1450	1 - 2	Bashkatov 2005[26]
Human Skin	1875	~1.5	Bashkatov 2005[26]
Rat Brain	1460	~0.75	Golovynskyi 2018[39]
Rat Brain	1875	~0.6	Golovynskyi 2018[39]
Rabbit Sciatic Nerve Paste	850	1.5 - 3	Chan 1996[21]
Human Dura Mater	1460 (extrapolated)	0.87	Bashkatov 2018[36]
Human Dura Mater	1875 (extrapolated)	0.77	Bashkatov 2018[36]
Rat Brain	750	0.1-0.61	Johns 2005[29]
Human Cortex	956	0.42-0.89	Bevilacqua 1999[30]
Human Optic Nerve	956	1.52	Bevilacqua 1999[30]
Rabbit Brain	808	0.62	Pitzschke 2015[31]
Human Grey Matter	1064	0.57	Yaroslavsky 2002[32]

Table 3.2. Extrapolated μ_s' [mm^{-1}] in various tissues and the theoretical limits at INI wavelengths using equation 2.11.

Tissue	Extrapolated μ_s'		Lower Bound (f_{ray}= 1)		Upper Bound (f_{ray}= 0)		Reference
	1460 nm	1875 nm	1460 nm	1875 nm	1460 nm	1875 nm	
Normal Optic Nerve	0.75	0.56	0.036	0.013	0.75	0.562	Jacques 2013[25]
Muscle	0.48	0.38	0.018	0.007	0.482	0.382	Jacques 2013[25]
Average Brain	0.60	0.45	0.038	0.014	0.855	0.651	Jacques 2013[25]
Average Fibrous Tissues	0.77	0.64	0.04	0.015	1.464	1.247	Jacques 2013[25]
Average Soft Tissue	0.51	0.38	0.026	0.01	0.593	0.452	Jacques 2013[25]

output from an optical fiber, or a specific pattern input by the user based on beam profiler measurements to adequately approximate the complex light distributions resulting from spatial modes from the multimode laser after beam shaping. Due to the GPU parallelization, geometries greater than 4 x 4 x 4 mm with 0.01 mm size voxel could be run using at least 50 million photons in <60 seconds. Time-dependent simulations were run for 1 ns, and it was noted that all photons were absorbed within the first 0.1 ns. The 3-dimensional distributions of absorbed photons were generated which are probability maps of where any given photon may be absorbed in the geometry. Absorption distributions were exported into text files in a format readable by COMSOL. Data was organized into an N x 4 array where column 1 is the X location, column 2 is the Y location, column 3 is the Z location, and column 4 is the absorbed energy value at that (X,Y,Z) location. Thus, each row from 1 to N is a different voxel in the geometry (N voxels exported).

3.3.2.2 COMSOL Thermal Model

Thermal simulations which solve Pennes' bio-heat equation[10] were run using three-dimensional geometries in COMSOL Multiphysics version 5.5 which performs a finite element analysis to compute the heat distribution. Computational geometries were generated from simple shapes, such as cubes and cylinders, and subsequently meshed to generate elements over which the heat equation could be solved. While particular simulations utilized different geometries and thermal boundary conditions, this joint optical-thermal model relied on two components common to all models which allowed the Monte Carlo simulations to guide the heat source term. First of these is the interpolation function (defined here as *Source*(x,y,z)) which interpolates the text file containing the results of the Monte Carlo simulations so that COMSOL can apply the appropriate value to each mesh element. This was used to guide the distribution of the heat source term. The second commonality is the Heat Source block which is used to apply the heat source term, q, using the absorbed photon distribution with the equation:

$$q = \frac{AveragePower}{dh^3} * Source(x, y, z) \qquad \text{Equation 3.1}$$

where AveragePower is the average power applied from the irradiation source, dh is the voxel size used in the Monte Carlo simulation, and *Source*(x,y,z) is the interpolation function which acts to spatially weight the irradiated power.

Table 3.3. Agarose Phantom Recipes

Agarose Weight [g]	Volume of DI Water [mL]	Volume of Bead Solution [mL]	Bead Volume [% solid]	Measured μ_s' [mm^{-1}]
Thermal Imaging Phantoms				
0.5	25	0	0	0.31
0.5	24.75	0.25	0.027	0.49
0.5	24.5	0.5	0.054	0.74
0.5	24	1	0.108	1.19
0.5	23.6	1.4	0.151	1.67
0.5	23	2	0.216	2.29
Thermocouple Phantoms				
1	50	0	0	0.35
1	49.5	0.5	0.027	0.51
1	48	2	0.108	1.29

3.3.3 Phantom Creation

Agarose gels were mixed using high melting temperature agarose (A7174, Millipore-Sigma, Burlington, MA), deionized (DI) water, and polystyrene microspheres (μ=0.99 mm, CV = 3%, 2.7% solids) (Cat# 07310-15, Polysciences Inc., Warrington, PA) to create 2% (w/v) agarose gels with different optical scattering coefficients (Table 3.3). Thermal camera experiments and optical property measurement required the creation of flat gel phantoms of known thickness that could be placed on a microscope slide for imaging. To repeatably generate these phantoms, molds were created using polydimethylsiloxane (PDMS) (Sylgard 184, Dow Inc., Midland, MI) using the process shown in Figure 3.1A. Samples used to measure optical properties required optically thin slabs, thus coverslips were glued together and placed on the bottom of a curing dish to create thin vacancies (~0.55 mm and ~0.88 mm thick stacks. PDMS (10:1 base:curing agent) was poured into the dish to completely immerse the coverslip stacks and allowed to cure at room temperature for 48 hours. Once cured, the PDMS was peeled from the dish, leaving vacancies in the PDMS in the shape of the coverslip stacks. These steps were also performed using two 1 mm thick microscope slides glued together to form a 2 mm thick vacancy to generate the samples for the thermal imaging validation. PDMS molds were turned upside down relative to their curing orientation (Figure 3.1B), and coverslips were laid across the flat surface over the vacancies. Hot agarose phantom mixture was then micro-pipetted into the mold, and the space under the coverslip was filled and allowed to set, resulting in agarose gels with repeatable thicknesses. The PDMS mold was then removed, leaving the gel in contact with the coverslip. This was then mounted on either another coverslip to form the optical property measurement sample (Figure 3.1B), or on a microscope slide to form the thermal imaging sample (Figure 3.4A).

3.3.4 Optical Property Determination

Optically thin optical property measurement samples were created from a portion of the agarose mixture from each phantom using the previously cured PDMS molds (in Figures 3.1A-B). Once cured, thin samples were sandwiched between two coverslips. Transmission measurements were performed to estimate the total attenuation coefficient of the samples using the setup shown in Figure 3.1C. An infrared laser (λ=1463 nm) was ported via an optical fiber (M18L01, Thorlabs Inc., Newton, NJ) to a collimation lens (F260APC-C, Thorlabs Inc., Newton, NJ). Collimated transmission through the optically thin samples (irradiant spot diameter ~ 3 mm) was measured using a sensor (PS19Q, Coherent Inc. , Santa Clara, CA) connected to a power meter (EPM 2000, Coherent Inc. (formerly Molectron), Santa Clara, CA) with an

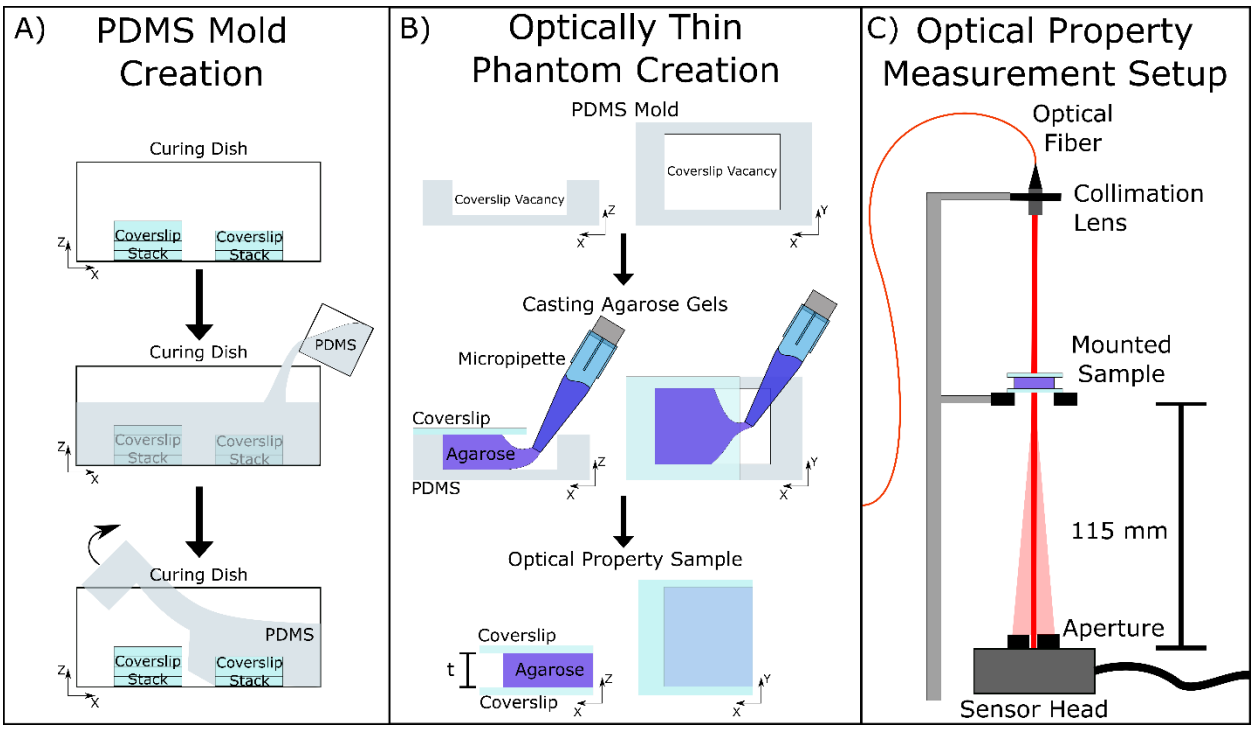

Figure 3.1. Phantom creation and characterization. A) Molds were created by curing PDMS around stacks of coverslips. Once cured, the PDMS was peeled away. B) To create optically thin slabs to measure the optical properties of agarose phantoms, coverslips placed over PDMS molds and hot liquid phantom mixture was injected via micropipette into the vacancy under the coverslip. The agarose was allowed to solidify and cool to room temperature prior to measurement. Gels were removed from the molds, but kept in contact with the coverslips, and a second coverslip was used to sandwich the agarose slab. C) Optical property samples were mounted on a holder beneath an irradiating laser.

aperture imposed (diameter ~ 7 mm) over the sensor to reject the majority of the forward scattered photons. Thus, by comparing the collimated transmission to the total power incident on the sample using a Beer's law approximation and accounting for reflections, the extinction coefficient can be calculated.

$$\frac{P_{col}}{P_0} = \exp(\mu_t\ t)\left(1 - R_{air-glass}\right)^2\left(1 - R_{glass-media}\right)^2 \qquad \text{Equation 3.2}$$

Where P_{col} is the power measured from the collimated transmission, P_0 is the total power incident on the sample, μ_t is the total attenuation coefficient [mm^{-1}], t is the thickness of the agarose slab, and R_{i-j} is the reflection at the interface between material i and material j:

$$R_{i-j} = \left(\frac{n_i - n_j}{n_i + n_j}\right)^2 \qquad \text{Equation 3.3}$$

Where n_i is the refractive index of material i and n_j is the refractive index of material j.

The absorption coefficient of water (the major chromophore in the gels) at λ = 1463 nm was fixed at μ_a = 2.75 mm^{-1} as determined by Hale and Querry 1973[16]. Thus, $\mu_s' = \mu_t - \mu_a$. Optical anisotropy was approximated using a Mie scattering simulation available through Virtual Photonics[40] from the Beckman Laser Institute, and inputting the particle distribution of polystyrene beads and the refractive indices of polystyrene[41,42] and agarose[43] (1.57 and 1.343, respectively). Resulting optical properties of each phantom can be found in Table 3.3.

3.3.5 Thermal Camera Validation Study

3.3.5.1 Experimental Measurements

Agarose gel slabs (n = 6 phantoms) (made using the process in Figure 3.4A) were mounted between a microscope slide and a coverslip and placed on a stage (MP100-RCH2 mounted on a PLS-XY, Thorlabs Inc., Newton, NJ) mounted below a thermal camera (FLIR A8313sc, FLIR Systems, Inc., Wilsonville, OR) with a 4x objective lens such that the camera focused on the gel through the coverslip (Figure 3.4B). A collimation lens (F260APC-1550, Thorlabs Inc., Newton, NJ) delivering collimated light from an IR laser (Innovative Photonic Solutions, Monmouth, NJ) via an optical fiber (M18L01, Thorlabs Inc., Newton, NJ) was positioned above the sample at a 50° angle so that it could irradiate the center of the top of the gel without being clipped by the objective lens. Thermal imaging was performed at 40 frames per second for

10 second trials where the first 2 seconds consisted of baseline temperature information prior to CW laser irradiation. Six trials were collected for each scattering phantom, and the next phantom. The light distribution at the sample was measured using a beam profiler (BP209-IR2, Thorlabs Inc., Newton, NJ).

3.3.5.2 *Simulations*

A 3D volume was generated in MATLAB using 0.02 mm voxels to mimic the experimental setup in which a 2mm thick agarose slab was sandwiched between a 0.2 mm thick coverslip and a 1 mm thick microscope slide. The length and width of these slabs were truncated to be 6 x 8 mm to reduce simulation time. The optical properties of silica glass used for the slide and coverslip and for the agarose phantoms can be found in Table 3.4. A patterned irradiation source was used to allow for applying a custom initial launch distribution of photons which utilized the previously measured spot distribution. For each simulation, a collimated beam of 100 million photons were launched at a 50^{o} angle relative to normal from the sample.

The computational geometry in COMSOL was created with the agarose slab (22 x 25 x 2 mm) sandwiched between a 0.2 mm and a 1 mm thick piece of Corning 7940 (fused silica) of the same length and width (material properties in Table 3.4). A Dirichlet boundary condition (T = 20^{o}C) was used for all side and bottom boundaries. A heat flux condition was defined for the top boundary (coefficient of convection = 50 W/(m^2 K))[44]. At t = 0 seconds a heat source (Equation 3.1) was applied using (dh = 0.02 mm) and AveragePower = 63 mW. A cylindrical region (r = 3.5 mm) in the center of the geometry was created for mesh control to apply very fine meshing where the temperature rise was applied, and large mesh elements were used outside of the cylinder where a lower sampling density was acceptable. A time-dependent study was run for 8 seconds in 0.1 s steps.

3.3.5.3 Data Analysis

Thermal imaging sequences were directly exported to MATLAB using the MATLAB-FLIR SDK[45]. The time at which the laser turned on was extracted from each trial by identifying the first frame containing a temperature rise. Images were background subtracted using the mean of the first 25 images (prior to irradiation) to generate a temperature rise image sequence. The maximum temperature rise over time was tracked for all trials. Spatial information about the temperature distribution was extracted by thresholding the image. Since the collimation lens was angled (Figure 3.4B) this resulted in an elliptical spot on the phantom, creating an elliptical temperature distribution at the surface. Ideally, the 1/e drop in the temperature rise or the full width at half maximum of the temperature distribution along the major and minor axes of this ellipse would be quantified since these are common metrics to quantify spatial distributions, however, the field of view (FOV) of the camera was too small to capture the full temperature

Table 3.4. Optical and thermal properties of simulated materials

Material	Refractive Index	Absorption [mm^{-1}]	Scattering [mm^{-1}]	Anisotropy	Thermal Conductivity @ 300 K [W/m/K]	Density @ 300 K [kg/m^3]	Heat Capacity @ 300 K [J/kg/K]
Agarose[43,46]	1.343	2.75	Sample Specific (Table 3.3)	0.776	0.6	1010	4180
Glass (Corning 7940 (fused silica))	1.445[47,48]	1e-4	1e-11	0	1.381	2220	716
Nerve[49]	1.4	2.0, 2.5, 3.0, 3.5	0 – 1.5	0.7	0.49	1075	3643

distribution. It was found that the contour formed at 75% of the maximum temperature rise was entirely contained within the FOV for all time points. A mask was created for each frame by thresholding based on 75% of the maximum temperature rise in the frame to form this 75% rise ellipse. The mask was then assessed using the "regionprops" function in MATLAB to calculate the major and minor axes of the ellipse after rejection of any noisy pixels outside of the ellipse. For each of the three metrics, trials (6 trials per phantom) were aligned in time relative to the laser on time and the mean +/- standard deviation of each metric was calculated over the 8 seconds of heating.

For simulated temperature distributions, all data were exported from COMSOL to text files and imported into MATLAB for analysis. Distributions were interpolated to achieve regular sampling of 0.02 mm over a depth of 0.26 (full X and Y dimensions) to include heating contributions sensed by the camera from the coverslip and the first 0.06 mm of agarose (the approximate penetration depth of thermal imaging a water-rich sample[16]). This volume was then averaged in depth to recreate the information captured through thermal imaging of the phantoms. These 2-dimensional distributions were then analyzed in the same manner as the thermal images to calculate the maximum temperature rise and the lengths of the major and minor axes of the 75% temperature rise ellipse.

Linear regression was performed to assess the trends in the characteristics of heating as a function of scattering. Slopes of the best fit lines for both measured and simulated results were compared to flat line to determine if optical scattering influences the calculated metrics.

3.3.6 Thermocouple Validation Study

3.3.6.1 *Experimental Measurements*

Inside of plastic wells (Catalog # 140675, Thermo Fisher Scientific Inc., Waltham, MA), a cleaved and polished 400 μm diameter optical fiber (P400-2-VIS-NIR, Ocean Optics Inc., Largo FL) was placed orthogonal to, just out of contact with, and centered on a 80 μm diameter bare wire junction thermocouple (time constant < 0.1 s) (Item # 5TC-TT-EI-40-2M, Omega Engineering Inc., Norwalk, CT), both held on micromanipulators (Kite Manual Micromanipulator, World Precision Instruments, Sarasota, FL). The optical fiber was then translated backwards along the z-axis either 0, 0.5, 1.0, or 2.0 mm from the TC. Once placed, agarose mixture (n = 3 phantom mixtures) was poured into the well so that the setup was completely immersed with at least 5 mm of agarose above the fiber output (Figure 3.5A). The agarose was left to cure and drop to room temperature (~ 20 ^{o}C) prior to experiment trials. The TC was connected to a thermocouple data acquisition system with cold-junction compensation (DI-245, Dataq Instruments Inc., Akron, OH), which allowed for temperature sampling at 200 Hz. Five trials, each 60 seconds in duration, were recorded

for each TC placement. Laser irradiation was applied from at t=5 seconds to provide an initial baseline phase. To limit the computation time needed for simulations, a practical steady state was defined as the temperature changing by less than or equal to 1% per second which was noted at ~30 seconds after irradiation was initiated.

3.3.6.2 *Simulations*

Optical-thermal simulations were performed similar to the thermal imaging study, but with geometries appropriate to mimic the TC setup. Monte Carlo simulations used a 4 x 4 x 4 mm homogeneous geometry with 0.01 mm voxels. A 0.4 mm diameter cylinder representing the optical fiber was placed in the center of the X-Y plane which extended from Z = 0 mm to a depth of 1 mm. A uniform disk source was placed at the tip of this cylinder, which diverged at 9.43^{o} (0.22 NA fiber in agarose).

COMSOL simulations created a single block representing agarose. A cylinder (radius = 0.2 mm) representing the optical fiber was placed inside the block extending from the top surface to 1 mm into the geometry at the center of the X-Y plane. Planes of symmetry at X = 0 and Y = 0 were utilized to reduce computation time, and the geometry was quartered so that only the region of X > 0 and Y > 0 were kept. At the output of the fiber, two blocks were created for fine and ultrafine mesh control (2 x 2 x 2 mm and 0.5 x 0.5 x 0.6 mm). Material properties are defined in Table 3.4. Symmetric boundary conditions were applied to all boundaries along the planes of symmetry at X = 0 and Y = 0 ($dT/dX = 0$ and $dT/dY = 0$, respectively). A Dirichlet boundary condition (T = 20^{o}C) was used for all side and bottom boundaries. Thermal insulation was applied at the top boundary. Simulations of 35 seconds in duration with 0.05 second timesteps were run with an initial temperature of 20^{o}C. A heat source guided by the distribution of absorbed photons from the Monte Carlo simulation was initiated at t=0.

3.3.6.3 Data Analysis

Times at which the laser turned on were first identified for each heating trial based on when the temperature rise first began. The 0.5 seconds prior to irradiation were averaged to determine the baseline temperature for the trial. All trials for a TC placement were temporally aligned at the laser on time (t = 0 s) and averaged together. Average temperatures at 30 seconds of heating were then assessed as a function of distance from the optical fiber across scattering phantoms. At each depth, an analysis of variance (ANOVA) was performed to assess if the temperature in the three phantoms were statistically significant. For each simulation, the temperature with depth from the optical fiber was exported to compare to the TC measurements.

3.3.7 Optical Property Parametric Sweep

Validation studies served to demonstrate that the optical-thermal model was capable of predicting the temperature distributions in laser-irradiated tissue phantoms; however, a clear picture of the intricate role of optical scattering was still lacking. Therefore, a simplified setup representing irradiating a semi-infinite volume of neural tissue with an optical fiber just out of contact with the tissue was created to assess how laser heating is affected by optical properties. The absorption coefficient was chosen based on values of water absorption at INI wavelengths available in the literature[16]. The reduced scattering coefficients were varied over the theoretical limits of μ_s' calculated in Table 3.2.

Monte Carlo simulations utilized a homogeneous medium of 200 x 200 x 300 voxels (X x Y x Z) with dh = 0.01 mm spatial step size (2 x 2 x 3 mm total size) was used with a refractive index of n=1.4[36]. A uniformly emitting source in the shape of a 400 μm diameter disk was placed in the X-Y plane at the top of the medium, centered at X=Y=0 to mimic an irradiating 0.22 NA (in air) optical fiber at the top of the geometry. This disk source emitted 50 million photons into the medium with a divergence angle of ~9.1°. Monte Carlo trials were performed for all combinations of μ_a = 2.0, 2.5, 3.0, 3.5 mm^{-1} and μ_s' = 0 – 1.5 mm^{-1} (in 0.1 mm^{-1} steps) with g = 0.7. Changes in the distributions were quantified using the optical penetration depth (the 1/e drop in fluence rate from the surface) and by assessing how many photons were absorbed inside versus outside the diverging NA of the optical fiber.

A cubic volume (20 x 20 x 20 mm) was created in COMSOL that was large enough so that the thermal boundaries did not affect the temperature distribution. One corner (X = Y = Z = 0) was designated as the center of the irradiated zone so that symmetric boundary conditions could be applied at the planes X = 0 and Y = 0. All other side and bottom thermal boundaries applied a Dirichlet boundary condition (T = 20°C), and the top boundary applied convective cooling (h = 10 W/m/K). A block (0.5 x 0.5 x 1 mm) was defined to provide extra fine meshing where the heat source term from the Monte Carlo simulation was applied. Around this block, another block (3 x 3 x 3 mm) was defined to ease the mesh transition from extra fine in the heated region to coarse in the rest of the medium. Material properties for the neural tissue are found in Table 3.4. Values of 10 mW and 0.01 mm were used for Equation 3.1. A stationary simulation was performed which simulated the steady state temperature distribution resulting from laser irradiation.

Resulting temperature distributions were exported to MATLAB and assessed for changes in temperature rise and spatial extent of heating by comparing (1) the maximum temperature rise, (2) the thermal penetration depth at the center, defined as the depth at which the temperature rise drops by 1/e of the maximum temperature rise, and (3) the full width at half maximum (FWHM) of temperature rise at the surface of the geometry.

3.3.8 Water Bath Scattering Trend Validation

To provide one more method of validation of the trend between the temperature distribution and optical scattering, a third setup was created by thermally imaging laser heating in a water bath through a glass coverslip (Figure 3.3). One of the difficulties of performing thermal measurements of tissue heating is obtaining spatial information at a depth, especially when high spatial resolution is needed due to the small scale of optical fiber-based heating. Lothet *et al.* developed a method to probe the heating from an optical fiber at a depth using a thermal camera and placing the optical fiber so that its output was bisected by a water-window interface[11]. Scattering phantoms were created using deionized water mixed with suspended polystyrene beads as a scattering agent, thus a different method of optical property determination was needed to accommodate the liquid phantoms.

3.3.8.1 Phantom Creation

Target optical properties were chosen to fall within the theoretical bounds of μ_s' (Table 3.2). A Mie scattering simulator[24,40] was used to simulate the reduced scattering coefficient using a polydisperse distribution of particle sizes based on the PS particle distribution provided by the supplier (mean diameter = 0.96 μm, coefficient of variance=0.08 μm, percent solid= 2.6%). The concentration of beads was then changed in the simulator to achieve μ_s'= 0, 0.1, 0.2, 0.6, 1, 1.4 mm^{-1}. Thin cuvettes were made by super gluing two coverslips between two glass microscope slides, leaving ~0.19-0.26 mm air gap in the middle of each cuvette (Figure 3.2A). The thickness of each gap was calculated by subtracting the caliper measured thickness of each individual slide from the total measured thickness of the cuvette. Stock PS mixture was diluted to the identified concentrations and pipetted into the cuvettes (n = 4 slides per μ_s'). The transmitted power through each filled cuvette was measured with a power sensor (PS19Q; Coherent Inc., Santa Clara, CA) using the setup in Figure 3.2B where 1875 nm light (Capella Neurostimulator; Lockheed Martin, Bethesda, MD) delivered via an optical fiber was collimated and incident on the face of the filled cuvette. Using Beer's law, the loss due to absorption and scattering, μ_t, was calculated. A linear fit was applied, and μ_a was identified as the y-intercept of this fit. Subtracting μ_a from μ_t yielded the μ_s' for each concentration of polystyrene beads (Figure 3.2C).

3.3.8.2 Experimental Measurements

A setup was created using a plastic 12 cylindrical well plate which was cut in half along a row of the wells, and a glass coverslip was glued to the cut face of one of the wells (Figure 3.3). The half well was filled to the top of the coverslip with polystyrene bead mixtures. A thermal camera (A8303sc, FLIR Systems, Inc., Wilsonville, OR), imaged the bead mixture through the glass window. An optical fiber was placed 0.2 mm

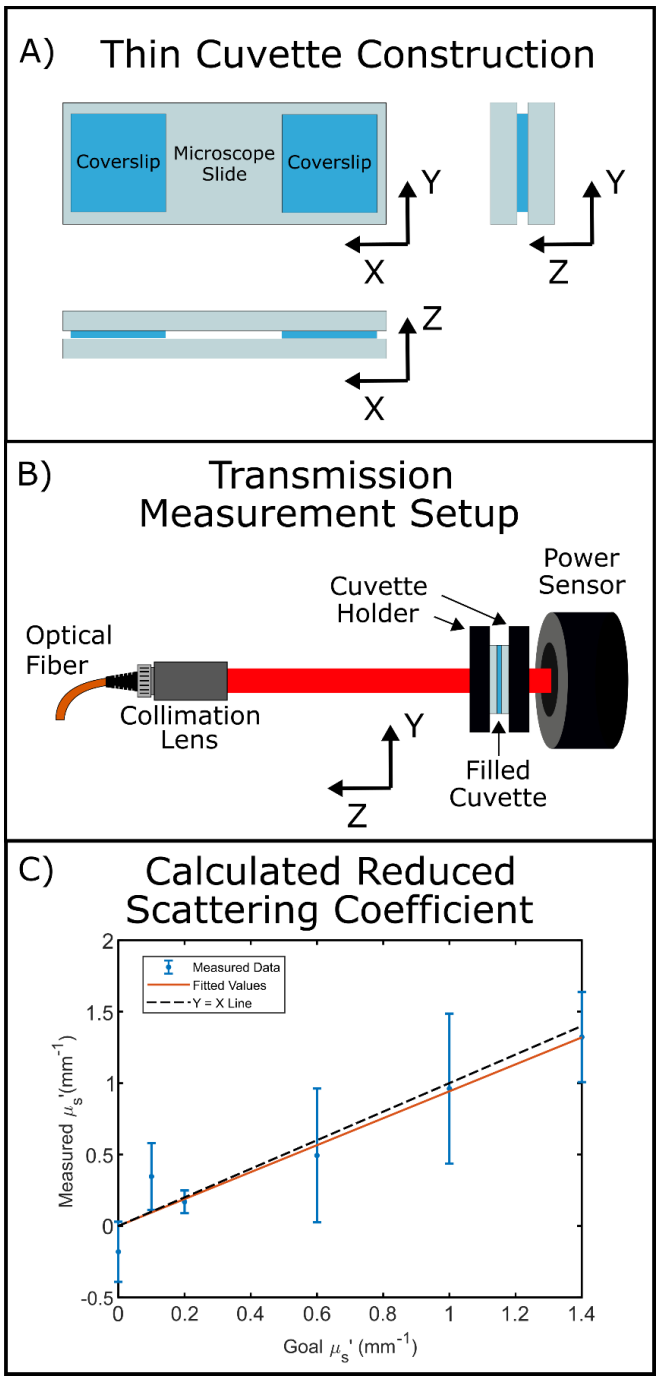

Figure 3.2. A) Thin cuvette construction. Two coverslips were glued between two microscope slides as spacers leaving the center of the slides open for sample insertion. Polystyrene mixtures were then pipetted into the cuvette. B) A collimated beam of 1875 nm light was incident on the face of each slide and transmission measurements were made using a power meter placed immediately behind each cuvette, n=4 cuvettes per phantom. C) Reduced scattering coefficients were determined for each phantom. Total attenuation coefficients, μ_t, for each cuvette were calculated and averaged across trials. A line was fit to data and the y-intercept was determined to be the absorption coefficient, μ_a, which was then subtracted from μ_t to determine μ_s'.

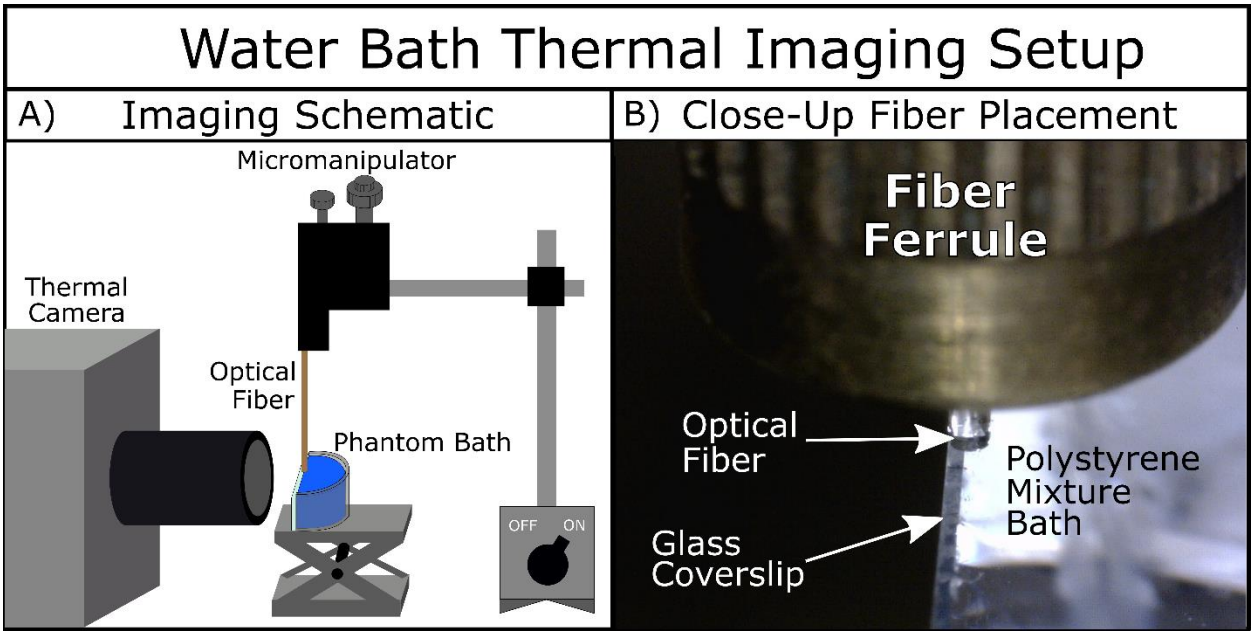

Figure 3.3. A) Temperature measurements were performed on polystyrene bead mixtures with various amounts of optical scattering using the shown schematic. The half-well was placed on a stage and a mounted micromanipulator was used to place a 400 μm core diameter optical fiber half over the bath and half over the coverslip. A thermal camera was used to image laser heating through the coverslip window. B) A close-up view of the optical fiber placed over the bath.

above the coverslip using a micromanipulator such that the glass-PS mixture interface bisected the output of the fiber (Figure 3.3B). Placement was aided by both the thermal camera and a separate digital microscope camera which was focused on the tip of the optical fiber. Once the fiber was placed, it was not moved for the rest of the experiment to maintain the same sectioning of the light distribution across all bead mixtures. Bead mixtures were added and removed from the half cylindrical well using a dropper, and the well was rinsed multiple times with DI water between every bead mixture. For each trial, thermal imaging captured 18 second recordings at 15 frames per second. Laser irradiation (24.2 mW, 0.2 ms pulses at 200Hz) from an IR laser (λ= 1875, Capella Neurostimulator, Aculight-LockheedMartin) was triggered 2-3 seconds into each trial. Five trials were recorded for each PS bead mixture.

3.4 Results

3.4.1 Thermal Camera Measurements

Thermal imaging of laser heating in agar gels was able to interrogate surface information of the temperature distribution as a function of optical scattering. Temperature distributions were assessed for the maximum temperature and for spatial information which was calculated by thresholding the measured and simulated images based on 75% of the maximum temperature rise in the image. The major and minor axes of the ellipse formed by this threshold value were then calculated to inform on the size of the temperature distribution. Figure 3.4C shows the response of these three quantified characteristics: the maximum temperature rise (Figure 3.4Ci), the major axis of the 75% temperature rise ellipse (Figure 3.4Cii), and the minor axis of the 75% temperature rise ellipse (Figure 3.4Ciii). Simulated and measured temporal responses of these three characteristics are plotted in Figure 3.4C, left column, and different scattering phantoms are color-coded. The values at 8 seconds of heating for these data are plotted as a function of the reduced scattering coefficient in Figure 3.4C, right column. Simulated results on average fall within ~5 % of the measured values (< 5.2%, < 11.8%, and < 2.8% error for the maximum temperature rise, major axis, and minor axis, respectively). Linear regression was performed on the simulated and measured results as a function of μ_s', and the slope of the regression lines were tested for a significant difference from a flat line. One fit, the simulated trend of the maximum temperature with scattering, demonstrated a 95% confidence interval of the fitted slope coefficient that did not include a slope of 0, meaning that the maximum temperature demonstrates a significant positive trend with increased scattering. For all other fits, both

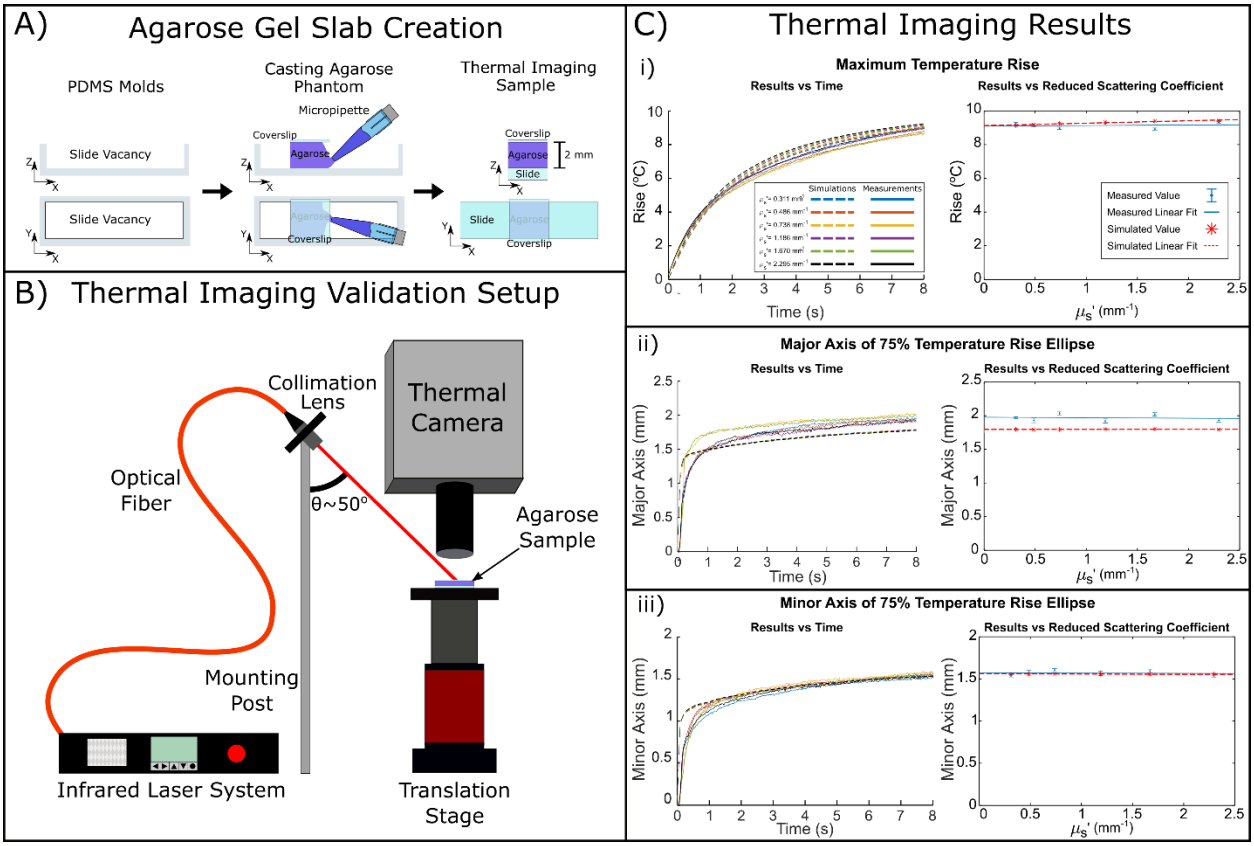

Figure 3.4. Thermal camera validation study. A) A method similar to that shown in Figure 3.1 A-B was used to make agarose phantoms for the thermal camera validation dataset. PDMS molds were made with a stack of 2 microscope slide. Final molds had a coverslip placed to span the formed vacancy, and a micropipette was used to fill the vacancy with agar solution. Once set and cooled, the agar and coverslip were peeled away from the PDMS and placed in contact with a microscope slide to form the phantom. B) Phantoms were mounted on a motorized stage (coverslip on top) underneath a thermal camera. A collimation lens was mounted on a post next to the sample at an angle of 50° so that the phantom could be irradiated without clipping the beam on the camera's objective lens. An optical fiber connected to the collimation lens delivered light from an infrared laser (λ= 1463, continuous wave). C) Thermal imaging results. From thermal image sequences, the maximum temperature rise (i), major axis of the 75% rise ellipse (ii), and minor axis of the 75% rise ellipse (iii) were quantified. Average temporal responses are plotted on the left for simulated (dashed) and measured (solid) results. Characteristics at 8 seconds are plotted as a function of μ_s' on the right for the simulated (red) and measured (blue) result.

simulated and measured, a zero slope fell within the 95% confidence interval of the fitted coefficient, demonstrating that there is no significant trend between these surface metrics and optical scatting. Since this includes the measured temperature rise, it is likely that experimental variability masked the true trend between scattering and temperature.

3.4.2 Thermocouple Results

A thermocouple was used to measure the temperature at various depths from an irradiating optical fiber in agarose phantoms with different amounts of optical scattering (Figure 3.5A). Note that all measured temperatures are plotted at the depth from the fiber plus the radius of the TC (0.04 mm). It was discovered that fluctuations in laser output over different days resulted in different power levels for the same laser settings (26.4 mW for $\mu_s' = 0.346$ mm^{-1}, 24.2 mW for $\mu_s' = 0.507$ mm^{-1}, 24.6 mW for $\mu_s' = 1.288$ mm^{-1}), therefore, results were normalized to the temperatures sensed when the TC was just out of contact with the fiber (z = 0.04 mm) to overcome this variation. These normalized results for both the simulated and measured depth distributions are plotted in Figure 3.5B. These results show that higher μ_s' results in a greater drop-off of the temperature with depth (i.e. higher spatial thermal gradient) since the temperature rise values at z = 0.54 mm follows a decreasing trend with increased optical scattering (decrease by 15.5% from 0.346 – 1.288 mm^{-1}). The temperatures at this depth were shown to be significantly different using a one-way ANOVA and multiple comparisons test ($p<0.05$). Simulated results (dashed lines) also exhibit a greater thermal gradient with increased scattering, predicting a 12.8% decrease in the temperature rise at z = 0.54 mm between $\mu_s' = 0.346$ and 1.288 mm^{-1}. At greater depths, the differences in temperature between scattering phantoms is lost in the variability of the setup.

To overcome the power fluctuations in the experimental setup, an idealized set of simulations with the same average power across simulations was used to compare how optical scattering affects the temperature rise amplitudes instead of the relative values. Results from simulations run with 22 mW average power are plotted in Figure 3.5C. This analysis demonstrates that the maximum temperature rise increases slightly with greater μ_s' (0.2^{o}C from $\mu_s' = 0.346$ to 1.288 mm^{-1}), as well as this maximum temperature occurs shallower (0.02 mm shallower over $\mu_s' = 0.346$ to 1.288 mm^{-1}). Despite this greater maximum temperature, a faster drop off (higher spatial thermal gradient) occurs at greater depths with higher scattering, corresponding to a reduced 1/e thermal penetration depth (0.86, 0.835, and 0.76 mm for $\mu_s' = 0.346$, 0.507, and 1.288 mm^{-1}, respectively).

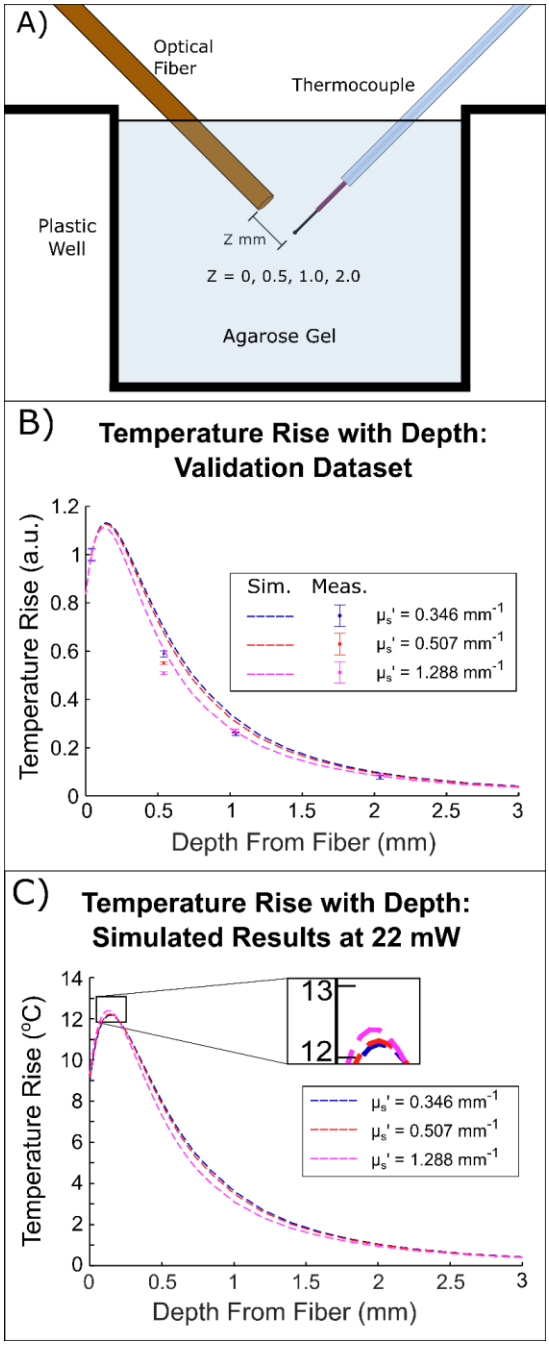

Figure 3.5. Thermocouple validation. A) Experimental setup. In a well, an optical fiber and thermocouple were placed using micromanipulators. The optical fiber was initially placed just in contact and centered with the thermocouple (aided by the pilot light). The thermocouple was then translated either 0, 0.5, 1.0, or 2.0 mm backwards (the z direction)). The well was then filled with agarose which was allowed to set. B) Validation dataset. Measured temperatures are plotted over depth along with the simulated depth distributions using the measured laser powers for each experiment. Data were normalized to the temperatures at z = 0.04 mm. C) Idealized results. Simulated temperatures using a consistent 22mW average power (CW) for different μ_s' values are plotted over depth at the center of the fiber.

3.4.3 Parametric Sweep Results

3.4.3.1 Optical Distribution Dependence on Scattering

Monte Carlo simulations were performed across a range of physiologically expected absorption and reduced scattering coefficients. Figure 3.6A shows slices taken at Y=0 in the X-Z plane of the resulting absorption distributions, shown on the same color scale. The values in these maps can be interpreted as the probability of any photon being absorbed in a given voxel, and this map can be multiplied by laser power to give the distribution of absorbed power. Only $\mu_s' = 0$, 0.7, and 1.5 mm^{-1} are shown for clarity, however, a more complete data set can be seen in Figure 3.7 where the reduced scattering coefficient is shown in steps of 0.2 mm^{-1}. The most noticeable difference in these maps is that the maximum value of the color scale increases with increased scattering, representing an increase in the maximum number of absorbed photons in a single voxel which ultimately corresponds to a larger heat source term. This same trend is seen as μ_a increases, which would be expected since, as per definition of the property, more photons are absorbed. The 1/e penetration depth is seen to be inversely proportional to both μ_a and μ_s' increase. This is difficult to visualize on the distribution images but has been quantified in Figure 3.6B. Changes in the penetration depth with μ_s' were on the order of the Monte Carlo spatial step size, resulting in the stepwise nature of the data points (dots) since the penetration depth was calculated using these discrete grid locations. This is overcome by applying an exponential fit to the data (lines). Most of the absorbed photons are confined within the divergence angle of light emitted from fiber (dictated by the NA), however, this decreases as μ_s' increases (Figure 3.6C) due to radial scattering of photons from underneath the fiber outward. The location of where this scattered light is absorbed can be more easily visualized through difference maps (Figure 3.8) which were created by taking the difference between the absorbed photon distribution at a particular μ_s' value and subtracting the distribution at $\mu_s' = 0$ mm^{-1} for the corresponding μ_a value. Therefore, each map for $\mu_s' = 0$ mm^{-1} has a value of 0 everywhere since that absorption map was subtracted from itself. These maps show that at higher μ_s', photons are more likely to be absorbed superficially in the tissue and outside the NA of the fiber (at a depth within a few hundred μm from the surface). The tradeoff of this is shown by the dark blue regions within 0.5 mm of the surface just inside of the fiber's NA where fewer photons are absorbed. While photon absorption distributions are informative of where heat is initially generated, it is ultimately the temperature distribution that guides the heat block effect of INI; thus, thermal simulations will help elucidate to what extent these differences in the light distribution translate to changes in the temperature distributions.

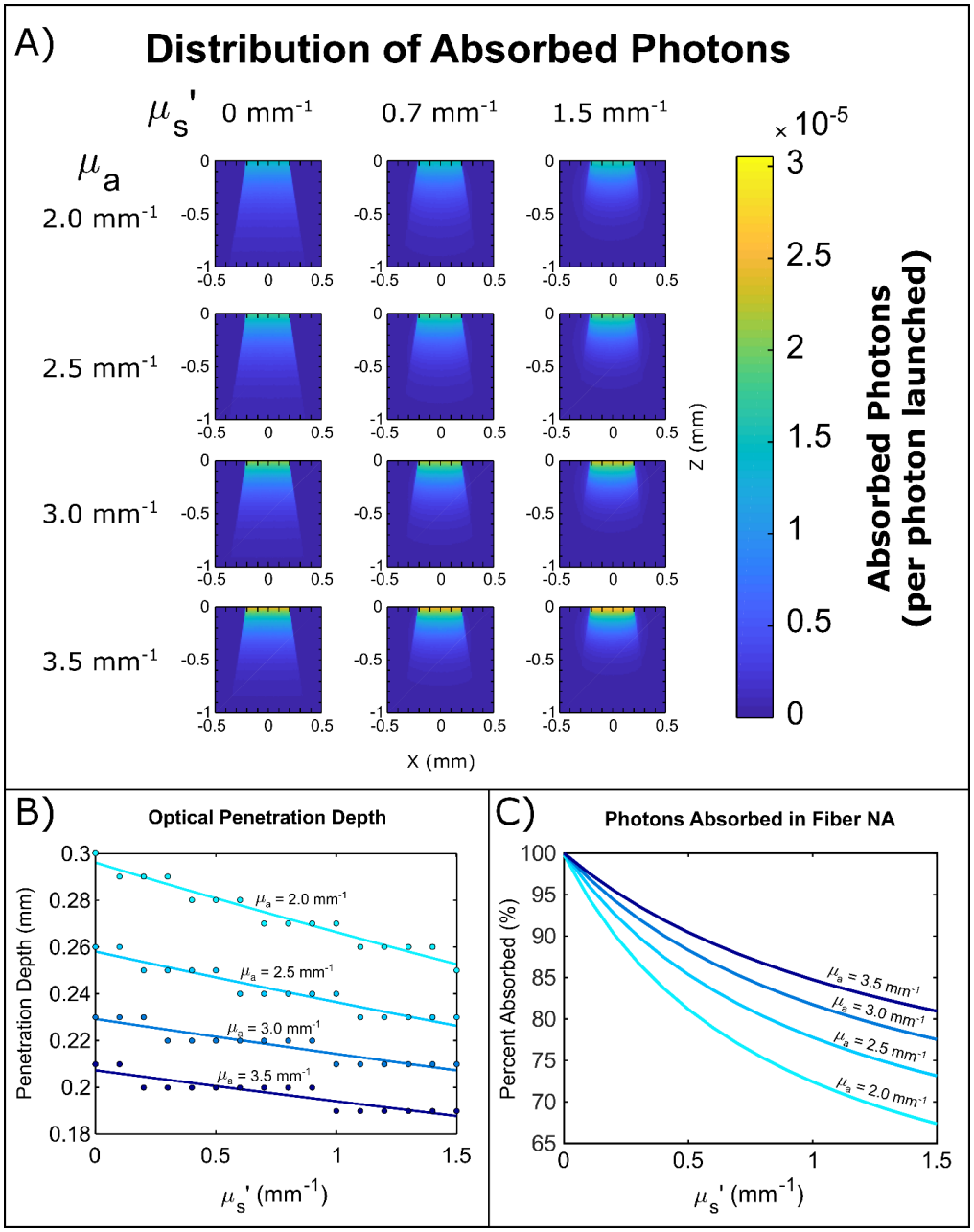

Figure 3.6. Parametric sweep optical results. A) Representative absorbed photon distributions from Monte Carlo simulations across SWIR tissue absorption and scattering coefficients. All images are taken from the X-Z plane at Y=0, and are plotted on the same color scale. Values correspond to the probability of a photon being absorbed in each voxel. A more complete set of light distributions can be found in Figure 3.7. B) Optical penetration depth at the center of the absorbed photon distributions is plotted over scattering for different absorption coefficients. Some scattering induced changes occurred on a scale smaller than the spatial step size of the Monte Carlo (0.01 mm), so an exponential was fit to each dataset. C) The percent of total photons launched that are absorbed within the diverging NA of the fiber is plotted as a function of scattering.

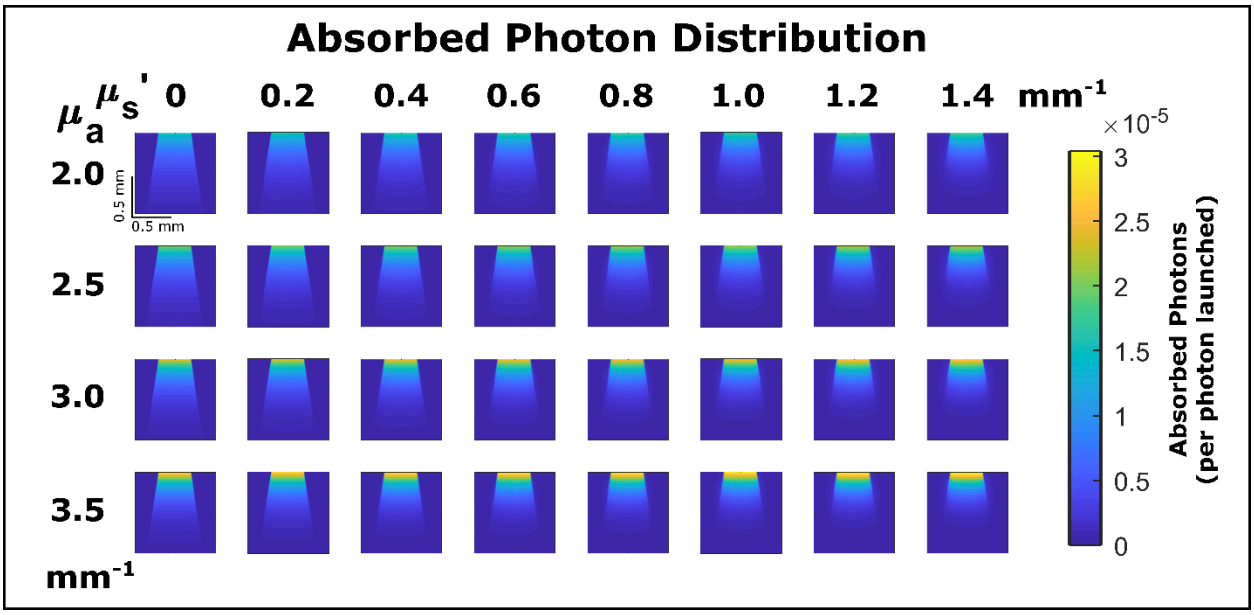

Figure 3.7. Absorbed photon distributions in the X-Z plane at Y=0 from the Monte Carlo simulations are shown in 0.2 mm^{-1} steps of μ_s' for all values of μ_a used in the parametric sweep. All images are plotted on the same color scale. Color represents the probability that a photon is absorbed in a voxel. Each image is 1 mm x 1 mm with the shown 0.5 mm scale bars.

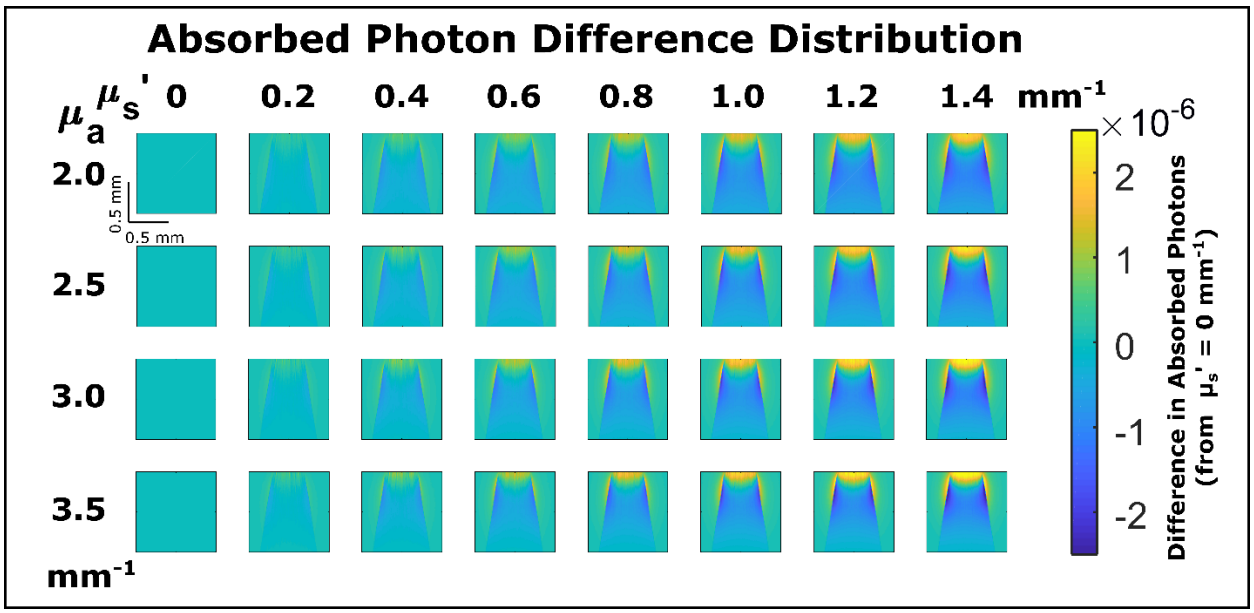

Figure 3.8. Absorbed photon difference maps are shown for the X-Z plane at Y=0. These maps represent the change in the absorbed photon distribution simulated at the shown μ_s' compared to μ_s'=0 mm^{-1} for each μ_a in Figure 3.7. Thus, the difference map at μ_s' for each μ_a is zero everywhere since that image is subtracted from itself. All images are plotted on the same color scale where a positive value designates an increase in absorbed photons over the μ_s'=0 mm^{-1} distribution. Color represents the probability that a photon is absorbed in a voxel. Each image is 1 mm x 1 mm with the shown 0.5 mm scale bars.

3.4.3.2 Temperature Distribution Trends with μ_a and μ_s'

Steady state temperature maps were generated for all sets of optical properties. For each map, three characteristics were calculated: (1) maximum temperature rise, (2) 1/e thermal penetration depth, and (3) FWHM at the surface. Figure 3.9A shows the temperature maps in the Y=0 plane at the extreme values of μ_a and μ_s' simulated. Each distribution is set to the same color scale. The FWHM at the surface is highlighted with the black bar above each distribution and the contour of the 1/e drop from the maximum temperature rise is outlined in black. A more complete set of temperature distributions can be seen in Figure 3.10. These correspond to the temperatures induced by the absorption distributions in Figure 3.7. The maximum temperature rise above 20^{o}C of each distribution and the percent change in maximum temperature rise compared to μ_s' = 0 mm^{-1} are shown in Figure 3.9B. As would be expected, the induced temperature rise increases with increased optical absorption (shades of blue). This was observed to be ~32.4% increase from μ_a = 2.0 mm^{-1} to μ_a = 3.5 mm^{-1}. It is also seen that the maximum temperature increases with increased optical scattering and that the effect of scattering is diminished at higher absorption coefficients. An increase by ~7 % was observed over the 1.5 mm^{-1} range of μ_s' at μ_a = 2.0 mm^{-1}, while this was ~ 4.5 % increase at μ_a = 3.5 mm^{-1}. Trends in the thermal penetration depth (the 1/e drop in maximum temperature rise at the center of the fiber) were also quantified (Figure 3.9C). The thermal penetration depth was observed to decrease with both increasing absorption and increasing scattering. With no scattering, an increase in μ_a from 2.0 mm^{-1} to 3.5 mm^{-1} decreases the thermal penetration depth by 28.9%. An increase in μ_s' from 0 mm^{-1} to 1.5 mm^{-1} resulted in a ~21 % decrease when μ_a = 2.0 mm^{-1}, and a ~ 15 % decrease when μ_a = 3.5 mm^{-1}. The FWHM was quantified (data not shown), however it was observed that changes were less than 1.5% over 1.5 mm^{-1} range of μ_s' for all μ_a. At μ_s' = 0 mm^{-1}, the FWHM decreased by 13% from μ_a = 2.0 mm^{-1} to 3.5 mm^{-1}.

3.4.4 Water Bath Results

A set of measurements was made by thermally imaging a water bath with PS beads added as a scattering agent to validate the predicted trends from the parametric sweep. This validation was not meant to mimic the setup used in the simulations, but to probe if changing the scattering resulted in the same predicted changes in the maximum temperature rise, the 1/e thermal penetration depth, and the surface FWHM. Figure 3.11 shows how the metrics quantified from the measured temperature distributions vary over time and as a function of scattering. Results show that the maximum temperature rise increases with an increasing reduced scattering coefficient (Figure 3.11A), validating the predictions of the optical-thermal model in Figures 3.4, 3.5, and 3.9. Over the range of μ_s' tested, an increase of ~2 ^{o}C from the highest to

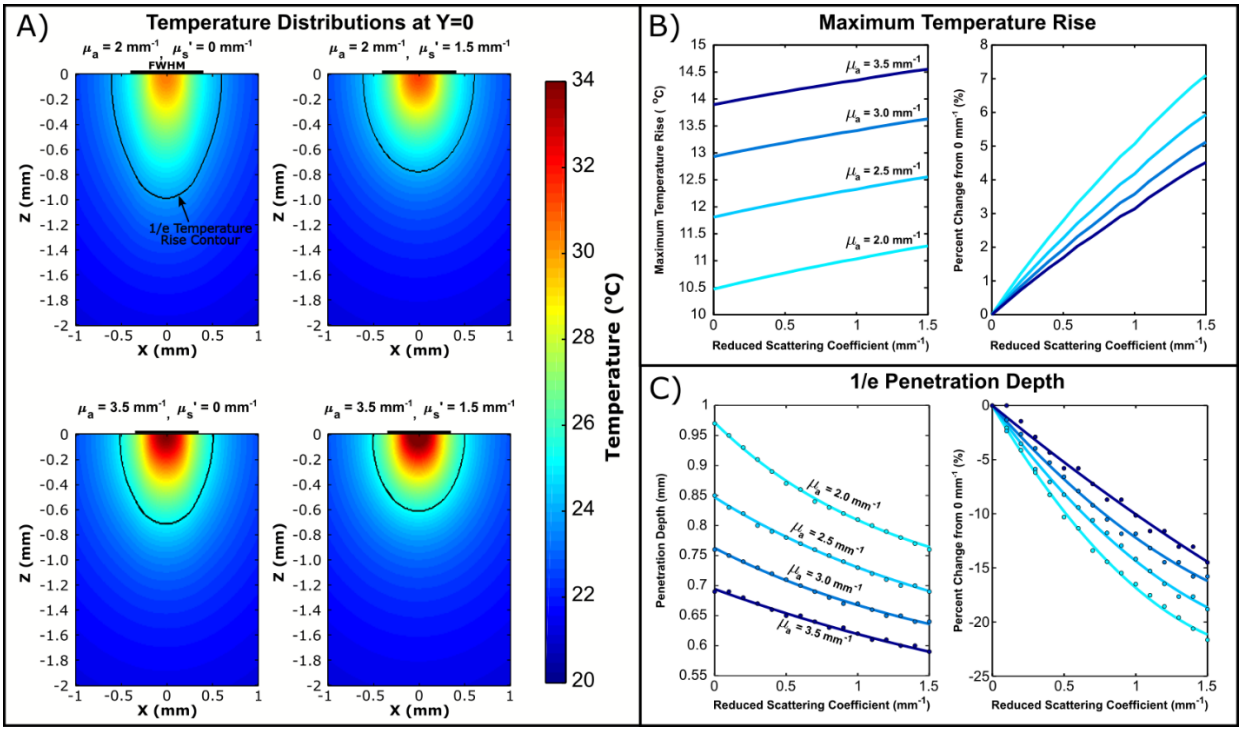

Figure 3.9. A) Simulated temperature distributions taken from the X-Z plane at Y=0 are shown for the extreme values of μ_a and μ_s' assessed. All distributions are plotted on the same temperature color scale. The FWHM at the surface is highlighted by the black bar above the image, and the contour showing the 1/e drop in maximum temperature rise is outlined in black which highlights how the thermal penetration depth decreases as μ_a and μ_s' increase. A more complete set of distributions can be found in Figure 3.10. B) The maximum temperature rise is plotted over μ_s' for different μ_a (left) and the percent change from $\mu_s' = 0$ mm^{-1} is shown (right) demonstrating an increasing trend with scattering that is more pronounced at lower μ_a. C) The thermal penetration depth is plotted over μ_s' for different μ_a (left) and the percent change from $\mu_s' = 0$ mm^{-1} is shown (right) demonstrating a decreasing trend with scattering that is more pronounced at lower μ_a. Some changes were smaller than the spatial scale of the interpolation (0.01 mm), so exponential curves were fit to the data to show the trends.

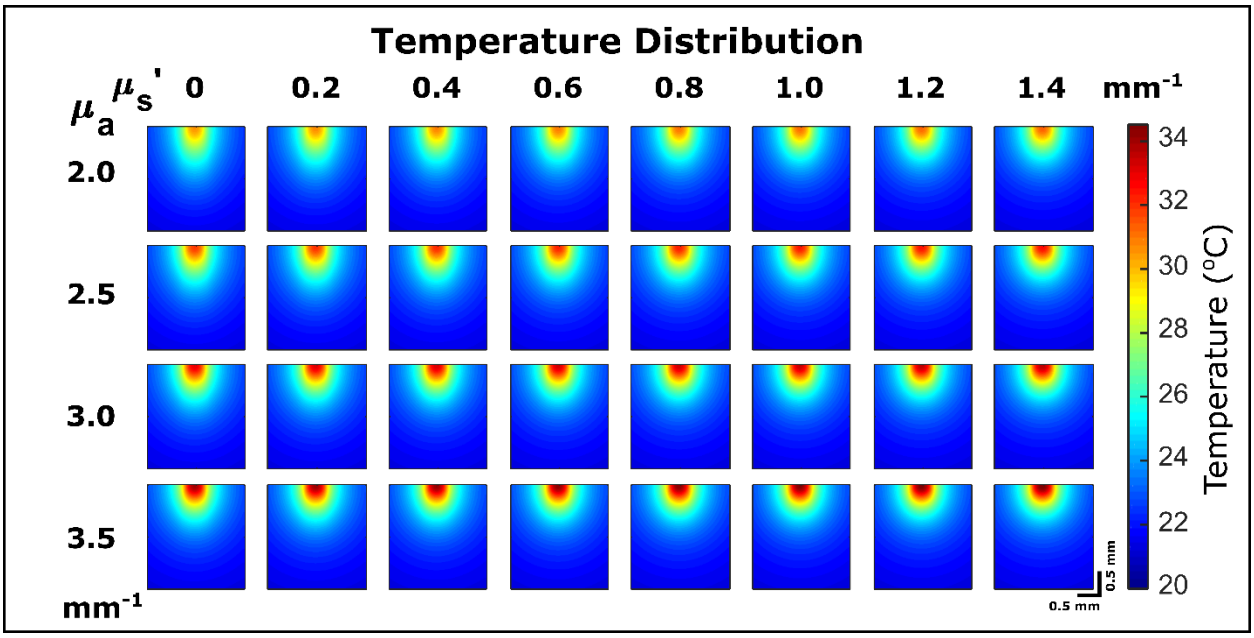

Figure 3.10. Simulated temperature distributions taken from the X-Z plane at Y=0 are shown in μ_s' steps of 0.2 mm^{-1} for all values of μ_a. All distributions are plotted on the same temperature color scale. Each image is 2 mm x 2 mm with the shown 0.5 mm scale bars. Laser heating is shown to increase with both increasing μ_a and μ_s'.

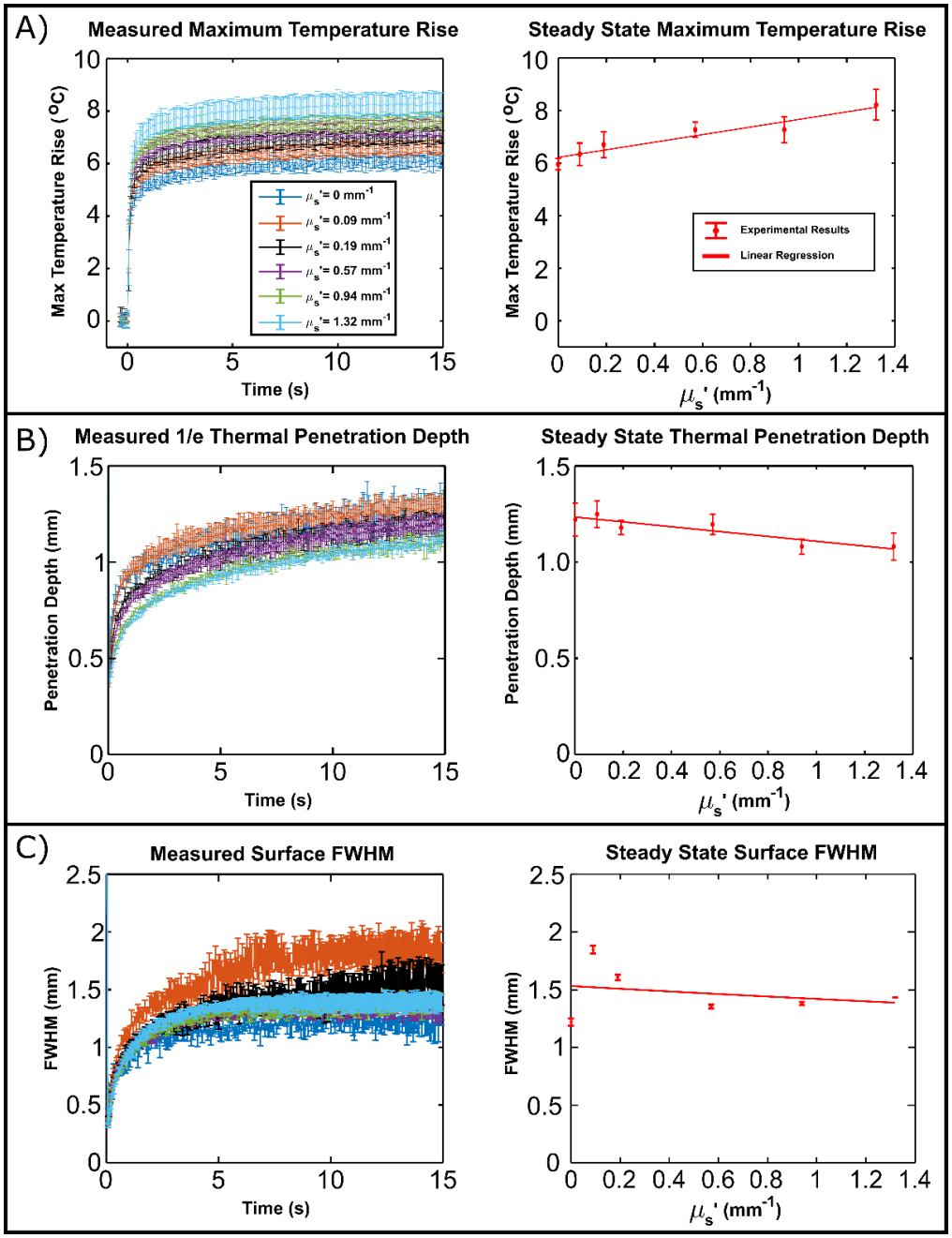

Figure 3.11. Left column) The maximum temperature rise (A), 1/e thermal penetration depth (B), and full width at half maximum at the surface (C) are plotted (mean +/- standard deviation) over time for different scattering phantoms (μ_s' = 0 (blue), 0.09 (orange), 0.19 (black), 0.57 (purple), 0.94 (green), and 1.32 (cyan) mm^{-1}). Right column) Steady state rise values (mean +/- standard deviation) taken from temporal results are plotted as a function of the reduced scattering coefficient, and a linear regression is applied to each. It is seen that increased scattering leads to higher temperature rises, lower thermal penetration depths, and no significant trend with FWHM.

the lowest values of μ_s' is seen (Figure 3.11A, right). The 1/e thermal penetration depth was calculated and is shown in Figure 3.11B. Plotting the steady state penetration depth as a function of μ_s' (Figure 3.11B, right) shows that greater scattering results in a decrease in the penetration depth, from 1.257 to 1.11 mm. The full width at half maximum of the thermal profile at the surface was calculated (Figure 3.11C). The measured steady state FWHM shows variations, but do not appear to correlate with μ_s', and this variability is likely due to a different source of variation. Linear regression was performed for each metric as a function of μ_s'. By assessing the 95% confidence interval of the slope coefficient the significance of the identified trend from a flat line was determined. Both the maximum temperature rise and the thermal penetration depth demonstrated significant deviation from a line of zero slope which validate the predicted increase in temperature and decrease in thermal penetration depth with increased scattering (Figure 3.9). This same analysis determined that no significant trend with scattering is observed for the thermal FWHM at the surface.

3.5 Discussion

3.5.1 The effect of scattering on the temperature distribution

Overall, the effects of optical scattering can be summarized as the following: 1) increases in scattering will increase the maximum temperature induced in the volume (depending on the thermal boundary conditions), 2) increases in scattering will not measurably affect the spatial distribution of heating at the surface, and 3) increases in optical scattering will reduce the 1/e thermal penetration depth. Each of these responses are driven by changes in the distribution of absorbed photons. This is most easily understood by assessing the parametric sweep simulations. Recall that as scattering increases, photons are absorbed more superficially (Figure 3.8). This results in a greater maximum absorption value with greater scattering (Figure 3.7) that drives this increased temperature. Since these photons do not penetrate as deeply, neither does the heat source, and thermal conduction is not able to propagate the heat as deeply. Some of the photons are scattered radially outward as evidenced by the yellow regions outside of the NA of the fiber in Figure 3.8. This would initially suggest the temperature distribution at the surface increases in size, however, this is counteracted by the reduced heat source immediately next to these regions (Figure 3.8, dark blue within the NA of the fiber) and any change in the absorption distribution is not substantial enough to drive a larger lateral distance of heating at the surface. Additionally, any initial changes in the

spatial temperature distribution will be smoothed out over time due to thermal conduction. The magnitude of the effect that scattering has on the heating is reduced with increased absorption (Figure 3.9), likely due to the reduced mean free path of photons leading to fewer scattering events. These predicted trends from the simulations are supported by each of the measurements. Figure 3.11A demonstrates that the temperature increases with greater scattering, and Figure 3.4Ci demonstrates how this change in temperature may not be large, depending on the variability in the setup and the thermal boundary conditions. Figure 3.5B and figure 3.11B demonstrate that a lower thermal penetration depth is indeed observed with greater scattering. Last, figures 3.4Cii, 3.4Ciii, and 3.6C highlight that the spatial temperature distribution at the surface do not trend with optical scattering.

3.5.2 Model and Experimental Limitations

All models are not without their limitations; however, it is important to understand when those limitations do and do not detract from the goal of the simulations. The optical-thermal simulations developed here demonstrate a range of errors when comparing amplitudes, however one of the main goals of this work has been to understand the trends in the temperature distribution associated with changes in optical scattering. To validate the optical-thermal model, two validation studies were developed: a thermal camera validation and a thermocouple validation. The thermal camera validation is the more idealized setup since thermal cameras allow for interrogating spatial information and since the sample here allowed for fewer unknown sources of cooling. The agarose sample in this setup was insulated on most of its surface by the presence of glass, except for the sides of the slab. This was not a concern, however, because the temperature rise was centered in the gel, and these edges were far from the induced temperature distribution (> 8 mm). The glass top and bottom limits the contact with air, which is beneficial because air contact may result in water evaporation at the surface (causing evaporative cooling) and limits the effect of convective cooling directly on the gel. The amplitude of this convective cooling can be difficult to estimate. It is noted that for this more idealized setup, errors between simulated and measure values were typically less than 10%. One surprising aspect from this thermal camera validation is that the simulations suggest that a positive trend exists between the maximum temperature rise and the reduced scattering coefficient, but this was not visualized in the measurements. To understand this, the thermal images were assessed early in the heating period (the first 1-2 frames of heating). Looking at these heat distributions provides an indirect way of assessing the light distribution since the camera is sampling at 40 fps (every 25 ms) which is fast enough to where only minimal thermal diffusion occurs between frames (thermal diffusivity of agarose ~ 0.142 mm^2/s). This analysis revealed slight changes in the light distribution between agarose phantoms that are

likely due to the spatial modes from the multimode laser diode varying over time (and with the temperature of the diode). When the data were plotted in chronological order instead of over μ_s', a trend was seen, demonstrating that the variability of the laser output was masking any subtle changes in the temperature. It was calculated that the percent difference between the maximum and minimum value of each metric (i.e. the total variation over the entire range of μ_s' sampled) was 4.15%, 5.6%, and 4.3% for the measured and 3.05%, 0.55%, and 0.45% for the simulated maximum temperature rise, major axis, and minor axis, respectively. This indicates that the amplitude of the real trends would be masked by the variability in the experiment and are smaller than the variability values calculated here. For example, the fact that the maximum temperature trend is covered up by 4.15% error suggests that any trend with scattering is not substantial. While direct measurement of the simulated temperature trend is not shown using the thermal camera, evidence of this is demonstrated by TC measurements and by the water bath validation. For the spatial metrics, the simulations predicted that these do not change with scattering, and a change of 0.5% over a range of 2 mm^{-1}, whether positively or negatively associated with scattering, is negligible in practical applications, so this is not so worrisome.

The thermal camera measurements provided validation of superficial aspects of the model, but the TC measurements were needed to validate the trends between the temperature depth distribution and optical scattering. TCs provide point measurements, and so the workflow was developed where the gels were cured around each placement of the optical fiber relative to the TC. The sample, while contained within a plastic well, required that the entire top of the gel be exposed to air, which adds the concern of unknown cooling terms. Additionally, one key difference here is that the optical fiber is embedded in the gel which provides a route for conductive cooling which is not present in the thermal camera validation. This cooling causes the maximum temperature to occur at a depth away from the optical fiber (Figure 3.5). This is unlike non-contact irradiation methods (such as in the parametric sweep, thermal camera validation, and water bath validation) where the maximum temperature occurs at the surface (Figure 3.9). For a direct comparison between a fiber in contact and just out of contact with the tissue, the parametric sweep was re-run for μ_s' = 0 and 1.5 mm^{-1} at μ_a = 2.5 mm^{-1} with the fiber placed in contact with the medium (Figure 3.12), which highlights just how much the fiber acts as a heat sink.

Considering the accuracy associated with the quantified metrics, errors in the thermal camera validation were on average 4.1% and all errors were less than 12%, while in the thermocouple validation, errors were 16.7% on average with all errors less than 47.5%. TC measurements here presented higher errors, however, it was noted that the μ_s' = 0.346 mm^{-1} trials exhibited the greatest deviation from the simulation results, and removing these from the analysis dropped the errors to 7.7% on average with all simulated values < 20.5%. Errors associated with these TC measurements are most likely to come from TC placement errors.

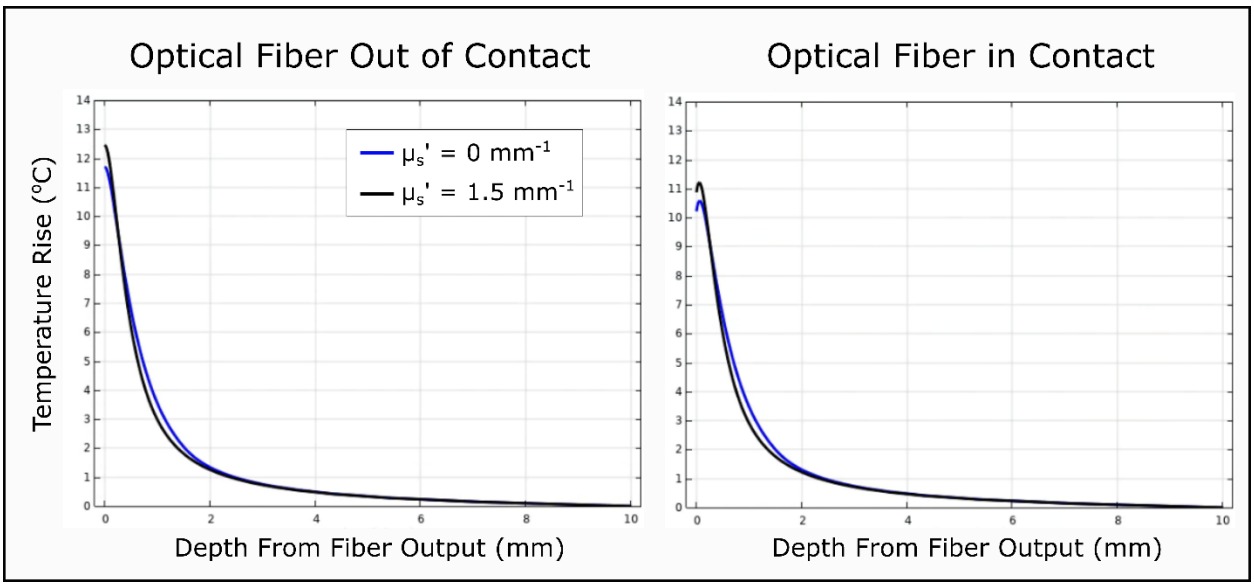

Figure 3.12. To highlight how the temperature distribution with depth changes depending on the irradiation setup, parametric sweep simulations were performed at μ_a = 2.5 mm^{-1} and μ_s' = 0 (blue line) and 1.5 mm^{-1} (black line) with the irradiating optical fiber out of contact (left) and in contact (right) with the surface of the tissue. When the fiber is in contact, the maximum temperature rises in the tissue decreases and the maximum temperature moves from the surface to a depth within the tissue. This highlights how the optical fiber acts as a heat sink and how a small change in the thermal boundary conditions can have a large effect on the temperature distribution.

Water bath temperature measurements were used to help validate the trends predicted by the parametric sweep and model validation measurements; however, the exact values measured are not comparable to the values in the main text. A liquid water-based sample was used instead of the solid agarose samples which has different material properties. Secondly, the thermal boundary conditions are different in this setup compared to the other setups. Last, the light distribution in this case is bisected, which may greatly change the light distributions relative to the other experimental setups. Initial work attempted to apply the optical-thermal model to this setup, however it was observed that ideal placement of the optical fiber relative to the coverslip is challenging, and invariably some unknown offset or angle will be present. Without this information the light distribution cannot be properly simulated because the distribution of initial photon launch locations and angles cannot be matched. Since a coverslip window is used, this leads to further complications due to reflections off the glass and potential coupling of light into the coverslip which would result in photons slowly leaking out of the coverslip over extended distances compared to their penetration depth in water. These interactions then compound with other errors already present in the setup or optical-thermal model. While this setup was not able to be simulated, these results serve to further validate the predictions of the optical-thermal model since an independent investigation was able to corroborate previously simulated and measured effects of optical scattering on the temperature distribution during laser heating.

Taking the prior discussion into account highlights that while this model may not be equipped to offer exact absolute values, it can serve to predict the expected trends in the heat distribution due to optical scattering. Knowledge of these trends are needed in the field of INI because, up until this point, optical scattering has been mostly neglected as playing a role in the temperature distribution. Understanding the role of scattering at these INI wavelengths will help guide the application of optical-thermal models for predictive and optimization applications which can aid in the selection of laser irradiation parameters used to apply neuromodulation and will clarify how uncertainty in μ_s', whether from measurement error or extrapolation error, affects the expected light and heat distributions.

Understanding the role of scattering at these wavelengths and validating simulated trends is difficult. Validation requires using experimental setups that are easily simulated, and ideally both the light and heat distributions would be measured to validate the optical and thermal models, respectively. The problem is that the sensitivity of common optical sensors drop off drastically in the short wave infrared which adds to the problem that measurements will be signal-starved due to photon propagation being very low at these wavelengths. This can be overcome by using the temperature distribution as an indirect method of informing the light distribution, which is also helpful in the context of the optical-thermal model for INI since the temperature is ultimately the important factor. Since indirect methods need to be used, and since absorption is already known to be the dominating optical interaction at these wavelengths, even if the role

of scattering is significant, the measurable signals are likely to be quite small, and experimental variability can pose a problem if it is on the order (or greater than) the change in signal due to scattering. Towards this end, the contribution from the thermal boundary conditions can be difficult to approximate but plays a major role in the formation of the temperature distribution and teasing out the effects due to boundary conditions versus scattering can be a challenge. Nonetheless, this study attempts to probe the role of scattering despite these difficulties, and while each set of experiments in this study has its caveats, taken together they begin to inform the role of μ_s' during laser heating. It is again emphasized that the trends identified in this study should be focused on rather than the exact values. Moving forward, validation of exact values would be needed for each future experimental setup utilized, but with this awareness the optical-thermal model may be used to help understand how various changes to tissue optical properties and modifications to irradiation methods may change the expected temperature distributions.

3.5.3 Practical Implications for Simulations of INI

Past INI studies[2,11,50–53] have been performed using wavelengths in the bands of 1450-1470 nm and 1860 – 1880 nm because their relatively high optical absorption and because of the abundance of low cost diodes at these wavelengths due their usage in the telecom industry. These two wavelength bands have been functionally considered equivalent since the absorption coefficient in these regimes can be matched, and since optical scattering is typically ignored. The present study can probe the similarities between the heat distributions at these wavelengths. Take two absorption-matched wavelengths: 1470 nm and 1875 nm where $\mu_a \sim 2.5$ mm^{-1}. The expected differences in the temperature distributions can be identified in Figure 3.9 by comparing the values along the $\mu_a = 2.5$ mm^{-1} line at the expected μ_s' values for 1470 nm and 1875 nm (Table 3.2). If optic nerve properties are used, $\mu_s'(1470) \sim 0.75$ mm^{-1} and $\mu_s'(1875) \sim 0.56$ mm^{-1}. In terms of the maximum temperature rise, the difference between the two wavelengths only corresponds to <1%, a negligible difference. The difference in thermal penetration depth is ~2.5%. Figure 3.10 provides a visual of the approximate heat distributions ($\mu_a = 2.5$ mm^{-1}, μ_s' = 0.6 and 0.8 mm^{-1}), which qualitatively appear similar. Thus, for matched μ_a values, the temperature distributions induced by 1450-1470 nm and 1860 – 1880 nm bands are effectively the same (2.5% different). This differences will increase slightly at lower matched μ_a and decrease at higher μ_a. Functional experiments between these two wavelengths should be performed prior to concluding that there are no differences between using these two wavelength bands, and the distinction between infrared neural inhibition (INI) and infrared neural stimulation (INS) should be emphasized. This prediction should hold for INI since the timescales of irradiation are long enough for thermal conduction to occur, however, this conclusion cannot be drawn for INS because single pulses are

typically used[54–56] or irradiation timescales are relatively short[57] and need to be assessed separately from this investigation.

Knowledge of how the temperature distribution changes with scattering can be used to help plan INI experiments and understand results of studies. In some cases the effect of scattering is small (e.g. metrics at the surface and differences between λ = 1470 and 1875 nm), however, the parametric sweep demonstrates that these difference can be large over greater ranges of μ_s' (up to 7% difference in the temperature and 20% difference in thermal penetration depth (Figure 3.9)) demonstrating that, overall, optical scattering has a non-negligible effect on the temperature distribution. Because of this, Beer's law approximations are not sufficient to estimate the distribution of absorbed photons unless the μ_s' is substantially low enough ($\mu_s' < 0.25$ mm^{-1} at $\mu_a = 2.5$ mm^{-1} to maintain <5% simulation error for all heating metrics). Otherwise, a Monte Carlo simulation is required to simulate the light distribution. Conversely, differences in these metrics are low when comparing temperature distributions across similar μ_s', and therefore uncertainty in the value of μ_s' used in Monte Carlo simulations is mostly inconsequential except for large errors. Exact errors will depend on the assumed μ_s' based on Figure 3.9 and on what degree of error is deemed tolerable in the overall temperature distribution. This assessment suggests that making estimates of μ_s' based on extrapolated values from equations in literature is likely sufficient for the purposes of simulating the temperature distribution at INI wavelengths. Using equation 2.11, it is estimated that at λ = 1470 nm, $\mu_s' = 0.75$ in optic nerve (Table 3.2). If it is assumed that this is the true μ_s' value and that < 5% difference is tolerable between the simulated temperature distribution and the true temperature distribution, acceptable estimates of μ_s' used in the simulation will fall between ~0.4 – 1.1 mm^{-1} based on the plots in Figure 3.9. Therefore, the estimate of μ_s' can be 46 % off from the true value and simulated errors from scattering will still be below 5%.

3.6 Conclusions

In this study, various simulated and real setups were used to probe the effect of scattering on laser heating. Simulations used a paired optical-thermal model which combined a Monte Carlo simulation of photon propagation with a finite element analysis that solves Penne's bioheat equation. Validation studies which used measurements from a thermal camera and a thermocouple showed agreement between the trends induced by changes in the reduced scattering coefficient of optical phantoms. Notably, the results demonstrated that greater optical scattering creates increased maximum temperature rises, reduced 1/e thermal penetration depths, and have a negligible effect on the spatial temperature distribution at the

surface. The effect of scattering was seen to be reduced with higher absorption coefficients. Prior assumptions that the effect of scattering is negligible appear viable in particular scenarios, but ultimately oversimplify the interactions occurring. Not accounting for μ_s' when estimating the distribution of absorbed photons (such as when using a Beer's law approximation) will result in moderate errors in the maximum temperature rise (up to 7% simulation error) and significant error in the thermal penetration depth (>20% simulation error), thus a best estimate of μ_s' should be made and a Monte Carlo simulation of photon propagation should be performed.

Evaluation of how optical scattering effects the temperature distribution due to laser heating is greatly important in the field of infrared neural modulation since the inhibition and stimulation responses of neural tissue is driven by the either the temperature or the temporal and spatial temperature gradients. The lack of published optical properties for nerve in the SWIR for *Aplysia*, mouse, rat, rabbit, dog, and many other research animals creates a problem when trying to simulate or predict the biophysical response of these tissues to laser irradiation. This study made a first attempt to assess the role that optical scattering plays in the development of the temperature distribution in in various simplified homogeneous tissue phantoms. Further analysis is needed to understand how cellular structure and tissue organization will affect the light and heat distributions generated and these will be the subject of more complex and further validated models. The analysis presented here provides a baseline understanding of the relationship between optical scattering and laser heating which may serve to inform and guide the development of these future studies.

3.7 References

1. Wells J, Kao C, Mariappan K, et al. Optical stimulation of neural tissue in vivo. *Opt Lett.* 2005;30:504-506. doi:10.1109/LEOS.2003.1251809

2. Duke AR, Jenkins MW, Lu H, McManus JM, Chiel HJ, Jansen ED. Transient and selective suppression of neural activity with infrared light. *Sci Rep*. 2013;3:2600. doi:10.1038/srep02600

3. Hodgkin AL, Katz B. the Effect of Temperature on the Electrical Activity of the Giant Axon of the Squid. *J Physiol Lucas Gasser Schoepfle Erlanger Cardot Arvanitaki*. 1949;09:240-249.

4. Ganguly M, Jenkins MW, Jansen ED, Chiel HJ. Thermal block of action potentials is primarily due to voltage-dependent potassium currents: A modeling study. *J Neural Eng*. 2019. http://iopscience.iop.org/10.1088/1741-2552/ab131b.

5. Fang Q, Boas DA. Monte Carlo Simulation of Photon Migration in 3D Turbid Media Accelerated by Graphics Processing Units. *Opt Express*. 2009. doi:10.1364/oe.17.020178

6. Kocbach J, Folgerø K, Mohn L, Brix O. A Simulation Approach to Optimizing Performance of Equipment for Thermostimulation of Muscle Tissue using COMSOL Multiphysics. *Biophys Bioeng Lett*. 2011;4(2).

7. Hines ML, Carnevale NT. The NEURON Simulation Environment. *Neural Comput*. 1997;9(6):1179-1209. doi:10.1162/neco.1997.9.6.1179

8. Thompson AC, Wade SA, Brown WGA, et al. Modeling of light absorption in tissue during infrared neural stimulation. *J Biomed Opt*. 2012;17:075002. doi:10.1117/1.JBO.17.7.075002

9. Abaya TVF, Diwekar M, Blair S, Tathireddy P, Rieth L, Solzbacher F. Deep-tissue light delivery via optrode arrays. *J Biomed Opt*. 2014. doi:10.1117/1.JBO.19.1.015006

10. Welch AJ, Van Gemert MJC. *Optical-Thermal Response of Laser-Irradiated Tissue.*; 2011. doi:10.1007/978-90-481-8831-4

11. Lothet EH, Shaw KM, Lu H, et al. Selective inhibition of small-diameter axons using infrared light. *Sci Rep*. 2017;7(1). doi:10.1038/s41598-017-03374-9

12. Dewhirst MW, Viglianti BL, Lora-Michiels M, Hanson M, Hoopes PJ. Basic principles of thermal dosimetry and thermal thresholds for tissue damage from hyperthermia. In: *International Journal of Hyperthermia*. Vol 19. ; 2003:267-294. doi:10.1080/0265673031000119006

13. Ganguly M, Jenkins MW, Jansen ED, Chiel HJ. Thermal block of action potentials is primarily due to voltage-dependent potassium currents: A modeling study. *J Neural Eng*. 2019. doi:10.1088/1741-2552/ab131b

14. Mou Z, Triantis IF, Woods VM, Toumazou C, Nikolic K. A simulation study of the combined thermoelectric extracellular stimulation of the sciatic nerve of the xenopus laevis: The localized transient heat block. *IEEE Trans Biomed Eng*. 2012;59(6):1758-1769. doi:10.1109/TBME.2012.2194146

15. Ford JB, Ganguly M, Poorman ME, et al. Identifying the Role of Block Length in Neural Heat Block to Reduce Temperatures During Infrared Neural Inhibition. *Lasers Surg Med*. 2019. doi:10.1002/lsm.23139

16. Hale GM, Querry MR. Optical Constants of Water in the 200-nm to 200-microm Wavelength Region. *Appl Opt*. 1973;12(3):555-563. doi:10.1364/AO.12.000555

17. Fox M. *Optical Properties of Solids*. 2nd Editio. Oxford University Press; 2010.

18. Pickering JW, Prahl SA, van Wieringen N, Beek JF, Sterenborg HJCM, van Gemert MJC. Double-integrating-sphere system for measuring the optical properties of tissue. *Appl Opt*. 1993. doi:10.1364/ao.32.000399

19. Bargo PR, Prahl SA, Goodell TT, et al. In vivo determination of optical properties of normal and tumor tissue with white light reflectance and an empirical light transport model during endoscopy. *J Biomed Opt*. 2005. doi:10.1117/1.1921907

20. Cuccia DJ, Bevilacqua F, Durkin AJ, Ayers FR, Tromberg BJ. Quantitation and mapping of tissue optical properties using modulated imaging. *J Biomed Opt*. 2009. doi:10.1117/1.3088140

21. Chan E, Menovsky T, Welch AJ. Effects of cryogenic grinding on soft-tissue optical properties. *Appl Opt*. 1996;35(22). doi:10.1364/ao.35.004526

22. Bargo PR, Prahl SA, Jacques SL. Optical properties effects upon the collection efficiency of optical fibers in different probe configurations. *IEEE J Sel Top Quantum Electron*. 2003. doi:10.1109/JSTQE.2003.811287

23. Wilson RH, Nadeau KP, Jaworski FB, et al. Quantitative short-wave infrared multispectral imaging of in vivo tissue optical properties . *J Biomed Opt*. 2014. doi:10.1117/1.jbo.19.8.086011

24. Bohren CF, Huffman DR. *Absorption and Scattering of Light by Small Particles*.; 1998. doi:10.1002/9783527618156

25. Jacques SL. Optical properties of biological tissues: a review. *Phys Med Biol*. 2013;58(11):R37-61. doi:10.1088/0031-9155/58/11/R37

26. Bashkatov AN, Genina EA, Kochubey VI, Tuchin V V. Optical properties of human skin, subcutaneous and mucous tissues in the wavelength range from 400 to 2000 nm. *J Phys D Appl Phys*. 2005. doi:10.1088/0022-3727/38/15/004

27. Bashkatov AN, Genina EA, Kozintseva MD, Kochubei VI, Gorodkov SY, Tuchin V V. Optical properties of peritoneal biological tissues in the spectral range of 350–2500 nm. *Opt Spectrosc (English Transl Opt i Spektrosk*. 2016. doi:10.1134/S0030400X16010045

28. Bashkatov AN, Genina EA, Tuchin V V. Optical properties of skin, subcutaneous, and muscle tissues: A review. *J Innov Opt Health Sci*. 2011. doi:10.1142/S1793545811001319

29. Johns M, Giller CA, German DC, Liu H. Determination of reduced scattering coefficient of biological tissue from a needle-like probe. *Opt Express*. 2005. doi:10.1364/opex.13.004828

30. Bevilacqua F, Piguet D, Marquet P, Gross JD, Tromberg BJ, Depeursinge C. In vivo local determination of tissue optical properties: applications to human brain. *Appl Opt*. 1999. doi:10.1364/ao.38.004939

31. Pitzschke A, Lovisa B, Seydoux O, et al. Optical properties of rabbit brain in the red and near-infrared: changes observed under in vivo , postmortem, frozen, and formalin-fixated conditions . *J Biomed Opt*. 2015. doi:10.1117/1.jbo.20.2.025006

32. Yaroslavsky AN, Schulze PC, Yaroslavsky I V., Schober R, Ulrich F, Schwarzmaier HJ. Optical properties of selected native and coagulated human brain tissues in vitro in the visible and near infrared spectral range. *Phys Med Biol*. 2002. doi:10.1088/0031-9155/47/12/305

33. Jiang W, Almadi M, Salas N, Rajguru S. Optical properties of biological tissues measured at infrared wavelengths. In: ; 2014. doi:10.1364/biomed.2014.bt3a.42

34. Sanchez-Cano A, Saldaña-Díaz JE, Perdices L, Pinilla I, Salgado-Remacha FJ, Jarabo S. Measurement method of optical properties of ex vivo biological tissues of rats in the near-infrared range. *Appl Opt*. 2020. doi:10.1364/ao.384614

35. Filatova SA, Shcherbakov IA, Tsvetkov VB. Optical properties of animal tissues in the wavelength range from 350 to 2600 nm. *J Biomed Opt*. 2017. doi:10.1117/1.jbo.22.3.035009

36. Bashkatov AN, Berezin K V., Dvoretskiy KN, et al. Measurement of tissue optical properties in the context of tissue optical clearing. *J Biomed Opt*. 2018. doi:10.1117/1.jbo.23.9.091416

37. Troy TL, Thennadil SN. Optical properties of human skin in the near infrared wavelength range of 1000 to 2200 nm. *J Biomed Opt*. 2001. doi:10.1117/1.1344191

38. Parsa P, Jacques SL, Nishioka NS. Optical properties of rat liver between 350 and 2200 nm. *Appl Opt*. 1989. doi:10.1364/ao.28.002325

39. Golovynskyi S, Golovynska I, Stepanova LI, et al. Optical windows for head tissues in near-infrared and short-wave infrared regions: Approaching transcranial light applications. *J Biophotonics*. 2018. doi:10.1002/jbio.201800141

40. Virtual Photonics: Mie Scattering Simulator. Beckman Laser Institute. UC Irvine.

41. Ma X, Lu JQ, Brock RS, Jacobs KM, Yang P, Hu XH. Determination of complex refractive index of polystyrene microspheres from 370 to 1610 nm. *Phys Med Biol*. 2003. doi:10.1088/0031-9155/48/24/013

42. Polyanskiy M. Optical Constants of (C8H8)n (Polystyrene, PS). RefractiveIndex.info: Refractive Index Database. https://refractiveindex.info/?shelf=organic&book=polystyren&page=Sultanova. Published 2020. Accessed August 21, 2020.

43. Wang Y, Wang RK. High-resolution computed tomography of refractive index distribution by transillumination low-coherence interferometry. *Opt Lett*. 2010. doi:10.1364/ol.35.000091

44. Kosky P, Balmer R, Keat W, Wise G. Mechanical Engineering. In: *Exploring Engineering*. ; 2013. doi:10.1016/b978-0-12-415891-7.00012-1

45. FLIR. MATLAB Resources for FLIR R&D/Science Cameras. https://www.flir.com/discover/rd-science/matlab/.

46. Zhang M, Che Z, Chen J, et al. Experimental determination of thermal conductivity of water-agar gel at different concentrations and temperatures. *J Chem Eng Data*. 2011. doi:10.1021/je100570h

47. Optical Constants of Fused silica (fused quartz). RefractiveIndex.info: Refractive Index Database. https://refractiveindex.info/?shelf=glass&book=fused_silica&page=Malitson. Published 2020.

48. Malitson IH. Interspecimen Comparison of the Refractive Index of Fused Silica*,†. *J Opt Soc Am*. 1965. doi:10.1364/josa.55.001205

49. Hasgall P, Di Gennaro F, C B, et al. IT'IS Database for thermal and electromagnetic parameters of biological tissues. Version 4. doi:10.13099/VIP21000-04-0

50. Lothet EH, Kilgore KL, Bhadra N, et al. Alternating current and infrared produce an onset-free reversible nerve block. *Neurophotonics*. 2014;1(1):011010. doi:10.1117/1.NPh.1.1.011010

51. Ford JB, Ganguly M, Poorman ME, et al. Identifying the Role of Block Length in Neural Heat Block to Reduce Temperatures During Infrared Neural Inhibition. *Lasers Surg Med*. 2020. doi:10.1002/lsm.23139

52. Ganguly M, Ford JB, Zhuo J, et al. Voltage-gated potassium channels are critical for infrared inhibition of action potentials: an experimental study. *Neurophotonics*. 2019. doi:10.1117/1.nph.6.4.040501

53. Zhu X, Lin J-W, Sander MY. Infrared inhibition and waveform modulation of action potentials in the crayfish motor axon. *Biomed Opt Express*. 2019. doi:10.1364/boe.10.006580

54. Wells J, Wells J, Kao C, et al. Application of infrared light for in vivo neural stimulation. *J Biomed Opt*. 2005;10:64002-64003. doi:10.1117/1.2121772

55. Cayce JM, Wells JD, Malphrus JD, et al. Infrared neural stimulation of human spinal nerve roots in vivo. *Neurophotonics*. 2015;2(1):015007. doi:10.1117/1.NPh.2.1.015007

56. Duke AR, Cayce JM, Malphrus JD, Konrad P, Mahadevan-Jansen A, Jansen ED. Combined optical and electrical stimulation of neural tissue in vivo. *J Biomed Opt*. 2009;14:060501. doi:10.1117/1.3257230

57. Cayce JM, Friedman RM, Jansen ED, Mahavaden-Jansen A, Roe AW. Pulsed infrared light alters neural activity in rat somatosensory cortex in vivo. *Neuroimage*. 2011;57:155-166. doi:10.1016/j.neuroimage.2011.03.084

Chapter IV

Identifying the Role of Block Length in Neural Heat Block to Reduce Temperatures during Infrared Neural Inhibition

4.1 Abstract

Objective: The objective of this study is to assess the hypothesis that the length of axon heated, defined here as block length, affects the temperature required for thermal inhibition of action potential propagation applied using laser heating. The presence of such a phenomenon has implications for how this technique, called infrared neural inhibition (INI), may be applied in a clinically safe manner since it suggests that temperatures required for therapy may be reduced through proper spatial application of light. Here, we validate the presence of this phenomenon by assessing how the peak temperatures during INI are reduced when two different block lengths are applied using irradiation from either one or two adjacent optical fibers.

Study Design: Assessment of the role of block length was carried out over 2 phases. First, a computational proof of concept was performed in the neural conduction simulation environment, NEURON, simulating the response of action potentials to increased temperatures applied at different full width at half-maxima (FWHM) along axons. Second, *ex vivo* validation of these predictions was performed by measuring the radiant exposure, peak temperature rise, and FWHM of heat distributions associated with INI from one or two adjacent optical fibers.

Methods: Electrophysiological assessment of radiant exposures at inhibition threshold were carried out in *ex vivo Aplysia californica* (sea slug) pleural-abdominal nerves (n=6), an invertebrate with unmyelinated axons. Measurement of the maximum temperature rise required for induced heat block was performed in a water bath using a fine wire thermocouple. Finally, magnetic resonance thermometry (MRT) was performed on a nerve immersed in saline to assess the elevated temperature distribution at these radiant exposures.

Results: Computational modeling in NEURON provided a theoretical proof of concept that the block length is an important factor contributing to the peak temperature required during neural heat block, predicting a 11.7% reduction in temperature rise when the FWHM along an axon is increased by 42.9%. Experimental

validation showed that, when using two adjacent fibers instead of one, a 38.5 ± 2.2 % (mean ± S.E.M.) reduction in radiant exposure per pulse per fiber threshold at the fiber output (p = 7.3E-6) is measured, resulting in a reduction in peak temperature rise under each fiber of 23.5 ± 2.1 % (p = 9.3E-5) and 15.0 ± 2.4 % (p = 1.4E-3) and an increase in the FWHM of heating by 37.7 ± 6.4 % (p = 1E-3), 68.4 ± 5.2 % (p = 2.4E-5), and 51.9 ± 9.9 % (p = 1.7E-3) in three MRT slices.

Conclusions: This study provides the first experimental evidence for a phenomenon during heat block in which the temperature for inhibition is dependent on the block length. While more work is needed to further reduce the temperature during INI, the results highlight that spatial application of the temperature rise during INI must be considered. Optimized implementation of INI may leverage this cellular response to provide optical modulation of neural signals with lower temperatures over greater time periods, which may increase the utility of the technique for laboratory and clinical use.

4.2 Introduction

Clinical pain management techniques typically utilize pharmacological agents or electrical therapies. For intervention in disease states involving chronic pain, first action often includes pharmacological agents such as NSAIDS (nonsteroidal anti-inflammatory drugs), antidepressants, muscle relaxants, or opioids[1]. In particular, chronic opioid therapy has increased in prevalence[2], carrying with it a high risk of habituation, tolerance, and dependence that increases the risk of overdose and other deleterious effects[3–8]. Development of non-pharmacological therapies is critical, resulting in government initiatives to better understand and treat chronic pain[9–11]. Electrical interventions such as spinal cord stimulation[12–14] and high frequency alternating current[15–17], whether used in acute applications or implanted for chronic therapy, can provide relief, but are limited in their spatial specificity (precise spatial targeting of neurons) due to the tendency of electric current to spread in tissue and tolerance effects where more current is needed for therapy as time progresses, which results in even more current spread and reduced specificity. It has been shown that combining electrical therapy with optical modulation may help overcome some of these limitations[18]. Ultrasonic technologies offer a method of neuromodulation that can be applied non-invasively but are limited by focal size and spatial selectivity[19–21]. In contrast, optical technologies for neuromodulation, while inherently being more invasive compared to ultrasound and transcutaneous electrical stimulation[22], have high spatial precision and would require a similar level of surgery as that used for implantable electrodes. Infrared neural modulation (INM) in particular offers both neural stimulation

and inhibition without introducing exogenous agents. Infrared neural stimulation (INS) has shown to be an effective method for stimulating action potentials in many animal models[23–29], and has been applied in human dorsal rootlets[30], but its complementary technique, infrared neural inhibition (INI), has yet to be translated for human use due to the temperature rise required for therapy.

INI works through heat block mechanisms elicited by water's absorption of infrared light[31]. Heat block was first described by Hodgkin and Katz in 1949[32] who noted that, at elevated temperatures, action potentials in the squid giant axons decreased in amplitude and increased in conduction velocity (CV), and that further increasing the temperature resulted in failure of the axons to conduct. Since this foundational article, thermally induced silencing of neural activity has been explored for a range of animal models and applications[33–36]. Mechanistically, heat block is hypothesized to act through changes in voltage-gated potassium channel dynamics[37–39]. At high enough temperatures, hyperpolarizing voltage-gated potassium ion currents overwhelm depolarizing voltage-gated sodium ion currents so that the axon can no longer generate an action potential[40].

Using a laser to apply a temperature rise has allowed for smaller regions to be targeted for spatially precise and acutely reversible heat block without functional damage[31,41–43]. This method can be non-contact with tissue, however in many cases probes delivering irradiation are placed in contact with the nerve, especially when delivering IR light in a fluid environment since the surrounding media will absorb the light before it reaches the nerve. The proximity to the neural tissue needed for INI highlights that clinical application would require surgical exposure of neural tissues for therapy, however, this is often performed when applying spinal cord stimulation[14]. The greatest barrier to clinical implementation is the temperatures associated with INI. A single temperature rise does not appear to be sufficient to elicit INI's neuromodulatory effect across all systems (Table 4.1). Furthermore, the magnitude of these temperatures needed for therapy, while viable for acute inhibition experiments, cause concern when considering sustained application, and this needs to be addressed before translation to humans. The parameter space of INI has yet to be fully explored, and thus insights are needed into how to properly apply this technology to different neural tissues in a non-damaging, sustained manner. Developing methods that can be applied across many neural model systems will greatly aid in the growth of this technology by providing understanding of the fundamental mechanisms governing heat block. When considering thermal damage to tissue, it is known that damage probability increases with not only greater temperature, but also with increased duration of application[44,45]. Thus, duration of application for any INI therapy may be extended if the temperature rise in that region of tissue is decreased. It is this concept that drives the work described in this study.

Currently unknown is how the spatial extent of heating along axons affects heat block. Based on prior mathematical analysis of the cable equation[43], we hypothesize that heating greater lengths of axon,

Table 4.1. Temperature Rise for Heat Block across Model Systems		
Model System	**Temperature Rise at Inhibition Threshold**	**Reference**
Squid Giant Axon	~20°C	Hodgkin and Katz, 1949[31]
Computational Model of *Xenopus laevis*	26-32°C	Mou *et al*., 2012[37]
***Aplysia* Buccal Nerve**	7.02°C	Duke *et al*., 2013[30]
Rat Sciatic Nerve	5.2°C	Duke *et al*., 2013[30]
***Aplysia* Pleural Abdominal Nerve**	9.7°C	Lothet *et al*., 2017[42]
Musk Shrew Vagus Nerve, Small Diameter Neurons	2.9°C	Lothet *et al*., 2017[42]

increasing the block length (BL), will decrease the temperature required. Applying INI in this manner would spread the effect over a greater volume of tissue, allowing for INI to be applied for longer periods of time. Here, we demonstrate the role of BL during INI by doubling the optical irradiation length using two adjacent optical fibers, and comparing the radiant exposure, temperature rise, and the full width at half maximum (FWHM) of the heat distribution at INI threshold both *in silico* and *ex vivo*.

4.3 Methods

4.3.1 Computational Modeling

For an initial proof of concept that block length plays a role in the peak temperature rise required for INI, the conductivity of an *Aplysia* pleural abdominal nerve axon was simulated using the Hodgkin-Huxley model implemented in the NEURON simulation environment[46], which models the equivalent circuit of the axonal membrane as batteries (ion Nernst potentials), resistors (ion channel conductivities), and a capacitor (membrane capacitance). *Aplysia* neuron parameters[47], representative of neurons in the pleural abdominal nerve that can be tested *ex vivo*, were used to model an unmyelinated axon that was 2 μm in diameter[48] and 25 mm in length. This was implemented over 9999 computational nodes with 0.025 ms timesteps for a stable simulation environment. At the end of the axon, a passive segment was placed to overcome the closed end effect which causes voltage increases at the end of a closed cable. Temperature rises were applied to the axon for two different BLs which were based on thermal camera (SC8303, FLIR Systems Inc.) measurements from temperature rises due to irradiation from one or two adjacent optical fibers. During these measurements, a probe with two adjacent 400 μm core diameter optical fibers irradiated a 20% polyacrylamide gel with similar optical and thermal properties to tissue using either one or both optical fibers. One-dimensional slices were taken from the image through the hottest point in the temperature distribution and applied in the simulation to the axon as shape templates that could be modulated by a scaling factor to apply arbitrary temperature rises to the nerve *in silico* with the expected temperature distributions from one and two fibers.

Four different simulations were performed. First, an axon held at room temperature (20^{o}C) was simulated as a control to understand the neural conduction of an unheated axon. The axon was stimulated using the Iclamp function to inject a 0.5 nA electric pulse for 1 ms at one end of the axon, and the resulting propagation of the action potential along the axon was tracked. The maximum membrane voltage of the action potential at each computational node was used to visualize the strength of the action potential as it

propagated along the axon. Next, the temperature rise required for inhibition when heated with a single 400 μm core diameter optical fiber was modeled. Inhibition was defined as a maximum membrane potential less than -60 mV at the most distal computational node, which is below the voltage required to activate voltage-gated sodium ion channels in the model[49]. The scaling factor of the one-dimensional temperature profile along the nerve was modulated until the lowest peak temperature rise that resulted in inhibition was identified as T_{S1}. A temperature rise profile which approximated heating from to two adjacent optical fibers was then applied to the axon and the temperature rise at inhibition threshold was identified using the same procedure as for one optical fiber. This simulated peak temperature rise at inhibition threshold was recorded as T_{S2}. Last, as a control to test that a greater length of heated axon is required to achieve inhibition at a lower peak temperature, the temperature profile from one optical fiber was again applied, now with its peak temperature set at T_{S2}.

4.3.2 Probe Design

A custom dual fiber probe was designed and built in-lab from two bifurcated 400 μm core diameter optical fibers (fiber A and fiber B) (BIF400-VIS-NIR, Ocean Optics, Inc.) to reliably apply INI over two block lengths with constant monitoring of the power from each laser. For each bifurcated fiber, all distal ends (after the bifurcation) were cleaved and polished. One of the two paths from each fiber set was chosen as the monitoring path which was used to measure laser power during tissue irradiation. The other path from each of the bifurcated fibers were used to construct the probe. The two probe paths were brought together and secured parallel to each other using plastic casing and optical epoxy and were further polished together. Flatness of the probe output was checked and separation distances between the fibers was measured with a stereoscope and a thermal camera with a resolution of 3.5 μm x 3.5 μm per pixel. A second probe was created in the same way as the first but with longer fibers after the bifurcation (20 feet) to be compatible with a magnetic resonance (MR) imaging scanner, allowing for the instruments containing metal, such as the lasers, power meter, and triggering electronics, to remain outside of the scanning room.

The proximal end of each bifurcated fiber was connected to a separate laser system such that fiber A was connected to laser A and fiber B was connected to laser B. Two diode laser systems (Capella Neurostimulator, Lockheed Martin) (λ= 1875 nm, 200 μs pulse duration, 200 Hz) were used to irradiate the samples. These diodes were triggered using a pulse generator (DG535, Stanford Research Systems) and optical powers (converted to radiant exposure per pulse at the output of the probe) were measured using a high-sensitivity thermopile (PS19Q, Coherent Inc.).

4.3.3 *Ex Vivo* Electrophysiology Setup

Experimental validation of computational predictions was performed in n=6 different pleural abdominal nerves from 6 *Aplysia californica* (Marinus Scientific, Long Beach, CA) weighing 250-350 grams (one nerve per animal). *Aplysia* were anesthetized using injection of 333mM $MgCl_2$ (~50% of body weight), and one of the pleural abdominal nerves were dissected and placed in a room temperature (~20^{o}C) recording dish lined with polydimethylsiloxane (PDMS) (Sylgard 184, Dow Corning) containing *Aplysia* saline (460 mM NaCl, 10 mM KCl, 22 mM MgCl, 33 mM $MgSO_4$, 10 mM $CaCl_2$, 10 mM glucose, 10 mM HEPES, pH ~7.6). The ends of the nerve were suctioned into hand pulled, pre-filled, polyethylene suction electrodes such that the nerve was taut. Bipolar leads terminating in chlorided silver wires were placed with one polarity in the suction electrode and the other polarity placed into the grounded saline bath. One end of the nerve was electrically stimulated with one of the suction electrodes while the other end was used for recording. The previously described optical probe was placed in contact with the nerve between the two electrodes such that each optical fiber fully irradiated the nerve while immersed in saline (Figure 4.1, A).

4.3.4 Neural recordings

Compound action potentials (CAPs), the summation of the multiple (>1,000) individual action potentials, were stimulated at one end of the nerve using monophasic pulses of current (90-275 μA, 5 ms pulse width, 2 Hz, 90 second duration, 179 stimulations) and recorded in Axograph data acquisition software. Signals were amplified by 10,000x and 100-1000 Hz bandpass filtering was applied using a differential amplifier (Model 1700, A-M Systems). The signal was digitized using a Digidata 1440 digitizer. Initial recordings established the normal response of the nerve to the 90 s electrical stimulation protocol. Next, the nerve was irradiated to identify the radiant exposures per pulse occurring at INI threshold. These inhibition protocols provided laser irradiation for the middle 30 seconds of the 90 second recording (Stimulations 60-119) (Figure 4.1, B). First, only one laser (Laser A) was used to irradiate with one of the fiber paths (Fiber A), and the applied radiant exposure was modulated until an inhibition threshold value, H_1, was identified where only one of peaks in the CAP was inhibited. During the experiment, inhibition was defined as the first visual disappearance of a CAP peak, however, this disappearance was later quantified, and inhibition was confirmed in post-processing by showing a statistically significant drop in the rectified area under the curve of this peak. Consequently, radiant exposures above threshold were tested. Since inhibition threshold was determined in post-processing, 1-3 repetitions of inhibition at the radiant exposure threshold were performed for each nerve.

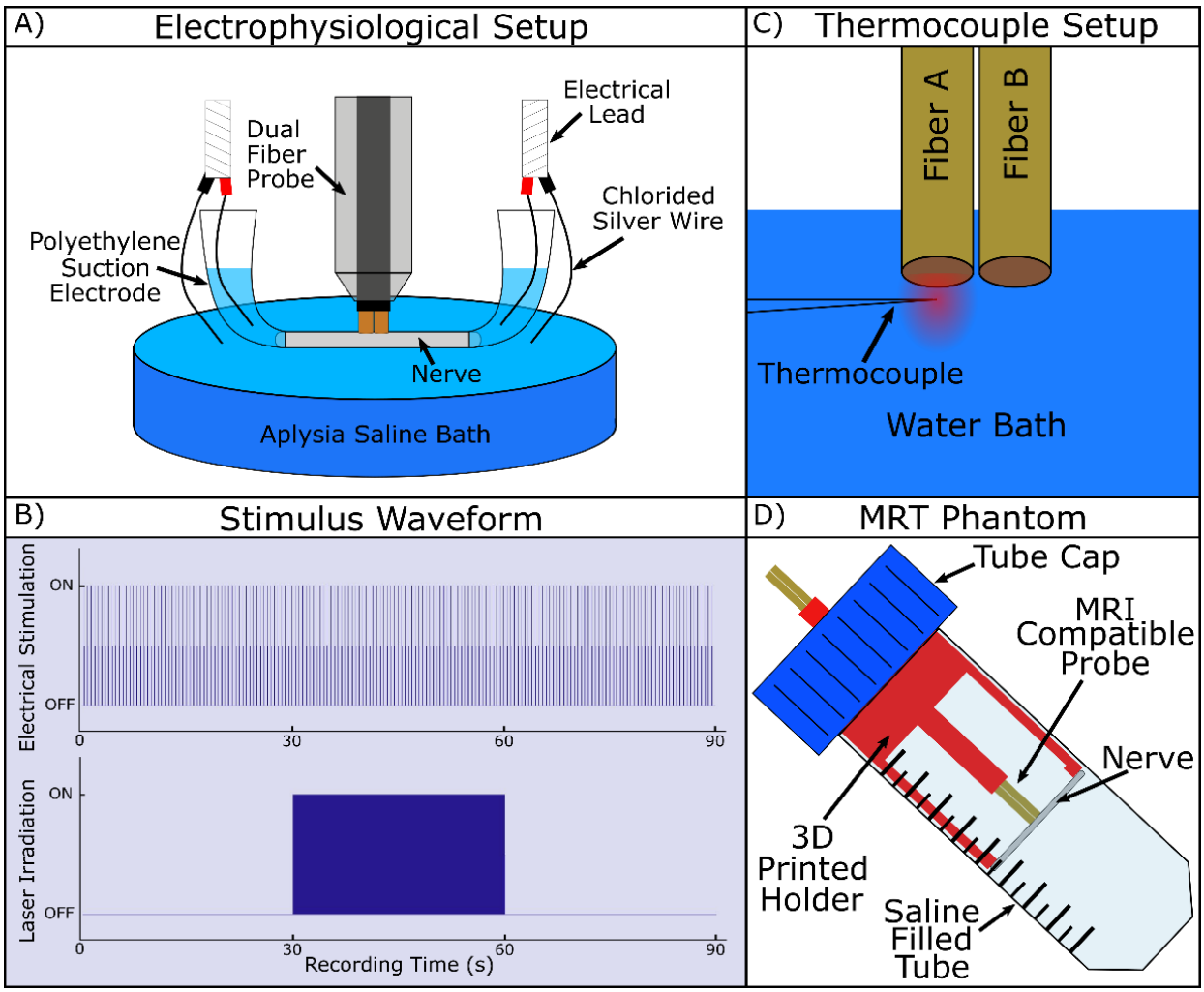

Figure 4.1. (A) Electrophysiology setup. An *Aplysia* nerve is immersed in a dish filled with *Aplysia* saline at room temperature. Nerve ends are suctioned into polyethylene suction electrodes. Bipolar electric leads terminating in chlorided silver wires are placed in the setup with one polarity in the suction electrode and the other polarity in the grounded bath. One of these provides electrical stimulation of neural activity while the other records neural signals. A dual fiber probe was placed in contact with the nerve and connected to two infrared laser diodes. (B) Stimulus waveform during each recording in which 179 electrical stimulation pulses are applied to the nerve at 2 Hz with 5milliseconds pulse width for 90 seconds. At 30 seconds (stimulation 60), the laser(s) is/are turned on, providing optical pulses 0.2 milliseconds in pulse width at 200Hz for 30 seconds. (C) Thermocouple setup. A fine wire thermocouple was immersed in a water bath and positioned under the optical probe at the location of maximum heating due to laser irradiation from fiber A or fiber (B, D) MRT Phantom. This three dimensional (3D) printed nerve holder (red) was secured in the cap (blue) of a 50m tube with a hole drilled in the center allowing for insertion of the probe. The probe was positioned in the central channel of the holder, and the nerve (gray) was strung across the gap at the bottom of the holder and secured with glue so that it was in contact with both optical fibers. This whole setup was placed in a tube filled with *Aplysia* saline and positioned in the magnetic resonance (MR) scanner for imaging.

Once the single fiber threshold was identified, inhibition threshold was found using two fibers (Fibers A & B together). Laser powers per pulse out of each optical fiber were kept equal throughout the experiment. Initially, the radiant exposure values were set to 50% of H_1, and then slowly increased until the two-fiber inhibition threshold, H_2, was found by the same criteria as for H_1.

4.3.5 Thermal recordings

A two-pronged approach was used to estimate the heating occurring at INI radiant exposure thresholds using one and two fibers. First, a thermocouple was used to measure the time-dependent heating at the spot of maximum temperature rise in a water bath. Second, MR thermometry (MRT) was used to determine the spatial extent of heating at INI thresholds. These temperature measurements were made for the previously identified radiant exposure thresholds for each of the six nerves (six H_1 values and six H_2 values).

4.3.5.1 Thermocouple recordings

Thermocouple measurements were taken using a fine wire (12.7 μm diameter) type E thermocouple (FW05, Campbell Scientific Inc.) connected to a DATAQ model DI-245 with built-in cold-junction compensation for signal acquisition. The thermocouple was secured and placed in a beaker of tap water at room temperature (Figure 4.1, C). A micromanipulator (KITE-R, World Precision Instruments) was used to hold the optical probe and was mounted on a motorized translation stage (PLS-XY, ThorLabs Inc.) for fine motion control during placement of the probe over the thermocouple. A total of 3 trials were performed for 3 different conditions, 1) only laser A irradiating with H_1 measuring under fiber A, 2) laser A and B both irradiating with H_2 measuring under fiber A, and 3) laser A and B irradiating with H_2 measuring under fiber B. For each trial, the probe was positioned with the laser(s) on, and the probe was positioned at the spot of maximum temperature. When two fiber temperature measurements were performed, the probe was first placed with only laser A or B on (for condition 2 and 3, respectively), and then further positioned with both lasers on to account for any shift in the hotspot due to the addition of the second laser. With this placement, an estimate of the maximum temperature experienced by each of the nerves could be obtained. Once positioned, the laser(s) was turned off so that the reading relaxed back to baseline at room temperature. The laser(s) was then triggered at 200 Hz with 200 μs pulses, mimicking irradiation during the electrophysiological inhibition protocol. All H_1 and H_2 values were tested to identify the maximum temperature rise for one and two fiber inhibition for each of the 6 nerves. A steady state temperature consistently occurred within 5 seconds of heating at any given radiant exposure. Temperatures were

sampled at 200 Hz and the recorded steady state temperature rises were averaged over 15 seconds once at steady state. This procedure was performed three times for each of the three conditions listed above, which were then averaged to calculate the maximum temperature rise at H_1 for each nerve and the maximum temperature rise at H_2 under each fiber for each nerve. These results were then used to calculate a percent change in temperature rise for each nerve under each fiber.

4.3.5.2 MR Thermometry Setup

While thermocouple measurements can provide information about the amplitude of heating, spatial information is needed to assess how much greater of a region is being affected. Methods which measure spatial temperature distributions within tissue at high spatial resolutions are limited. This is especially true when considering temperatures at a depth in tissue or in water-rich environments. MRT was used to provide spatial thermal data at a depth within a setup that mimicked the boundary conditions of heating in the electrophysiological experiments.

MR thermometry[50] was used to obtain spatially resolved temperature maps of the nerve and surrounding media during heating. An MR-compatible phantom setup was constructed to mimic the boundary conditions of heating that the nerves experienced during the electrophysiological experiments: being immersed in *Aplysia* saline with the probe in contact.

A nerve holder (Figure 4.1, D) was designed and 3D printed from ABS plastic to allow for repeatable, precise, and secure placement of the optical probe in contact with the nerve throughout the study within a 50mL Falcon tube (Fisher Scientific, Pittsburgh, PA). This nerve holder featured a keyed central channel for guidance of the probe so that the only possible orientation of probe insertion caused both optical fibers to be in contact with a nerve when the nerve was strung across the two extended ledges at the bottom of the holder. The nerve holder was epoxied to the inside of the tube cap, forming a water-tight seal and allowing for the removal of the entire setup from the tube with the cap.

During phantom preparation, an *Aplysia* was anesthetized and the pleural-abdominal nerve was dissected out using the same protocol as previously described. The nerve was strung across the gap between the two extended ledges at the bottom of the nerve holder while the probe was inserted into the channel so that it lay in contact across both optical fibers. Once placed, super glue was used to secure the ends of the nerve to the ledges. The nerve and probe holder were then placed in the 50 mL tube filled with *Aplysia* saline and screwed shut. This phantom setup was then secured in a 38 mm diameter quadrature volume coil and placed in the bore of a 9.4 Tesla small animal MR scanner (21 cm bore, Varian DirectDrive, Agilent) at the Vanderbilt University Institute of Imaging Science.

4.3.5.3 MR Thermometry Scan Parameters

Multi-slice, T1-weighted images of the setup volume were acquired to localize the optical fiber prior to heating. A three contiguous slice imaging plane (0.25 mm thick slices) was defined and used for temperature mapping. The imaging plane was oriented so that each image captured both optical fibers and the nerve/bath region below the probe where heating was induced (Figure 4.5 A). Slice two acquired the center 0.25 mm of the nerve and probe, and slices one and three imaged voxels containing the edges of the probe/nerve and the adjacent saline bath. A gradient echo sequence was used to dynamically acquire pre-heated and heated images around the optical probe tip (repetition time (TR)= 78 ms, echo time (TE) = 10 ms, FOV = 28 x 28 mm, 0.218 x 0.218 x 0.25 mm voxels, 3 averages, 30 s temporal resolution). Three baseline pre-heating images were acquired of all slices before triggering the laser(s) for a 30 second INI heating image. The acquired images were zero-padded in-plane to a 512 x 512 matrix (0.055 x 0.055 x 0.25 mm voxels) and temperature maps were computed from the resulting images using baseline-subtracted proton resonance frequency-shift MR thermometry[51] which was adapted to run on the scanner[52].

4.3.6 Data analysis

4.3.6.1 Electrophysiology

Compound action potentials were analyzed to identify the radiant exposure at inhibition threshold for both one and two optical fibers. The rectified area under the curve (RAUC) is a relative measure of the number of neurons contributing to the signal and has been shown to decrease during INI due to fewer neurons firing[31]. To increase sensitivity to the inhibition of neural subpopulations, the RAUC was only taken over the peak which was inhibited. The variance of the CAP was used to guide choosing the bounds over which the RAUC was calculated in each recording. Regions of local minima in the variance of the signal were chosen which minimized the variability in the RAUC due to normal signal shift. RAUCs of inhibited CAP peaks were compared to RAUCs of normal CAP peaks before and after laser irradiation using a two-sided paired t-test implemented in MATLAB (R2017a, MathWorks Inc.), and the significance threshold was adjusted using the Bonferroni correction ($p<0.0042$) to account for increased type I error due to the 12 tests being performed (six tests for H_1 and six tests for H_2). Once radiant exposures were identified at both the one and two fiber thresholds for each nerve, a two-sided student's t-test ($p<0.05$) tested for a significant change in H_2 compared to H_1.

4.3.6.2 Thermal Data

The percent change in temperature rise was calculated under each fiber and for each of the six nerves. These distributions of percent changes were tested for a significant deviation from a normal distribution centered at a 0 % change using a two-sided t-test ($p<0.05$).

For assessing changes in block length, MRT images were inspected after zero-padding, and the phase change was calculated between the average of the baseline images and the heated images. Phase wrapping in the images was removed with a one-dimensional phase unwrapping algorithm implemented in MATLAB. After unwrapping, the temperature for each voxel was calculated using the previously described equation 2.24:

$$\Delta T = \frac{\Delta \varphi}{\gamma \alpha B_0 TE} \qquad \text{Equation 2.24}$$

where $\Delta\varphi$ is the phase difference between the current image and the baseline average for each voxel, γ is the gyromagnetic ratio in Hz/T, α is the proton resonance frequency change coefficient in ppm/^{o}C, B_0 is the magnetic field strength in Tesla, and TE is the echo time in seconds[50].

On a separate nerve from a 318 gram *Aplysia*, the diameter was measured using optical coherence tomography and found to be 267 ± 7 μm. Based on this measurement of the nerve height, the middle of the nerve could be estimated as being 3 voxels (corresponding to 110 -165 μm) below the average probe tip location in each slice (determined by setting a threshold in the T1 magnitude images). The FWHM of heating was calculated along the nerve at this depth in each of the imaged heating slices. The percent change in FWHM when switching from one to two fibers was tested for a significant increase against a zero-centered normal distribution with a one-sided students t-test using the Bonferroni correction ($p < 0.017$) to account for the separate analysis of each of the three slices from the same volumetric image.

4.4 Results

4.4.1 Computational Modeling Suggests Increased Block Length Can Decrease Peak Temperatures

The importance of block length during heat block was first tested *in silico* by simulating the temperature rises required to inhibit neural conduction for two different FWHMs of heating. These simulations of neural conduction suggested that greater block lengths could lower the peak temperature required for inhibition.

Figure 4.2 shows the resulting temperatures at inhibition threshold when applying temperature rises similar to what occurs from laser heating in a nerve when irradiated with one and two adjacent optical fibers. In all columns, the top row is the one-dimensional temperature distribution applied over the length of the axon and the bottom row is the maximum membrane potential that the action potential reaches at each computational node along the length of the axon. Column 1 shows the baseline neural conduction when the axon is held at 20°C. A slight decrease in the maximum membrane potential is exhibited as the action potential reaches the end of the axon due to the passive segment placed at the end, but this does not affect conduction in the center of the axon, nor the occurrence of inhibition. Columns 2-4 show the results during heating. Inhibition was achieved when a peak temperature rise of T_{S1}=23.1°C was used (Figure 4.2, column 2) with the profile for one fiber heating. The maximum membrane potential of the action potential propagates identically to the baseline case until the action potential encounters the region of elevated temperature (Figure 4.2, column 2, bottom row). In this region, the maximum membrane potential decreases, with the rate of decrease related to the amplitude of elevated temperature, and this rate reaches a maximum at the hottest point. By the end of the axon, the action potential has dropped to -65mV, the resting potential, and has failed to recover, demonstrating successful inhibition. A similar membrane potential trend is noted when a temperature profile which mimics two irradiating optical fibers is applied at inhibition threshold (Figure 4.2, column 3). With this heating configuration, it was found that the peak temperature rise at inhibition threshold drops to T_{S2}=20.4°C, a 11.7% reduction as compared to using one fiber.

As a control, T_{S2} was applied to the axon using the one fiber temperature distribution (Figure 4.2, column 4, top row). While the maximum membrane potential drops in the heated region, the action potential recovers, and inhibition does not occur (Figure 4.2, column 4, bottom row). Measuring the spatial extent of these temperature rises, the FWHM of heating at inhibition threshold when modeling one optical fiber was 0.84 mm and this increased to 1.20 mm when two adjacent optical fibers were simulated, a 42.9% increase.

4.4.2 Using Two Fibers to Inhibit Decreases the Required Radiant Exposure per Fiber

Using electrophysiological methods, the voltage vs. time data were acquired for *Aplysia* pleural-abdominal nerve undergoing INI. A representative recording of CAPs in the pleural abdominal nerve in *Aplysia* and its response to INI is displayed as a surface plot to visualize how individual peaks in the CAP are affected over a full recording (Figure 4.3, A). This particular recording shows the two-fiber inhibition threshold for nerve 1 where each fiber irradiates with 122.2 mJ/cm^2/pulse. Here, the color of the surface indicates CAP voltage and each row corresponds to a different CAP over the 179 electrical stimulations

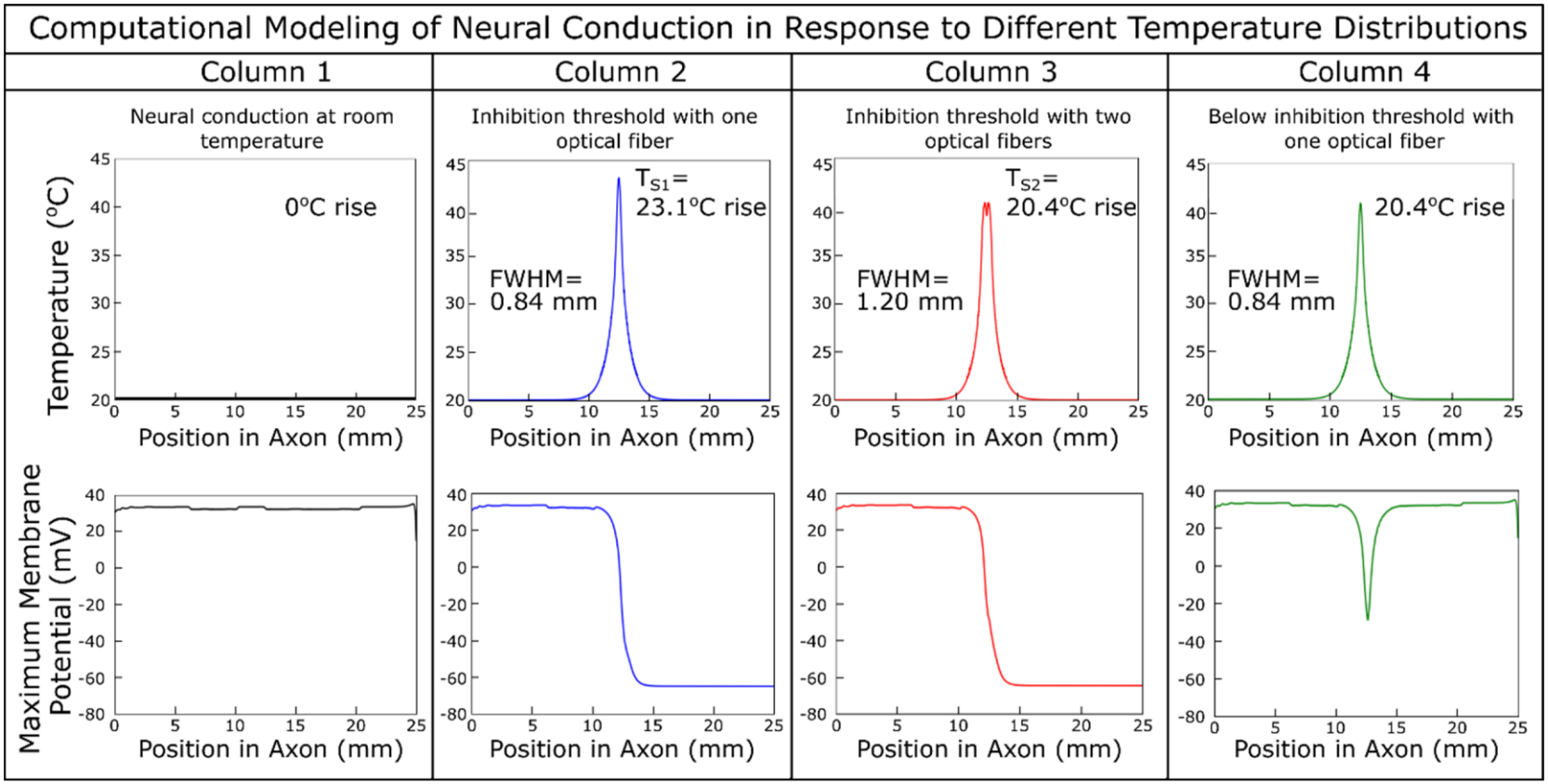

Figure 4.2. Computational modeling results. One-dimensional temperature profiles were applied to axons in NEURON to simulate the propagation of neural signals during heat block. The top row shows the temperature distribution applied along the neuron in each case, and the bottom row shows the maximum membrane potential of the action potential as it propagates along the axon. Column 1 depicts a baseline case in which no temperature elevation is applied to the axon. The peak voltage is unchanged along the entire length of the axon. Column 2 shows a temperature profile similar to that experienced from irradiation from a single optical fiber with a peak temperature rise at the inhibition threshold of TS1 = 23.1°C and FWHM= 0.84 mm. The peak voltage in the heated region decreases to a point where inhibition is experienced and the action potential is blocked. In column 3, the temperature rise similar to irradiation from two adjacent optical fibers is applied with a peak temperature rise at the inhibition threshold of TS2 = 20.4°C and FWHM= 1.22 mm. Again, the peak voltage decreases in the heated region and does not recover. Column 4 provides a control situation in which TS2 in column 3 is applied to the shape of the one fiber temperature rise, FWHM= 0.84 mm. Here, despite a reduction in the action potential strength in the heated region (note the dip in the peak voltage in the heated region), inhibition does not occur, demonstrating that the length of heating is important.

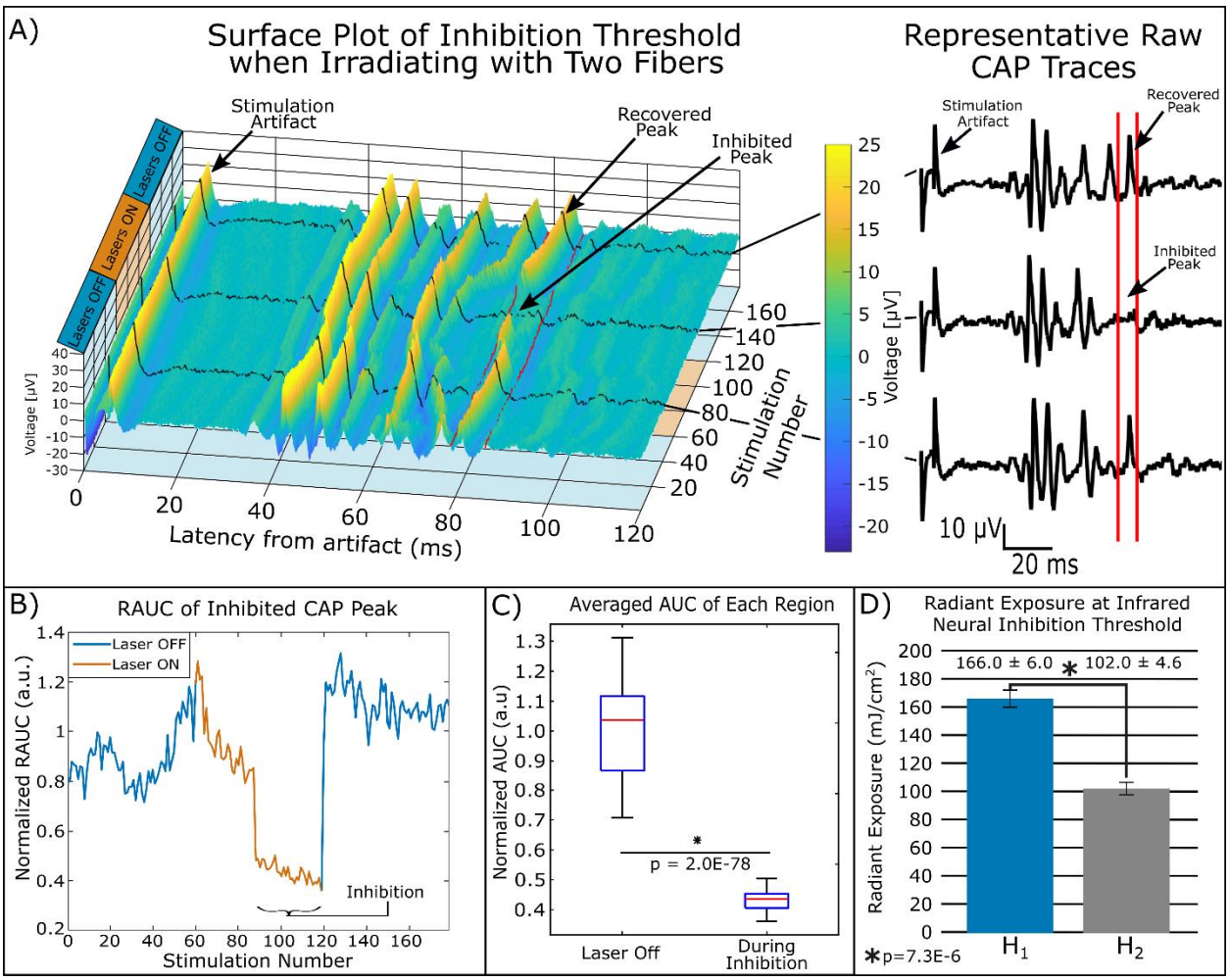

Figure 4.3. Electrophysiological results. (A) A surface plot demonstrating the results of a typical recording at inhibition threshold. Each compound action potential (CAP) trace elicited from the 179 sequential stimulations is plotted as a function of latency from the artifact at time t = 0. The height and color of the surface correspond to voltage amplitude. This particular recording is from nerve 1 at the two-fiber inhibition threshold. The recording begins at the bottom row; stimulation number (2Hz stimulation) increases from the bottom to the top of the y axis; each row shows the subsequent CAP. Boxes on the left designate when the lasers are off or on, with the lasers turned on for the middle 60 stimulations (30 seconds). Three representative CAPs taken from the black lines on the surface, one from each region, are shown on the right as representative voltage versus time traces to demonstrate inhibition of a single peak. The two red lines at ~79 and 87milliseconds on these three traces correspond to the red lines on the surface plot and designate the region over which the rectified area under the curve (RAUC) was calculated. (B) RAUC from the region between the red lines in (A), normalized to the average RAUC when the laser is off, plotted as a function of stimulation number. Blue points denote when the lasers are off whereas orange points denote when the lasers are on. (C) The distribution of RAUCs is plotted for both when the laser is off (stimulations 1–59 and stimulations 120–179) and during infrared neural inhibition (INI) (stimulations 88–119). Inhibition can be identified as a significant reduction in RAUC (P = 2.0E−78). (D) The distribution of radiant exposures resulting in inhibition threshold using one fiber, H1, and two fibers, H2. Values are reported (mean ± standard error of the mean) above each bar. A significant decrease is noted when using two fibers instead of one (P = 7.3E−6).

(90 seconds at 2Hz stimulation). The first CAP is at stimulation 1. The x axis represents the time latency from the electrical stimulation artifact. This artifact can be seen in the region of ~1 to 6 ms. The lasers are off for stimulations 1-59, on for stimulations 60-119, and off for stimulations 120-179. Representative CAP traces from each region (Laser off, Laser On, Laser off) are taken from the surface (designated by black lines) and are plotted on the right. Notice that the inhibited peak is missing from the middle trace. Baseline activity can be seen for stimulations 1-59. Once the lasers are turned on at stimulation 60, the CAP begins reacting to the heat generated by increasing in conduction velocity (decreasing in latency). Inhibition eventually occurs in the peak with the slowest CV (between the two red lines, Figure 4.3, A). The inhibited peak immediately returns once the laser is turned off. RAUC of the inhibited peak, calculated between the red lines, is plotted as a function of stimulation number (Figure 4.3, B) where blue indicates RAUCs when the lasers are off, and orange indicates RAUCS when the lasers are on. Inhibition was confirmed as a statistically significant drop ($p = 2.0E-78$) in the average RAUC during inhibition (stimulations 88-119) when compared to the average RAUCs prior to irradiation and after irradiation. The distribution of these RAUCs are shown (Figure 4.3, C). This method was used to confirm INI radiant exposure thresholds for one and two fibers for all six nerves. The average H_1 and H_2 are plotted in Figure 4.3, D. The single fiber radiant exposure threshold was found to be 166.0 ± 6.0 mJ/cm^2 (mean ± standard error of the mean), and using two optical fibers resulted in a significant drop in the radiant exposure threshold, 102.0 ± 4.6 mJ/cm^2 per optical fiber. This corresponds to a 38.5 ± 2.2 % ($p=7.3E-6$) reduction in radiant exposure per fiber at the probe output when using two adjacent optical fibers. Since using two fibers changed the boundary conditions of heating compared to using one fiber, this change cannot be directly translated into a reduction in temperature rise at inhibition threshold. Consequently, temperature rises were directly measured at each H_1 and H_2 value.

4.4.3 Peak Temperatures Decrease when Using Two Fibers

Thermocouple measurements yielded dynamic temperature rise data from which the temperature at steady state was extracted. These measurements were performed in a water bath so that the thermocouple could be precisely placed at the site of maximum temperature rise within the thermal distribution. While an artifact is present due to direct irradiation of the thermocouple when irradiated in air, the amplitude of this when in immersed in water is minimized due to the high amount of optical absorption in the water between the optical fibers and the thermocouple. This greatly reduces the amount of direct irradiation on the thermocouple, and the greater sensitivity of the thermocouple to the induced temperature rather than the artifact is evidenced by that a maximum temperature was not measured when

the thermocouple was in contact with the fiber output (where the radiant exposure is maximum), but at away from the fiber tip (where a temperature maxima is expected to occur). The maximum recorded temperatures under each fiber are reported in Figure 4.4 when irradiating with the identified H_1 and H_2 for each of the six nerves tested. For all nerves, the temperature at inhibition threshold was reduced by using two fibers for inhibition. The temperature under fiber B consistently yielded higher temperatures than fiber A. The table on the right of Figure 4.4 shows the percent reduction in maximum temperature rise for each nerve sample when using two optical fibers compared to one. The average percent reduction in temperature rise controls for variability from nerve to nerve since different axons may have been inhibited across samples. Overall, by using two adjacent fibers instead of one, the peak temperature rise was significantly reduced under fiber A by 23.5 ± 2.1 % (p = 9.3E-5) and under fiber B by 15.0 ± 2.4 % (p = 1.4E-3).

4.4.4 Block Length is Increased when using Two Fibers

Estimates of the FWHM of heating for the previous six pairs of radiant exposure measurements were made with the phantom setup described in the methods. Temperature map slice orientations are shown in Figure 4.5, A, where slice 2 (light blue) samples the center of the nerve and probe and is sandwiched between slices 1 and 3 (magenta and orange, respectively). A large artifact was persistent in slice 2 near the output of the probe that is believed to be due to a change in magnetic susceptibility from the probe to the nerve/water and interfered with the zero-padding and obscured the region of interest of heating for all scans. Due to this, temperature maps generated in this slice were analyzed 275 – 330 μm below the probe tip where the artifact did not affect the results. In all other images, line profiles were taken 110 – 165 μm below the probe tip. The results when using radiant exposure values found for nerve 1 are shown in Figure 4.5, B-D. Figure 4.5, B displays the computed temperature map for slice 1 when one fiber irradiates with H_1 (176.3 mJ/cm^2) and Figure 4.5, C displays the same for when two fibers irradiate with H_2 (122.2 mJ/cm^2). The artifact from the probe has been removed by thresholding. Line profiles taken from these images (the red lines in B and C) are plotted in Figure 4.5, D. The FWHM of heating for one fiber (blue) was calculated as 0.66 mm, compared to 1.10 mm for two fiber heating (orange). Assessing the percent increase in FWHM across all radiant exposure values in all slices (Figure 4.5, E) showed a 37.7 ± 6.4 % (p = 1E-3), 68.4 ± 5.2 % (p = 2.4E-5), and 51.9 ± 9.9 % (p = 1.7E-3) increase in slices 1, 2, and 3 respectively.

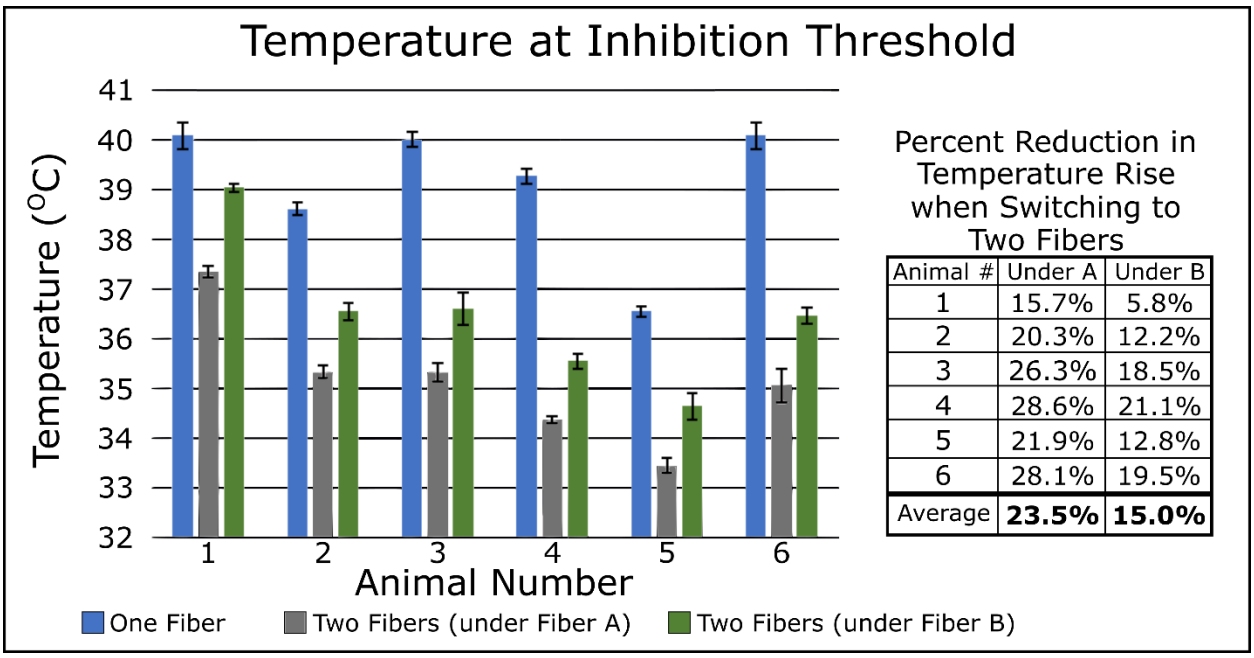

Percent Reduction in Temperature Rise when Switching to Two Fibers

Animal #	Under A	Under B
1	15.7%	5.8%
2	20.3%	12.2%
3	26.3%	18.5%
4	28.6%	21.1%
5	21.9%	12.8%
6	28.1%	19.5%
Average	**23.5%**	**15.0%**

Figure 4.4. Thermocouple temperature rise results measured in a water bath. Peak temperature rises due to electrophysiologically determined H1 and H2 values are shown for each of the six nerve, where three trials are averaged for each condition (mean ± standard error of the mean). Blue bars show the maximum temperature at inhibition using one fiber. Gray bars show the maximum temperature during two fiber inhibition measured under fiber A. Green bars show the maximum temperature during two fiber inhibition measured under fiber B. The percent reduction in peak temperature rise by switching to two fibers is reported for each nerve in the table on the right. The average percent reduction was 23.5 ± 1.2% under fiber A and 15.0 ± 2.4% under fiber B.

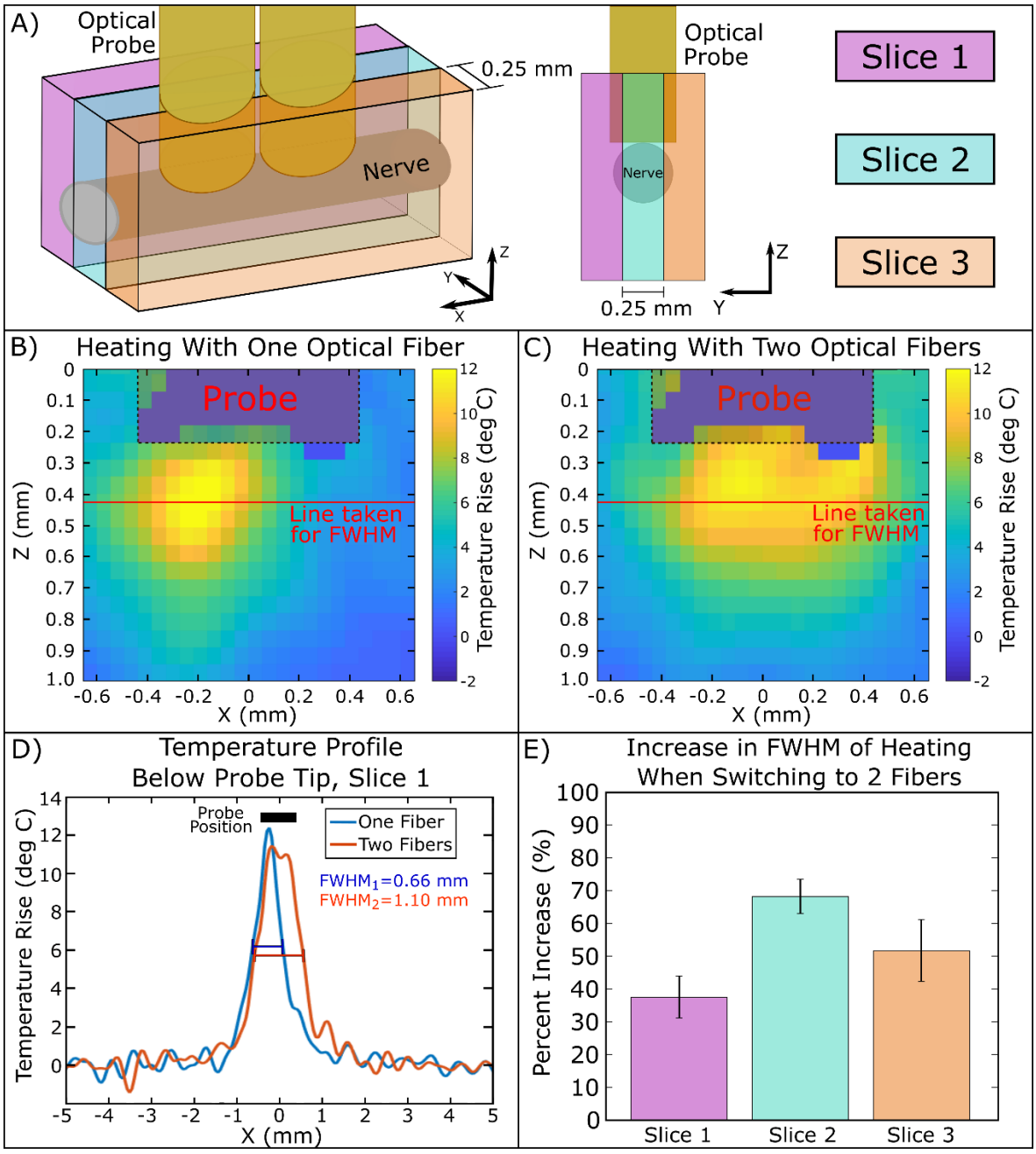

Figure 4.5. Magnetic resonance thermometry (MRT) results. (A) Schematic of the temperature mapping slice orientations and positions in relation to the nerve and probe, where slice 2 (light blue) measures the center of the nerve and probe and is sandwiched between slice 1 (magenta) and slice 3 (orange). Slices are 0.25-mm thick and contiguous. (B) MRT image of heating in slice 1 using one optical fiber irradiating with H1 for Nerve 1 (176.3 mJ/cm2/pulse). The artifact due to the presence of the optical probe has been removed by thresholding the raw magnitude image and a dashed line has been placed around the location of the probe for clearer visualization of the data. (C) MRT image of heating in slice 1 using two optical fibers irradiating with H2 for Nerve 1 (122.2 mJ/cm2/pulse/fiber). (D) Temperature rise line profiles taken from 110 to 165 μm below the probe in (B) and (C) are plotted. The probe position is shown as a thick black line. The FWHM was calculated for both one (blue) and two (orange) fiber heating. From these, the percent increase in FWHM of heating when using two fibers instead of one was calculated. (E) The distribution of percent increase in the FWHM for all six sets of radiant exposure thresholds was calculated as 37.7 ± 6.4% (P = 1E−3), 68.4 ± 5.2% (P = 2.4E−5), and 51.9 ± 9.9% (P = 1.7E−3) for slices 1, 2, and 3, respectively.

4.5 Discussion

4.5.1 Utilizing the Computational Model to Explore INI Parameter Space

Both modeling and experimental data support the hypothesis that longer block lengths reduce the temperatures required to achieve INI. The computational modeling of the effect of block length was crucial in the development of this study. Lothet *et al.* first analytically derived how the minimum block length scales with the square root of axon diameter using the cable equation[43]. From this analysis, one can hypothesize that, assuming effects along the length increase monotonically with temperature, that less thermal energy is needed to induce block if a greater length of axon is heated. Ganguly *et al.* simulated the mechanism of heat block and in their investigation computationally tested this hypothesis, describing how the block length required to inhibit varied with both the axon diameter and the temperature rise across a uniformly heated region[40]. Here, this hypothesis was computationally tested with temperature distributions similar to what actually occurs from heating when irradiating with an optical fiber and with a simulation mechanism in NEURON that is tailored towards *Aplysia* neurons. Modeling predicted a decrease in the maximum temperature rise by 11.7 % when the FWHM of heating increases by 42.9 %. Experimental measurements revealed a 15.0 ± 2.4 % and 23.5 ± 1.2 % reduction in maximum temperature rise under fibers B and A, respectively, when the FWHM of heating was extended by 68.4 ± 5.2 % in the center MRT slice. The results of this study support the hypothesis that this model can be used to test trends associated with INI, providing a means to relatively quickly and cheaply test the parameter space to optimize laser light application, which can then be experimentally validated.

4.5.2 Hypothesized Mechanism of Block Length

The trends shown in this study highlight that when applying INI, attention must be paid to the spatial extent of heat application. This concept of block length directly arises from the relatively recent advance in laser technology of stable diode lasers with wavelengths centered at water absorption peaks. This technology, coupled with small diameter fiber optics, allows for application of heat block on a spatial scale at which the phenomenon of block width arises. Prior work in the field of heat block[31,32,38–40,43,53] suggests that heat block is due to the interplay of changes in the dynamics of voltage-gated sodium, Na_V, and voltage-gated potassium, K_V, ion channels. It is hypothesized that, at increased temperatures, the effect of the hyperpolarizing K_V currents overwhelm the effect of the depolarizing Na_V currents, resulting in neurons being unable to reach the threshold voltage in the adjacent region of axon[40]. Furthermore, it is

known that smaller diameter axons are inhibited at lower temperatures[43]. Since ionic currents are temperature dependent, if a particular temperature rise requires one specific block length, it should follow that a higher temperature will require a shorter block length[43]. Ganguly *et al.* assessed the ratio of the total charge transfer of potassium, Q_K, to the total charge transfer of sodium, Q_{Na}, at a single computational node and found that, at increased temperatures, the absolute value of this ratio increases[40]. In other words, as the axon is heated, the amount of potassium charge transfer increases compared to the amount of sodium charge transfer. This observation was also replicated in this study using *Aplysia* parameters in NEURON (data not shown) and the same conclusion was reached. At higher temperatures, lower block length was required and a greater Q_K/Q_{Na} ratio was calculated across all heated computational nodes. This analysis does suggest that if the irradiated region is increased past the length tested in this study (two adjacent optical fibers), the temperature at inhibition threshold can be further reduced. This topic is of great interest when considering how INI threshold temperatures may be clinically viable, and while outside the scope of this manuscript, assessing methods of applying longer block lengths and assessing their effect is under investigation.

4.5.3 Sensitivity of INI to Probe Placement

Infrared neural inhibition of particular neural populations is very sensitive to probe placement. Laser heating effects must be decoupled from the tissue's normal response. When assessing the CAP in *Aplysia* pleural abdominal nerve, the following effects are seen. Prior to laser heating, peaks shift to longer latencies which can be characterized as a "fatigue" effect due to build-up of sodium ion channel inactivation[54,55] from the 2Hz electrical stimulation. Once the laser turns on, both the inhibited and non-inhibited peaks shift to the left, having a lower latency from the electrical artifact, which is consistent with the previously published trends that axons at higher temperatures demonstrate faster conduction velocities[32]. At some critical point (critical temperature), INI takes place in the inhibited peak. When the laser turns off (Stimulation 120), the inhibited peak's CV is similar to its initial CV at Stimulation 1 as if INI provided time for the neurons to "rest" and overcome the sodium channel "fatigue"; however, as electrical stimulation continues, there is again an increase in latency of the peak due "fatigue". Non-inhibited peaks show increased latencies when the laser is turned off, likely due to the tissue cooling. Note that only one peak was inhibited (Figure 4.3, A), demonstrating the ability to preferentially block the conduction of only a subset of neurons within the entire nerve. This selectivity of INI may be used to specifically inhibit subpopulations of neurons within a nerve[43].

As INI is currently understood, factors that contribute to which neurons are inhibited include temperature rise, a neuron's axon diameter, and the block length. Placement of the probe is crucial for

neural targeting since it dictates the location of the temperature distribution, which modifies the temperature rise and the FWHM of heating along the targeted neurons. In this study, the variability of probe placement was accounted for in three ways. 1) The probe was placed on the nerve in the same way for each experiment. With the pilot lights on, the probe was placed in contact with the nerve under stereoscope viewing so that both fibers completely irradiated the nerve. Maximal scattering of the pilot light was used as an indirect measure that the probe was fully on the nerve. 2) Once inhibition was achieved, the probe was left in the same position for the entire experiment. Despite these efforts, probe placement may have targeted different neural populations between nerves, and the axon diameter and complement of ion channels of the targeted neurons may have resulted in different temperature rises required to elicit INI. Note how nerve 5 in Figure 4.4 displayed temperature rises lower than the other samples, with the one fiber temperature rise lower than the two-fiber temperature rise for nerve 1. While the population of neurons targeted varied between nerves, it was found that for a given probe placement the same population of neurons was inhibited independently of whether one or two fibers were used. Therefore, 3) the percent reductions in both the temperature rise and the FWHM of heating were calculated for each nerve before statistical assessment of their distributions was performed, so that the variation in inhibition of different neural populations between nerve samples could be overcome. In this way, the reported trends can be applied across neuron populations in the slug, demonstrating that this phenomenon of block length is not confined to any particular population of unmyelinated neurons.

4.5.4 Targeting Neural Subpopulations

Targeting specific neurons for inhibition relies on more than just probe placement. It is known that INI naturally results in block of smaller diameter neurons at lower radiant exposures according to the "size principle" as demonstrated by Lothet *et al*.[43]. This trend may allow for selective inhibition of pain conducting C fibers in humans because they are similar in diameter to neurons in the slug, have the smallest diameter axons in the peripheral nervous system, and are unmyelinated[48,56]. When considering how the size principle affects a CAP, it is seen that later signal peaks are inhibited first[43] since smaller axon diameters have slower conduction velocities[57]. In this study, when radiant exposures higher than threshold were tested, slower CVs were inhibited prior to the fastest CVs (data not shown) supporting the conclusion of Lothet *et al*.[43]. It is important to note, however, that the very slowest conduction velocity signal was not always the first signal peak inhibited. This variability is likely due to the spatial specificity of INI, the probe placement across experiments, and the complement of ion channels in the targeted neurons. For each nerve, the inhibited peak was consistent regardless of whether one or two fibers were used to inhibit, demonstrating

that the selectivity of inhibition was not altered by increased block length. This is expected, as the spatial selectivity is determined by the size of the laser spot in the direction across (transverse to) the nerve and the optical penetration depth (in the z-direction); the increase in block length (i.e. the size of the laser spot in the direction axial to the nerve) is not expected to change that selectivity since all neurons are heated in both the one and two fiber cases. It is unclear how selectivity of inhibition will change when the irradiation spot is smaller than the diameter of the nerve. The time course of inhibition is governed by the speed at which heat is accumulated in the nerve, which in practice is controlled by the radiant exposure. Using higher radiant exposures results in quicker INI, but this also runs the risk of overheating to a point beyond a "therapeutic zone" and causing damage. Lower radiant exposures reduce the risk of damage but increase the time to inhibition. In this study, INI was achieved in a 30 second window of irradiation which governed the effective radiant exposures used, and a statistically significant INI threshold typically resulted in inhibition of the signal in the last 5 to 15 seconds of irradiation.

In this study, the probe was placed in contact with the tissue, however, this is not necessary to deliver the required temperature rise for inhibition. The drawback of positioning the probe not in contact when the nerve is immersed in media is that energy density losses occur due to both divergence from the probe and due to absorption of the light by the saline. The same limitation occurs if any other tissue is between the probe and the nerve. Besides resulting in unnecessary heating, this would raise the optical power required for inhibition. Consequently, close proximity of any optical emitter to the nerve would be ideal in a clinical scenario to minimize laser power and superfluous heating. Compare this to electrical inhibition where contact with the tissue is required. It is known that application of both high frequency alternating current (AC)[15,17] and direct current (DC)[58] can block neural conduction. It has been shown that high frequency AC can preferentially target either larger or smaller diameter axons depending on the frequency used[59,60], whereas DC stimulation preferentially blocks large diameter and myelinated neurons first[61]. Specificity in electrical modulation of neurons has been boosted by using focused multipolar and tripolar stimulation methods[62]. The advantage of INI is that it can be performed using less complex hardware. Moreover, at least in theory, INI is potentially much more spatially precise than even the most sophisticated electrical modulations techniques since the interrogation zone is dictated by the optical spot size (which in extremis is diffraction limited). Whether that level of spatial precision is either practical or necessary remains to be seen. In cell and animal models, an optical fiber may be brought into the vicinity or in contact with the sample, while spatially precise electrical modulation may require complex devices and careful placement of electrodes, especially when working with cultured cells. For example, while safe DC inhibition was described in Fridman *et al*.[58], a complex device was necessary to achieve this, whereas INI modulates activity in small axon diameters in a non-functionally damaging manner with just the introduction of an optical fiber delivering light from a laser source. Clinical feasibility of INI would be

greatly improved by demonstrating even greater improvements in spatial and neural specificity, even over what was shown in Duke *et al.*[31]. We hypothesize that more complex irradiation schemes that utilize INI's size principle and block length phenomena along with the ability to focus light to a small spot will provide more targeted inhibition of specific neural populations, and this can be used for providing targeted therapy. Further, INI and electrical inhibition may be implemented synergistically, as was demonstrated by Lothet *et al.*[18], and as was demonstrated during neural excitation by Duke *et al.*[41,63].

4.5.5 Considerations for Thermal Measurements

Temperature measurements were required to confirm that extending the block length decreased the temperature rise required for heat block. When two fibers are used, while each individual fiber outputs less energy per pulse per fiber ($H_2 < H_1$), there is still more total energy being deposited into the tissue since there are now two fibers irradiating ($2*H_2 > H_1$). Using one fiber, the average power applied to the nerve at inhibition threshold was 41.7 mW, and this was increased to 51.3 mW in total when using two fibers. This greater power is now distributed over a greater volume of tissue, and while it was hypothesized that the combined effect of more energy and greater application volume would result in a lower temperature rise, thermal measurements were required to validate this. Precise thermal recordings in tissue pose a serious challenge. In this study, a thermocouple and magnetic resonance thermometry were used to provide complementary information about the heating produced by the inhibition probe. The advantage of thermocouples is that they provide fast thermal dynamics with high thermal precision, however, contact with the sample is required and only a single point can be interrogated. The thermocouple measurements must be evaluated carefully since a classic problem of using this temperature measurement approach to elucidate the thermal effects of laser irradiated tissues is direct radiation of the thermocouple which may result in an overestimation of the measured temperature as well as actually increasing the temperature of the laser-irradiated medium due to heat conduction from the irradiated thermocouple itself. Secondly, the thermocouple wires may act as a heat sink which could result in an underestimation of the temperature of the irradiated volume. Given the specific parameters of our experiment where the laser pulses are 200 µs in duration, of relatively low intensity, and are delivered at a repetition rate of 200 Hz (i.e. the duty cycle is 4%) and the physical properties of the thermocouple we used (thermal time constant ≈10 ms, thermocouple wires of 12.7 µm diameter and a physical thermocouple junction size of ~25 µm, made of chromel/constantan (which has a heat capacity of ~ 400 J/kg K; roughly $1/10^{th}$ of that of water[64,65]), our calculations indicate (data not shown) that: 1) the thermocouple is too slow to track the direct laser heating and the laser pulse repetition rate is too slow (200 Hz, i.e. 2 pulses during the 10 ms thermal response time

of the thermocouple) to cause significant heating due to pulse-to-pulse temperature superposition; 2) the 'thermal mass' of the thermocouple is more than 3 orders of magnitude smaller than thermal mass of the surrounding aqueous medium (given by the laser spot diameter and the optical penetration depth) and hence conduction of heat either from the thermocouple to the surrounding aqueous media (due to direct laser irradiation of the thermocouple) or from the surrounding media to the thermocouple (heatsink) is negligible.

Another aspect of this temperature data is that the temperature recorded under fiber B was consistently higher. This was investigated, and it was found that fiber B had a smaller divergence angle than fiber A, which resulted in the spot diameter from fiber B being smaller than fiber A past the output of the fiber. This difference appeared to be due to different couplings at the SMA ports from the two lasers. Therefore, while the power output was the same between the two lasers, there was a slight increase in the volumetric energy deposition from fiber B compared to fiber A. While this created a noticeable difference in the temperature rise from the two fibers, all nerves showed a statistically significant drop in temperature at inhibition threshold when using two fibers instead of one.

Magnetic resonance thermometry[66] is another method of temperature measurement that has been applied for guidance of thermal therapy[67–69], and has been applied for assessing temperature rise during infrared neural stimulation[70]. MRT provides information with lower thermal precision, spatial resolution, and temporal resolution compared to thermocouples and thermal cameras. In contrast, however, MRT gives volumetric information within tissue and water-rich environments that these other two methods cannot provide. While thermal dynamics could not be measured with MRT, the field of temperature was probed at a depth in solution, adding to the single point information provided by a thermocouple. Limitations in the spatial resolution of MRT for measuring heating from an optical probe was overcome by using a scanner with a high magnetic field strength, reducing the temporal resolution, performing averaging, and interpolating the data. Infrared imaging was considered as a method to measure the temperatures being generated because it is a non-contact method which provides images at high spatial and temporal resolutions, but the drawback in tissue and other water-rich environments is its limited imaging depth. The absorption coefficient of water in the infrared regions used by thermal cameras is high enough that temperature sensing is confined to only a very superficial layer (tens of microns)[71]. Additionally, when using thermal imaging with INI, the optical probe can physically block the field of view of the camera if it is in contact with tissue, and the maximum temperature rise may occur at a depth greater than the camera can detect. To confirm that the maximum temperatures were reduced by using two optical fibers for inhibition, it was important to measure the temperature generated at a depth in solution, meaning that thermal cameras were not appropriate. Other methods for monitoring temperature exist such as fluorescent sensors[72], temperature spatially offset Raman spectroscopy (TSORS)[73] and fiber Bragg gratings[74], and each

has their respective advantages and drawbacks. Experiments must be carefully designed to adequately approximate the temperature generated in the nerve during INI.

The computational predictions, thermocouple measurements, and magnetic resonance thermometry recordings all present similar temperature rise values at inhibition threshold. For example, from Figure 4.4, the temperature rise for nerve 1 is ~20^{o}C when using one fiber. The MRT data for nerve 1 shows a rise of ~12.4^{o}C. With two fibers, the temperature rise as measured by the thermocouple was ~17.5-19^{o}C for two fibers, while this was measured as ~11.4^{o}C using MRT. This lower temperature in the MRT data may be due to greater spatial averaging during MRT, which could underestimate the maximum temperature rise and/or direct irradiation to the thermocouple, which could overestimate the temperature rise measured using the thermocouple. Nonetheless, the multiple methods of measurement serve to validate each other and highlight that the reported values are reasonable estimates.

MRT measurements confirmed that the FWHM of heating along the nerve increased when two optical fibers were used. Despite this trend being consistent through all trials, care must be taken when interpreting these results. Averaging of multiple accumulations was required to maintain a usable SNR and achieve a voxel size of 0.055 x 0.55 x 0.25 mm (acquired size of 0.218 x 0.218 x 0.25 mm), which limited the temporal resolution. Zero-padding in the frequency domain was required to boost spatial sampling, which can exacerbate artifacts and noise within the images. The noise is observed as the oscillations in Figure 4.5, D outside of the heating. Additionally, the two temperature peaks in Figure 4.5, D are not exactly equal. This could be due to slight differences in the outputs from laser A and B, differences in the outputs from fibers A and B, a slight offset in the location of the output of fibers A and B, or due to a rotation in the imaging plane relative to the probe. Despite this, for all tested radiant exposures and in all imaged slices, the FWHM increased when two optical fibers were used instead of one.

4.5.6 Temperature Measurements Across Animal Models

In this study, it was shown that the average temperature rise at inhibition threshold was 17.6^{o}C (~37.6^{o}C) using one fiber and 13.5^{o}C (~33.5^{o}C) using two fibers. These values are higher than what was reported for animal studies in Table 4.1. Different model systems may require different temperature rises to elicit heat block. This may depend on nerve thickness, axon diameter, block length, myelination, vertebrate vs. invertebrate, and complement of ion channels, and the reported values may further differ due to temperature measurement methodology, to name some possible sources of variability. Hodgkin and Katz[32] demonstrated that heat block takes place near 40^{o}C which is slightly higher than the temperatures reported in this study. Importantly, Hodgkin and Katz provide a validation of heat block using a non-laser

method of heating where, instead, heated saline was used in the bath. The proposed mechanism of heat block is agnostic about the energy source driving the temperature rise and relies solely on a thermal response of the tissue. There is no evidence that INI works through a non-photothermal effect: photons do not contain enough energy to drive photochemical reactions at 1875 nm, and laser pulses that are 0.2 ms in duration at this wavelength do not fall in the stress confinement regime[75], eliminating mechanical modulation.

The most comparable study to the work presented here is Lothet *et al.* 2017[43] because the *Aplysia* pleural abdominal nerve was also used. This study published a 9.7°C temperature rise when using a 600 μm core diameter optical fiber and 1860 nm light compared to this study using a 400 μm core diameter fiber and 1875 nm light. Using a 600 μm fiber would extend the block length on the nerve, possibly accounting for some of the discrepancy of temperature rise at INI threshold using one fiber. In the current study, however, a higher temperature rise than 9.7°C was needed for two fiber inhibition, so this cannot be the only factor. The wavelength used in the current study, 1875 nm, has higher absorption in water than 1860 nm[71] which would reduce the optical penetration depth, causing more light to be absorbed more superficially in the nerve and changing the temperature distribution, affecting which axons were targeted spatially, but more work is needed to understand the effect of this on neural conduction.

In this study, a fine wire thermocouple that is 12.7 μm in diameter was used to measure temperature compared to thermal cameras in other studies. Thermal cameras can only sense superficial temperature increases, which may not correspond to maximal heating. Additionally, averaging over pixel area occurs, possibly explaining some of the difference in reported temperature rise between this study and other studies. In Lothet *et al.*[43], the limitation of the sensing depth of thermal imaging was overcome by creating a glass window setup. While this provides information at a depth, underestimation of the temperature may have occurred due to optical transmission through the window that was less than 100% in the wavelength sensing range of the camera (3-5 μm)[76]. Additionally, other variations in the setups may have led to higher temperature requirements in the current study than what was needed for INI in Lothet *et al*[43]. Further characterization efforts will be required to identify what is the necessary temperature rise for any given model system, and why the reported variations occur. Using the *Aplysia* model (a cold-blooded animal), the biophysics of neural conduction can be tested, but as reported in this study and others, heat block sets in at mammalian physiological temperatures. Ganguly *et al.* predicted that squid giant axons (500 μm in diameter) similarly could not conduct at temperatures higher than 29.5°C, and that smaller diameter axons required lower temperatures for heat block[40], demonstrating the limitation of trying to computationally model heat block at mammalian temperatures. Trends observed in *Aplysia*, such as the effect of block length, can be used to inform prediction of the biophysics in mammalian systems. For example, Lothet *et al*. demonstrated that the size selectivity of INI was conserved between the *Aplysia* and the musk shrew vagus nerve[43], therefore, while exact temperatures and temperature rises that result in INI in mammals

(including humans) will differ from those published here, it is expected that the trend of block length will hold. To further assess INI for mammalian neurons, *in silico* work will require new computational models with proper neural conduction parameters and experimental validation in mammalian nerves will be needed.

4.6 Conclusions

This study provides the first experimental evidence of the importance of block length during heat block. Both computational predictions and experimental measurements support the hypothesis that the peak temperature for INI can be reduced by targeting a greater length of axon. Despite higher reported temperature rises in this study compared to others (Table 4.1), this work demonstrates a proof of concept that can be applied to more targeted setups and other neural systems. The ability to thermally manipulate neural tissue on a scale at which block length is important has emerged with the development of INI since lasers provide a convenient way to apply spatially precise heating. In the future, the temperature trends exhibited in the current study can be used to guide the implementation of INI in safer ways. Key factors affecting the presence and degree of thermal damage are the temperature rise and duration of elevated temperatures, according to the Arrhenius model[44,77]. Therefore, a technique that reduces temperature rise, such as modulating the targeted block length, will result in lower probabilities of damage and increase the potential duration of application.

When considering clinical implementation of INI, there is a practical limit to the length of nerve that can be manipulated based upon surgical constraints. We postulate that laser heating may be an ideal modality to perform neural heating due to the development of laser diodes with relatively low cost, smaller sizes that can be worn on the body, and compatibility with pacemakers and electrical recording devices. By using an optical approach to neural heating, high spatial and temporal specificity can provide precise control over heating that can be optimized to reduce the thermal load during therapy. Damage studies that investigate both histological and functional endpoints are required to assess the safety of INI. We do not currently claim to be below laser irradiation safety guidelines, however, this study lays the foundation for optimizing irradiation parameters such that INI adheres to ANSI safety standards. Nonetheless, techniques such as modulating block length have the potential to precisely target neurons within bulk tissue and can reduce the probability of damage to adapt INI for a wide range of applications.

4.7 References

1. Treatment options for chronic pain. American Society of Regional Anesthesia and Pain Medicine. https://www.asra.com/page/46/treatment-options-for-chronic-pain. Published 2018. Accessed March 13, 2018.

2. Chou R, Fanciullo GJ, Fine PG, et al. Clinical Guidelines for the Use of Chronic Opioid Therapy in Chronic Noncancer Pain. *J Pain.* 2009;10(2). doi:10.1016/j.jpain.2008.10.008

3. Chou R, Turner JA, Devine EB, et al. The effectiveness and risks of long-term opioid therapy for chronic pain: A systematic review for a national institutes of health pathways to prevention workshop. *Ann Intern Med*. 2015;162(4):276-286. doi:10.7326/M14-2559

4. Vowles KE, McEntee ML, Julnes PS, Frohe T, Ney JP, van der Goes DN. Rates of opioid misuse, abuse, and addiction in chronic pain: a systematic review and data synthesis. *Pain.* 2015;156(4):569-576. doi:10.1097/01.j.pain.0000460357.01998.f1

5. Edlund MJ, Martin BC, Russo JE, DeVries A, Braden JB, Sullivan MD. The role of opioid prescription in incident opioid abuse and dependence among individuals with chronic noncancer pain: the role of opioid prescription. *Clin J Pain*. 2014;30(7):557-564. doi:10.1097/AJP.0000000000000021

6. Saunders KW, Dunn KM, Merrill JO, et al. Relationship of opioid use and dosage levels to fractures in older chronic pain patients. *J Gen Intern Med*. 2010;25(4):310-315. doi:10.1007/s11606-009-1218-z

7. Li L, Setoguchi S, Cabral H, Jick S. Opioid use for noncancer pain and risk of myocardial infarction amongst adults. *J Intern Med*. 2013;273(5):511-526. doi:10.1111/joim.12035

8. Dunn KM, Saunders KW, Rutter CM, et al. Opioid prescriptions for chronic pain and overdose: A cohort study. *Ann Intern Med*. 2010;152(2):85-92. doi:10.7326/0003-4819-152-2-201001190-00006

9. National Institutes of Health. Strategy for Pain Management. NIH Initiative to Help End the Opioid Crisis. https://www.nih.gov/research-training/medical-research-initiatives/opioid-crisis/strategy-pain-management.

10. NIH Pain Consortium. NIH-DoD-VA Pain Management Collaboratory Funding Opportunity Announcement. https://grants.nih.gov/grants/guide/rfa-files/RFA-AT-17-002.html. Published 2016.

11. US Department of Health and Human Services. Development of Medications to Prevent and Treat Opioid Use Disorders and Overdose (UG3/UH3) (Clinical Trial Optional). https://grants.nih.gov/grants/guide/rfa-files/RFA-DA-19-002.html.

12. Perruchoud C, Eldabe S, Batterham AM, et al. Analgesic efficacy of high-frequency spinal cord stimulation: A randomized double-blind placebo-controlled study. *Neuromodulation*. 2013;16(4):363-369. doi:10.1111/ner.12027

13. Grider JS, Manchikanti L, Carayannopoulos A, et al. Effectiveness of Spinal Cord Stimulation in Chronic Spinal Pain: A Systematic Review. *Pain Physician*. 2016;19(1):E33-E54.

14. Verrills P, Sinclair C, Barnard A. A review of spinal cord stimulation systems for chronic pain. *J Pain Res*. 2016;9:481-492. doi:10.2147/JPR.S108884

15. Kilgore KL, Bhadra N. Nerve conduction block utilising high-frequency alternating current. *Med Biol Eng Comput*. 2004;42(3):394-406. doi:10.1007/BF02344716

16. Ackermann DM, Foldes EL, Bhadra N, Kilgore KL. Conduction block of peripheral nerve using high-frequency alternating currents delivered through an intrafascicular electrode. *Muscle and Nerve*. 2010. doi:10.1002/mus.21496

17. Kilgore KL, Bhadra N. Reversible nerve conduction block using kilohertz frequency alternating current. *Neuromodulation.* 2014;17(3):242-254. doi:10.1111/ner.12100

18. Lothet EH, Kilgore KL, Bhadra N, et al. Alternating current and infrared produce an onset-free reversible nerve block. *Neurophotonics.* 2014;1:011010. doi:10.1117/1.NPh.1.1.011010

19. Naor O, Krupa S, Shoham S. Ultrasonic neuromodulation. *J Neural Eng*. 2016;13(3):031003. doi:10.1088/1741-2560/13/3/031003

20. Hynynen K, Jolesz FA. Demonstration of potential noninvasive ultrasound brain therapy through an intact skull. *Ultrasound Med Biol.* 1998. doi:10.1016/S0301-5629(97)00269-X

21. White J, Clement GT, Hynynen K. Transcranial ultrasound focus reconstruction with phase and amplitude correction. *IEEE Trans Ultrason Ferroelectr Freq Control*. 2005. doi:10.1109/TUFFC.2005.1516024

22. Jones I, Johnson MI. Transcutaneous electrical nerve stimulation. *Contin Educ Anaesthesia, Crit Care Pain*. 2009;9(4):130-135. doi:10.1093/bjaceaccp/mkp021

23. Wells J, Kao C, Mariappan K, et al. Optical stimulation of neural tissue in vivo. *Opt Lett*. 2005;30:504-506. doi:10.1109/LEOS.2003.1251809

24. Cayce JM, Friedman RM, Jansen ED, Mahavaden-Jansen A, Roe AW. Pulsed infrared light alters neural activity in rat somatosensory cortex in vivo. *Neuroimage*. 2011;57:155-166. doi:10.1016/j.neuroimage.2011.03.084

25. Izzo AD, Walsh JT, Ralph H, et al. Laser stimulation of auditory neurons: Effect of shorter pulse duration and penetration depth. *Biophys J*. 2008;94(8):3159-3166. doi:10.1529/biophysj.107.117150

26. McPheeters MT, Wang YT, Werdich AA, Jenkins MW, Laurita KR. An infrared optical pacing system for screening cardiac electrophysiology in human cardiomyocytes. *PLoS One*. 2017. doi:10.1371/journal.pone.0183761

27. Jenkins MW, Duke AR, Gu S, et al. Optical pacing of the embryonic heart. *Nat Photonics*. 2010. doi:10.1038/nphoton.2010.166

28. Fried NM, Lagoda G a, Scott NJ, Su L-M, Burnett AL. Laser stimulation of the cavernous nerves in the rat prostate, in vivo: optimization of wavelength, pulse energy, and pulse repetition rate. *Conf Proc IEEE Eng Med Biol Soc*. 2008;2008:2777-2780. doi:10.1109/IEMBS.2008.4649778

29. Cayce JM, Friedman RM, Chen G, Jansen ED, Mahadevan-Jansen A, Roe AW. Infrared neural stimulation of the primary visual cortex in non-human primates. *Neuroimage*. 2013;84:181-190. doi:10.1016/j.neuroimage.2013.08.040

30. Cayce JM, Wells JD, Malphrus JD, et al. Infrared neural stimulation of human spinal nerve roots in vivo. *Neurophotonics*. 2015;2(1):015007. doi:10.1117/1.NPh.2.1.015007

31. Duke AR, Jenkins MW, Lu H, McManus JM, Chiel HJ, Jansen ED. Transient and selective suppression of neural activity with infrared light. *Sci Rep*. 2013;3:2600. doi:10.1038/srep02600

32. Hodgkin AL, Katz B. the Effect of Temperature on the Electrical Activity of the Giant Axon of the Squid. *J Physiol Lucas Gasser Schoepfle Erlanger Cardot Arvanitaki*. 1949;09:240-249.

33. Letcher FS, Goldring S. The effect of radiofrequency current and heat on peripheral nerve action potential in the cat. *J Neurosurg*. 1968;29(1):42-47. http://thejns.org/doi/abs/10.3171/jns.1968.29.1.0042?url_ver=Z39.88-2003&rfr_id=ori:rid:crossref.org&rfr_dat=cr_pub%3Dpubmed.

34. Klumpp D, Zimmermann M. Irreverisble differential block of A- and C-fibres following local nerve heating in the cat. *J Physiol*. 1980;298(1):471-482. doi:10.1113/jphysiol.1980.sp013095

35. Douglas WW, Malcolm JL. The effect of localized cooling on conduction in cat nerves. *J Physiol*. 1955;130(1):53-71. https://www.ncbi.nlm.nih.gov/pmc/articles/PMC1363452/.

36. Zhang Z, Lyon TD, Kadow BT, et al. Conduction Block of Mammalian Myelinated Nerve by Local Cooling to 15-30 ℃ after a Brief Heating. *J Neurophysiol*. 2016;115(3):1436-1445. doi:10.1152/jn.00954.2015

37. Frankenhaeuser B, Moore LE. The effect of temperature on the sodium and potassium permeability changes in myelinated nerve fibres of Xenopus laevis. *J Physiol*. 1963. doi:10.1113/jphysiol.1963.sp007269

38. Mou Z, Triantis IF, Woods VM, Toumazou C, Nikolic K. A simulation study of the combined thermoelectric extracellular stimulation of the sciatic nerve of the xenopus laevis: The localized transient heat block. *IEEE Trans Biomed Eng*. 2012;59(6):1758-1769. doi:10.1109/TBME.2012.2194146

39. Huxley AF. Ion Movements During Nerve Activity. *Ann N Y Acad Sci*. 1959;81:221-246.

40. Ganguly M, Jenkins MW, Jansen ED, Chiel HJ. Thermal block of action potentials is primarily due to voltage-dependent potassium currents: A modeling study. *J Neural Eng*. 2019. http://iopscience.iop.org/10.1088/1741-2552/ab131b.

41. Duke AR, Lu H, Jenkins MW, Chiel HJ, Jansen ED. Spatial and temporal variability in response to hybrid electro-optical stimulation. *J Neural Eng*. 2012;9(3):36003. doi:10.1088/1741-2560/9/3/036003

42. Wang YT, Rollins AM, Jenkins MW. Infrared inhibition of embryonic hearts. *J Biomed Opt*. 2016;21(6):60505. doi:10.1117/1.JBO.21.6.060505

43. Lothet EH, Shaw KM, Lu H, et al. Selective inhibition of small-diameter axons using infrared light. *Sci Rep*. 2017;7(1). doi:10.1038/s41598-017-03374-9

44. Dewhirst MW, Viglianti BL, Lora-Michiels M, Hanson M, Hoopes PJ. Basic principles of thermal dosimetry and thermal thresholds for tissue damage from hyperthermia. In: *International Journal of Hyperthermia*. Vol 19. ; 2003:267-294. doi:10.1080/0265673031000119006

45. Yarmolenko PS, Moon EJ, Landon C, et al. Thresholds for thermal damage to normal tissues: An update. *Int J Hyperth*. 2011;27(4):320-343. doi:10.3109/02656736.2010.534527

46. Hines ML, Carnevale NT. The NEURON Simulation Environment. *Neural Comput*. 1997;9(6):1179-1209. doi:10.1162/neco.1997.9.6.1179

47. Lu H, Chestek CA, Shaw KM, Chiel HJ. Selective extracellular stimulation of individual neurons in ganglia. *J Neural Eng*. 2008;5(3):287-309. doi:10.1088/1741-2560/5/3/003

48. Coggeshall RE. A Light and Electron Microscope Study of the Abdominal Ganglion of *Aplysia* Californica. *J Neurophysiol*. 1967;30(6):1263-1287.

49. Platkiewicz J, Brette R. A threshold equation for action potential initiation. *PLoS Comput Biol*. 2010. doi:10.1371/journal.pcbi.1000850

50. Rieke V, Butts Pauly K. MR thermometry. *J Magn Reson Imaging*. 2008;27(2):376-390. doi:10.1002/jmri.21265

51. De Poorter J, De Wagter C, De Deene Y, et al. Noninvasive MRI Thermometry with the Proton Resonance Frequency (PRF) Method:In Vivo Results in Human Muscle. *Magn Reson Med*. 1995;33(1):74-81. doi:10.1002/mrm.1910330111

52. Poorman ME, Chaplin VL, Wilkens K, et al. Open-source, small-animal magnetic resonance-guided focused ultrasound system. *J Ther Ultrasound*. 2016. doi:10.1186/s40349-016-0066-7

53. Rattay F, Aberham M. Modeling Axon Membranes for Functional Electrical Stimulation. *IEEE Trans Biomed Eng*. 1993;40(12):1201-1209. doi:10.1109/10.250575

54. De Col R, Messlinger K, Carr RW. Conduction velocity is regulated by sodium channel inactivation in unmyelinated axons innervating the rat cranial meninges. *J Physiol*. 2008;586(4):1089-1103. doi:10.1113/jphysiol.2007.145383

55. De Col R, Messlinger K, Carr RW. Repetitive activity slows axonal conduction velocity and concomitantly increases mechanical activation threshold in single axons of the rat cranial dura. *J Physiol*. 2012;590(4):725-736. doi:10.1113/jphysiol.2011.220624

56. Kandel ER, Schwartz JH, Jessell TM, Siegelbaum SA, Hudspeth AJ. *Principles of Neural Science*. Fifth Edit. The McGraw-Hill Companies, Inc.; 2013.

57. Lee KH, Chung K, Chung JM, Coggeshall RE. Correlation of cell body size, axon size, and signal conduction velocity for individually labelled dorsal root ganglion cells in the cat. *J Comp Neurol*. 1986. doi:10.1002/cne.902430305

58. Fridman GY, Della Santina CC. Safe direct current stimulation to expand capabilities of neural prostheses. *IEEE Trans Neural Syst Rehabil Eng*. 2013. doi:10.1109/TNSRE.2013.2245423

59. Tai C, De Groat WC, Roppolo JR. Simulation analysis of conduction block in unmyelinated axons induced by high-frequency biphasic electrical currents. *IEEE Trans Biomed Eng*. 2005. doi:10.1109/TBME.2005.847561

60. Bhadra N, Vrabec TL, Bhadra N, Kilgore KL. Reversible conduction block in peripheral nerve using electrical waveforms. *Bioelectron Med*. 2017. doi:10.2217/bem-2017-0004

61. Whitwam JG, Kidd C. The use of direct current to cause selective block of large fibres in peripheral nerves. *Br J Anaesth*. 1975. doi:10.1093/bja/47.11.1123

62. George SS, Wise AK, Fallon JB, Shepherd RK. Evaluation of focused multipolar stimulation for cochlear implants in long-term deafened cats. *J Neural Eng*. 2015. doi:10.1088/1741-2560/12/3/036003

63. Duke AR, Peterson E, Mackanos MA, Atkinson J, Tyler D, Jansen ED. Hybrid electro-optical stimulation of the rat sciatic nerve induces force generation in the plantarflexor muscles. *J Neural Eng*. 2012;9(6):066006. doi:10.1088/1741-2560/9/6/066006

64. Sundqvist B. Thermal diffusivity and thermal conductivity of Chromel, Alumel, and Constantan in the range 100–450 K. *J Appl Phys*. 1992;72(2):539-545. doi:10.1063/1.351885

65. Incropera FP, De Witt DP. *Fundamentals of Heat and Mass Transfer*. 3rd ed. Wiley Publishers; 1995.

66. Ishihara Y, Calderon A, Watanabe H, et al. A precise and fast temperature mapping using water proton chemical shift. *Magn Reson Med*. 1995;34(6):814-823. doi:10.1002/mrm.1910340606

67. Willie JT, Laxpati NG, Drane DL, et al. Real-time magnetic resonance-guided stereotactic laser amygdalohippocampotomy for mesial temporal lobe epilepsy. *Neurosurgery*. 2014. doi:10.1227/NEU.0000000000000343

68. McNichols RJ, Gowda A, Kangasniemi M, Bankson JA, Price RE, Hazle JD. MR Thermometry-Based Feedback Control of Laser Interstitial Thermal Therapy at 980 nm. *Lasers Surg Med*. 2004. doi:10.1002/lsm.10243

69. Hynynen K. MRI-guided focused ultrasound treatments. *Ultrasonics*. 2010. doi:10.1016/j.ultras.2009.08.015

70. Xu A, Roe A, Xiaotong Z, Xi W. Quantifying tissue temperature change induced by infrared neural stimulation by 7T MR thermometry. *Sci Adv*.

71. Hale GM, Querry MR. Optical Constants of Water in the 200-nm to 200-microm Wavelength Region. *Appl Opt*. 1973;12(3):555-563. doi:10.1364/AO.12.000555

72. Okabe K, Sakaguchi R, Shi B, Kiyonaka S. Intracellular thermometry with fluorescent sensors for thermal biology. *Pflugers Arch Eur J Physiol*. 2018. doi:10.1007/s00424-018-2113-4

73. Gardner B, Matousek P, Stone N. Temperature Spatially Offset Raman Spectroscopy (T-SORS): Subsurface Chemically Specific Measurement of Temperature in Turbid Media Using Anti-Stokes Spatially Offset Raman Spectroscopy. *Anal Chem*. 2016;88(1):832-837. doi:10.1021/acs.analchem.5b03360

74. Rao YJ, Webb DJ, Jackson DA, Zhang L, Bennion I. In-fiber bragg-grating temperature sensor system for medical applications. *J Light Technol*. 1997;15(5):779-784. doi:10.1109/50.580812

75. Jacques SL. Laser-Tissue Interactions: Photochemical, Photothermal, and Photomechanical. *Surg Clin North Am*. 1992;72(3):531-558. doi:10.1016/S0039-6109(16)45731-2

76. Kitamura R, Pilon L, Jonasz M. Optical constants of silica glass from extreme ultraviolet to far infrared at near room temperature. *Appl Opt*. 2007. doi:10.1364/AO.46.008118

77. Welch AJ, Van Gemert MJC. *Optical-Thermal Response of Laser-Irradiated Tissue.*; 2011. doi:10.1007/978-90-481-8831-4

Chapter V

Optimizing Thermal Block Length During Infrared Neural Inhibition to Minimize Temperature Thresholds

5.1 Abstract

Objective: Infrared neural inhibition (INI) is a method of blocking the generation or propagation of neural action potentials through laser heating that targets wavelengths strongly absorbed by water. Recent work has identified that the distance heated along axons, the block length (BL), modulates the temperature needed for inhibition; however, this relationship has not been characterized. This study explores the BL parameter during INI to identify how it may be utilized towards minimizing the temperature required for INI.

Approach: To understand the relationship between BL and the temperature required for INI, excised nerves from *Aplysia californica* were laser-heated over different lengths of axon during electrical stimulation of compound action potentials. INI was provided by irradiation (λ=1470 nm) from a custom probe (n=6 nerves), and subsequent validation was performed by providing heat block using perfused hot media over nerves (n=5 nerves).

Main Results: Two BL regimes were identified. Short BLs (thermal full width at half maximum (tFWHM) = 0.81 - 1.15 mm) demonstrated that increasing the tFWHM results in lower temperature thresholds for INI ($p < 1.37e-5$), while longer BLs (tFWHM = 1.15 - 3.03 mm) show no significant change in the temperature for INI threshold with increased tFWHM ($p > 0.0167$). Validation of this longer regime was performed using perfused hot media over different lengths of nerves. This secondary heating method similarly showed no significant change ($p > 0.0167$) in the temperature threshold (tFWHM = 1.25 - 4.42 mm).

Significance: This work characterized how the temperature threshold for neural heat block varies with BL and identified an optimal BL around tFWHM = 1.15 mm which minimizes the maximum temperature applied to tissue during INI. Understanding how to optimally target lengths of nerve to minimize temperature during INI can help inform the design of devices for longitudinal animal studies and human implementation.

5.2 Introduction

Developing infrared neural inhibition (INI) as a clinically viable technology may aid in therapy of various diseases requiring neuromodulation treatment. Due to INI's high spatial specificity[1], lack of exogenous agents, and preferential block of small diameter neurons at lower temperatures compared to large diameter neurons[2], it has been hypothesized that INI may be used to mitigate chronic pain since many pain signals are propagated via unmyelinated, small-diameter neurons (C-fibers)[3]. INI applies infrared irradiation that targets relatively strong absorption bands of water (λ=1450-1470 nm, 1860-1880 nm) compared to visible wavelengths, resulting in tissue heating. This induces a heat block[4] through the temperature dependence of voltage-gated potassium ion channel activation[5,6] that can be applied with high spatial precision. This laser-induced heat block has been shown to inhibit conduction in small diameter[2] and unmyelinated neurons[7], conduction in myelinated motor neurons[1], cardiac contractions from embryonic quail hearts[8], and action potentials in isolated embryonic rat hippocampal neurons[9].

The parameter space of inhibition, including laser power and irradiation distribution considerations, needs to be explored to identify optimal techniques for providing safe, efficacious, and therapeutic INI. INI has been shown to be non-damaging in the acute setting[1], and damage probabilities have been investigated[10], but techniques are needed to lower the induced temperatures to make them viable during sustained laser applications (minutes - days). Hybrid techniques offer one potential route for this. Inhibition utilizing laser irradiation paired with KHFAC (kilohertz frequency alternating current) has been tested to overcome the "onset response" associated with KHFAC[11]. This, however, forgoes the size selectivity benefit of INI since the main inhibition mechanism is through KHFAC, which is problematic when targeting pain conducting neurons since INI is only applied briefly at the start of the hybrid inhibition process. Another hybrid technique pairs INI with the application of glucose to ultimately lower the radiant exposure needed for INI[12]. Considering purely optical modulation, prior exploration[7] into the spatial application of INI has indicated that the block length (BL), the spatial length of axon heated, plays a role in the radiant exposure, and therefore the temperature, needed to elicit INI. This presents an important consideration for any potential clinical device as improper nerve targeting may result in excessive heating leading to an increased potential for tissue damage. BL may serve as a parameter that can be readily optimized. Thus far, only two BLs have been tested[7], suggesting that using greater BL reduces the INI temperature threshold, but more exploration is needed to understand the extent to which this phenomenon can be optimized.

One limitation of prior experiments is a lack of adequate temperature monitoring of the tissue during inhibition. Temperature measurements have been performed in tissue or tissue phantoms after the identification of INI radiant exposure thresholds[1,2,7,13], or computational modeling has been utilized to

estimate the temperature[9,13,14]. Performing measurements directly in the tissue during INI application is difficult, and has thus far only been feasible using the open patch technique[10,15]. Therefore, a methodology is needed to provide simultaneous electrophysiological and thermal information, and the spatial distribution of heating needs to be probed for the purpose of exploring the effect of BL. Thermal imaging serves as an ideal technique to measure spatial thermal information, but has a penetration depth in tissue of 80 μm or less due to water's strong absorption of the electromagnetic radiation spectrum sensed by these cameras[16]. This renders thermal imaging ineffective at measuring temperatures in aqueous environments such as in experiments utilizing *Aplysia californica* nerves which have typically involved immersing the entire nerve in solution.

Here, a setup was developed that exposed a region of nerve by temporarily bringing it out of saline solution, freeing it for simultaneous non-contact irradiation and thermal imaging. Using this design, the effect of BL along the nerve was characterized for INI by utilizing different lengths of irradiation along *Aplysia* pleural-abdominal nerves. Validation of the trend seen at longer BLs was then performed using perfused hot saline rather than IR laser heating in a separate custom dish.

5.3 Methods

5.3.1 Electrophysiological Recordings

Aplysia left pleural-abdominal nerves were used to assess the temperature at inhibition threshold across different block lengths. *Aplysia* have proven to be a valuable animal model for neural conduction studies involving INI[1,2,6,7,11] due to 1) the robustness of the system, 2) the similarity of the morphology of their neurons to unmyelinated pain conducting neurons in humans (C fibers)[3,17,18], and 3) their length (>5 cm) which allows for the separation of neural signals due to temporal dispersion as a function of conduction velocity (CV). *Aplysia* were anesthetized using 333 mM $MgCl_2$ (0.5 mL/g) and left pleural-abdominal nerves were dissected out of the animal and placed into one of two custom dishes (described below) containing *Aplysia* saline (460 mM NaCl, 10 mM KCl, 22 mM MgCl, 33 mM $MgSO_4$, 10 mM $CaCl_2$, 10 mM glucose, 10 mM HEPES, pH ~7.6). For all excised nerves, nerve ends were suctioned into separate hand-pulled polyethylene suction electrodes providing electrical stimulation of compound action potentials (CAPs) at one end and electrophysiological recording at the other end. Acquired signals (20kHz sampling for cylindrical lens probe experiments, 5kHz for perfusion channel experiments) were amplified and filtered

(10k gain, 100-1000 Hz bandpass filtered) (Model 1700, A-M Systems, Sequim, WA) and then digitized (Digidata 1440a, Molecular Devices, San Jose, CA) and recorded using protocols in pClamp10 (Molecular Devices, San Jose, CA).

5.3.2 Infrared Neural Inhibition Protocols

5.3.2.1 Nerve Dish

An 8.5" Petri dish was coated with PDMS (Sylgard 184, Dow, Midland, MI) to create a raised platform (width = 1 cm) in the center of the dish (Figure 5.1). Once the PDMS cured, the dish was mounted in a 3D printed holder that was secured to a z-axis translation stage. This stage was mounted on an optical breadboard, along with the optical probe, and set in a Faraday cage for low noise electrophysiological recordings. When the *Aplysia* saline level in the dish is below the platform height, a nerve may be laid across it, providing simultaneous suctioning of the immersed nerve ends and free beam irradiation of the out of solution region of the nerve on the platform. A notch was cut into the PDMS for repeatable positioning of the nerve (see below for how nerve hydration was maintained).

5.3.2.2 Cylindrical Lens Probe

A probe that focused the light in one dimension was constructed to vary the length over which the nerve was irradiated. This probe (Figure 5.1) first collimated the light from an optical fiber using a fiber coupled collimation lens (F260APC-1550, Thorlabs Inc., Newton, NJ), and then focused the light in one dimension using a cylindrical lens (f=12.5 mm, 1-inch diameter). This cylindrical lens provided a means to irradiate different lengths along the nerve since the spot size along the nerve could be changed based on the distance between the probe output and the nerve due to the divergence of the light in one dimension. The orthogonal collimated axis reduced the needed precision of nerve placement relative to the invisible IR irradiated spot. Spot sizes ($1/e^2$ width) at various distances from the probe output were calibrated using a beam profiler (BP209-IR2, Thorlabs Inc., Newton, NJ). This cylindrical lens probe was positioned over the nerve using a 3-axis translation stage and rotated such that the focusing axis of the cylindrical lens was parallel to the axial direction of the nerve, providing an irradiated $1/e^2$ spot diameter between 0.4 and 5 mm along the nerve. The non-focused, collimated axis spot width perpendicular to the nerve was ~5 mm for all probe distances. This resulted in losing a significant amount of the light since it did not irradiate the nerve (diameters ~ 0.35 mm), but this methodology did allow for easier targeting and greater confidence of the nerve placement within the invisible laser spot. The light that did not hit the nerve was instead irradiating the surrounding PDMS. Due to the relative low absorption at 1470 nm, the temperature rise in the PDMS

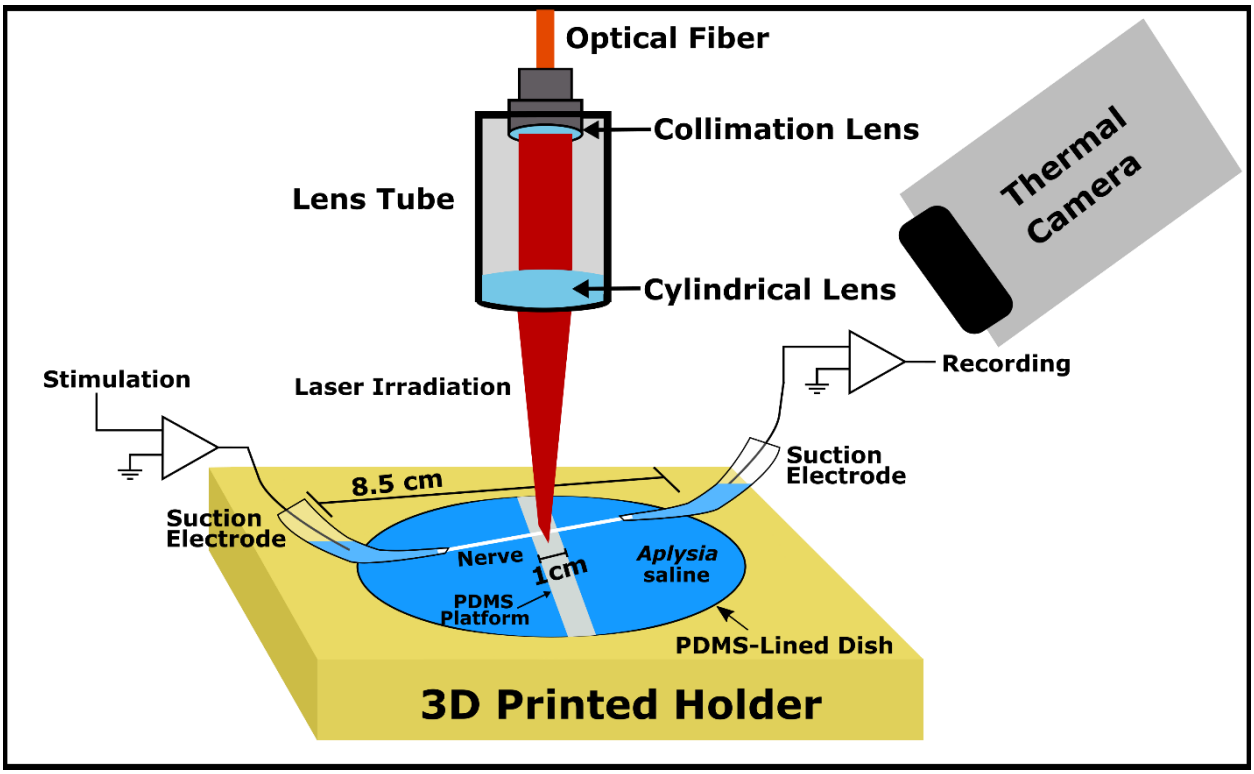

Figure 5.1. Infrared neural inhibition experimental setup. An *Aplysia* nerve is excised and placed in a bath such that the ends are immersed, and the center is temporarily raised out of solution on a PDMS platform. Suction electrodes provide electrical stimulation of compound action potentials at one end and recording at the other end. An optical probe, utilizing a cylindrical lens with the focusing axis aligned axially with the nerve, is positioned over the nerve between the suction electrodes to apply INI to the exposed region. Changing the probe's distance to the nerve alters the irradiation length along the nerve, changing the applied block length. A thermal camera is used to measure the induced temperature rise. *Aplysia* saline was regularly applied to the exposed nerve to maintain hydration.

was shown to be < 20% of the temperature rise generated in the nerve.

5.3.2.3 Cylindrical Lens Probe Experiments

For experiments applying INI using the cylindrical lens probe, n=6 *Aplysia* (118-287 grams) nerves were used. Conventional setups have relied on measuring the radiant exposure used to elicit inhibition, making temperature measurements after the fact[1,2,7], but the temperature of the tissue is the important factor because of the thermal mechanism of INI[4,5]. Differences between the temperature induced during INI and the value measured in a phantom can arise due to changes in materials used and differing thermal boundary conditions that cannot always be predicted (such as changes in the coefficient of convection or the presence of evaporative cooling). Accurate temperature measurements at a depth in tissues pose a serious challenge. Bringing the nerve out of solution on the raised platform offers both the opportunity for focused, non-contact irradiation and for direct, simultaneous measurement of the superficial temperature with a thermal camera during INI. A thermal camera (FLIR A8313sc, FLIR Systems, Inc., Wilsonville, OR) was mounted in the setup which recorded the temperature in thermal image sequences at ~15 frames per second (fps) with ~50 μm pixel size, allowing for time correlated electrophysiological and thermal information. Once the nerve was suctioned, positioned in the cut notch, and the probe was placed, electrical stimulation (1 ms pulses, 2 Hz, 150-400 μA) was applied for 40 seconds to elicit compound action potentials (CAPs) with 20 seconds of laser (Innovative Photonic Solutions, Monmouth, NJ) irradiation between t=10 s and t=30 s (λ= 1470 nm, 200 μs pulses, 200 Hz). Irradiation lengths ($1/e^2$ spot diameters along the nerve) between 0.4 and 5 mm were applied to each nerve (Table 5.1), and for each irradiation length a set of recordings (4-10 each) was measured using a range of laser pulse energies (0.09 – 1.25 mJ/pulse). These recordings probed how different induced temperatures result in varying degrees of inhibition of the compound action potentials which aided in the application of a PROBIT regression to determine the temperature threshold for INI. An exact measure of absorbed power is not easily obtainable since the majority of the light does not hit the nerve, but instead irradiates the PDMS, and because this methodology resulted in many different radiant exposures due to the various irradiation lengths applied along the nerve. Ultimately the important factor for inhibition is the temperature of the nerve since temperature has been implicated as the driver of heat block effects[4–6], and from the safety perspective the mechanism of damage will be thermal. INI wavelengths are non-ionizing and too low in photon energy to drive photochemical processes[19,20], and pulse parameters are not utilized within the stress confinement regime[21] where acoustic damage and ablation would be possible. Thus, the thermal camera provides the important predictive parameter. Immediately after each trial, saline was applied to the exposed region of the nerve to maintain tissue hydration (>2 mL every 3-5 minutes). After application, an equal amount of saline was removed to ensure the nerve remained exposed. For each new set of irradiation length trials, the saline level was raised to immerse the entire nerve and the distance

Table 5.1. $1/e^2$ Spot Diameters (Irradiated Axon Length) Tested for Each Nerve

Nerve	Spot Diameters Tested [mm]
1	0.4, 0.5, 0.7, 0.8, 1, 3, 5
2	0.4, 0.8, 5
3	0.4, 0.5, 0.6, 0.8, 1, 2, 3, 5
4	0.4, 0.5, 0.7, 0.8, 1, 2, 2.5, 3, 5
5	0.4, 0.7, 1, 5
6	0.4, 0.6, 0.7, 0.8, 1, 2, 3, >5

of the probe from the nerve was repositioned. For each new irradiation length, the saline level was lowered to expose the nerve and the laser power was again varied across recording trials. The order of applied irradiation lengths was randomized for each nerve to account for any hysteresis, long-term effects, or deterioration of the nerves.

5.3.3 Hot Media Inhibition Protocols

5.3.3.1 Perfusion Experiments

A 3D printed dish (Figure 5.2) as described in Ganguly *et al.* was used that allows for a nerve to span 3 isolated chambers[6]. Nerves (n = 5) were excised and placed in the dish as shown in Figure 5.2. A suction electrode was applied to each nerve end (chambers 1 and 3). The central portion of the nerve traversed the middle chamber (chamber 2) which could be varied in length by changing the position of the partition between chamber 2 and chamber 3. This was modulated to apply chamber lengths of 1, 3, and 5 mm. Doors were placed to separate the three chambers and lined with Vaseline to create a water-tight seal. After door placement, the saline level was raised in each chamber to completely immerse the nerve.

Tubing connected to a circulation pump and in-line heater (SC-20, Warner Instruments, LLC, Hamden, CT) was connected to the central chamber (Chamber 2) to provide an inlet and outlet for media flow. Circulated saline was heated using an externally triggered temperature control system (CL-100, Warner Instruments, LLC, Hamden, CT) with feedback from a thermistor (TA-29, Warner Instruments, LLC, Hamden, CT) placed just downstream of the nerve in the middle chamber. Recordings made in pClamp10 (Molecular Devices, San Jose, CA) consisted of 410 second trials during which electrical stimulation (150-300 μA, 1 Hz, 0.8 ms) was provided for 240 seconds and the heating was applied for the first 70-150 seconds of electrical stimulation, allowing for a return to baseline temperature (20^{o}C) and a rest period of no activation during the final ~170 seconds of the trial. For each channel width, 7 trials were sequentially recorded during which the applied holding temperature of the heater was varied from 20^{o}C to 50^{o}C in 5^{o}C steps per trial. Extra trials applying either longer heating times or higher temperature settings were performed if complete inhibition of the CAP was not achieved.

5.3.3.2 Perfusion tFWHM Estimation

The thermal full width at half maximum (tFWHM) of heating was estimated using a thermal camera (Thermovision A20, FLIR Systems Inc., Wilsonville, OR) with spatial resolution ~0.45 mm and ~7 fps imaging. The camera was positioned directly above the perfusion chamber, and thermal image sequences

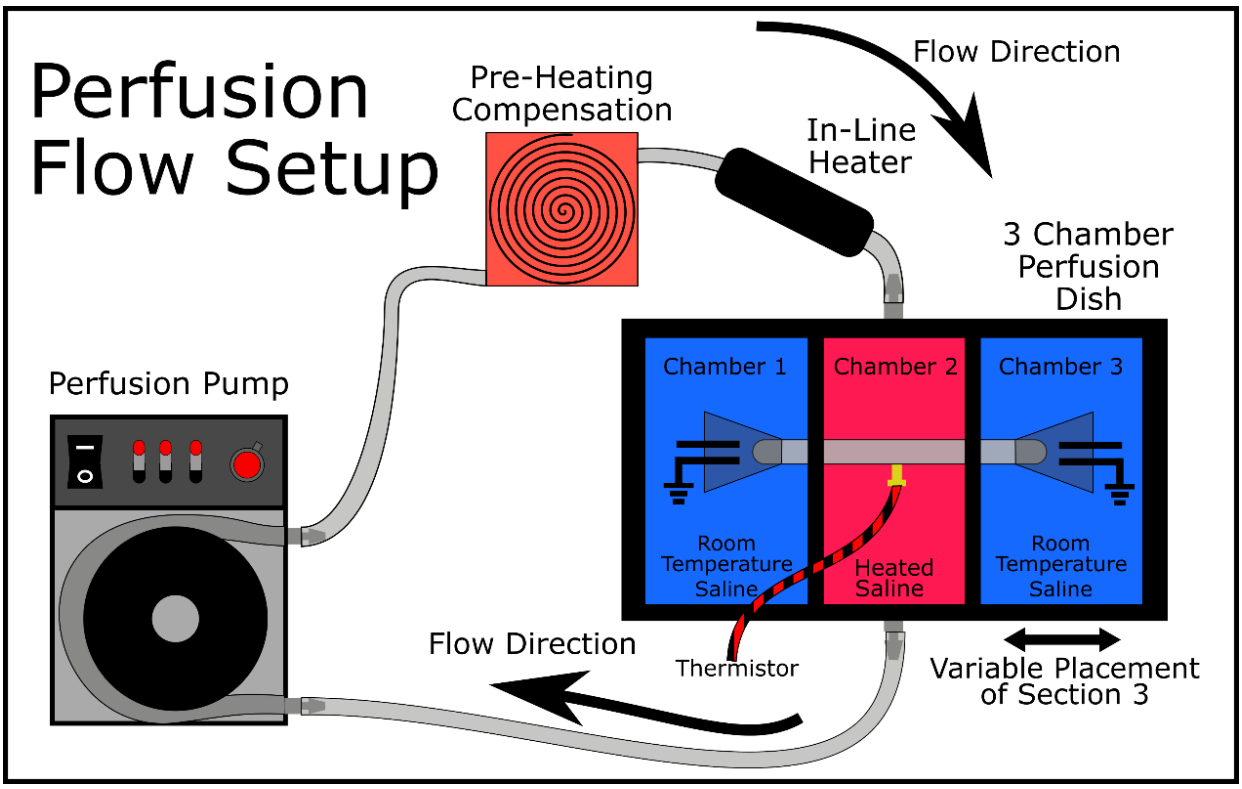

Figure 5.2. Perfusion Heating Setup. A 3D printed dish containing 3 chambers was used to perfuse heated saline over select lengths of nerve. The partition between chambers 2 and 3 could be moved in relation to chamber 1, providing different lengths for chamber 2 (tFWHM tested = 1.25, 2.55, and 4.42 mm). Suction electrodes were applied to nerve ends in chambers 1 and 3 so that a middle region traversed chamber 2 in which media heated by an in-line heater was circulated with a pump. Temperature at the nerve was measured using a thermistor placed just downstream.

were recorded for an entire heating/cooling cycle. Three trials of each chamber length were performed. The average tFWHM of the temperature distribution along the nerve was calculated by linearly interpolating thermal images along the nerve's location in the chamber. This assessment was performed after 120 seconds of heating. These measurements were then used to determine how the tFWHM due to perfusion heating compared to the tFWHM due to laser heating described in the previous section.

5.3.4 Data Analysis

5.3.4.1 Electrophysiological Data

CAP signals were separated into 3 conduction velocity (CV) regions corresponding to slow, medium, and fast CV neurons (Figure 5.3A). By doing this, the effect of BL on the temperature for inhibition could be distinguished across axon diameter populations since conduction velocity is proportional to the square root of axon diameter[22]. CAP shapes and distributions were generally consistent across nerves, but fatigue-dependent[23,24] or temperature-dependent[4] CV shifts, as well as some variability in the CAP distribution across preparations, made it difficult to select a set of fixed boundaries that universally fit all nerves without consistently cutting through individual peaks within CAPs. Doing this would conflate a decrease in signal due to inhibition with a decrease in signal due to signals shifting between CV regions. Therefore, CV boundaries were found for each nerve. Inner boundaries, i.e. those that separate slow from medium components and medium from fast components of the CAP, were determined for each recording by selecting CVs where the variance in the voltage across the 40 second recordings (80 CAPs) were minimized since these points correspond to a location in the CAP with minimal shifts in the CV. This minimum was found twice, first for the portion of the signal slower than 0.5 m/s and then for the portion of signal faster than 0.5 m/s, to select the two inner boundaries (Figure 5.3A). Outer boundaries were selected to encompass the entire CAP. These four boundaries then separated the signal into the slow, medium, and fast CV regions. For each trial, the rectified area under the curve (RAUC), which informed the relative number of neurons contributing to the signal, was calculated for each CV group, and the RAUC of the noise floor was subsequently background subtracted. These background subtracted RAUCs were then normalized to the average RAUC of CAPs in the first 5 seconds of the trial (Figure 5.3B). Inhibition was defined as a 50% or greater drop in RAUC, and this threshold was applied to RAUCs from all trials to achieve binary inhibition data for each CV group for all CAPs.

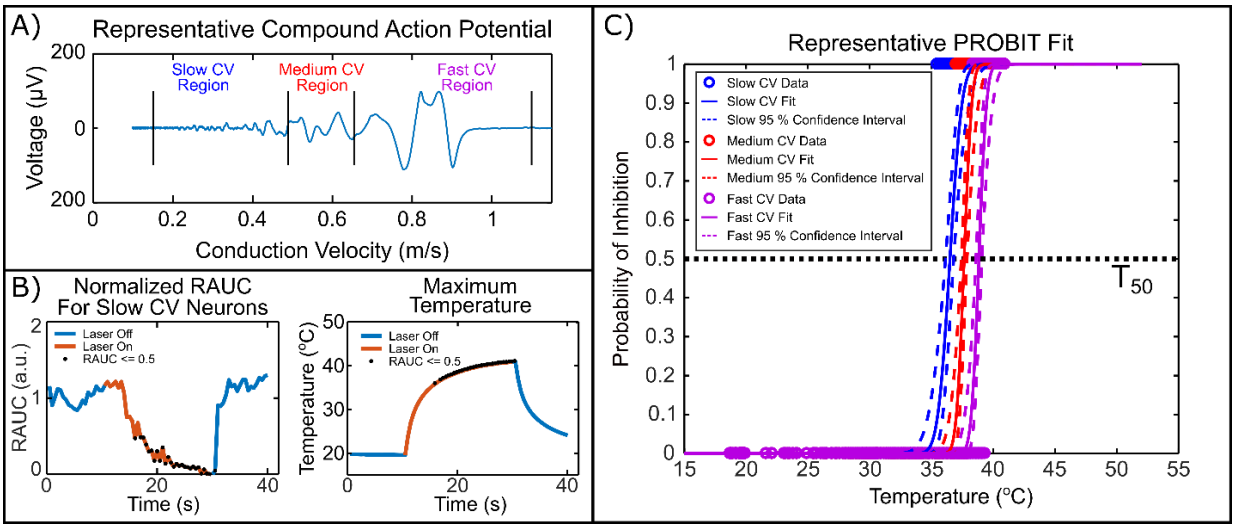

Figure 5.3. A) A representative CAP is plotted as a function of its conduction velocity. Boundaries (black lines) section the signal into slow, medium, and fast CV regions which were processed separately. B) A representative normalized rectified area under the curve (RAUC) of a slow CV region is plotted over time, and values below 0.5 are marked as inhibition. The maximum temperature of the nerve from thermal imaging was extracted for each CAP and used to inform the temperature for inhibition. C) Joint temperature and inhibition data were used in a PROBIT analysis. Each binary inhibition data point is plotted at its corresponding temperature (open circles) which overlay each other due to the large sampling density. These data are used to fit curves which predict the probability of inhibition as a function of temperature (solid lines), as well as the 95% confidence interval of the fits (dashed lines), and was performed for slow (blue), medium (red), and fast (magenta) CV neuron populations. The T_{50} was determined as the temperature that results in a 50% probability of inhibition (dotted black line).

5.3.4.2 Thermal Data

Thermal camera recordings were adjusted for any time offset from the electrophysiological data by assessing the time derivative of the maximum temperature. The time that the laser turned on was matched with the frame showing the largest increase in temperature. Similarly, the time that the laser turned off was associated with the frame with the largest drop in temperature. The location of maximum temperature rise was identified as the pixel that most often exhibited the maximum temperature while the laser was on. The temperature of this pixel was then tracked through the entire thermal image sequence and served as the predictor value in the PROBIT regression. Since the axis of the nerve was placed in the x-direction of the thermal image, the temperature information along the row of the image containing the maximum temperature pixel was extracted and used to assess the spatial information about the temperature rise along the nerves. The thermal full width at half maximum (tFWHM) of the temperature distribution along this row was calculated for each frame. Thermal data from each recording was then interpolated to obtain the maximum temperature and tFWHM at each electrical stimulation for each trial to estimate the temperature distribution for each CAP (Figure 5.3B). In perfusion heating trials, the thermistor was used to measure the temperature of the nerve during perfusion experiments and was collected in pClamp10 (Molecular Devices, San Jose, CA) along with electrophysiological data. The temperature information for each CAP was obtained by using the value corresponding to the time of each electric stimulation artifact.

5.3.4.3 PROBIT Regression Fits

Using the extracted temperature and inhibition information for each CAP, data across trials were pooled for each irradiation length and a PROBIT regression model was applied to each set of pooled data for each CV group. PROBIT models were applied using "glmfit", a built-in MATLAB function, with a PROBIT linker function (Figure 5.3C). The maximum temperature along the nerve served as the predictive variable and the binary RAUC observations was the response variable. Once fit, the temperature resulting in the fifty percent probability of inhibition (T_{50}) was calculated by interpolating the fitted PROBIT function. The tFWHM for each T_{50} was calculated as the average tFWHM of the last 10 seconds of heating across all trials used to compute that T_{50}.

5.3.4.4 Determining Block Length Trends

Paired tFWHM and T_{50} information were used to perform least squares fit of the inhibition temperature as a function of tFWHM. For perfusion heating trials, a linear fit was used. For laser heating trials, linear, quadratic, and exponential functions resulted in poor fits (Table 5.2), and it became apparent that a different trend was optimal for the data. Since two distinct trends with tFWHM were observed in the

data, a continuous piecewise function made of two linear lines joined at an intersection point was defined (Equation 5.1) and used in a least-squares regression. The location of the intersection point, S, was optimized by iterating from S=0.85 mm to S=1.5 mm in 0.005 mm steps, and the optimal S was chosen based on the best goodness of fit metric (highest R^2 value) for the entire piecewise equation. Any dependence of T_{50} on the tFWHM was assessed by comparing the fit slope coefficients of the trendline (the short and long regime of irradiated nerves and the singular slope of perfusion heated nerves) to a flat line. This applied a null hypothesis that these lines do not differ from a line with zero slope and the alternative hypothesis that the slopes do differ from zero. A Bonferroni correction was applied to account for each of the three CV populations that were being separated out from the original datasets, yielding an alpha significance value of $\alpha=0.05/3 = 0.0167$.

5.4 Results

5.4.1 Two Block Length Regimes Are Observed During INI

Across the 6 nerves tested, CAPs were split into slow, medium, and fast conduction velocity regions and a PROBIT regression was applied to identify the temperature for the 50% probability of inhibition (T_{50}) for each irradiation length. Representative data are shown in Figure 5.3. The analysis was performed for all irradiation lengths across all nerves, resulting in 39 data points in all for each CV population. All T_{50} are plotted at their corresponding tFWHM of heating in Figure 5.4. Analysis of the data show consistent trends across the three CV populations. Least squares regression was used to fit trendlines to the data. Visual inspection of the fits, assessment of the residuals, and the R^2 goodness of fit metric (Table 5.2) all demonstrated that neither a polynomial nor an exponential decay was appropriate to capture the observed trend.

To provide a fit consistent with the data, a continuous piecewise function was created (Equation 5.1) to apply two separate lines joined at an intersection point, S, to capture two distinct trends in the data:

$$T_{50} = \begin{cases} a * (tFWHM - S) + b, & (tFWHM < S) \\ b, & (tFWHM = S) \\ c * (tFWHM - S) + b, & (tFWHM > S) \end{cases} \quad \text{Equation 5.1}$$

Table 5.2. T_{50} Goodness of Fit Metrics for Various Fit Types

Population	Linear		Quadratic		Exponential *		Exponential +		Piecewise	
	R^2	Adjusted R^2	R^2	Adjusted R^2	R^2	Adjusted R^2	R^2	Adjusted R^2	R^2	Adjusted R^2
Slow	0.108	0.084	0.372	0.337	0.613	0.602	0.106	0.081	0.698	0.681
Medium	0.045	0.019	0.253	0.211	0.047	0.021	0.292	0.272	0.395	0.361
Fast	0.055	0.029	0.362	0.327	0.057	0.032	5e-4	-0.027	0.727	0.712

* All data points included in fit
+ Longest FWHM point removed from fit

where a, b, and c are coefficients fit to the data for each CV population, and b represents the T_{50} at tFWHM = S. The location of S corresponding to a maximal R^2 value was chosen.

Parameters for the optimal trendline fits can be found for each CV population in Table 5.3, and the trendlines can be found plotted for each CV region (Figure 5.4). Equations presented in Figure 5.4 are a simplified form of Equation 5.1. The value of S is similar for all three regions, 1.145 mm, 1.205 mm, 1.11 mm for slow, medium, and fast CV regions, respectively, with an average of ~1.15 mm. Slopes of the linear lines in the piecewise function were tested for a significant difference from a flat line. It was found that for all CV populations, the decreasing trend of T_{50} with increasing tFWHM in the short BL regime is significant (p = 5.54e-11, 1.37e-5, and 4.46e-12 for the slow, medium, and fast CV neurons, respectively). For the long BL regime, slow, medium, and fast CV populations demonstrated p-values of p = 0.096, 0.096, and 0.019, respectively, demonstrating that no significant trend is exhibited between the T_{50} and tFWHM in this longer BL regime ($\alpha = 0.0167$). To validate that this result at longer BL is real effect and not an experimental artifact, a secondary method of heating was applied.

5.4.2 Heat Block via Perfused Hot Media Validates the Longer Block Length Regime

Using the shown perfusion setup (Figure 5.2), heated *Aplysia* saline was perfused over nerves as a secondary method of applying neural heat block. The temperature throughout trials was measured using a thermistor that was placed at the depth of the nerve in the bath. PROBIT models were fit to inhibition trials to determine the T_{50}. Values of T_{50} from each set of measurements for each chamber width were averaged across the 5 nerves and are plotted in Figure 5.5 as a function of the tFWHM (tFWHM = 1.25, 2.55, and 4.42 mm) from the subsequent thermal camera analysis. A linear least squares fit was applied to these T_{50} means for each CV population. Trend lines show goodness of fits of $R^2 = 0.61$, 0.69, and 0.82 for the slow, medium, and fast CV neurons, respectively. These linear regressions were tested for a significant difference from a line with zero slope, and the resulting p-values were p= 0.075, 0.024, and 0.249 for the slow, medium, and fast CV populations, respectively, demonstrating that no significant trend between T_{50} and BL is exhibited for all CV populations ($\alpha = 0.0167$), mimicking the trend from laser irradiation in the long BL regime.

Table 5.3. Optimal fits of piecewise function parameters

CV Population	S (Intersection Point)	Coefficient a (Short Regime Slope) [95% CI]	Coefficient b (Temperature at S) [95% CI]	Coefficient c (Long Regime Slope) [95% CI]
Slow	1.145	-23.61 [-29.06, -18.16]	36.01 [35.32, 36.69]	0.56 [-0.30, 1.42]
Medium	1.205	-16.52 [-23.55, -9.49]	38.54 [37.41, 39.67]	0.93 [-0.49, 2.36]
Fast	1.11	-25.49 [-30.84, -20.14]	39.76 [39.19, 40.33]	0.76 [0.04, 1.47]

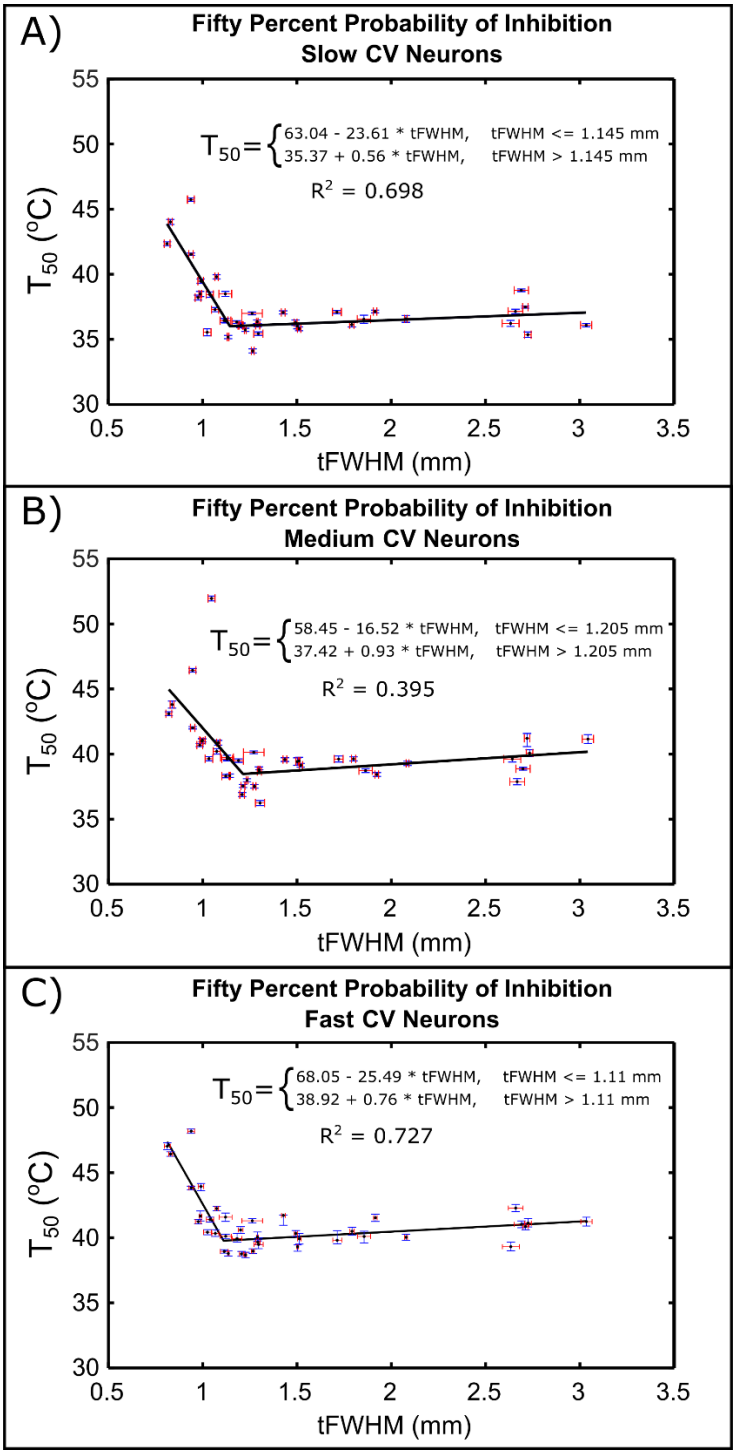

Figure 5.4. The T_{50} for all irradiation lengths across all nerves are plotted against the extracted tFWHM of heating for the slow (A), medium (B), and fast (C) CV neurons. Data are represented as T_{50} +/- 95% CI from the PROBIT fit (vertical error bars), plotted at the mean tFWHM +/- standard error of the mean (horizontal error bars). Piecewise fits utilizing the value of S in Equation 1 which maximized the goodness of fit are plotted for each CV region, and the corresponding equations and R^2 are shown. Slopes of the linear lines were tested for a significant difference from a line with a slope of zero, with an alpha value of 0.0167. In the short regime, all lines demonstrated a significant difference from zero slope (p = 5.54e-11, 1.37e-5, and 4.46e-12 for the slow, medium, and fast CV populations, respectively). Long tFWHM regime fits demonstrated no significant difference from a flat line (p > 0.0167).

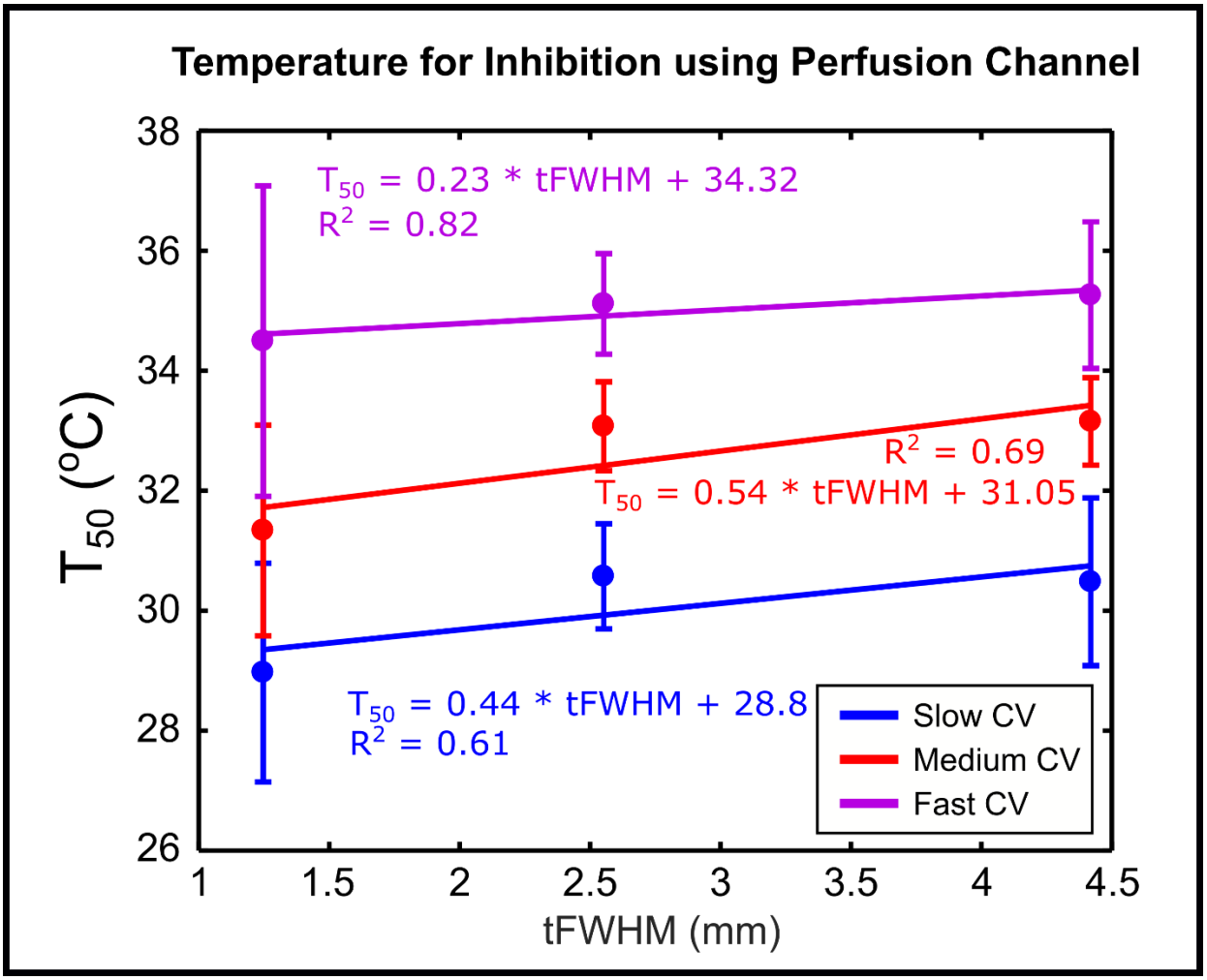

Figure 5.5. Perfusion heating results showed a similar trend to the INI results. T_{50} values (mean +/- standard deviation) are plotted over tFWHM for the slow (blue), medium (red), and fast (magenta) CV neurons. Linear least squares fits are applied to each CV population with the shown equations and R^2 values. Testing the regressions against a flat line show that for BL's > 1.15 mm, the T_{50} is not dependent on the tFWHM required for INI ($p > 0.0167$), just as in the INI analysis (Figure 5.4).

5.5 Discussion

5.5.1 Inhibition Trends with Block Length

Prior investigation established that the temperature required for inhibition is expected to change with BL[7]. The present study validates this hypothesis. The response of T_{50} to different BLs for INI showed two distinct trends: one in a regime of short tFWHM, and the other in a regime of longer tFWHM. At short tFWHM of 0.81 - 1.15 mm, increasing the BL leads to a reduction in the T_{50} with a steep slope in the trendline. Prior experimental interrogation compared inhibition thresholds for single peaks of slow CV within CAPs using one and two adjacent optical fibers[7]. Interestingly, this study would have just been able to capture the trend at low tFWHM considering that the reported tFWHM from one and two fibers were 0.66 mm and 1.10 mm, respectively. Applying the equation for T_{50} determined in this study from Figure 5.4A to the tFWHM from Ford *et al*. 2020, it is predicted that T_{50} = 47.5 ^{o}C for one fiber and T_{50} = 37.1 ^{o}C for two fiber inhibition, resulting in a 21.9 % drop in temperature rise over room temperature (20^{o}C) by using two fibers instead of one. This prediction falls within the 15 - 23.5 % decrease reported in Ford *et al*. 2020. It is important to compare the percent decrease in INI threshold because that accounts for variation across experiments and for differences in the absolute temperature based on the temperature sensing techniques used. By considering Ford *et al*. 2020 in conjunction with the results from this study, strong evidence is presented for the existence of this short regime where increasing BL leads to a reduction in T_{50}.

At long BLs (tFWHM = 1.15 - 3.03 mm), no significant change in the T_{50} with BL was noted ($p > 0.0167$). This is the case for both the laser irradiated and perfusion heated nerves, highlighting that a BL dependence may only exist over a finite range of tFWHM. This was an unexpected finding since prior computational modeling[5] and experimental data[7] showed that longer irradiation lengths are expected to exhibit a drop in the temperature for inhibition, but a longer BL regime of no change in temperature threshold was not explicitly seen. In Ganguly *et al*. 2019[5], Figure 4J suggests that the benefit of BL may saturate, where inhibition temperature appears to decay exponentially with increasing BL. In this investigation, however, an exponential fit poorly captured the trends in the data ($R^2 < 0.3$) (Table 5.2). One caveat present is that an exponential resulted in a relatively good fit for the slow CV data ($R^2 = 0.613$). It was determined that this was due to the longest BL (tFWHM = 3.03 mm) having a T_{50} lower than many of the adjacent data points, while this same BL for the medium and fast CV neurons showed a T_{50} greater than many of the adjacent data points. To overcome this relatively extreme singular tFWHM value, it was removed from the exponential fit process based on the assumption that if T_{50} truly does follow an

exponential relationship with BL, the removal of one extreme data point should not greatly affect the fit. Performing this analysis greatly reduced the goodness of fit of an exponential for the slow CV neurons (R^2 = 0.106) (Table 5.2). With this analysis, it was determined the piecewise function best approximated the data, which demonstrates that increasing the BL does not have an effect on the temperature required for INI in this longer regime, and should be avoided to minimize the volume of tissue heated.

5.5.2 Optimizing Targeting

The work presented here suggests that there is a true optimal block length to apply INI. To minimize the temperature needed for inhibition and minimize the volume of tissue heated, irradiation of nerves should target BLs around tFWHM = 1.15 mm, at the intersection point between the two linear regimes (Figure 5.4). The current commonly held irradiation paradigm using optical fibers can achieve this BL by selecting the correct optical fiber diameter, and specialized nerve cuffs might be designed that specifically target this BL for research and clinical applications. The caveat here is that care must be taken to ensure the proper thermal distribution as opposed to focusing on the light distribution. While the distribution of irradiated light no doubt plays a major role in the temperature distribution, the thermal boundary conditions also greatly affect the BL applied. For example, originally this study set out to test irradiation lengths ($1/e^2$ spot diameters) of 0.4, 0.5, 0.6, 0.7, 0.8 1, 2, 3, and 5 mm. A minor offset in probe placement resulted in irradiating slightly different lengths than expected, and differences in thermal boundary conditions across experiments resulted in tFWHM that varied for a given irradiation length, potentially causing overlap in the tFWHM for the shorter regime. Ultimately, the parameter of interest is the heat distribution; thus, these variations are inconsequential since the tFWHM was directly measured for every INI trial and used in the PROBIT model instead of an assumed irradiation length. This analysis does highlight that careful attention must be given to the actual temperature distribution when designing experiments and irradiation techniques, and that temperature measurement during INI application can aid in proper targeting of the tissue.

Targeting the nerve's entire diameter (i.e., irradiating all neurons) still allowed for specific inhibition of slow conducting neurons while remaining below the T_{50} for medium and fast CV neurons; therefore, this may be an effective method for applying heat block specifically to pain conducting neurons. Investigation is needed to identify if optimally targeting BL to minimize T_{50} results in safer application of INI, allowing for extended laser application times. By lowering the temperature induced, the thermal load on the tissue inherently drops for a fixed exposure time[25]. This would allow for longer duration of heat application before the onset of damage, but how long these temperatures can safely be applied during INI remains to be seen. This study was performed in an invertebrate that makes no myelin, so there were no

myelinated neurons, and native body temperatures are much lower in *Aplysia* than in mammalian vertebrates. Studies are needed to assess whether the trends identified here are also found in vertebrate unmyelinated neurons, and how myelinated neurons within compound nerves respond. In *Aplysia*, it is predicted that the T_{50} for slow CV neurons at a block length of 1.145 mm is 36 ^{o}C (a ~16 ^{o}C rise above room temperature), near where mammalian systems function. In mammals, it is known that damage effects begin to occur above 42 ^{o}C[25]. Heat applications bringing the tissue temperature higher than 42 ^{o}C would not inherently incur an immediate damage response but would have a duration window for therapy prior to the onset of damage. This onset time is dependent on the amplitude of heating above 42 ^{o}C and places an upper limit on the irradiation time allowable for therapeutic use. Some evidence exists that inhibition of the slowest neurons in the vagus nerve of the musk shrew occurred with a 2.9 ^{o}C rise over a 37 ^{o}C baseline[2], suggesting that safe and effective sustained inhibition is possible. Optimal targeting of neurons, including through the appropriate application of BL, will help minimize the temperature needed for inhibition which will in turn minimize the maximum temperature applied to the tissue, ideally below 42 ^{o}C. One potential change when investigating the effect of BL in a vertebrate nerve is that the intersection point between the short and long regimes may occur at a different BL, which would be an important distinction for optimally targeting invertebrate versus vertebrate neurons for INI. To apply optimal BL to vertebrates, validation of the trends shown here will be needed. Studies in the *Aplysia* should attempt to target BLs of tFWHM = 1.15 mm to minimize extraneous heating, while other systems will require their own investigation of block length to identify optimal targeting.

5.5.3 Mechanistic Considerations

Prior mechanistic exploration into INI has suggested that heat block is the result of hyperpolarizing currents from voltage-gated potassium channels, K_V, overwhelming the depolarizing currents from voltage-gated sodium channels, Na_V, at greatly elevated temperatures causing a failure to conduct an action potential in the heated region of an axon[5,6]. Both Na_V and K_V currents exhibit a temperature sensitivity in which increased temperature induces greater maximum currents and faster channel gating, and K_V currents demonstrate a greater temperature sensitivity of the current onset time at INI temperatures[26–29]. Ganguly *et al*. 2019 demonstrated this computationally. In addition, the ratio of potassium charge transfer per unit area to sodium charge transfer per unit area (Q_K/Q_{Na}) increases as temperature is elevated[5]. These temperature dependences are what we hypothesize gives rise to the effect of BL. If, in a given axon, INI is achieved at a temperature, T1, which is applied over a length of axon, BL1, it would stand to reason that for a greater temperature, T2, a shorter length of axon, BL2, would be needed since the K_V ion channels open more

quickly and the Q_K/Q_{Na} will be greater at T2 compared to T1. In other words, the amount of hyperpolarizing effect per unit surface area of axon will be increased at greater temperatures, requiring less surface area to overcome the incoming action potential, and therefore a shorter distance of axon will be needed for a given axon diameter. This effect can be observed in Figure 4 of Ganguly *et al*. 2019 where BL is compared over different top-hat temperature applications[5]. When no ion channels are present, the BL is dictated by the length constant of the axon and decays due to passive currents. When only K_V are present, BL then begins to play a role in the temperature needed for inhibition, and the BL is determined by the axon length constant and the temperature sensitivity of K_V currents. When both K_V and Na_V are present, the temperature for inhibition has a greater dependence on the BL due to the interplay between ion current temperature sensitivities. At the longest BL, the reduction in temperature for increasing BL is diminished, suggesting a saturating effect. This diminished response with heating greater lengths can also be seen in Mou *et al.* 2012[14]. Action potential propagation was simulated in *Xenopus laevis* myelinated neurons and in Figure 6 the temperature at which heat block occurs decreases as the number of computational nodes that are heated increases. It should be noted that the drop in temperature from increasing the block length from 2 to 3 nodes is less than the drop in temperature from increasing the block length from 1 to 2 computational nodes, highlighting this diminished effect. Based on this effect, it would be expected that there is a BL regime where the measured T_{50} would no longer change with tFWHM. Indeed, we observe no significant change in T_{50} with BL at tFWHM = 1.15 – 3.03 mm (Figure 5.4) and at tFWHM = 1.25 – 4.42 mm (Figure 5.5). One point to note from the above assessment is that a BL effect was observed in both myelinated and unmyelinated axons (*Aplysia*, squid, and frog axons were tested in the present study, Ganguly *et. al.*[5], and Mou *et. al*[14]., respectively). Therefore, we hypothesize that this phenomenon occurs across species, and thus would be effective in reducing the temperature needed for INI in human C fibers.

5.6 Conclusions

An assessment of the parameter space of block length was performed for tFWHM of heating between 0.81 and 3.03 mm along nerves using laser heating and between 1.25 and 4.42 mm using perfused hot media to induce neural heat block. Probing the relationship between BL and the temperature for the 50% probability of inhibition (T_{50}) revealed two distinct trends, 1) at relatively short BLs (tFWHM = 0.81 - 1.15 mm), a statistically significant drop in T_{50} was measured as BL increases, and 2) at longer BLs (tFWHM = 1.15 – 3.03 mm), no significant change in T_{50} was measured with BL. This trend is best approximated by a continuous piecewise function defined by two lines. The shorter BL regime is consistent

with previous computational and experimental findings. The longer BL regime was validated using perfused hot media as a secondary method of heating and may be predicted from computational investigations currently present in literature. A minimum in the T_{50} occurs at the transition from the shorter regime to the longer regime providing an optimal BL to minimize the tradeoff between the applied temperatures and the volume of tissue heated. Future studies should consider the BL that is applied to the tissue to understand how it may affect the temperatures needed for inhibition, and how improper targeting may cause extraneous heating. Additionally, a similar study in mammals would greatly aid in understanding and optimizing BL towards preclinical and clinical implementation of INI. The work presented here provides one example of how the parameter space of INI can be optimized towards performing targeted, effective, and safe heat block of neurons for potential future therapeutic applications.

5.7 References

1. Duke AR, Jenkins MW, Lu H, McManus JM, Chiel HJ, Jansen ED. Transient and selective suppression of neural activity with infrared light. *Sci Rep*. 2013;3:2600. doi:10.1038/srep02600

2. Lothet EH, Shaw KM, Lu H, et al. Selective inhibition of small-diameter axons using infrared light. *Sci Rep*. 2017;7(1). doi:10.1038/s41598-017-03374-9

3. Armstrong SA, Herr MJ. Physiology, Nociception. StatPearls [Internet]. https://www.ncbi.nlm.nih.gov/books/NBK551562/#. Published 2020.

4. Hodgkin AL, Katz B. the Effect of Temperature on the Electrical Activity of the Giant Axon of the Squid. *J Physiol Lucas Gasser Schoepfle Erlanger Cardot Arvanitaki*. 1949;09:240-249.

5. Ganguly M, Jenkins MW, Jansen ED, Chiel HJ. Thermal block of action potentials is primarily due to voltage-dependent potassium currents: A modeling study. *J Neural Eng*. 2019. doi:10.1088/1741-2552/ab131b

6. Ganguly M, Ford JB, Zhuo J, et al. Voltage-gated potassium channels are critical for infrared inhibition of action potentials: an experimental study. *Neurophotonics*. 2019. doi:10.1117/1.nph.6.4.040501

7. Ford JB, Ganguly M, Poorman ME, et al. Identifying the Role of Block Length in Neural Heat Block to Reduce Temperatures During Infrared Neural Inhibition. *Lasers Surg Med*. 2020. doi:10.1002/lsm.23139

8. Wang YT, Rollins AM, Jenkins MW. Infrared inhibition of embryonic hearts. *J Biomed Opt*. 2016;21(6):60505. doi:10.1117/1.JBO.21.6.060505

9. Walsh AJ, Tolstykh GP, Martens S, Ibey BL, Beier HT. Action potential block in neurons by infrared light. *Neurophotonics*. 2016. doi:10.1117/1.nph.3.4.040501

10. Xia Q, Nyberg T. Photothermal inhibition of cortex neurons activity by infrared laser. In: *IFMBE Proceedings*. ; 2019. doi:10.1007/978-981-10-9023-3_18

11. Lothet EH, Kilgore KL, Bhadra N, et al. Alternating current and infrared produce an onset-free reversible nerve block. *Neurophotonics*. 2014;1:011010. doi:10.1117/1.NPh.1.1.011010

12. Zhuo J, McPheeters MT, Jackson EM, et al. Comparing infrared neuromodulation (IRN) with isotonic glucose solution for selective inhibition of small-diameter axons (Conference Presentation). In: ; 2019. doi:10.1117/12.2510417

13. Horváth ÁC, Borbély S, Boros ÖC, et al. Infrared neural stimulation and inhibition using an implantable silicon photonic microdevice. *Microsystems Nanoeng*. 2020. doi:10.1038/s41378-020-0153-3

14. Mou Z, Triantis IF, Woods VM, Toumazou C, Nikolic K. A simulation study of the combined thermoelectric extracellular stimulation of the sciatic nerve of the xenopus laevis: The localized transient heat block. *IEEE Trans Biomed Eng*. 2012;59(6):1758-1769. doi:10.1109/TBME.2012.2194146

15. Zhu X, Lin J-W, Sander MY. Infrared inhibition and waveform modulation of action potentials in the crayfish motor axon. *Biomed Opt Express*. 2019. doi:10.1364/boe.10.006580

16. Hale GM, Querry MR. Optical Constants of Water in the 200-nm to 200-microm Wavelength Region. *Appl Opt*. 1973;12(3):555-563. doi:10.1364/AO.12.000555

17. Coggeshall RE. A Light and Electron Microscope Study of the Abdominal Ganglion of Aplysia Californica. *J Neurophysiol*. 1967;30(6):1263-1287.

18. Bedini C, Geppetti L. A morphological study on the amount and origin of axons in the pleuroabdominal connectives of Aplysia fasciata. *Ital J Zool*. 2000;67(1):9-18. doi:10.1080/11250000009356288

19. Welch AJ, Van Gemert MJC. *Optical-Thermal Response of Laser-Irradiated Tissue.*; 2011. doi:10.1007/978-90-481-8831-4

20. Wells J, Kao C, Konrad P, et al. Biophysical Mechanisms of Transient Optical Stimulation of Peripheral Nerve. *Biophys J*. 2007;93(7):2567-2580. doi:10.1529/biophysj.107.104786

21. Jacques SL. Laser-tissue interactions: Photochemical, photothermal, and photomechanical. *Surg Clin North Am.* 1992. doi:10.1016/S0039-6109(16)45731-2

22. Matsumoto G, Tasaki I. A study of conduction velocity in nonmyelinated nerve fibers. *Biophys J*. 1977. doi:10.1016/S0006-3495(77)85532-X

23. De Col R, Messlinger K, Carr RW. Conduction velocity is regulated by sodium channel inactivation in unmyelinated axons innervating the rat cranial meninges. *J Physiol*. 2008;586(4):1089-1103. doi:10.1113/jphysiol.2007.145383

24. De Col R, Messlinger K, Carr RW. Repetitive activity slows axonal conduction velocity and concomitantly increases mechanical activation threshold in single axons of the rat cranial dura. *J Physiol*. 2012;590(4):725-736. doi:10.1113/jphysiol.2011.220624

25. Dewhirst MW, Viglianti BL, Lora-Michiels M, Hanson M, Hoopes PJ. Basic principles of thermal dosimetry and thermal thresholds for tissue damage from hyperthermia. In: *International Journal of Hyperthermia*. Vol 19. ; 2003:267-294. doi:10.1080/0265673031000119006

26. Vandenberg JI, Varghese A, Lu Y, Bursill JA, Mahaut-Smith MP, Huang CL-H. Temperature dependence of human ether-a-go-go-related gene K+ currents. *Am J Physiol Cell Physiol*. 2006;291(1):C165-75. doi:10.1152/ajpcell.00596.2005

27. Yang F, Zheng J. High temperature sensitivity is intrinsic to voltage-gated potassium channels. *Elife*. 2014;3:e03255. doi:10.7554/eLife.03255

28. Collins CA, Rojas E. TEMPERATURE DEPENDENCE OF THE SODIUM CHANNEL GATING KINETICS IN THE NODE OF RANVIER. *Q J Exp Physiol*. 1982;67(1):41-55. doi:10.1113/expphysiol.1982.sp002623

29. Hyun NG, Hyun KH, Lee K, Kaang BK. Temperature dependence of action potential parameters in aplysia neurons. *NeuroSignals.* 2012. doi:10.1159/000334960

Chapter VI

Conclusions and Future Directions

6.1 Summary and Conclusions

6.1.1 Summary

The overall goal of this dissertation was to improve targeting of neurons within nerves for infrared neural inhibition. This took the form of optimizing how the light is applied to nerves to better understand and leverage the innate laser-tissue interactions. The need for this optimization stemmed from the high temperatures required for INI, restricting any long-term therapeutic applications of the technology. To improve targeting and reduce temperatures, an understanding was needed of where the light is absorbed, how the resulting heat is distributed, and the biophysical response of neurons to these different heat distributions.

The distributions of absorbed optical energy and resulting temperatures were investigated in Chapter III. A fundamental barrier in the field existed to computational modeling of arbitrarily irradiated neural tissue at INI wavelengths since the reduced scattering coefficient, μ_s', had not been characterized at these wavelengths. The limitation on optical property measurement techniques available restricts the accuracy and precision with which this value can be directly measured, therefore, a computational approach was developed, validated, and then used to estimate the sensitivity of temperature distributions to μ_s' with subsequent experimental validation. Both computational and experimental investigation revealed that higher μ_s' will yield higher temperature rises and lower thermal penetration depths, while a negligible dependence of the FWHM (full width at half maximum) of the surface temperature on μ_s' was observed. Prior assumptions in the optics community assumed that since μ_a is much greater than μ_s' at INI wavelengths, scattering could be largely neglected. Secondly, if scattering was considered, we wondered if an extrapolation of fitted μ_s' spectra to wavelengths in the visible (VIS) and near-infrared (NIR) regions of the electromagnetic spectrum would be sufficient for the sake of computational modeling. Thus, this investigation aimed to test these assumptions. It was revealed that computational modeling predicts < 7% increase in maximum temperature rise and < 20% decrease in thermal penetration depth over a range of 1.5

mm^{-1}. This investigation concludes that despite the absorption dominance, **scattering cannot be neglected** unless μ_s' is sufficiently close to zero ($\mu_s' < 0.25\ mm^{-1}$) to maintain <5% error in the simulated temperature distribution. This means that a Monte Carlo simulation is needed to determine the distribution of absorbed photons (a Beer's Law approximation is insufficient) for most cases. Despite the need for a Monte Carlo simulation, a best guess of μ_s' is likely sufficient without greatly affecting the simulation. As described in the discussion of Chapter III, for INI with $\lambda = 1875$ an error of up to 46% in the estimation of μ_s' is sufficient to maintain <5% error in the simulated distribution. With this result, researchers should have more confidence that errors in their approximations of μ_s' will not greatly affect simulation outcomes, and computational investigations into optimizing laser irradiation during INI for specific applications and in specific animal models can now be performed. These results also have implications for determining light and heat distributions for any material and any wavelength range where absorption is dominant over scattering, not just for tissue irradiation at INI wavelengths.

In Chapter IV, the hypothesis was put forth that the temperature required for INI exhibits an axonal length dependence. Primary proof of principle was performed computationally in the NEURON simulation environment which predicted that increasing the tFWHM (thermal full width at half maximum) of heating by 42.9% would lower the maximum temperature rise for inhibition by 11.9%. Subsequent validation of the effect was performed for two block lengths using one and two-adjacent optical fibers (tFWHM = 0.66 mm and 1.10 mm, respectively). Using two fibers resulted in a 38.5% lower radiant exposure thresholds per optical fiber which translated to at least a 15.0 % reduction in maximum temperature rise. It was not surprising that some length effect would be present since the length constant (Equation 2.10) is a well-known effect in neural conduction. Computational mechanistic analysis had suggested that this effect should exist[1].

Chapter V provided a more extensive analysis of the effect of BL on INI temperature thresholds. The study presented novel methodology of identifying INI thresholds which overcame previous experimental pitfalls. Simultaneous temperature monitoring of nerves during INI is critical for predicting biophysics as a function of temperature. Experiment to experiment and trial to trial variability can result in high uncertainty when trying to estimate temperature in a separate set of measurements. Using a PROBIT analysis which pooled multiple trials was an effective method of quantifying inhibition for populations of neurons while overcoming trial to trial variability. In the *Aplysia*, this type of analysis was only possible by bringing a region of nerve out of solution and applying INI via free beam irradiation. This work suggests that this may be a viable methodology in future studies that further probe the biophysics of INI. Peripheral nerves in the vertebrate nervous system such as the rat sciatic nerve do not need constant immersion in liquid but do require frequent hydration if brought out of the tissue bed. This study suggests that studies in

vertebrate nerve probing biophysical phenomena, whether for INI or INS, would benefit from non-contact irradiation so that the temperature distribution can be simultaneously monitored.

Chapter V resulted in a surprising finding: the identification of two different regimes of the block length. The fitted piecewise equation demonstrated that: 1) BL below 1.15 mm fell within a regime where increasing the BL leads to a drop in the fifty percent probability of inhibition (T_{50}) and 2) tFWHM above 1.15 mm fell within a regime where increasing the BL did not significantly change the T_{50}. This was observed for all conduction velocity populations of neurons. Initial skepticism hypothesized that this second regime was an artifact of the experimental setup; however, the effect persisted when using hot saline to provide a thermal block instead of laser irradiation. Further, the data from Chapter IV corroborate the results from Chapter V. Chapter IV showed that the advantage of 2 fibers was a ~23.5% reduction in the maximum temperature rise. Applying the piecewise equation developed in Chapter V to the FWHM of heating measured using magnetic resonance thermometry in Chapter IV, a ~21.9% reduction in T_{50} would be predicted by using 2 optical fibers. This study has important implications further than INI, as evidenced by this hot saline validation, since other neuromodulation modalities apply heat along axons to block propagating signals. In ultrasound neuromodulation of the peripheral nervous system, it is not fully clear to what degree inhibition is due to a mechanical mechanism or a thermal mechanism. If temperature plays a role in ultrasound inhibition, then it is expected that BL effects should be present and that two regimes of BL should be observed. Similar consideration should be applied to RF heating of axons.

6.1.2 Major Conclusions

The high temperatures required for INI which limited its potential for long-term therapeutic use was the motivation for the work performed in this dissertation. The work contained in this dissertation highlights methods of improving the targeting of neurons for infrared neural inhibition. Optimization of laser irradiation is possible through computational modeling of optical-thermal interactions in tissue. At INI wavelengths, scattering dependent changes in the temperature distribution are relatively small when considering the range of μ_s' viable in neural tissues, but these are still present. To that end, the major conclusion from Chapter III is that, except for in specific circumstances, **scattering cannot be ignored, and a Monte Carlo simulation is needed to simulate the light distribution**. While not able to neglect the contribution of scattering, an estimate of μ_s' may be sufficient to approximate the tissue computationally, and the results of this dissertation can be used to understand the error present in an optical-thermal simulation.

Optimization can also take the form of selecting the proper BL. Importantly, the results of Chapters IV and V **suggest that there is an optimal block length to apply INI that will minimize tissue heating and will minimize the volume of tissue heated.** For the slowest neurons, a block length of 1.145 would target the minimum temperature for a 50% probability of inhibition (T_{50}) at 36^{o}C. Since the measured FWHM for two optical fibers was ~1.10 mm (measured with a spatial resolution of 0.055 mm) not much more of a reduction of the temperature is possible. Thus, two adjacent optical fibers or an optical fiber diameter that results in a ~1.15 mm tFWHM would optimize the BL for INI in the *Aplysia*, minimizing both the temperature for inhibition and the volume of tissue heated.

Future INI studies should consider the BL when designing experimental protocols. A similar investigation in vertebrates must provide optimal block length and the minimum temperature for inhibition in C-fibers. If the INI threshold at minimum BL is greater than 42^{o}C^{2}, then a maximum duration of application must be imposed on INI for safe performance. Furthermore, this minimum temperature for INI in mammals will dictate if other strategies of minimizing the temperature and/or improving neural targeting may be needed which will help elucidate the overall viability of INI as a therapeutic technique.

6.2 Future directions

6.2.1 Computational Investigations

Based on the results from Chapter III where it was concluded that estimated μ_s' are sufficient to simulate temperature distributions, optical-thermal modeling can now be performed for specific INI applications with the best available approximation of μ_s' for the tissue of interest. One of the greatest advantages of using IR irradiation to elicit heat block is that light can be focused down to diffraction limited spots allowing for extreme spatial specificity of the energy deposition. Therefore, specific targeting of a small number of axons within nerves, or of single neuron cell bodies in ganglia is theoretically possible with proper beam shaping and laser application. Optical scattering and thermal diffusion reduce the spatial specificity of INI by spreading out the heat. Computational modeling of the temperature distribution is one way to optimize how light should be applied to achieve this specificity and understand targeting limitations due to the μ_s' of tissue and thermal conduction. Focusing of the light going into tissue would result in a much more confined distribution of the heat source, leading to more targeted heat application. Interestingly, the results from Chapter V may suggest that, despite the high spatial specificity, targeting small regions of

axon would greatly increase the temperature needed to inhibit. Perhaps specific targeting of axons within a nerve would benefit from spatial thermal confinement radial to the axon and thermal spread of the heat to tFWHM = 1.15 mm in the axial direction to take advantage of the effect of BL. Computational modeling could optimize laser parameters needed to achieve this. Practically targeting a single axon in tissue would require anatomical imaging to track axons and potentially complex hardware to shape the beam accordingly and is likely not be feasible in a clinical setting. Further experimental investigation would be needed to identify the feasibility, but computational modeling would at least assess feasibility of the basic physics of performing this technique.

By coupling these optical-thermal models with a NEURON simulation of action potential propagation, the biological response of tissue can be estimated. With the development of a more adequate approximation of action potential dynamics at elevated temperatures[1], more confidence exists in these computational neurological predictions. A coupling of these models has already been performed by Ganguly *et al.* (*in preparation*)[3], which highlights the predictive potential of these simulations and how 3D coupled simulations can predict the spatial distribution of inhibited axons. In addition, an assessment of the potential for thermal damage can be incorporated, as shown in Ganguly *et al*[3].

Last, the context in which this dissertation was written calls attention to the importance of computational modeling in the time of limited experimental investigations. Most of the final writing of this dissertation and the defense of this thesis took place during the beginning of the COVID-19 pandemic, resulting in the self-isolation of people around the world. Institutions have been closed, and non-essential research activities have been halted. Often times, the low cost, rapid optimization, and reduction of animal usage are touted as the main advantages of computational modeling prior to experimental exploration. This pandemic raises another major contribution: that computational modeling provides an outlet of investigation towards prior research goals in the time of crisis when social distancing is required, and research facilities are inaccessible. Experimental investigation since the beginning of this pandemic has become much more scrutinized, and greater detail now goes into the planning of each aspect of an experiment since in-lab time is limited and increases and individual's risk. In this context, the utility of computational modeling is even greater so that experiments are properly planned out and experimental parameters are properly understood. A worthwhile goal may be creating an open source modeling pipeline for simulating phenomena related to INM which would aid others in properly developing their experimentation. A computational workstation capable of running computationally large geometries and performing computationally intensive simulations was purchased with a mid-tier processor and high-end graphical processing unit, both of which are modular and can be upgraded. The optical, thermal, and neural components of the simulation pipeline already exist separately on the machine, but all require generation of their own geometries optimized for the specific simulation type and must be called separately. A pipeline

that allows generation of one geometry that then optimizes voxel, mesh elements, neuron computational segments, etc. and links the output of one simulation to the next would greatly aid in the user-friendliness of these coupled simulations. Predefined common geometries could be available for other users to build upon based on their own needs. Dr. Mohit Ganguly conducted the critical early work of developing a NEURON mechanism that better predicts the temperature dependence of neural conduction. Incorporating this mechanism into a simulation pipeline would significantly lower the barrier to entry for labs performing INM to perform computational modeling as a means to optimize setups and explore mechanistic questions. In addition, developing the NEURON mechanism to properly incorporate infrared neural stimulation would help provide a more universal understanding temperature's effect on neural conduction.

6.2.2 Mechanistic investigation

The emergence of multiple trends in response to different regimes of BL is curious and invites investigation. Based on sparse evidence from prior simulations in literature[1,4], the effect of block length may saturate at longer tFWHM. If this is true, it would explain why any change of the T_{50} with the tFWHM was not detectable at longer block lengths in Chapter V. One curious aspect of the trend identified in this dissertation is that the transition between the short regime and the long regime of BL occurs very quickly, and a piecewise function that is discontinuous in dT/d(tFWHM) better fits to this trend than an exponential decay. The other striking trend is that, while the long regime was not significantly different from a flat line in both the laser heated and perfusion heated experiments, all 6 of the linear regressions (slow, medium, and fast conduction velocities for the laser and perfusion heated experiments) demonstrated a positive slope. Because of these two occurrences, I hypothesize that there are actually two competing effects at play here, one that reduces the T_{50} with greater BL and another that increases the T_{50} with greater BL. This first effect would be the one highlighted in Chapter V where the temperature dependence of voltage gated potassium channels coupled with inhibition being an axon surface area effect leads to lower temperature for longer lengths of heating. In the shorter regime, the first effect dominates, and a reduction in T_{50} is seen. In the longer regime, the first effect becomes saturated as predicted by the literature, and the second effect becomes dominant, leading to a gradual rise in the temperature for inhibition with greater BL. First, a real trend of increasing T_{50} with greater tFWHM in this longer regime needs to be established. This can be done by using denser tFWHM sampling and a greater sample size. Also, the range of tFWHM tested should extend to even longer values. If a trend does exist, then mechanistic studies may first be performed computationally prior to experimental validation, similar to the initial probing of the mechanism of INI.

My hypothesis for the mechanism underlying why increasing the tFWHM reduces the temperature for inhibition (up to a point) is that, since the voltage gated potassium channels are situated in the axonal membrane, recruiting a greater length of membrane will recruit more channels, which will lower the needed contribution from each individual channel. Experimental validation will eventually be needed to test this hypothesis. Direct measurement of the contribution of sodium and potassium currents during application of INI with different BL would be the ideal way to perform this validation, but an intracellular patch along an axon that is also being heated is likely not practical or possible. A study of indirect observations may be sufficient to draw conclusions, though. Ganguly *et al*. describes a 3-chamber dish that applied channel blockers to a middle region of nerve where INI was simultaneously applied (Appendix A). A hybrid setup between Ganguly *et al.* and Chapter V of this dissertation would be needed to partially expose the top of nerves to allow free beam irradiation and thermal imaging, while the partial submersion of the bottom half in media allows application of pharmacologic agents. With this setup, voltage gated potassium and sodium currents can be abolished with tetraethylammonium and tetrodotoxin (or choline), respectively. A set of data similar to that gathered in Chapter V could then assess how the BL trends change with blocking of different ionic currents. Unfortunately, the experimental setup using the perfusion chamber was not suitable to test block lengths less than 1 mm because the size of the thermistor did not allow smaller chamber lengths and because the greater flow resistance which is induced by the narrowing the chamber length resulted in most of the saline flowing through an alternate path, bypassing the nerve. Overcoming this limitation could be possible by constructing a microfluidic device that could apply specific lengths of heating along the nerve.

6.2.3 Different threshold for different heating modalities

One secondary observation of Chapter V is that measured temperatures for inhibition were lower using the heated saline approach than laser heating. This can be explained to a large degree from the difference in temperature sensing method. The thermal camera measured the temperature of the nerve up to ~ 80 μm deep. From the investigation in Chapter III, the maximum temperature is expected to occur just under the surface of the tissue. Therefore, the measured temperature is very close to the maximum temperature experienced by the tissue, but this will be hotter than the temperature at the axons since the nerve is surrounded by a collagenous sheath. When perfusing hot saline, the temperature with depth in the nerve is expected to be more uniform, so surface temperatures are more representative of the entire cross-section of axon. The temperature in the dish was measured using a thermistor which was a ~ 1 mm diameter cylinder that was ~2 mm in height. This large sensing area means that a relatively large volume of water

was averaged over. Additionally, depths above and below the nerve would have been probed because of the height of this thermistor, likely leading to an underestimation of the temperature. This is all to point out that it is not surprising that a temperature discrepancy was noted between the two sensing modalities. However, a study has not been performed comparing the temperatures needed for heat block across different heating modalities, and this may yield some insight into whether applying block with hot media results in lower threshold temperatures than when applying INI.

6.2.4 Vertebrate validation of BL

Studies performed in vertebrate nerve are needed to confirm the identified trends with block length. It is possible that the effect of BL may not be consistent between invertebrates and vertebrates due to physiological differences such as the different complement of ion channels and the presence of myelin. Initial investigation should probe this effect in C-fibers. Not only can this put BL in the context of pain management, but C-fibers are the most likely population of neurons to demonstrate a similar BL response because of their lack of myelination and comparable axon diameters to the slow CV population in *Aplysia*. The sciatic nerve has proven to be an effective target to explore INI and INS, and would again provide a good model system to explore BL in mammals. The trunk of the sciatic is too short to adequately stimulate and sense C-fiber activity. The electrical stimulation artifact is too high amplitude and not enough propagation distance is present to separates the stimulation electrode from the recording electrode, leading to a large artifact that covers up much of the neural signal. Even if the artifact was minimized, the small propagation distance does not allow for enough signal dispersion to separate the C-fiber signal from motor and myelinated sensory neuron signals. Therefore, a longer length of nerve is needed. Electrical stimulation of distal nerves in the leg, such as the tibial or sural nerves, and electrical recording in the sciatic nerve or at spinal dorsal roots would provide enough separation to sense C-fiber contribution to the compound action potential if a high enough signal to noise ratio (SNR) is achievable. This could be performed on excised nerve setup[5] or *in vivo*[6], and may require impaling the tissue for adequate SNR. Non-contact irradiation would again be needed with thermal imaging to repeat the study from Chapter V. It would be informative to further investigate the effect that myelin has on inhibition thresholds and how myelination impacts the effect of BL by repeating this study for Aδ fiber signals and eventually for motor neurons.

6.2.5 Clinical Feasibility Considerations

The clinical feasibility of INI depends on whether it can be applied without damage for a therapeutic use. There are currently no universal rules on temperature rises allowable for FDA approved devices as each device is assessed on a case by case basis. Obviously, lower temperatures are better, but the question remains what amplitude of temperature rise can be applied therapeutically. It has been shown that temperatures need to rise to at least 42°C to evoke a damage response in tissue[2]. The relationship between temperature, time, and damage probability are captured by approximating the accumulation of damage as a chemical reaction using the Arrhenius model[7]. This model shows an exponential relationship between damage and temperature, and a linear relationship between damage and time of heating. For example, necrosis in human skin will result from heating to 44°C for > 300 minutes but will occur in less than a minute at 55°C[2]. This information can be used to inform acceptable heating protocols for INI. Because, in mammals, damage requires temperatures of 42°C, any heating that is limited to a 5°C rise (over a 37°C baseline) would likely be considered safe for long term use, with the appropriate safety studies, of course. Some evidence suggests that limiting INI to a 5°C rise is possible. Conduction block of motor signals in the rat sciatic nerve was achieved at ~ 5.2°C rise[8] and INI of the smallest diameter axons in the musk shrew vagus nerve was achievable with ~2.9°C rise[9]. Unfortunately, there are a few pitfalls with these measurements that likely push the true temperature rises at INI threshold above the 42°C range. First, for the rat sciatic nerve, a thermal camera with 0.3 mm pixel size was used which averages over a large surface area of tissue. The temperature distribution shown throughout this thesis, both simulated and experimentally measured, show how greatly the temperature can vary over 0.3 mm. Additionally, the tFWHM from an optical fiber (as measured in aims 2 and 3) constitutes only 2 to 3 pixels on this camera; thus, it is very likely that the maximum temperature rise being applied to the tissue in Duke et al. 2013 is well above 5°C. On the other hand, this study inhibited motor units, so it is expected that needed temperatures for inhibition of sensory neurons will be lower than what required in Duke *et al*., but it is not clear how much so. INI applied to the musk shrew presents the strongest evidence that sustained INI can be applied safely for clinical applications. It is likely that the 2.9 °C rise measured in Lothet *et al.* is an underestimate of the true temperature because emissivity corrections were not applied to account for the loss of signal through the glass imaging window during thermal imaging[9]. This would likely result in no more than a doubling of the measured temperature rise, resulting in a rise of ~5.8 °C. Thus, inhibition of fine vertebrate neurons may be possible at temperature thresholds below 43°C. While this is not below the goal of 42°C, this does mean that irreversible damage would take much longer to develop compared to applying temperatures of 55°C (an 18°C rise). Lothet *et al*. also does not account for optimizing the BL, and therefore this temperature rise may be further reduced.

Damage studies will be needed to make any real claims about the clinical feasibility of both short-term and sustained INI. Initial experiments should take place in animal model. Experiments which assess thermal damage using tissue staining and histology will be required for FDA approval. Once mammalian studies are performed, tissues should be fixed for subsequent damage analysis. A study applying the Arrhenius model to either histological or functional damage could greatly aid in the understanding of laser parameters that will be therapeutic.

Taking the previous discussion into account, INI appears feasible as a clinical neuromodulation modality, but has some major barriers that need to be addressed, most notably from a safety perspective. The temperature rises that are required in invertebrates that were measured in this thesis are obviously not acceptable to apply in humans for the purpose of INI, but it is also clear that these the amplitudes of these temperature rises do not reflect those that are required in mammals. What this thesis does present is a route by which to further reduce the temperature rise below what was measured in vertebrate studies by optimizing the BL and using computational models to improve irradiation techniques.

6.3 Protection of Research Subjects

No humans or vertebrate animals were used for the enclosed work. *Aplysia* are invertebrate animals, and thus do not fall under the purview of the Institutional Animal Care and Use Committee (IACUC). Care was taken to ensure the humane treatment of these animals. All surgeries were performed using the generally accepted anesthetic measures for these animals.

6.4 Significance and Societal Implications

This dissertation yielded various results about improving targeting of neurons during INI to address the current temperature rise thresholds that will be problematic for clinical implementation. To the best of my knowledge, this was first the systematic study that assessed the effect of scattering on the temperature distribution for biological tissues. Many prior studies have assessed the effects of heating on the scattering coefficient, but not vice versa. Much emphasis in the literature has been placed on understanding light distributions in scattering dominant conditions as this is the primary regime in the VIS and NIR spectrum

within tissue and is the more "interesting" problem. This dissertation took the approach that scattering in an absorption dominated regime is not negligible and does play a role in the laser heating. The results of this investigation calls into question the use of Beer's Law to determine the distribution of absorbed photons for certain applications. This analysis can be extended to other applications and other wavelengths where the optical properties of interest exhibit a 2 to >10 times greater absorption coefficient than scattering coefficient; however, an analysis will have to be rerun if the μ_a and μ_s' are on a different order of magnitude than what was used in the present study.

Considering the role of scattering during INI, care must be taken to understand how the optical properties of the tissue in a given setup will affect the light and heat distribution. Conversely, however, **the optical properties of the tissue, in conjunction with the wavelength, and the irradiation methodology can be specifically chosen to select the heated volume**. The relative amount of scattering can be chosen by selecting the wavelength regime since greater μ_s' values occur in the 1450-1470 nm range compared to the 1860-1875 nm range; however, the effect of optical scattering on the temperature distribution is largely negligible between these wavelength regimes, but will become slightly more of a factor if wavelengths with lower absorption are chosen. Ultimately **for INI, the 1450-1470 nm and 1860-1880 nm ranges should be considered functionally the same when assessing the temperature distribution (when irradiation is long enough for thermal diffusion)** if the absorption coefficient is matched. The absorption can be tuned by selecting a wavelength from within each range. Lower absorption will result in deeper penetration of the heat and greater absorption can be chosen to result in more shallow heating. Additionally, the optical albedo can be selected to choose how bulbous the heat distribution is. The irradiation paradigm can be chosen to either confine the maximum temperature to the surface (non-contact irradiation) or create a temperature maximum at a depth (contact irradiation). One caveat is that this all assumes that laser pulse trains are long enough in duration for thermal conduction to occur. In addition, this is less applicable for plated cells because the imaging media during experiments will have negligible scattering regardless of the wavelength used.

Based on the literature available in the field of axonal heating, Chapters IV and V were the first studies that have considered the effect of heating length on neural conduction. One barrier to exploring this effect may have been the lack of experimental techniques available to alter the length of heating with high spatial resolution while simultaneously measuring the temperature distribution. This dissertation may serve as a starting point of how to go about probing these temperature distribution effects since there are other aspects that could be interrogated (e.g. the effect of the spatial thermal gradient). The importance of this type of investigation extends to ultrasound and radiofrequency (RF) neuromodulation because an increase in temperature has been associated with both techniques. Thus, the revelation that the distance of axon heated alters temperature thresholds may also serve to inform optimization ultrasound and RF parameters.

This also raises the question of what other length effects may exist, such as with the length axon experiencing mechanical effects during ultrasound neuromodulation.

Chapter V developed a new setup for simultaneous monitoring of electrophysiological signals and temperature distributions. The field of INM has long relied on measuring radiant exposure thresholds and using these as the important parameters when targeting stimulation or inhibition in neural tissue. Ultimately, it has been determined that INS and INI are due to thermal effects, and therefore the temperature and the thermal gradient (temporal and/or spatial) should be reported for each study. Temperature investigations often times take place separately from the neurophysiological endpoint, but this can pose a problem when experimental conditions cannot be replicated adequately during thermal investigation. For example, in Chapter V, it was noted on the thermal camera that cooling of the tissue sometimes occurred primarily in one direction along the nerve. Interrogation of this showed that the effect was due to not allowing enough time for the saline to clear from around the bottom of the nerve which created a flow that convectively cooled the tissue. Looking back at trials where this flow occurred showed that consistently higher laser powers were needed to elicit INI despite the maximum temperature being approximately the same between trials with and without flow. If this study first quantified the radiant exposure threshold and then measured the temperature, this phenomenon would not have been identified, and this would have resulted in a higher temperature estimation. The methodology developed here can be adapted for other setups, but the take-home message for the field is clear, that more attention needs to be allotted to the temperature at the time of stimulation/inhibition. Radiant exposure may continue to be the guiding parameter for certain applications such as for clinical implementation, but the work in this dissertation makes clear that a better understanding is needed of the temperatures/temperature gradients being induced to guide targeting of INM, and this fundamental thermal understanding can then be used to inform the radiant exposures used.

Multiple hurdles still exist towards developing INI as a clinical technology. The jury is still out on whether it will be a viable neuromodulation method for sustained therapy in a human due to the problematic temperature rises, but results from vertebrate animal studies suggest that clinical INI is viable if the irradiation parameters can be optimized. This dissertation took the first step at trying to optimize these irradiation parameters by taking advantage of the tissue's innate response to temperature. Identifying the presence of a BL effect provided a real parameter to modulate the temperature for therapy. Optimizing the BL demonstrates a concrete value to target when designing research and clinical neural heating devices. Since temperatures for INI in the *Aplysia* are not representative of those needed in mammals, it is unclear whether optimizing BL will be sufficient to move INI into the realm of clinical viability. Even if this is not the case, this dissertation was able to address one parameter in a large parameter space of irradiation. **Factors such as the pulse protocol, focusing of light, superposition of beams at a depth in tissue, heating and cooling used together should also be tested to lower the temperature needed for INI and**

to reduce the amount of heating outside of the targeted location. Application of glucose has already been implicated in reducing the radiant exposure threshold needed for inducing INI[10]. These methods may be employed in tandem with optimized BL and with each other for a synergistic effect that may further reduce the thermal load on neural tissue. Future optimization studies in mammals will help identify the feasibility of INI as a clinically viable therapy, and because of the work in this dissertation, future researchers will know that optimizing the BL will help limit the temperature applied to the tissue.

6.5 References

1. Ganguly M, Jenkins MW, Jansen ED, Chiel HJ. Thermal block of action potentials is primarily due to voltage-dependent potassium currents: A modeling study. *J Neural Eng*. 2019. http://iopscience.iop.org/10.1088/1741-2552/ab131b.

2. Dewhirst MW, Viglianti BL, Lora-Michiels M, Hanson M, Hoopes PJ. Basic principles of thermal dosimetry and thermal thresholds for tissue damage from hyperthermia. In: *International Journal of Hyperthermia*. Vol 19. ; 2003:267-294. doi:10.1080/0265673031000119006

3. Ganguly M, Yeats E, Ford JB, et al. An integrated model for optimizing laser induced thermal inhibition in nerves (in preparation).

4. Mou Z, Triantis IF, Woods VM, Toumazou C, Nikolic K. A simulation study of the combined thermoelectric extracellular stimulation of the sciatic nerve of the xenopus laevis: The localized transient heat block. *IEEE Trans Biomed Eng*. 2012;59(6):1758-1769. doi:10.1109/TBME.2012.2194146

5. Waddell PJ, Lawson SN. The C-fibre conduction block caused by capsaicin on rat vagus nerve in vitro. *Pain*. 1989. doi:10.1016/0304-3959(89)90011-0

6. Handwerker HO, Kilo S, Reeh PW. Unresponsive afferent nerve fibres in the sural nerve of the rat. *J Physiol*. 1991. doi:10.1113/jphysiol.1991.sp018507

7. Welch AJ, Van Gemert MJC. *Optical-Thermal Response of Laser-Irradiated Tissue.*; 2011. doi:10.1007/978-90-481-8831-4

8. Duke AR, Jenkins MW, Lu H, McManus JM, Chiel HJ, Jansen ED. Transient and selective suppression of neural activity with infrared light. *Sci Rep*. 2013;3:2600. doi:10.1038/srep02600

9. Lothet EH, Shaw KM, Lu H, et al. Selective inhibition of small-diameter axons using infrared light. *Sci Rep*. 2017;7(1). doi:10.1038/s41598-017-03374-9

10. Zhuo J, Ou Z, Zhang Y, et al. (in review) Glucose can lower the threshold for infrared neural inhibition. *Neurophotonics*.

Appendix A

Voltage-gated Potassium Channels are Critical for Infrared Inhibition of Action Potentials: An Experimental Study

A.1 Abstract

Thermal block of unmyelinated axons may serve as a new modality for control, suggesting a means for providing novel therapies for pain. Computational modeling predicted that potassium channels are necessary for mediating thermal block of propagating compound action potentials (CAPs) with infrared (IR) light. This study tests that hypothesis. Results suggest that potassium channel blockers disrupt the ability of IR to block propagating CAPs in *Aplysia californica* nerves, whereas sodium channel blockers appear to have no significant effect. These observations validate the modeling results, and suggest potential applications of thermal block to many other unmyelinated axons.

A.2 Introduction

Precise control of neural activity (neuromodulation) is a challenge that has major scientific and clinical applications for treating and managing symptoms and conditions that are neuropathic in origin[1]. Electrical methods of neuromodulation have been used for some time, but suffer from disadvantages such as lack of selectivity, surgical complications, lead migration, lead breakage, MRI incompatibility, and tolerance buildup [2,3]. There is a need for an alternate modality of neuromodulation that can mitigate, if not completely eliminate, these disadvantages[4].

Use of infrared (IR) irradiation on nerves could be one such method. It has been shown that infrared light can be used for excitation [5–9] and inhibition of nerves [10–14]. The technique of infrared inhibition of nerves is spatially precise[10] and can be targeted to selectively inhibit axons of smaller diameters[12] . The ability to target axons of small diameters helps motivate IR inhibition as a modality that can target finer

sensory fibers carrying vital feedback information (e.g., pain, pressure, and temperature sensitivity). Understanding the mechanism of action of IR on nerves is critical to exploit the potential of IR inhibition as a clinical modality and optimize its parameter space. It has been shown that heating caused by IR absorption of nerves is responsible for inhibition[15–18]. From simulations using Hodgkin Huxley based computational models[17,18], we hypothesize that the mechanism underlying infrared inhibition of action potentials is a thermally-driven accelerated activation of voltage-gated potassium ion channels. This paper tests this hypothesis by studying infrared nerve inhibition in unmyelinated *Aplysia* nerves in the presence of voltage-gated ion channel blockers.

A.3 Methods

A.3.1 Animal preparation

After anesthetizing *Aplysia californica* (250-350 g, Marinus Scientific, Long Beach, CA) with isotonic magnesium chloride (333 mM, 50 % body weight), the right pleural abdominal (PA) nerves were dissected out and suctioned into extracellular recording electrodes to record their electrophysiological response. The nerves were maintained in room temperature (T ~20 ^{o}C) *Aplysia* saline (460 mM NaCl, 10 mM KCl, 22 mM $MgCl_2$, 33 mM $MgSO_4$, 10 mM $CaCl_2$, 10 mM glucose, 10 mM HEPES, pH 7.6) which was modified depending on the type of experiment (see below). Measurements using a calibrated microscope done in the laboratory show that the diameter of the *Aplysia* pleural abdominal nerve is 253.09 ± 144.70 μm in diameter (N = 12, for animals ranging 250-300g in weight).

A.3.2 Experimental setup

Nerve-recording electrodes were made by hand-pulling polyethylene tubing (1.27 mm outer diameter, 0.86 mm inner diameter) over a flame and cutting them to the desired diameter. Recording electrodes were suction-filled with *Aplysia* saline prior to suctioning the nerve. Nerve signals were amplified (×10,000) and band-pass filtered (300–500 Hz) using an AC-coupled differential amplifier (A-M Systems, Sequim, WA), digitized using an Axon Digidata 1440A digitizer (Molecular Devices, San Jose, CA) and recorded using Clampex computer software (Molecular Devices, San Jose, CA).

Monophasic stimulation current was supplied by a WPI A365 stimulus isolator (World Precision Instruments, Sarasota, FL) for all experiments (stimulation parameters: 200 μA current, τ_p = 2 ms, 1 Hz). The IR block was produced by a tunable diode laser (Capella Neurostimulator; Lockheed-Martin-Aculight, Bothell, WA) with a wavelength of λ = 1875 nm coupled to a 400 μm diameter multimode optical fiber (Ocean Optics, Dunedin, FL). The optical fiber was secured in place using micromanipulators. The laser was triggered at 200 Hz with 200 μs pulses for all experiments. Radiant exposures per pulse at the fiber output were calculated after measuring the power output using a power meter (Molectron EPM 2000, Coherent, Santa Clara, CA). The optical fiber was maintained in contact with the nerve surface for all irradiation experiments (Figure A.1A). The energy range used in the study was 215.29 ± 19.55 mJ/cm^2 per pulse.

A specially designed chamber was fabricated for our experiments. The chamber (Figure A.1B) consisted of 3 sections, and was 3D printed on a Form 2 printer using black Formlabs Standard Resin (Formlabs Inc., Somerville, MA, 50 μm layer height). The sections within the chamber were separated using 3D printed partitions (made of Hewlett Packard 3-Dimensional High Reusability PA {Polycyclic Aromatic} 12 to provide finer detail). Resin was used for printing, since it provided a good balance between quality and cost. For the experiments described in this paper, the width of the middle section (Δx, Figure A.1) was maintained between 2.5-3 mm. This width is small enough to allow passive currents to propagate past the middle chamber and re-initiate action potentials, even in the presence of voltage-gated sodium ion channel blockers. The width was also large enough to allow reliable placement of the optical fiber in contact with the nerve. Leaking was minimized by brushing the edges of the partitions with biocompatible Vaseline (Unilever, London/Rotterdam) petroleum jelly to provide a good seal.

A.3.3 Channel blockers and inhibitors

To test hypotheses derived from computational modeling studies[18], we used a blocker of voltage-gated potassium ion channels (Tetra-ethyl chloride, TEA), and a blocker of voltage-gated sodium ion channels (Tetrodotoxin). The formulation for TEA saline was 410 mM NaCl, 50 mM TEA, 10 mM KCl, 22 mM $MgCl_2$, 33 mM $MgSO_4$, 10 mM $CaCl_2$, 10 mM glucose, 10 mM HEPES, pH 7.6[19,20]. Prior studies[19,20] have shown that TEA blocks both voltage dependent and Ca^{+2} mediated potassium channels and disrupts potassium currents in *Aplysia* neurons. A solution of 60 μM of TTX saline solution (TTX, Enzo Life Sciences Farmingdale, NY) was prepared by adding 600 μL of 1 mM TTX normal *Aplysia* saline solution to make a final volume of 10 mL. The concentration of tetrodotoxin in saline was chosen to be

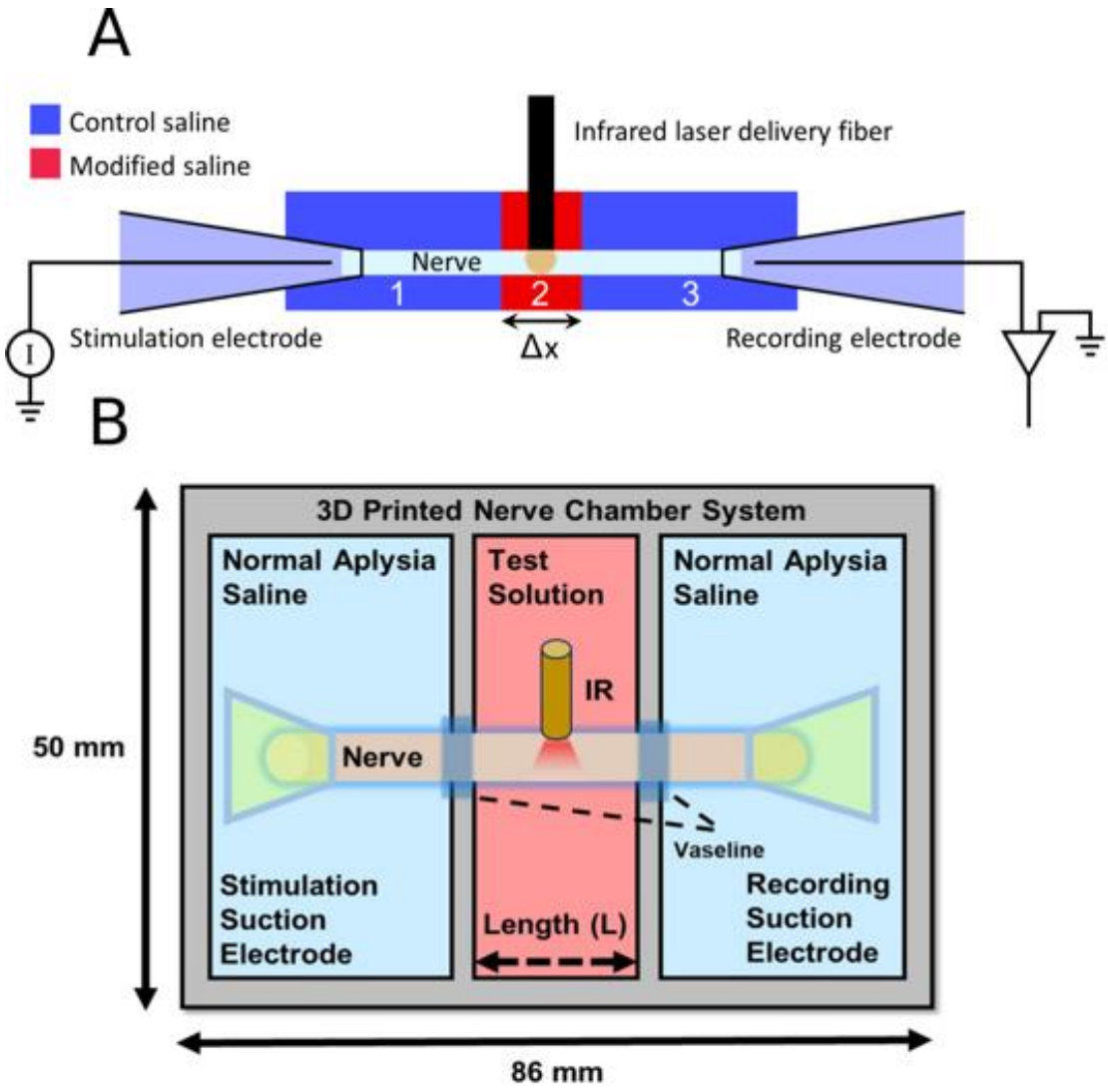

Figure A.1: Experimental setup. **(A)** Schematic of experimental setup, which consists of an *Aplysia* pleural abdominal connective nerve in a three-dimensional chamber that consists of three sections (1,2,3). The sections at the ends (shown in blue) contain normal saline. The section in the middle (2, colored red) contains saline solution with or without ion channel blockers. The nerve is irradiated with infrared laser radiation delivered via a fiber optic in the middle section. Suction electrodes at the ends of the nerve allow for stimulation and recording of compound action potentials. (Δx = 2.5 – 3 mm). **(B)** A schematic showing the layout of the nerve chamber with dimensions.

consistent with previously published experimental studies in *Aplysia* [21–23]. In these studies[21-23], it has been observed that use of TTX blocks inward currents and decreases spiking activity in *Aplysia* pacemaking and buccal neurons. The effect of all ion channel blockers was reversible, which was confirmed by performing recordings after washing out the ion channel blocker solutions. The effect of TEA was reversed after 2- 4 washouts over approximately 30 minutes. The effect of TTX was reversed after 2 - 3 washouts over approximately 15 minutes. The pH of all the saline solutions was adjusted to 7.6, which is the same as that of normal *Aplysia* saline. All solutions were brought to room temperature (T ~ 20^{o}C) prior to infusion into the chamber.

A.3.4 Experimental protocol

The nerve recording protocol consisted of multiple recordings of 20 second intervals. The nerve was electrically stimulated at a frequency of 1 Hz. Each recording consisted of three phases: 1) the time when the laser was OFF (t = 0 - 5 secs), 2) the time when the laser was ON (t = 5 - 15 secs), and 3) the time when the laser was again OFF (t = 15 - 20 seconds; Figure A.2A). Phase 3 of the recording allowed the nerve to recover from the thermal block induced by the IR laser irradiation during the second phase of the recording. In each study, the power of the laser was adjusted to obtain a complete block of the compound action potential (CAP) within the first five seconds after the laser turned on. Once the value of radiant exposure was determined, it was kept constant for the entire duration of a trial. Each trial consisted of three experimental conditions. The trials were conducted in a series of recordings in A-B-A-C-A format. Recording A refers to the observation of nerve activity in the control saline solution (with IR irradiation), before any ion channel blocker is introduced. Recording B refers to the observation of nerve activity in the presence of TEA (with IR irradiation), and Recording C refers to the observation of nerve activity in the presence of TTX (with IR irradiation). Experiments were repeated in six different animals (N = 6).

A.3.5 Data acquisition and analysis

CAPs were acquired at 50 kHz. Clampex (Molecular Devices, San Jose, CA) was used to record acquired data in the computer. After acquisition, data analysis was performed using a combination of AxoGraph X (Axograph Scientific, Berkeley, CA), Matlab (Mathworks, Natick, MA), Microsoft Excel (Microsoft, Redmond, WA) and *Mathematica* (Wolfram Inc., Champaign, IL). Each recording was

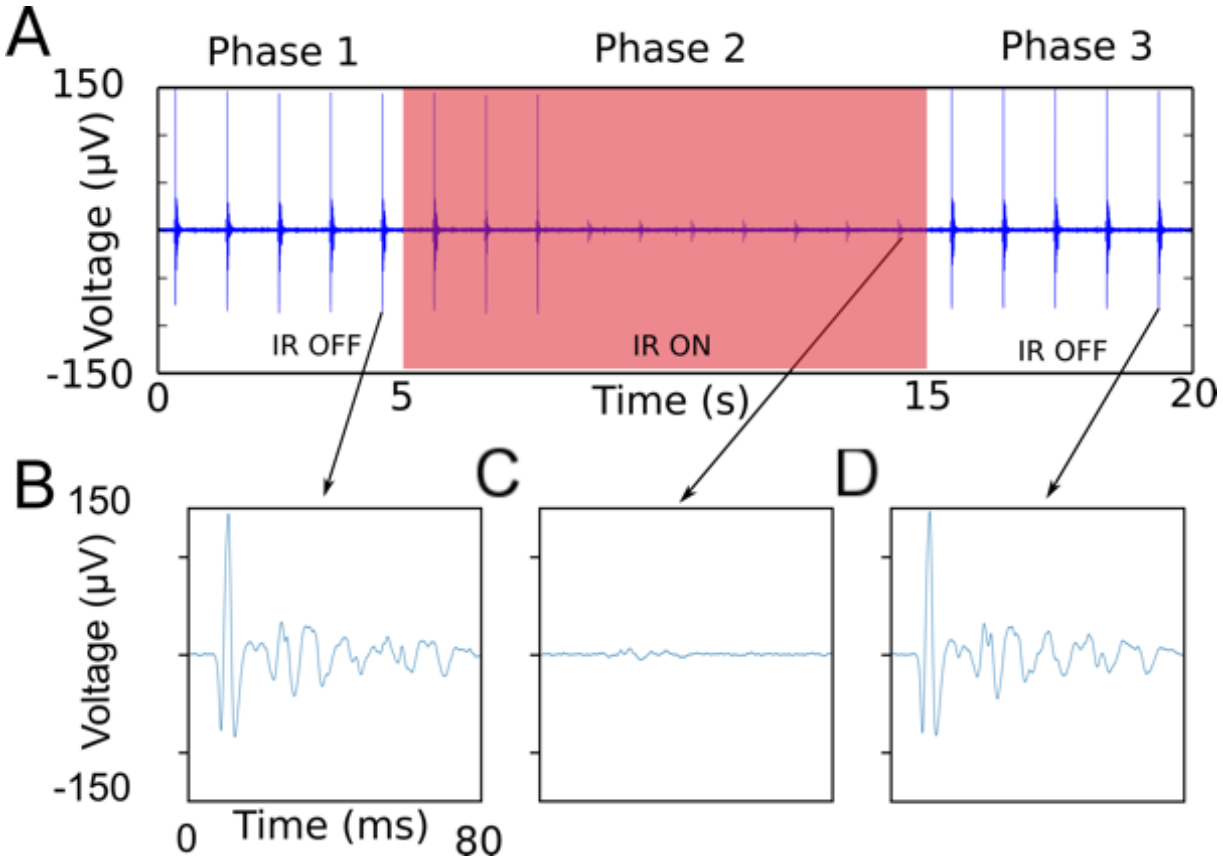

Figure A.2: **Typical Infrared Block**. (**A**) Recording showing infrared laser block obtained when the nerve is in normal *Aplysia* saline. The laser is switched on from t = 5 - 15 seconds and switched off for the last 5 seconds in each recording. (**B, C, D**). Signals from each phase of the recording are shown in high temporal resolution (pre-irradiation (B), during irradiation (C), and post irradiation (D)). In each of the high-resolution signals shown, the electrical recording artefacts are removed. (Laser parameters λ = 1875nm, optical fiber size = 400 μm, f = 200Hz, τ_p = 200 μs, H_o = 183 mJ/cm^2)

divided into three phases (laser OFF 0 - 5 sec, laser ON 5 - 15 sec, laser OFF 15 - 20 sec, Figure A.2A). The rectified area under the curve (rAUC) was evaluated for signals in each phase of the recording. The average of the areas under 'laser OFF' phase (phases 1 and 3) were plotted; since they were not significantly different (based on a paired t-test), the ratio of the rAUC in phase 2 relative to phase 1 were computed. For the 'laser ON' phase (phase 2), rAUC for the signals observed between t = 11 - 15 seconds of the recordings were measured. Prior studies had indicated that the effect of IR takes several seconds to occur[12], so focusing on the last five seconds of phase 2 ensured that the system had reached a stable state. The areas were normalized to the average area calculated for when the laser was off during the first phase of the recording. Tests for normality were performed using the Shapiro-Wilks test. The data also passed tests for heteroscedasticity, so that ANOVA could be applied. Post-hoc Tukey honest significant difference (HSD) tests were used to determine which changes were statistically significant at the $p = 0.05$ level.

A.4 Results

Control experiments using normal saline solutions (without any channel blockers) show a block when IR is used on the nerve (Figure A.2A – D; Figure A.3A-D). In the presence of TEA, the effect of IR in creating a propagation block is greatly reduced (Figure A.3E-H). Although TEA prevented laser-induced inhibition of the largest CAP units, it still appeared to inhibit smaller, slower units, which have a lower inhibition threshold, as predicted by modeling results[18]. In the presence of TTX, IR block is again observed (Figure A.3I - L).

Overall ANOVA for N = 6 independent experiments shows that the overall changes due to the presence of the blockers is highly significant ($p < 5x10^{-13}$). Post hoc Tukey HSD tests showed that normalized changes in areas of CAP's in saline and TTX (when IR was ON, phase 2) relative to control (IR laser off, phase 1) were not statistically significant, whereas normalized changes in the CAP's in TEA (laser ON, phase 2) relative to control (laser OFF, phase 1) showed no reductions during IR irradiation, are highly significantly different from the saline and TTX results ($p < 2 \times 10^{-6}$).

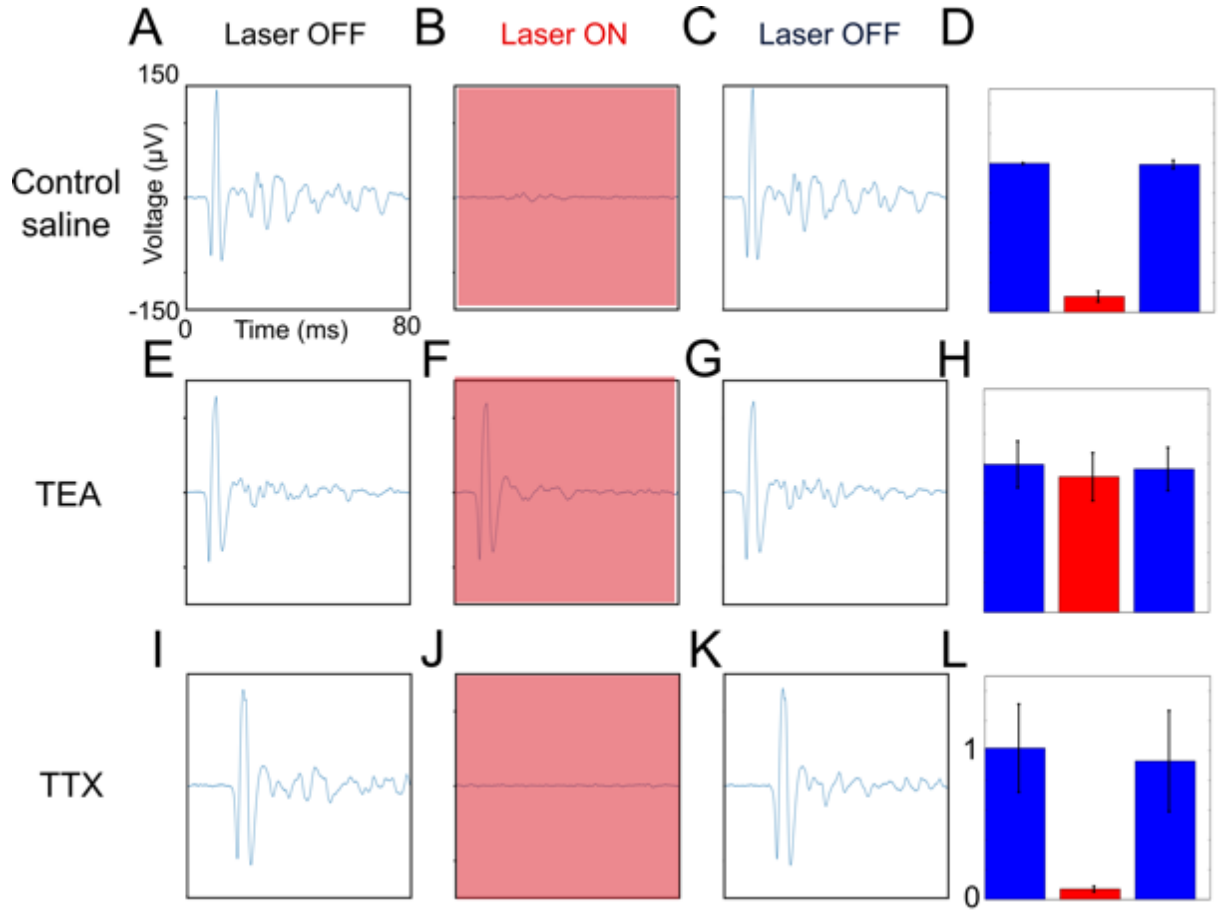

Figure A.3: **Blocking Potassium Ion Channels Eliminates IR Thermal Inhibition.** High temporal resolution views of representative signals from a nerve undergoing block in the presence of ion channel blockers. Signals prior to, during, and after laser irradiation in control saline (**A, B, C**), in TEA (**E, F, G**), and in TTX (**I, J, K**) are shown. Infrared-induced thermal inhibition is observed in control (normal) saline (**B**), and in TTX (**J**) when the IR laser is switched on. Thermal inhibition is reduced in the presence of a potassium channel blocker (tetraethylammonium chloride TEA) (**F**). Normalized rAUCs summarizing results from N = 6 observations in control saline (**D**), in the presence of TEA (**H**), and the presence of TTX (**L**). Lack of change in rAUC in TEA is highly significant (see text).

A.5 Discussion

The results presented in this paper support the hypothesis that the primary mechanism by which thermal block occurs is due to voltage-dependent potassium ion channels. As shown in previous modeling studies[17-18], in response to heating, voltage-dependent potassium channels in unmyelinated axons respond more rapidly than they do in unheated axons, generating a hyperpolarizing current in response to depolarizing currents. Results also suggest that sodium channels do not appear to play a significant role in establishing a thermal block. Increase in activity of potassium channels in mammalian models caused by accelerated kinetics and increased conductance at elevated temperatures have been reported in literature[24–26]. Potassium channel blockers have been reported to affect conduction block at elevated temperatures [27–29], but the underlying mechanism has remained elusive. While all studies mentioned above examined mammalian systems, to the best of our knowledge, the study presented here is the first to highlight the key role of potassium channels during thermal block induced by infrared laser radiation in an unmyelinated axon system. These results may lead to novel targeted therapies for unmyelinated axons, which carry sensory information such as pain and temperature in a wide range of species, including humans.

A.6 References

1. Mekhail, N. A. *et al.* Clinical Applications of Neurostimulation: Forty Years Later. *Pain Pract.* **10**, 103–112 (2010).

2. Shim, J. H. Limitations of spinal cord stimulation for pain management. *Korean J. Anesthesiol.* **68**, 321–2 (2015).

3. Bendersky, D. *et al.* Is Spinal Cord Stimulation Safe? A Review of Its Complications. *World Neurosurg.* **82**, 1359–1368 (2014).

4. Chernov, M. M. *et al.* Material considerations for optical interfacing to the nervous system. *MRS Bull.* **37**, 599–605 (2012).

5. Wells, J. *et al.* Optical stimulation of neural tissue in vivo. *Opt. Lett.* **30**, 504–6 (2005).

6. Wells, J. *et al.* Biophysical Mechanisms of Transient Optical Stimulation of Peripheral Nerve. *Biophys. J.* **93**, 2567–2580 (2007).

7. Duke, A. R. *et al.* Combined optical and electrical stimulation of neural tissue in vivo. *J. Biomed. Opt.* **14**, 060501 (2009).

8. Thompson, A. C. *et al.* Optical Stimulation of Neurons. *Curr. Mol. Imaging* **3**, 162–177 (2014).

9. Ford, S. M. *et al.* A review of optical pacing with infrared light. *J. Neural Eng.* **15**, 011001 (2018).

10. Duke, A. R. *et al.* Transient and selective suppression of neural activity with infrared light. *Sci. Rep.* **3**, 2600 (2013).

11. Lothet, E. H. *et al.* Alternating current and infrared produce an onset-free reversible nerve block. *Neurophotonics* **1**, 011010 (2014).

12. Lothet, E. H. *et al.* Selective inhibition of small-diameter axons using infrared light. *Sci. Rep.* **7**, 3275 (2017).

13. Wang, Y. T. *et al.* Infrared inhibition of embryonic hearts. *J. Biomed. Opt.* **21**, 60505 (2016).

14. Walsh, A. J. *et al.* Action potential block in neurons by infrared light. *Neurophotonics* **3**, 40501 (2016).

15. Huxley, A. F. Ion movements during nerve activity. *Ann. N. Y. Acad. Sci.* **81**, 221–46 (1959).

16. Mou, Z. *et al.* A simulation study of the combined thermoelectric extracellular stimulation of the sciatic nerve of the Xenopus laevis: the localized transient heat block. *IEEE Trans. Biomed. Eng.* **59**, 1758–69 (2012).

17. Ganguly, M. *et al.* Modeling the effects of elevated temperatures on action potential propagation in unmyelinated axons. in (eds. Madsen, S. J. et al.) **9690**, 96901O (International Society for Optics and Photonics, 2016).

18. Ganguly, M. *et al.* Thermal block of action potentials is primarily due to voltage-dependent potassium currents: A modeling study. *J. Neural Eng.* (2019).

19. Hermann, A. *et al.* External and internal effects of tetraethylammonium on voltage-dependent and ca-dependent k ÷ currents components in molluscan pacemaker neuron*S*. *Neuroscience Letters* **12**, (1979).

20. Hermann, A. *et al.* Effects of tetraethylammonium on potassium currents in a molluscan neurons. *J. Gen. Physiol.* **78**, 87–110 (1981).

21. Miller, N. *et al.* Neurons controlling *Aplysia* feeding inhibit themselves by continuous NO production. *PLoS One* **6**, e17779 (2011).

22. Geduldig, D. *et al.* Voltage clamp of the *Aplysia* giant neurone: early sodium and calcium currents. *J. Physiol.* **211**, 217–44 (1970).

23. Futamachi, K. *et al.* Action of tetrodotoxin on pacemaker conductances in *Aplysia* neurons. *Brain Res.* **233**, 424–30 (1982).

24. Fleischmann, B. K. *et al.* Control of resting membrane potential by delayed rectifier potassium currents in ferret airway smooth muscle cells. *J. Physiol.* **469**, 625–38 (1993).

25. Pahapill, P. A. *et al.* Modulation of potassium channels in human T lymphocytes: effects of temperature. *J. Physiol.* **422**, 103–26 (1990).

26. Beam, K. G. *et al.* A quantitative study of potassium channel kinetics in rat skeletal muscle from 1 to 37 degrees C. *J. Gen. Physiol.* **81**, 485–512 (1983).

27. Eliasson, S. G. *et al.* Potassium ion channel blockade restores conduction in heat-injured nerve and spinal nerve roots. *Exp. Neurol.* **93**, 128–137 (1986).

28. Bostock, H. *et al.* After-effects of near-threshold stimulation in single human motor axons. *J Physiol* **564**, 931–940 (2005).

29. Wu, B. S. *et al.* Heat shock-induced thermoprotection of action potentials in the locust flight system. *J. Neurobiol.* **49**, 188–199 (2001).